ORDERING OF CURVING INTERFACES

by

John R. Frank

B.S., Yale University, 1999

Submitted to the Physics Department
in partial fulfillment of the requirements for the degree of

Doctorate of Philosophy

at the

MASSACHUSETTS INSTITUTE OF TECHNOLOGY

June 2023

©John R. Frank, 2023. This work is licensed under CC BY 4.0. The author hereby grants to MIT a nonexclusive, worldwide, irrevocable, royalty-free license to exercise any and all rights under copyright, including to reproduce, preserve, distribute and publicly display copies of the thesis, or release the thesis under an open-access license.

Author . . . .
Physics Department
May 19, 2023

Certified by. . . . .
Mehran Kardar
Professor of Physics
Thesis Supervisor

Accepted by . . . .
Lindley Winslow
Associate Department Head of Physics

ORDERING OF CURVING INTERFACES

by

John R. Frank

Submitted to the Physics Department
on May 19, 2023, in partial fulfillment of the
requirements for the degree of
Doctorate of Philosophy

Abstract

Curved surfaces are fundamental parts of living systems. This thesis examines how materials can order on curving interfaces, resulting in shape changes and pattern formation. Many phenomena that are well-studied in flat space display new behavior when lifted onto a deformable surface: liquid crystals buckle membranes into peaked shapes, diffusing particles can sense curvature and localize patterns, and anisotropic growth can form branching structures over many scales.

The systems I study include fluid membranes and growing solids. My framework connects the study of liquid crystals to cytoskeletons of living cells, and provides tools for understanding the machinery of vesicles as well as the remodeling of entire cells. Orientational order plays a central role on these surfaces. Topological defects in an orientation field are an area of intense historical and on-going interest. This work was published in a paper with my coauthor and advisor Mehran Kardar.

I show that curvature modifies diffusion and can change the spatial patterns generated by Turing instabilities. Turing patterns have been studied extensively on flat substrates. To lift this patterning mechanism onto the highly curved shapes of living systems, we apply tools from perturbation theory and differential geometry to analytically compute modifications to the Laplacian and its normal modes on curved surfaces. This extends the framework of differential geometry to understand chemical concentrations diffusing on biological interfaces. In this thesis, I expand upon a paper I published with my coauthors Jemal Guven, Mehran Kardar, and Henry Shackleton.

I conclude with initial results from a new cellular automaton of anisotropic solid growth, which generates tree-shaped morphologies. This suggests that branching structures in botanical trees may result from a simple, universal growth process. Topological defects naturally appear at the branch points of these structures in simulations and in nature. By expanding biophysics from its historical focus on the molecular realm to include macroscopic living solids, we may eventually learn to save our global forests and engineer growing structures on Earth and beyond.

Thesis Supervisor: Mehran Kardar
Title: Professor of Physics

Acknowledgments

I am a planner. I schedule months out and scheme about decades-long projects. Consequently, I'm often humbled by serendipity. Each surprise has brought new people into my life. For this, I am immensely grateful. In 1998, I was admitted to MIT and won a Hertz Fellowship, so I've been a graduate student at MIT for 25 years. I must thank many people. These acknowledgments mention only a few of the many people who have shaped my thoughts and shared "spots of time."[30]

My advisor Mehran Kardar has been an inspirational reference point in my life ever since I took his statistical mechanics class, 8.333, in the fall of 1999. We were several weeks into the class when Mehran paused at the chalkboard, went to his leather satchel, and pulled out a set of paper notes. He explained that he was double checking that he used a γ for this particular variable. A whisper shot through the class as everyone finally realized how much knowledge we had received without his ever needing notes. At that point, all I knew about Mehran was that his class was my favorite. Years later, when Google Scholar came into existence, I learned just what a towering figure Mehran is in statistical physics.

Mehran set me on the task of understanding how cells divide in the middle. After developing some initial skills in differential geometry, I commented to Mehran that "all the derivatives disappeared" when I used a particular embedding vector to describe a cell. He's response was "I'd tell everyone about that," so we set to work on my first paper. Mehran's approach to seeking instructions from nature continues to fill me with a excitement.

I am indebted to Jemal Guven for many discussions and inspiration, see for example Ref. [193]. Jemal has been like a second advisor for me. I was lucky that Christoph Haselwandter's paper on synaptic patterning [253] inspired further discussions between Martin Müller, Jemal Guven, and Mehran, which then naturally led to my paper with Jemal, Mehran and Henry Shackleton [308]. Jemal's insistence that the geometry need not be complicated — actually *should* not be complicated — is an invaluable guide. His insight on conformal mapping was essential to Chapter 3. I am grateful to my coauthors' focus on getting that paper accepted while I was traveling six days a week selling Diffeo in 2019.

I am indebted to my committee, Professors Nikta Fakhri and Wolfgang Ketterle, for encouraging me to graduate. Without their wise counsel, I might not have gotten here!

I'd like to thank many professors and members of the MIT community who have influenced me, especially Dan Rothman for his guidance and long-range vision. I met my friend Erik Rauch in Dan's seminar. Erik and I founded MetaCarta together with Doug Brenhouse, our COO. MetaCarta led to my parallel career in information retrieval. I miss Erik. I'm grateful to Doug for his friendship and guidance over the last two decades. I'd also like to thank Tim Shepard for teaching me about many things, including linux, software engineering, and radio, and Jacques Dumais for teaching me about plants.

I must also thank Wikipedia and the Wikimedia Foundation, the Internet Archive, and the free software movement, especially Python and Linux. These cornerstones of civilization enable all of us to see farther.

I am profoundly indebted to the Hertz Fellowship for transforming my life trajectory many times over the past 25 years that I have been a graduate student. The Hertz Fellowship enabled me to always keep at least one foot firmly planted in research while I followed serendipity. At this point, I'd say that the Hertz Fellowship has re-trained me to plan to receive the unexpected. The Hertz Foundation also connected me with wonderful collaborators, especially my fellow physicist Dan Roberts, whose friendship and insights I've come to rely on in so many ways.

Dan and I started Diffeo together with Max Kleiman-Weiner, another wonderful Hertz Fellow. We were very lucky to gather such a great team at Diffeo. I'm especially grateful to our COO Jason Briggs for his friendship and guidance.

Thank you to everyone at MetaCarta, Diffeo, and TREC KBA. I learned so much from my remarkable cofounders, colleagues, advisors, investors, partners and customers.

At Yale, Peter Kindlmann's guidance taught me why I love design and sent me to IDEO for a semester with Rickson Sun. It was Professor Kindlmann who first pointed out to me the remarkable power of naming things — "once named, it takes on an existence of its own." Thank you to Bob Grober for helping me reach toward quantum microscopes.

My first startup-like experience was Team Lux, building Yale's solar car. Thank you to everyone on TEAM LUX! Thank you to Alan Bromley for showing me how the system works. Tony Massini for teaching me the ways of the machine shop.

I am deeply grateful to my wife, Professor Elsie Sunderland, for her thoughtful support and partnership through thick and thin — and for tolerating such an unqualified bag carrier.

Thank you to Jan Migaki at North Shore Country Day for inventing a physics curriculum when we asked. Thank you to Bob Jordan and his Apprentice Program Experimental School (APES). Bob's basement radio lab has been my reference point for "good clean living" ever since.

I was very lucky to meet Eugene Kuznetsov at North Shore. Thank you for being my friend all of these years.

Thank you to the Springer School in Cincinnati and especially Deb Barber for reconfiguring my alphabet.

Physics and chemistry entered my life early when my father, Richard Frank, taught me how to use the periodic table for thinking up firecrackers and sparkling volcanoes. I caught his passion for rocks & minerals and demonstrating physics through science fairs at the Springer School. I wish he were here to be thanked properly.

Finally, I want to thank my mother, Barbara Frank. She believed in me even when teachers informed her that I hadn't learned the alphabet on schedule.

– John R. Frank
Cambridge, Massachusetts
May 2023

Contents

1 Introduction 29

1.1 Geometry 31

1.2 Diffusion 37

1.3 Vortex Dynamics 42

1.4 Physics of Biology 44

1.4.1 Early Biophysics 44

1.4.2 Microscope Era of Biophysics 45

2 Defects in nematic membranes can buckle into pseudospheres 53

2.1 Background Review 54

2.2 Elastic Free Energy of Nematic Membranes 55

2.3 Buckled Defects Shapes 58

2.4 Conclusions and Outlook 65

2.5 Appendix: Nematic Membranes in Fixed Geometries 67

2.6 Appendix: Stability of Buckled Defect Shapes 70

3 Turing Patterns on Curved Interfaces 73

3.1 Motivation 73

3.2 Pinning of Diffusional Patterns by Non-Uniform Curvature 82

3.3 Perturbation Theory 92

3.3.1 Deformed Cylinder 92

3.3.1.1 Cylinder Ridge: Splits the Modes 102

3.3.1.2 Cylinder Ridge: First-Order Eigenfunction 106

3.3.1.3 Cylinder with Ripples 109
3.3.2 Conformal Mapping of a Deformed Sphere 113
3.3.3 Conformal Mapping of Deformed Planar Drum 118
3.4 Conclusion 119

4 Outlook 121

4.1 Filaments on Neck Geometries 121
4.2 Self-Directed Growth of Living Solids 123
4.2.1 Review of Previous Branching Models 124
4.2.2 Observations of Wood 127
4.2.3 2+1D Anisotropic Restricted Solid-on-Solid (ARSOS) 132
4.2.4 1+1D Self-Directed Solid (SDS) 137
4.2.5 2+1D Self-Directed Solid (SDS) 146
4.2.6 Covariant Model of Surface Growth 150
4.3 Conclusion 152

A Differential Geometry 155

A.1 Gauss-Codazzi-Weingarten and Similar Identities 158
A.2 Principle Two-Bein 159
A.3 Scalar Laplacian 160
A.4 Geometric Identities 161
A.5 Functional Derivatives 162

B Note on Cole-Hopf Solutions to the KPZ Equation 167

C Discussion of OPT in non-flat coordinates 171

D Operator Perturbation Theory with Euclidean Support 193

D.1 Non-Degenerate Perturbations 194
D.2 Degenerate Perturbation Theory 199
D.2.1 Second-Order Degenerate Perturbation Theory 201
D.3 Periodic Potentials 205

D.3.1 Periodic Boundary Conditions 207
D.3.2 Limit of Infinity System Size 218
D.3.3 Non-Periodic Boundary Conditions 220

Bibliography **227**

List of Figures

1-1 Monge's representation of a curved surface uses a Cartesian plane (x, y) to parameterize a single-valued height function $h(x, y)$ that cannot accommodate overhangs. R_1 and R_2 are the minimum and maximum radii of curvature at a point. These radii have a sign that identifies the two sides of the surface. 32

1-2 This is part of the marvelous phase diagram of minimum energy shapes for the Canham-Helfrich model augmented with volume and area constraints. These shapes are axisymmetric. The horizontal axis is the reduced volume that reaches 1 for a sphere. This segment of the overall diagram is at zero spontaneous curvature. As the reduced volume is increased from left to right, the energy minimum goes through two discontinous transitions. Reproduced from Fig. 9 with permission from Udo Seifert, Karin Berndl, and Reinhard Lipowski's "Shape transformations of vesicles: phase diagrams for spontaneous-curvature and bilayer coupling models," Phys Rev A 44 (2) p1182–1202 ©1991 by the American Physical Society. 37

1-3 Turing's Unstable Band of wavelengths resulting from the interplay of reaction and diffusion. 41

1-4 The bacterium *Bacillus Subtilis* on the right has a diameter of 600nm. “The furry appearance on the outside is due to a coat of long-chain sugars attached to the cell membrane. This coating helps trap water to prevent the bacterium from becoming dehydrated,” from Lipid Bilayer article in Wikipedia. Image taken with a Tecnai T-12 TEM by Allon Weiner, The Weizmann Institute of Science, Rehovot, Israel, figure from Wikipedia. Center diagram shows the extent water penetration into a lipid bilayer, figure from Wikipedia. On the left, a water molecule measures about a quarter of a nanometer[207] and has 10x higher electron density around Oxygen, figure from Martin Chaplin’s website on water, see Internet Archive’s copy. [311]. 47

1-5 (Left) A cortical ring in silkworm spermatocytes from Chen *et al* in PLOS Biology 2008.[233](Center) Overlays of two image series taken at 15 second intervals to show keratocyte crawling via its large lamelipodia, and (Right) keratocyte stained with rhodamine phalloidin to label the actin filaments.Reprinted from Cell 112 (4) “Cellular Motility Driven by Assembly and Disassembly of Actin Filaments” by Thomas D Pollard & Gary G Borisy ©2003, p453–465, with permission from Elsevier.[190] 48

1-6 **Illustrating four orders of magnitude.** A: BAR protein domain is a banana-shaped with a radius of curvature of 11nm. It is highly conserved in evolution and plays key roles in the formation of tubules and other structures. (Reprinted with permission from AAAS: “BAR Domains as Sensors of Membrane Curvature” by Peter *et al* in *Science* 2004.[200]) B+C: clathrin triskelions make cages and pits that form vesicles. Image reconstruction in B shows a 36 clathrin hexagonal barrel with D6 symmetry. (Reproduced with permission from Springer Nature, “Molecular model for a complete clathrin lattice from electron cryomicroscopy” by Fotin *et al* 2004.) C: clathrin pits forming in a chick fibroblast. (From Heuser *et al* “Hypertonic media inhibit receptor-mediated endocytosis by blocking clathrin-coated pit formation” in *JCB* 1989.[129] D: Epithelial cells stretched over a surface, from “An adaptive microscope for the imaging of biological surfaces by Abouakil *et al* in *DGD* 2021. 49

1-7 (Left) A –1 topological defect in the notch of a White Pine branch. (Right) Model of plant cell wells highlighting that the extra cellular matrix is extruded through the cell membrane by molecular machines that create a *ordered* array of filaments, often with orientational order. by Yoshimi Nakano, Masatoshi Yamaguchi, Hitoshi Endo, Nur Ardiyana Rejab, and Misato Ohtani, May 2015, in *Frontiers in Plant Science* 6 (288), CC BY 4.0.[281]. Note that the membrane thickness shown on the right side of Figure 1-7 is not to scale, because the cell walls extend for microns beyond the 4nm-thick membrane. This is necessary, because it shows that a transmembrane protein is extruding the cellulose. 50

2-1 Rod orientations around a general uniform +1 topological defect. $\xi = 0$ corresponds to an aster, and $\xi = \pi/2$ to a vortex. 58

2-2 An illustration of the coordinate system. 59

2-3 An example of buckled shape for $r_1 = 1$ and $c = 1$. 63

2-4 The tangent angle (not the height) as a function of radius in units of r_1. Solid curve: The Bessel function solution for $\chi(\epsilon)$ for $\nu = 1$. Dashed curve: $\cos^{-1}\left(\sqrt{\left((r/r_1)^2 + c\right)/(1+c)}\right)$ for $c = 2.5$ chosen to suggest matching in the crossover. 65

3-1 Spiral waves formed by Min proteins, showing only MinE. (Both MinD and MinE are 1 µM concentration.) Reprinted with permission from AAAS, "Spatial Regulators for Bacterial Cell Division Self-Organize into Surface Waves in Vitro" by Loose *et al.* in *Science* 2008.[237] . . 75

3-2 This torus illustrates different values of Gaussian curvature. The red outer region has positive Gaussian curvature where the MSD of a diffusing particle is shorter, so diffusion is slower. The interior neck region has negative Gaussian curvature and longer MSD, so faster diffusion. See Ref. [244] for further discussion. 78

3-3 Patterns from the Thomas-Murray RD model in Eqn. (3.14) are entrained to a Gaussian-shaped ridge, switching in phase between inward and outward deformations. Red (blue) indicates a high (low) concentration of chemicals. Vertical dimension magnified 3x. Parameters: $\nu_1 = 1$, $\nu_2 = 10$, $u_{10} = 92$, $u_{20} = 64$, $\alpha = 1.5$, $K = 0.1$, $\gamma = 2$, and $\rho = 18.5$. Unless specified otherwise, other figures have these parameters. (See Sec. 3.3.1.1 for details.) 86

3-4 (Left) three functions of wave-number: (blue) Laplacian eigenvalues on a rippled cylinder, including a band gap at the edge of the Brillouin zone (BZ) at $m/2$; (black dotted) Turing spectrum on a non-rippled cylinder; (red) Turing spectrum on a rippled cylinder. For the case shown with $k^* > m/2$, the sine mode is selected; (cosine selected if $k^* < m/2$). (Right) Numerical confirmation: Concentration patterns in the Thomas-Murray model switch from troughs to ridges as the unstable chemical wavelength, k^*, is dialed past twice the ripple wavelength by changing $\gamma = 1.125$ (upper) to $\gamma = 0.975$ (lower). Vertical dimension magnified 3x. Supplement includes video of sweeping m (Mathematica & COMSOL files). 88

3-5 Sufficiently large bumps entrain spotted patterns (top pair). Initial patterning on an undeformed sphere shows Y_5^5 (bottom-left); the inward bumps of a “pinched sphere” amplify lower harmonics, causing Y_3^0 to appear (bottom-right). 90

3-6 Noise-induced quasipatterns appear when geometric ripples split degenerate eigenmodes of an RD system below threshold. Deformations pin the time-averaged intensity of fluctuations in RD quasipatterns (top); compare this with the same intensity of extrinsic noise on a flat surface (bottom). For all two figures, $\nu_2 = 6$ and $K = 0.15$. 91

3-7 Illustration of three lengths and an angle that can be measured on a cylindrically symmetric shape. 93

3-8 Illustration of the conformal coordinate $v(z)$ as a function of z on three different cylinders of initial radius $R_0 = 3$ and $L = 20$. The two straight blue dotted lines are guides to the eye: the horizontal dotted line is located at the undeformed cylinder radius of $R_0 = 3$, and the diagonal dotted line has a slope of one. The two deformed cylinders have a Gaussian bump centered at $z = 0$ with $\sigma = 3$. The solid blue line shows shows a bump with amplitude $\epsilon = 0.3$, and dashed orange line $\epsilon = 0.6$. The corresponding diagonal lines show the $v(z)$ curves. The solid blue diagonal line is $v(z)$ for the lower amplitude bump. Note that these plots use $h = \exp\{-z^2/(2\sigma^2)\} - M$, where M is a constant that keeps the surface area of the cylinder the same as the undeformed cylinder, see Eqn. 3.40. 96

3-9 These parametric plots show show $\exp\{-z^2/(2\sigma^2)\}$ on the left and $\exp\{-v^2/(2\sigma^2)\}$ on the right. The dashed redlines are $R(v)$, and the solid blue lines are $R(z)$. The horizontal axes count both v and z. These use the same numerical values as the higher amplitude orange dashed line in Fig. 3-8. The lower two have $\epsilon \to -\epsilon$ to make an inward constriction. 97

3-10 **Ripple in v.** The horizontal axis is the lab frame coordinate z along the axis of the cylinder. The solid line is what is seen in the lab frame when we express the deformation as a function of the conformal coordinate, v. The dotted line has slope of one to guide the eye, and the dashed line is the value of the conformal parameter v. This is plotted parametrically in v using Eqn. 3.30. $\epsilon = 0.1, k = 5, R_0 = 10, L = 50$. 98

3-11 **Mode Splitting for Outward Bump** $0 < \epsilon$**:** The horizontal axis is the wavenumber, k, and the vertical axis is the eigenvalue $\lambda_{sk}^{(0+1)}$ at $s = 0$, $L = 1000$, and $\sigma = 10$, the mode splitting is largest at $k^* = 11$ and the cosine mode's eigenvalue is 184ϵ larger (less negative) than the sine mode's, for an outward bump. This means that the effective diffusion coefficient for the sine mode is larger than for cosine. These lines are produced with $\epsilon = 0.6$ and the difference between the $\lambda_{sk_\pm}^{(1)}$ made more visible by magnifying the vertical axis 20x. 106

3-12 For, $\epsilon = 0.6$, $L = 1000$, $\sigma = 10$, $k = k^* = 11$. The left shows an inward constriction and the right shows an outward ridge. The dashed lines show the unmodified mode, which is normalized. The perturbed mode is not normalized. The relative magnitude of the mode near the bump compared to far from the bump shows how much the mode is localized at the bump. 108

3-13 **Turning on the localization:** This shows the amplitude of the perturbed mode in Fig. 3-12 turning on gradually as ϵ sweeps from zero up to 0.6. 108

3-14 This shows the amplitude of first-order corrections for the perturbed mode in Fig. 3-12. 109

3-15 Illustration of the Bragg-like matrix for our momentum-dependent periodic potential ($\epsilon = 1$). This shows just one harmonic, so a single cosine. Other periodic ripple profiles could be decomposed into a superposition of multiple harmonics. For large L, these off-diagonal stripes will be well-separated. The three blue dashed squares show examples of the 2×2 Bragg matrix just below the BZ, exactly on the BZ, and just above it. 111

3-16 **Diffusion Band Gap**: the spectral band gap familiar from solid-state physics appears in this new context. The horizontal axis is the k labeling the eigenfunctions, and the vertical axis is the corresponding eigenvalue. $m = 100$, $\epsilon = 0.5$, $L = 50$ 112

3-17 Near the edge of the BZ, eigenfunctions have wavelengths approximately twice the ripple wavelength. The sine mode has extrema in the troughs of the ripples, and the cosine mode on the peaks. 113

3-18 Like the deformed cylinder, a sphere has several lengths and angles that can be measured in the lab. The examples on the right show $h = 0.3\cos(p\theta)$ for $p = 21$ and $p = 2$. The orange circles are the undeformed reference shape. 114

4-1 This remarkable stereo image shows a membrane constriction produced *in vitro*. Reproduced from "Architecture of the ring formed by the tubulin homologue FtsZ in bacterial cell division" by Szwedziak *et al* in *eLife* 2014.[276]. 122

4-2 "All the branches of a tree at every stage of its height when put together are equal in thickness to the trunk [below them]. All the branches of a water [course] at every stage of its course, if they are of equal rapidity, are equal to the body of the main stream." passage 394 in J.P. Richter's "The literary works of Leonardo da Vinci" [50], which comes from pages 78v – 79r in the *Paris Manuscript M*[4], see also Plate XXVII in Ref. [50]. [See 274, Minamino & Tateno] for an analysis of how closely real botanical trees obey da Vinci's Tree Rule. 124

4-3 Left: pulling back outer layers of a Lilac branch from my garden. Right: Helianthus stem in section showing A-Epidermis, B-Cortex, C-Pith, D-Xylem, E-Phloem fibers, F-Vascular cambium. Scale=0.2mm. "Cells of the vascular cambium (F) divide to form phloem on the outside, located beneath the bundle cap (E), and xylem (D)." This vascular cambium is in bundles of phloem and xylem together, and is starting to connect the bundles at point F. (Reproduced by Wikipedia, image made by Jon Houseman and Matthew Ford.) 127

4-4 (Top) basswood branch with bark soaked off in hot water, one finds +1 topological defects in the notches of branches. The defect core traces a line through the layers of growth that is visible in a cross-section on the top-left. (Bottom) From left to right: Basswood, White Pine, and Silver Maple branches have different grain sizes, and all exhibit defect structures in the notches. 128

4-5 (Left) Woody spike emerging below a –1/2 defect in Silver Maple, a dicot. The other –1/2 defect is on the other side of this small branch growing out of a larger branch. (Center) Cross section of Maize (Zea mays), a monocot, about 800 μm diameter. A lateral root is bursting out of the parent root. Root tips can diverge at any location. In contrast, shoots that form leaves and stems typically emerge only from the apical meristem. Image by John Bebbington FRPS. (Right) Diagram of tip geometry. 130

4-6 **Anisotropic RSOS of a Spin Wave.** These nematic test cases have a $\pi/2$ spin wave frozen at the boundaries: left spins pinned pointing inward and right spins pointing up. The initial height profile is a cosine wave in the horizontal direction, so there are "hills" on the left and right edges that are 80 height steps above the "valley" in the center. The left column shows low temperature (b=100), and the right shows high temperature (b=1). The bottom row shows small coupling of growth rate to alignment (p=0.1), and the top row shows stronger coupling (p=10). **upper-left:** at low temperature and high enough coupling constant, growth quickly moves the spin wave to a crevice that falls behind and the surface width diverges. In all other cases, even if crevices form, they lag behind only a small amount and the surface remains stable. **lower-left:** at lower coupling, the misaligned spins focus in a crevice that lags the rest of the surface by a small amount. **upper-right:** at high temperature and coupling, a network of crevices form between domains of mostly aligned spins. **lower-right:** at high temperature and low coupling, the surface becomes approximately uniform in height and the spin field evolves on a flat substrate. 135

4-7 **Anisotropic RSOS of a Spin Wave (zoom).** The same four cases as Fig. 4-6 zoomed in to show details. The deep crevices in the upper-left will fall farther and farther behind. This is analogous to the branch points with –1 topological defects in the SDS models below. 136

4-8 **Various Morphologies at mass=1e7.** This illustrates observed morphologies as a function of noise η on the horizontal axis versus aspect ratio α on the vertical axis. *Green* indicates a site that has open child sites, which we call "cambium" in analogy to woody trees. *Orange* indicates a site with no open child sites, which we call "wood." The colored contour plot back drop is discusssed below. 139

4-9 **Branches diverge and coalesce on many scales.** (left) zoom in on a portion of the shape on the right. (right) full view of 17,061,445 cells grown at $a = 2000$ and $\eta = 0.05$ using Vicsek-style noise. The black stair steps are a scale bar. The number of steps indicates the power of ten, so the largest step is 10^3 lattice sites. The stack bar chart shows that wood sites (orange) out number cambium sites (green) 58% versus 42% in this snapshot. The inner stacked bar chart indicates that there are roughly as many +1 defects as −1 defects. Eventually, all of this interstities shown here will fill in with wood; however, by that time, the farthest tendrils will have reached even farther. 141

4-10 **Concept of Statistical Self-Similarity**: Figure from Bouda, Caplan, & Saiers: "Construction of the Koch curve, following Falconer (2003). Each interval (A) is divided evenly into three and the middle section is replaced by the complementary two sides of an equilateral triangle (B). The process is repeated for each newly created interval, yielding the second (C), third (D), and nth iterations. The Koch curve is the limit approached as $n \to \infty$. The limit curve can be subdivided into four quarters, each an exact copy of the whole, scaled down by a factor of three. The curve is thus self-similar with a similarity dimension of $\log(4)/\log(3)$. Even with n = 10 (E), zooming in on the pinnacle of the curve by a factor of three yields an image visually indistinguishable from the largest magnification five times over, meaning the curve is approximately self-similar over a finite range of scales. Following the same construction, but randomly choosing the side of the old interval on which each new pair of intervals is placed, yields one of many "statistically self-similar" curves (F). These cannot be divided into sets of identical copies; rather, their parts are scaled random variations on the whole and they only conform to a fractal dimension on average."[283] 143

4-11 **Estimating Self-Similarity and Fractal Dimension**: Branched shapes in the middle region of Fig. 4-8 exhibit self-similarity over several scales. This plot comes from the shape in Fig. 4-9. ϵ is the side length of boxes in a grid. The blue-dashed line counts the number of boxes N that contain part of the shape at a given ϵ. The horizontal axis is $\log_2 1/\epsilon$. The blue circles mark reductions in ϵ by half. Right axis shows the slope of this line. Red dots are slopes of individual segments of the blue-dashed line within 2 σ of the average slope. Black x markers have been dropped. The green range shows seven segments used in the best fit. 145

4-12 **Proposed Draft of Phase Diagram for 2+1D self-directed growth**: Like the morphologies found in 1+1D (Fig. 4-12, the 2+1D SDS model generates pillars and trees and spheres. (Left) very small noise $\eta = 0.01$. (Middle) small noise $\eta = 0.07$. (Right) high noise $\eta = 1$. I have sketched possible boundaries lines between the three modes of growth. 146

4-13 **−1 defect appears at branch**: (Right) Surface pattern in the shape of a −1 topological defect appears in the notch of this branch. The "view" angle shown on the right is the camera position for the image on the left. (Left) Looking through the trunk with wood cells hidden. This was grown at $\alpha = 50$ and low temperature, $\eta = 0.01$, so new branches do not emerge and disrupt our view. 148

C-1 Illustration of the Bragg-like matrix *in the lab frame z surface parameter* ($\epsilon = 1$). In these coordinates, the momentum-dependent potential has the inconvenient challenge of being zero on the anti-diagonal, hence the utility of the conformal coordinates. 188

D-1 The matrix is non-zero on diagonal stripes only. The blue, red, and green diagonal lines are fixed values of $\tilde{V}_{pN}$. The center diagonal is $\lambda_k^{(0)} = -\nu\left(2\pi k/L\right)^2$ is symmetric around its center point. Elements near the dashed orange line ($j = -k$) lead to near degeneracies. For example, the inner dashed blue box illustrates a two-by-two matrix with nearly equal diagonal elements. 210

D-2 Eigenvalues with first order corrections as a function of p_δ, see Eqn. D.42, in units of $\nu = 1$, $L = 1$, $\epsilon\left|\tilde{V}_{pN}\right| = \frac{1}{10}\lambda_{pN/2}^{(0)}$, and $pN = 100$. 213

D-3 The periodic potential opens a gap in the spectrum at half the periodicity. Degenerate perturbation theory shows the perturbed eigenfunctions on either side of the gap connect with sine and cosine standing waves constructed from superpositions of the unperturbed basis functions. 214

D-4 Examples of $\mathcal{V}_{jk}$ in Fourier space for various values of ω_p. The lower row illustrates how wavelengths commensurate with L lead to alternating zero and non-zero values. The upper row illustrates how non-commensurate wavelengths blur the matrix into all non-zero values. . 222

D-5 Illustration of $\mathcal{V}_{jk}$ for a cosine potential in a space with sine eigenfunctions, such as a non-periodic compact space. The diagonal stripes are the same as Fig. D-1, and the anti-diagonal stripes are of equal and opposite magnitude. The two orange boxes indicate the near degeneracy that results from the anti-diagonal stripes crossing the center diagonal at $pN/2$, which is also where the off-diagonal stripes cause degeneracy. The four corners of the orange boxes that sit on the center diagonal represent states of nearly equal energies that get mixed by the perturbation. 223

List of Tables

2.1 Stability criteria when $\bar{\kappa}_\times = 0$, and $K_1 = 0 = K_3$ and $C_1 < C_2$. 69

Chapter 1

Introduction

Highly curved surfaces are essential parts of physical systems on many length and time scales, including galaxies, stars, rivers, and living things. For living systems, the *boundaries* of individuals are curved surfaces. Interfaces between individual cells, colonies, and whole organisms are closed surfaces and thus must be sufficiently curved to have an inside and outside. Fields defined on these surfaces can couple to curvature such that emerging patterns and order are inherently non-flat.

When materials adhere to or embed in an interface, the particles can form oriented phases, such as liquid crystals. Such an orientation field can interact strongly with the curvature. In Chapter 2, I will show that topological defects in such orientational order can drive shape changes in membranes. Chapter 2 is a paper that I wrote with my advisor, Mehran Kardar, and published in Physical Review E in 2008 [235]. In Chapter 3, I will show that Turing patterns are also strongly influenced by curvature and can act as a chemical measuring stick for cell shape deformations. Section 3.2 of Chapter 3 is a paper that I wrote with my coauthors Jemal Guven, Mehran Kardar, and Henry Shackleton, which we published in European Physics Letters in 2019 [308]. The other sections of Chapter 3 and Appendix C are my extensions and clarifications of the ideas produced by our collaboration. In Chapter 4, I will conclude by presenting preliminary data from simulations of directional order coupled with solid growth, which suggests that cells in woody trees could be an exciting area of further exploration in biophysics. Chapter 4 is not published yet. These shapes and patterns occur for simple physical reasons without requiring active matter or the machinery of life (ribosomes, actin, etc). In this sense, these phenomena are more foundational. Life emerges out of them, or on them. Thus, by understanding the interactions between ordering and curvature, we are building infrastructure for understanding living systems.

Several historical threads are converging to make our present era an exciting time to study biophysics. These threads standout on backdrop of human history.[1] To put my work in context, this Introduction highlights the history of *geometry* in Section 1.1, *diffusion* in Section 1.2, *vortex dynamics* in Section 1.3, and *bio-physics* in Section 1.4.

These historical developments were motivated by art, engineering, and science. Art and engineering seek control, and thus more parameters. In contrast, we seek the simplest model that can capture essential features observed in nature.

Biology and geometry began with Aristotle[1] and Euclid[2] in the fourth century BCE. Intellectual progress was slow until the Renaissance when innovators like da Vinci[4, 5] and Mercator[6] brought observational inquiry and geometric reasoning back to center stage.

In the two millennia between Euclid and Newton[12], Earth's human population doubled to half a billion [326]. At this time, North America was still "filled with immense tall forests."[8][2]

In the next two hundred years of Enlightenment, the human population doubled again, crossing a billion before Gauss established differential geometry with his paper of 1827 [25], see Section 1.1 on *geometry.* In this time, laws of nature based on *potentials* came into clear view with works by Laplace[22], Fourier[23], and many others. See Section 1.2 on *diffusion.*

Over the next hundred years, the human population doubled again, reaching two billion by 1930. During this Technical Revolution, our exponential growth became evident to the general public as concepts of globalization and macroeconomics entered public discourse. In 1858, Hermann von Helmholtz explained that previous hydrodynamic theories based on potentials did not allow vortices [37]. Ramifications of this essential insight are summarized in Section 1.3 on vortex dynamics and orientational order.

---

[1] Citations are sorted by year, so earlier citation numbers were published earlier.

[2] Today, Earth has about 3 trillion trees, possibly half as much as before humans.[280]

A year after von Helmholtz paper on vortices, Darwin published his *Origin of Species*, which finally provided a non-teleological mechanism for life's diversity [39]. Further advancement in biophysics had to wait until the atomistic view of nature matured enough to explain muscles[74, 75], nerves[77], and DNA[79]. The convergence of such mechanistic understanding marks the beginning of modern biophysics in the 1950s, see Section 1.4. The world's population doubled again to four billion by the mid-1970s when I was born. It has doubled again during my life thus far.

1.1 Geometry

A mathematical understanding of curvature developed only gradually. Euclid's rectilinear geometry[2] was sufficient for two thousand years of engineering, architecture[111], da Vinci's art[4], and even Isaac Newton[12] (1687 CE).

To support the spread of commerce across oceans, Mercator made his world map to depict sailing at a constant compass heading (rhumb lines) as a *straight line* on paper [6].

In 1673, Huygens famous *Horologium Oscillatorium* formalized the concept of the curvature of a line [10]. In the 1760s, Lagrange extended Euler's work on variational calculus to integrals of two variables so he could consider minimal surfaces [70]. In the same time period, Euler identified the minimum and maximum radii of curvature at each point on a surface, and questioning whether curvature could be defined at saddle points [15]. More than fifty years passed before Gauss resolved that and many other questions in his important paper of 1827 based on lectures he gave in 1825 [25]. Gauss' paper founded differential geometry.

That said, Gauss relied on previous innovations, including those of Gaspard Monge, the "father of projective geometry." His approach to representing a patch of surface as a height $h(x, y)$ above a Cartesian plan is now known as the "Monge patch", see Figure 1-1. It is still a central tool today. Quantities built from $h(x, y)$ are defined *on* the surface. Monge developed his geometry tools while designing forts and river embankments 1765-1781[17], and they were so useful that the French treated them as military secrets [111].

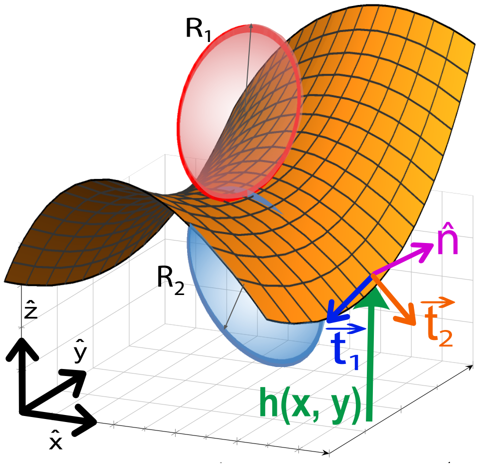

Figure 1-1: Monge's representation of a curved surface uses a Cartesian plane (x, y) to parameterize a single-valued height function $h(x, y)$ that cannot accommodate overhangs. R_1 and R_2 are the minimum and maximum radii of curvature at a point. These radii have a sign that identifies the two sides of the surface.

By construction, the Monge height field $h(x, y)$ cannot wrap around a closed shape or accommodate overhangs. Staying within the Monge representation, one constructs an "embedding vector" that locates a patch of surface within a fixed lab frame, which is assumed to be three-dimensional Euclidean space:

$$\vec{\boldsymbol{X}}(\sigma^1, \sigma^2) \xrightarrow{\text{MONGE}} \vec{\boldsymbol{X}}(x, y) = \begin{pmatrix} x \\ y \\ h(x, y) \end{pmatrix} \in \mathbb{R}^3 .$$

The embedding vector is a vector-valued function of two parameters. For the Monge representation, $\sigma^a = (x, y)$. As sketched in the figure, each point on a surface has a two-dimensional tangent plane. A convenient way to construct basis vectors for the tangent planes is to consider derivatives of an embedding vector,

$$\vec{\boldsymbol{t}}_a \equiv \frac{\partial \vec{\boldsymbol{X}}}{\partial \sigma^a} \equiv \partial_a \vec{\boldsymbol{X}} \equiv \vec{\boldsymbol{X}}_{,a} \,,$$

where subscript a indexes over the two parameters. A comma in the subscript denotes a partial derivative. These partial derivatives appear in many calculations involving the surface. For example, an infinitesimal line element constrained to the surface has arclength,

$$ds^2 = d\sigma^a \underbrace{\vec{\boldsymbol{t}}_a \cdot \vec{\boldsymbol{t}}_b}_{g_{ab}} d\sigma^b \,,$$

where repeated indices imply summation – the so-called Einstein summation convention. The two-by-two matrix g_{ab} is just the dot product of the tangent vectors. Gauss called this the "first fundamental form." Today, it is called the "metric tensor." On a Monge patch, it is

$$g_{ab} = \begin{pmatrix} 1 + h_{,x}^2 & h_{,x} h_{,y} \\ h_{,x} h_{,y} & 1 + h_{,y}^2 \end{pmatrix} .$$

Gauss considered a more general embedding vector. Taking *second* derivatives, he constructed his "second fundamental form" and showed that, when diagonalized, its diagonal elements are the reciprocals of the maximum and minimum radii of curvature at each point,[25]

$$\begin{aligned} K_{ab} &= \frac{1}{\sqrt{1 + h_{,x}^2 + h_{,y}^2}} \begin{pmatrix} h_{,xx} & h_{,xy} \\ h_{,yx} & h_{,yy} \end{pmatrix} \\ \xrightarrow{\text{PRINCIPAL}} K_{ij} &= \begin{pmatrix} 1/R_1 & 0 \\ 0 & 1/R_2 \end{pmatrix} . \end{aligned}$$

The arrow marked PRINCIPAL indicates rotating and rescaling to an orthonormal frame aligned with the principal directions of minimum and maximum curvature, where Gauss' curvature tensor is diagonal with elements equal to the reciprocal of the radii of curvature. Gauss' accomplishment is all the more amazing because he did not have the more modern technology of Christoffel (born 1829) and Levi-Cevita (born 1873). We will use it below. After Gauss' 1827 paper [25], decades passed again before Riemann introduced the Riemann surface in his thesis (1851) and the concept of an n-dimensional object in 1854 [34].

The "covariant" derivative is a central concept in differential geometry. To motivate it, consider that in a Euclidean frame, basis vectors are constant, so

$$\partial_i \hat{\boldsymbol{x}}_j = 0\,.$$

We use Latin-letter indices $i, j, k \in [1, 2, 3]$ to refer to the lab frame directions. This constancy of the basis vectors greatly simplifies expressions in a Euclidean frame. This property is lost when we lift a problem onto a curving surface, because coordinate frames *on* the surface change from point to point. Fortunately, we can recover this property that basis vectors do not contribute to derivatives by defining a new derivative operator that co-varies with the surface frame. We denote this *covariant derivative* by ∇_a. It is defined such that

$$\nabla_a g_{bc} \equiv 0\,. \tag{1.1}$$

There are several ways to make this equation true. The most direct route is via the "Christoffel symbols", Γ^a_{bc}, which Erwin Christoffel introduced in his study of second-order differential equations [44]. This became a cornerstone of the tensor analysis developed by Levi-Cevita, Cartan, and others, and is essential to general relativity. Briefly, the covariant derivative in Eqn. 1.1 can be written:

$$0 = \nabla_a g_{bc} = \partial_a g_{bc} - \Gamma^d_{ab} g_{dc} - \Gamma^d_{ac} g_{db} \tag{1.2}$$

where Γ^d_{ab} is the Christoffel symbol,

$$\Gamma^d_{ab} \equiv \frac{1}{2} g^{dc} \left(g_{cb,a} + g_{ac,b} - g_{ab,c} \right) ,$$

where a subscript comma denotes partial derivative, $\partial_c g_{ab} = g_{ab,c}$, and $g^{ab} = \left[g_{ab} \right]^{-1}$ the matrix inverse of the metric. Since the metric can be constructed from the tangent vectors, and the tangent vectors from an embedding vector, the Christoffel symbols provide a key element of practical calculations on curved surfaces.

With these tools in hand, consider the covariant derivative of the tangent vectors. By construction, this quantity is always along the surface normal. The coefficients are Gauss' curvature tensor, K_{ab}:

$$\nabla_a \vec{\boldsymbol{t}}_b = K_{ab} \hat{\boldsymbol{n}} , \tag{1.3}$$

where $\hat{\boldsymbol{n}}$ is the unit normal vector, which can be constructed as the normalized cross product of the tangent vectors. As final step for this brief summary of differential geometry of curved surfaces, the trace of the curvature tensor is a *reparameterization invariant scalar*, so it must be the same in any coordinate system. Gauss showed that K^b_a is diagonal in coordinates aligned with the principle principle curvatures, so we know that its trace is an invariant scalar:

$$g^{ab} K_{ab} = K^a_a = \frac{1}{R_1} + \frac{1}{R_2} \tag{1.4}$$

The determinant of Gauss' curvature tensor is also an invariant scalar and is now called the "Gaussian curvature."

$$\det K^b_a = \frac{1}{R_1 R_2} \tag{1.5}$$

These tools are sufficient to study most curved two-dimensional surfaces that appear in biology, see Appendix A for further details.

In 1920, Einstein made differential geometry famous with his theory of gravity [63, 64]. Einstein replaced Newton's $1/r^2$ gravity force law *with geometry.* This inspired revolutions in field theory, gauge theory, Yang-Mills theory and the Standard Model — all based on differential geometry.

Even with the success of differential geometry in Einstein's theory of gravity, it was not until the second half of the 1900s that it entered biology with papers like Canham's "The Minimum Energy of Bending as a Possible Explanation of the Biconcave Shape of the Human Red Blood Cell" in 1970[92]. Helfrich[102] extended Canham's model with the concept of spontaneous curvature, so the energy of a closed vesicle can be computed by integrating over the surface, S,

$$F_{\mathrm{CH}} = \oint_S dA \left[\sigma + \frac{\kappa}{2} \left(K^a_a - H_0 \right)^2 \right] , \tag{1.6}$$

where σ is a cost for creating more surface area; κ is a bending rigidity; K^a_a is the trace of the curvature tensor and equal to twice the mean curvature; and H_0 is a preferred curvature. A productive industry emerged to calculate and enumerate the shapes of fluid vesicles, see the review by Seifert [164]. It is on-going today [182, 255, 298, 310].

Udo Seifert, Reinhard Lipowsky and coworkers carried the Canham-Helfrich model to several successful conclusions. Figure 1-2 shows part of their phase diagram of vesicle shapes that minimize the F_{CH}, which they computed by numerically integrating the shape equation obtained from taking a functional derivative:

$$0 = \frac{\delta F_{\mathrm{CH}}}{\delta \vec{\boldsymbol{X}}} .$$

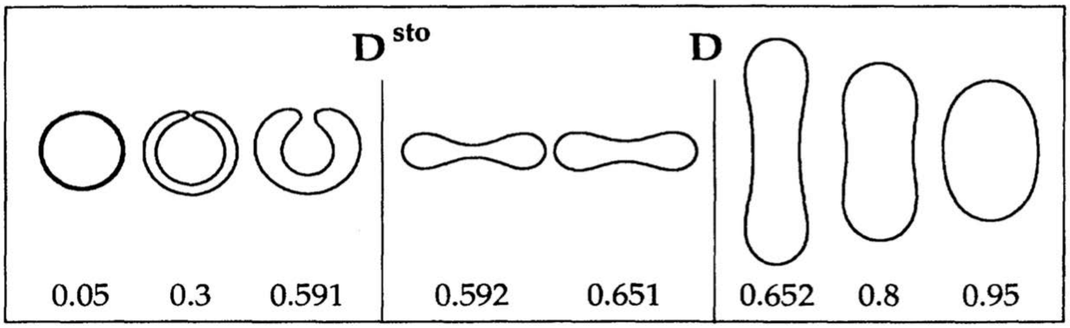

Figure 1-2: This is part of the marvelous phase diagram of minimum energy shapes for the Canham-Helfrich model augmented with volume and area constraints. These shapes are axisymmetric. The horizontal axis is the reduced volume that reaches 1 for a sphere. This segment of the overall diagram is at zero spontaneous curvature. As the reduced volume is increased from left to right, the energy minimum goes through two discontinous transitions. Reproduced from Fig. 9 with permission from Udo Seifert, Karin Berndl, and Reinhard Lipowski's "Shape transformations of vesicles: phase diagrams for spontaneous-curvature and bilayer coupling models," Phys Rev A 44 (2) p1182–1202 ©1991 by the American Physical Society.

Note that recent measurements have suggested that the abrupt transition from prolate barbell to discocyte should move to the right (higher reduced volume), which is likely the result of tilt in the lipid tails [182, 255, 298, 310].

Fluid flows inspired the earliest field theories[13, 14, 16], so it is interesting that differential geometry only reached hydrodynamics in 1970, the same year Canham's paper on red blood cells [93], and is still an active subject of research [284].

In Chapter 2, we will extend the Canham-Helfrich model F_{CH} to include orientational order embedded in the surface and solve the shape equations for some biologically relevant configurations. We use a variant of the tangent angle surface parameterization used by Seifert *et al.*

Today, the tools of differential geometry are used [262, 312] by fields as diverse as machine learning[286, 317] and dynamical systems[208].

1.2 Diffusion

Around 60 B.C.E., the Roman philosopher Lucretius wrote a widely cited poem arguing for the existence of atoms based on observing dust motes dancing in a sunbeam [3]. His description foreshadowed the kinetic theory of gasses. However, a quantitative understanding was still lacking in 1827, the same year as Gauss' paper, when English botanist Robert Brown examined pollen grains jittering from thermal fluctuations in water [27]. Brown used a magnifying glass hardly more advanced than what Hooke used 152 years earlier to produce his *Micrographia* (1665) [9].

While Brown did not present a analytical theory, the mathematical tools were already known. Laplace had introduced his famous solutions to second-order differential equations [18]. He had been studying the tides using the tools that Euler and Lagrange had developed on top of Newton's variational calculus. In 1805, Laplace explained Young's observations[21] of capillary action and surface tension [22].

In 1822, Fourier extended these early successes of *potential theory* to describe heat conduction and his famous decomposition of a function into a series of sine waves [23]. In 1827, Georg Ohm published his book explaining his potential theory of electrical conduction.[26]

Thus, these tools were available when Brown made his observations.[27] He followed up with an experiment to confirm that the motion also occurred for small particles of non-biological origin [29], i.e. the machinery of life is not the source of Brownian motion. Yet, he refrained from asserting a cause. That would have to wait until 1905 when the idea of atoms was more developed.

In 1828, Green wrote his long paper introducing integral expressions as solutions to Poisson equations,[28] which Gauss further formalized in 1840. In the 1850s, Graham & Fick[35], Darcy[36] found potential theories for chemical diffusion and flow through porous media.

In 1860, J.C. Maxwell refined the concept of diffusion in order to write a kinetic theory of gases. His velocity distribution function for gas particles was the first *statistical* law of physics.[40, 41]

In 1863, J.W. Gibbs wrote the first doctoral thesis in engineering in the United States using geometry to optimize gears [42]. Ten years later, his first two published papers presented geometrical tools for reasoning about thermodynamics [45, 46]. Maxwell immediately appreciated this and added it to the next addition of his book, *The Theory of Heat* [47]. In the same decade, Boltzmann was extending

Maxwell's work with his H-theorem [48]. Gibbs' classic 1902 text book on statistical mechanics generalized Boltzmann's analysis of entropy to a general ensemble. This clarified the derivation of the second law of thermodynamics and set the stage for Shannon's information theory [56].

Building on this foundation of kinetic theory of gasses, Einstein (1905)[57] and Smoluchowski (1906)[59] were finally able to restate Lucretius' poem[3] and calculate the mean-square displacement of particles experiencing Brownian motion. This offered an experimental procedure for measuring Avogadro's number, which Perrin accomplished in 1908 and wrote about in his famous book "Brownian Movement and Molecular Reality" [60]. Perrin won the Nobel Prize in 1926.

In 1926, Schrödinger presented his wave equation[65] and used the perturbation theory developed by Lord Rayleigh in studying sound vibrations in 1896 [55], which we will use in Chapter 3 to analyze Turing patterns.

In 1953, Turing brought diffusion to a new level by explaining how chemical reactions plus diffusion can be linearly unstable and generate patterns, which he proposed could describe morphogenesis [78]. Specifically, consider a (nonlinear) chemical reaction involving multiple constituents. Denote the concentrations of these chemicals as $\Psi_1, \Psi_2, ...$, which are functions of space and time. Consider a steady-state fixed point of the chemical reaction dynamics, denoted Ψ_i^*, and consider small deviations from these concentrations, denoted ψ_i To be a *stable* fixed point, small deviations must fade away under the action of the chemical reactions. Mathematically, this means that if one linearizes the reaction around the fixed point and computes the reaction Jacobian, it must have only negative eigenvalues. Illustrating this with just two concentrations, one has:

$$\frac{\partial}{\partial t}\begin{pmatrix}\psi_1\\ \psi_2\end{pmatrix} = \underbrace{\begin{pmatrix}R_{1,1} & R_{1,2}\\ R_{2,1} & R_{2,2}\end{pmatrix}\Bigg|_{\vec{\Psi}^*}}_{\text{Reaction Jacobian}}\begin{pmatrix}\psi_1\\ \psi_2\end{pmatrix},$$

and the eigenvalues,

$$\omega(0)_{\pm} = \frac{R_{1,1} + R_{2,2}}{2} \pm \sqrt{R_{1,2}R_{2,1} + \left(\frac{R_{1,1} - R_{2,2}}{2}\right)^2}$$

must be negative for $\vec{\boldsymbol{\Psi}}^*$ to be a *stable* fixed point. Note that this field theory representation of a reaction proceeds at each point in space independently, so no spatial derivatives appear.

Diffusion is also stable. That is, if only diffusion is active, small deviations fade away. Mathematically, this is because the Laplacian has negative eigenvalues. However, Turing pointed out that the combination of a stable chemical reaction and diffusion leads to a new situation in which an instability can arise:

$$\frac{\partial}{\partial t}\begin{pmatrix} \psi_1 \\ \psi_2 \end{pmatrix} = \left[\underbrace{\left.\begin{pmatrix} R_{1,1} & R_{1,2} \\ R_{2,1} & R_{2,2} \end{pmatrix}\right|_{\vec{\boldsymbol{\Psi}}^*}}_{\text{Reaction Jacobian}} + \underbrace{\begin{pmatrix} \nu_1 & 0 \\ 0 & \nu_2 \end{pmatrix}\nabla^2}_{\text{Diffusion}}\right]\begin{pmatrix} \psi_1 \\ \psi_2 \end{pmatrix} + \mathcal{O}(\psi_i^2)\,.$$

Note the higher-order terms on the right! Fourier transforming both space and time:

$$0 = \sum_q e^{i\vec{\boldsymbol{q}}\cdot\vec{\boldsymbol{x}}} e^{\omega_q t}\left[\left.\begin{pmatrix} R_{1,1} - \nu_1 q^2 & R_{1,2} \\ R_{2,1} & R_{2,2} - \nu_2 q^2 \end{pmatrix}\right|_{\vec{\boldsymbol{\Psi}}^*} - \omega_q\right]\begin{pmatrix} \tilde{\psi}_1(q) \\ \tilde{\psi}_2(q) \end{pmatrix}. \tag{1.7}$$

This new matrix can have positive eigenvalues, ω_q, see Figure 1-3. The wavelengths corresponding to these positive eigenvalues are linearly unstable.

After higher order terms stabilize the pattern, the characteristic length scale of the pattern will be approximately $1/q^*$. In order to make $\omega^+_{q^*} > 0$, these two inequalities must hold:

$$\begin{aligned} &1 < \frac{-R_{2,2}}{R_{1,1}} < \frac{\nu_2}{\nu_1} \\ &0 < -R_{2,2}R_{1,1} < -R_{1,2}R_{2,1} < \frac{\left(R_{2,2}\nu_1 - R_{1,1}\nu_2\right)^2}{4\nu_1\nu_2}\,. \end{aligned}$$

The study of reaction-diffusion systems has focused on selecting higher order terms and adding more chemical components to generate patterns that match various goals. Artistic goals often require adding more parameters to control the resulting patterns. Here, we're focused on capturing physical processes with as few parameters as possible.

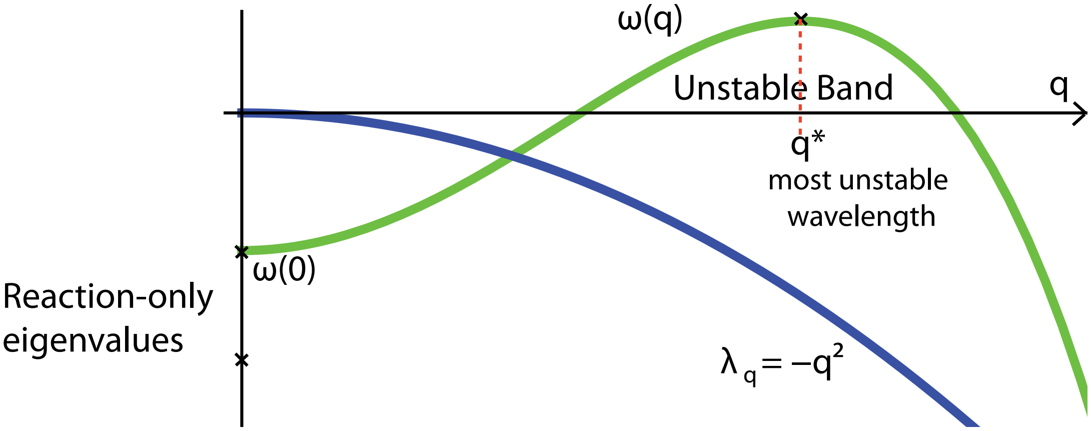

Figure 1-3: Turing's Unstable Band of wavelengths resulting from the interplay of reaction and diffusion.

While many expressed interest in using Turing's remarkable idea, concrete progress lagged for more than a decade. In 1968, Lindenmayer proposed a formal grammar for iteratively generating patterns inspired by Turing's ideas.[89, 90] Now called "L-systems," these string rewriting rules are widely used in computer science to generate realistic-looking plants and scenes. In 1972, Gierer & Meinhardt examined systems of nonlinear equations that can stabilize the patterns initiated by a Turing instability [99]. This led up to Meinhardt's influential 1982 book "Models of Biological Pattern Formation"[120], which was a precursor to Cross & Hohenberg's widely cited 1993 article in Reviews of Modern Physics on "Pattern formation outside of equilibrium."[142] We will expand on this line of discussion in Chapter 4.

Turing's instability depends on short-range autocatalysis and long-range inhibition [99]. This occurs when the inhibitor diffuses much faster than activator, which appears unlikely to occur via diffusion *between* cells, because materials diffuse at similar rates through the intracellular environment. However, Rauch[3] & Millonas showed that accounting for signal transduction through the cell membrane leads to *effective* diffusion rates that can generate Turing-type patterns in realistic physiological conditions, such as during embryo morphogenesis.[203]

---

[3] Erik Rauch and I became friends through Dan Rothman's seminar. He had the unusual hobby of collecting place names. We founded MetaCarta together with Doug Brenhouse in early 2001.

Reaction-diffusion (RD) models are now a widely used framework for understanding biological pattern formation.[247] RD systems have now been found in systems as diverse as starfish embryogenesis[323, 329], parrot fish coloration [217, 340], and the internal structuring of tree tissues [333].

In Chapter 3, we lift Turing-type patterns onto curved interfaces. To do this, we lift the Laplacian onto a curved surface and study how curvature changes its eigenfunctions and eigenvalues. Using differential geometry, conformal mapping and Rayleigh-Schrödinger perturbation theory, we show how curvature can *anchor* Turing patterns to regions of curvature. This paper was published in 2019 with my coauthors Jemal Guven, Mehran Kardar, and Henry Shackleton [308].

How curvature influences time-varying patterns is an on-going area of research [323, 328, 329, 337].

1.3 Vortex Dynamics

Swirling motions in fluids mesmerize observers. For example, Leonardo da Vinci studied bubbles rising through water and found that small bubbles move in a straight line and larger bubbles move in a rising circular path (spiral) [5]. This spiralling remained a “paradox” until recently [201, 313, 336].

While Newton[11] and Euler[14] reasoned about vortex motion, it was not until 1858 that the *topological* nature of vorticity emerged as a framework for understanding. In 1755, Euler had used vortex motion as a counterexample to show that there are fluid motions for which no velocity potential exists. In 1822, Navier extended Euler’s inviscid fluid equations to derived his eponymous fluid mechanics in 1822[24]. Stokes re-derived the viscous flow equations and extended the analysis in 1845.[31] The Navier-Stokes equations admit vortices. However, the concept of deriving *all* of the motion of a fluid from a potential was still often tacitly assumed.

In 1858, Hermann von Helmholtz referenced Euler and explained methodically that hydrodynamics based on a potential does not *allow* rotating motion. His construction of vortex lines and studies of integrals of the hydrodynamic equations established the beginning of our topological understanding of vorticity [37]. This was a watershed moment. Vortex dynamics and the topological nature of these special points immediately became essential areas of study. In 1885, Poincaré showed that a tangent vector field on any even-dimensional closed manifold must have vortices surrounding special points where the vector field vanishes [51].

In 1958, one hundred years after Helmholtz' paper, Charles Frank provided a free energy functional of a orientational order to describe liquid crystals [81]:

$$F_{\text{Charles}} = \oint d^3x \left[\frac{K_1}{2} \left(\vec{\boldsymbol{\partial}} \cdot \hat{\boldsymbol{m}} \right)^2 + \frac{K_2}{2} \left(\hat{\boldsymbol{m}} \cdot \left(\vec{\boldsymbol{\partial}} \times \hat{\boldsymbol{m}} \right) \right)^2 + \frac{K_3}{2} \left(\hat{\boldsymbol{m}} \times \left(\vec{\boldsymbol{\partial}} \times \hat{\boldsymbol{m}} \right) \right)^2 \right] \tag{1.8}$$

The unit vector $\hat{\boldsymbol{m}}$ is aligned with the rod-shaped particles in a fluid that is sufficiently dense that the rods are forced to align their orientations. Vortices are a defining feature of liquid crystals. Liquid crystals quickly grew into an active field, including P.G. de Gennes' Nobel Prize.[143] The topological nature of these defects in the orientation field are a central to their study in condensed matter.[113]

A year earlier, in 1957, Abrikosov explained that Type II superconductors involved a lattice of vortices.[80] This built on the free energy model of Ginzburg-Landau.[76] Over the next fifteen years, intense research in phase transitions led to the renormalization group and our modern understanding of phase transitions.[103] In particular, Berezinski[97] and Kosterlitz & Thouless[100] showed how an orientation field in two dimensions can undergo a transition in which pairs of vortices of opposite orientation can "unbind" from each other and interact with a Coulomb-like potential.

Defect dynamics are now an essential part of understanding diverse systems, including Bose-Einstein condensates, crystals, active nematics, and many other dynamical systems that exhibit phase transitions [339].

In 1995, Vicsek *et al*[154] and Toner & Tu[153] extended such orientational order to a non-equilibrium, dynamical setting.[109, 123]

In vitro assays of cytoskeletal filaments and motor proteins have been found to produce striking dynamic patterns with orientational order. Vortex shapes were observed in tubulin and myosin in a petri dish in 1997 [162, 165]. More recently actin has been observed to develop polar patterns on synthetic cell membranes [321].

Recently, defects have been identified as playing a role in morphogenesis.[314, 319, 322, 327, 330, 331]

In Chapter 2, we lift Eqn. 1.8 onto a two-dimensional membrane and show that defects can buckle a deformable membranes into the third dimension. Defects will appear again in Chapter 4 on branch points in woody trees and my simulations of directed growth of living solids.

1.4 Physics of Biology

1.4.1 Early Biophysics

Biology began with Aristotle. His studies of living systems are still foundational. For example, he originated our modern theory of angiogenesis[1, 213]. However, Aristotle often resorted to “final causes” to explain observations in terms of future outcomes. Questions about causality continue to be *central* to biology.

Darwin’s explanation of evolution provided a partial solution: once life emerges, genetic variation and natural selection drive diversification into niches [39]. However, much remains to be understood in terms of underlying causes, including origin(s) of life, how intelligence works, and what aspects of life could be universal in the cosmos.

Ninety years ago, classical mathematics was dethroned by Gödel’s incompleteness theorem[68] and Turing’s halting problem [72]. Ironically, many great minds reacted to these impossibility results by turning attention to computing and understanding errors. Claude Shannon’s masters thesis at MIT implemented Boolean algebra [73] and his famous paper spanning two issues of the Bell Technical Journal described what *is possible* in a noisy communication channel [32]. Leslie Valiant’s 1984 paper on “A Theory of the Learnable” provided mathematical basis for learning from errors [121]. Perhaps this or one of its intellectual descendants will someday be seen as a Darwin-like moment for intelligence.

In 1892, Pearson coined the name "bio-physics" as better than the previous name "ætiology" from the Greek *αιτιον* meaning *a cause.* He predicted that only after applied mathematics and bio-physics are "fully accomplished, shall we be able to realize von Helmholtz' prediction and conceive all scientific formulæ, all natural laws, *as laws of motion*" [54]. D'Arcy Thompson published his carefully researched tome "On Growth and Form" in 1917 [62]. It still receives many citations, because it articulates a central theme: new knowledge in biophysics expands the arena in which life is not slave to final causes.

This uncovering of causes in biology has been underway for at least 200 years, and we're far from done. In the same decade that Young[21] and Laplace[22] were figuring out capillary action, Galvani was experimenting with nerve conduction in frogs [19], which inspired Volta to further develop his invention of the battery [20]. von Helmholtz measured the speed of nerve conduction and published a book about it in 1850 [33, 186]. In 1864, Kühne published his book about protoplasm and muscle contraction. He isolated and named "myosin" [43]. As electrical tools improved, Adrian & Matthews measured action potentials in humans [69], and Hodgkin & Huxley identified the biochemistry of axons [77]. Further studies of the contituents of muscle fibers led to an understanding of actin and the cytoskeleton [74, 75].

1.4.2 Microscope Era of Biophysics

These biochemistry successes motivated new microscopy techniques. As microscopes became more powerful, biophysics gradually took on a new character. By the early 1970s, when Canham[92] and Helfrich[102] proposed their mechanical model of cell shapes, it was commonplace to take pictures of cells. Both microscopes and telescopes had come a long way from Robert Hooke[9] and Galileo[7]. Today, we can track particles in fluid membranes [270, 275] as well as topological defects (vortices) in ordering fields in non-equilibrium, living matter [314].

To put my work in context, I highlight two big-picture aspects of biophysics:

1. 10^{11}: Biological interfaces exist over at least eleven orders of magnitude, from

surfaces of proteins embedded in membranes (nanometers) up to the branching cambium of woody trees as large as 100 meters.

2. Gaps: As mentioned in the famous "Powers of Ten" film, activity appears at alternating scales [108]. These separations of scales enable *effective* theories.

Surface orderings appear at many scales, and biophysics has not yet explored all them. I will highlight four.

Early motivations for biophysics focused on our own nerves, muscles, and genes. After isolating polymers of DNA and actin, it was natural to focus on the amazing molecular machines that operate on these one-dimensional filaments. The discovery of ribosomes and mRNA helped establish the (first) central dogma of biology that genetic information flows from DNA to RNA to proteins.

As proteins fold into their active conformations, the "second" central dogma of biology says that shape determines function [239]. While myosin and ribosomes are not transmembrane proteins, many essential molecular machines operate *in* a membrane, including many ATPases, chlorophyll, and ion channels. As the membrane influences the shape of these proteins, it also adjusts their functioning.

Treating DNA or actin as a filament is one separation of scales. Treating a lipid membrane as a continuum surface is a second, see Figure 1-4.

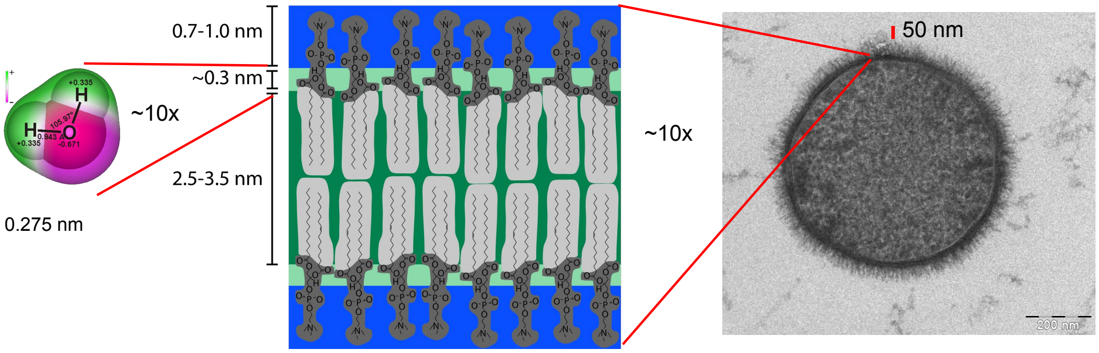

Figure 1-4: The bacterium *Bacillus Subtilis* on the right has a diameter of 600nm. "The furry appearance on the outside is due to a coat of long-chain sugars attached to the cell membrane. This coating helps trap water to prevent the bacterium from becoming dehydrated," from Lipid Bilayer article in Wikipedia. Image taken with a Tecnai T-12 TEM by Allon Weiner, The Weizmann Institute of Science, Rehovot, Israel, figure from Wikipedia. Center diagram shows the extent water penetration into a lipid bilayer, figure from Wikipedia. On the left, a water molecule measures about a quarter of a nanometer[207] and has 10x higher electron density around Oxygen, figure from Martin Chaplin's website on water, see Internet Archive's copy. [311].

Many open questions in biophysics remain at the scale of a single cell. For typical lipid bilayers, the bending modulus $\kappa \approx 20 k_B T$, where $k_B T \approx 4.1 \times 10^{-21} J \approx 0.6$ kcal/-mol is the thermal energy. Using the Canham model of Eqn. 1.6, one can estimate the energy needed to bend a membrane into a sphere of radius R as approximately $\frac{1}{2}\kappa(2/R)^2 \times 4\pi R^2 \approx 8\pi\kappa \approx 500 k_B T$ [227]. This sets the energy scale for many cellular processes acting in and around the membrane. We will comment on this more in Chapter 2 when we calculate the equilibrium shapes of defects in a nematic membrane.

Figure 1-5 shows whole cell remodeling during mitosis and chemotaxis. Lamellipodia are of a few microns [190]. The mitotic spindle and cortical ring of cell division are often tens of microns in size [233].

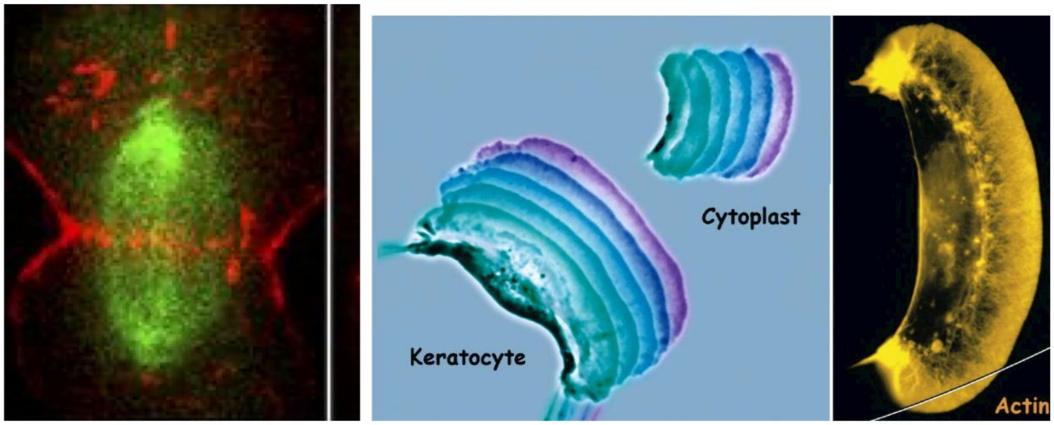

Figure 1-5: (Left) A cortical ring in silkworm spermatocytes from Chen *et al* in PLOS Biology 2008.[233](Center) Overlays of two image series taken at 15 second intervals to show keratocyte crawling via its large lamelipodia, and (Right) keratocyte stained with rhodamine phalloidin to label the actin filaments.Reprinted from Cell 112 (4) “Cellular Motility Driven by Assembly and Disassembly of Actin Filaments” by Thomas D Pollard & Gary G Borisy ©2003, p453–465, with permission from Elsevier.[190]

Much of biophysics has focused on building up from molecules. Endocytosis is a good example. Clathrin coated pits were first observed in the 1960s in tissues from mosquitos and guinea pigs [85, 91]. In 1975, Barbara Pearse extracted clathrin from pig brain tissue, purified it, and named it [104]. See the incredible picture in C of Figure 1-6 showing pits forming in muscle cells from a chicken [129]. Work in the 2000s continued in refining the molecular structure of proteins like clathrin[192] and BAR domains [200]. Today, it is still an open question how the cell’s machinery selects locations for creating vesicles [304].

In recent decades, biophysicists have developed models of epithelial sheets, which are 300X larger, see D in Figure 1-6. This third separation of scales allows for analytical modeling with coarse-grained effective theories, like polygonal vertex models [292]. Many of the shapes observed in embryogenesis, and epithelial sheets in general, resemble the simpler shapes of vesicles shown in Fig. 1-2, however the theory of epithelial sheets is a work-in-progress [271, 297].

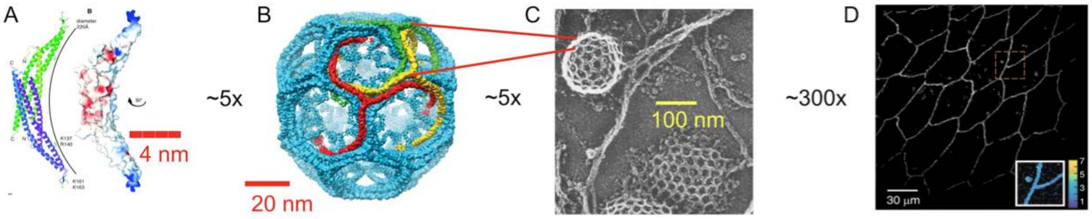

Figure 1-6: Illustrating four orders of magnitude. A: BAR protein domain is a banana-shaped with a radius of curvature of 11nm. It is highly conserved in evolution and plays key roles in the formation of tubules and other structures. (Reprinted with permission from AAAS: "BAR Domains as Sensors of Membrane Curvature" by Peter *et al* in *Science* 2004.[200]) B+C: clathrin triskelions make cages and pits that form vesicles. Image reconstruction in B shows a 36 clathrin hexagonal barrel with D6 symmetry. (Reproduced with permission from Springer Nature, "Molecular model for a complete clathrin lattice from electron cryomicroscopy" by Fotin *et al* 2004.) C: clathrin pits forming in a chick fibroblast. (From Heuser *et al* "Hypertonic media inhibit receptor-mediated endocytosis by blocking clathrin-coated pit formation" in *JCB* 1989.[129] D: Epithelial cells stretched over a surface, from "An adaptive microscope for the imaging of biological surfaces by Abouakil *et al* in *DGD* 2021.

Even on the scale of just single cells, models must account for phenomena ranging from 0.1 nm up to 10^4nm. As illustrated in Figure 1-4, lipid bilayer membranes are typically 4nm thick, and their lipid tails can tilt a fraction of that [272]. Endocytosis makes vesicles of 60–140nm in diameter.[304] Extracellular synaptic vesicles garrying neurotransmitters between neurons are smaller, e.g. 40nm [219].

Forces between inclusions in membranes can extend distances of 10^2nm.[144] However, membranes are typically so crowded that they resemble "cobblestone pavement, with the proteins organized in patches that are surrounded by lipidic rims, rather than icebergs floating in a sea of lipids."[219] Typical membranes have more molecular mass in proteins than in lipids (ratio approximately 3:2), and the center-to-center spacing of transmembrane macromolecules is only about 10nm![242] However, a crucial point has emerged that the local curvature of the membrane often changes the functioning of transmembrane proteins, because all of these materials are soft and biochemical function is often shape-dependent [242]. Membrane deformations between inclusions is a fruitful area of application for differential geometry [209, 225].

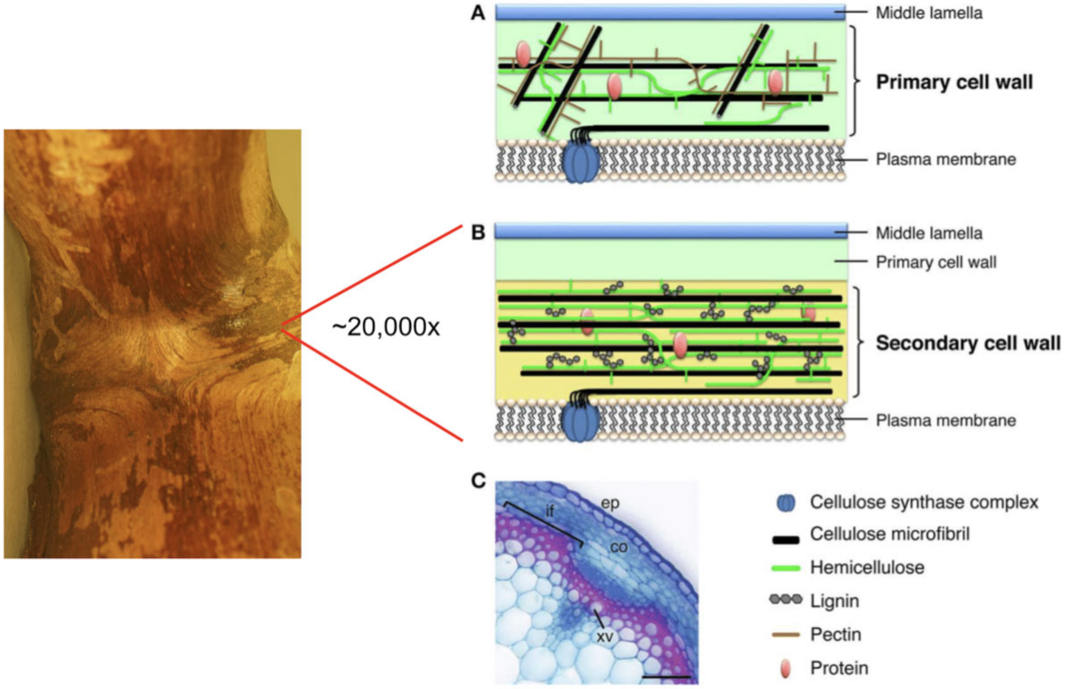
~20,000x
A
Middle lamella
Primary cell wall
Plasma membrane
B
Middle lamella
Primary cell wall
Secondary cell wall
Plasma membrane
C
if
ep
co
xv
Cellulose synthase complex
Cellulose microfibril
Hemicellulose
Lignin
Pectin
Protein

Figure 1-7: (Left) A –1 topological defect in the notch of a White Pine branch. (Right) Model of plant cell wells highlighting that the extra cellular matrix is extruded through the cell membrane by molecular machines that create a *ordered* array of filaments, often with orientational order. by Yoshimi Nakano, Masatoshi Yamaguchi, Hitoshi Endo, Nur Ardiyana Rejab, and Misato Ohtani, May 2015, in *Frontiers in Plant Science* 6 (288), CC BY 4.0.[281]. Note that the membrane thickness shown on the right side of Figure 1-7 is not to scale, because the cell walls extend for microns beyond the 4nm-thick membrane. This is necessary, because it shows that a transmembrane protein is extruding the cellulose.

Membrane inclusions and their orientations affect the coarse-grained mechanical properties of membranes. In fact, work continues beyond the Canham-Helfrich model to account for tilted tails of lipids [255]. This accounts for membrane fusion processes, which the Canham-Helfrich failed to accurately predict [182]. Biophysical systems at many scales exhibit such orientational order, including:

1. 0.1 to 2nm: tilted tails of lipids in bilayer membranes,
2. 1 to 10nm: protein waves on membranes [315],
3. 10 to 100nm: actin filaments in the cortical cytoskeleton [321],
4. 10 to 100µm: epithelial sheets of cells with planar cell polarity [261, 269], and
5. 1cm to 100m: elongated cells in plant tissues.

Botany offers a fourth separation of scales that is under-explored in biophysics. Plant cell walls are an active area of engineering research. The shapes of woody plants are many orders of magnitude larger than their constituents, so ripe for effective theories. See Figure 1-7 I will revisit this last point in Chapter 4.

In the next chapter, we will study a model of orientational order in fluid membranes.

Chapter 2

Defects in nematic membranes can buckle into pseudospheres

This chapter was published in Physical Review E in 2008 with my co-author Mehran Kardar[235].

A nematic membrane is a sheet with embedded orientational order, which can occur in biological cells, liquid crystal films, manufactured materials, and other soft matter systems. By formulating the free energy of nematic films using tensor contractions from differential geometry, we elucidate the elastic terms allowed by symmetry, and indicate differences from hexatic membranes. We find that topological defects in the orientation field can cause the membrane to buckle over a size set by the competition between surface tension and in-plane elasticity. In the absence of bending rigidity the resulting shape is universal, known as a parabolic pseudosphere or a revolved tractrix. Bending costs oppose such buckling and modify the shape in a predictable manner. In particular, the anisotropic rigidities of nematic membranes lead to different shapes for aster and vortex defects, in principle enabling measurement of couplings specific to nematic membranes.

2.1 Background Review

By "nematic membrane" we refer to any flexible sheet incorporating ordered rod-like constituents. For example, thin films of smectic-C liquid crystals are nematic membranes [94, 112, 146, 160]. Also, recently developed sheets of carbon nanotubes have nematic character [194, 231]. Nematic order arises in lipid membranes with inclusions [167] and in the cell cytoskeleton, e.g. during mitosis [135]. Interestingly, *in vitro* experiments on mixtures of cytoskeletal filaments and protein motors observe topological defects (asters and vortices), which spontaneously self-organize into a variety of patterns [162, 165, 198]. These experiments, and related simulations, use *flat* geometries with various boundary conditions [177, 211]. Similar topological defects influence the shapes of real cells. For example, cells of the alga Bryopsis sprout branches out of vortex-shaped defects that appear naturally in their cell wall of cellulose microfibrils [83]. To take a step toward understanding such living and *in vitro* systems, we consider equilibrium shapes around defects in deformable nematic membranes.

We show that topological defects can buckle the membrane. This has similarities to two other systems. One is bulk nematic liquid crystals, which buckle into the third dimension around defect lines [96, 98, 101] in a manner directly analogous to the shapes we find. A second example is provided by deformable triangular latices, which have been studied extensively in the theory of two-dimensional melting. While the physical picture is different, the model energy is equivalent to a nematic membrane with isotropic elastic constants. Disclination defects culminating in a site with five or seven bonds (instead of the usual six) can lower their energy by buckling [125, 128, 147, 184]. When draped over curved surfaces, collections of such defects arrange in specific patterns [204, 205, 220, 221]. If surface tension is neglected, five-fold disclinations assume an approximately cone-shaped form [128].

In contrast to the above cases, competition between the cost of surface area and rod misalignment determines the shape of the defects we consider. When bending rigidity is neglected, we find that topological defects deform membranes into a simple universal shape known as a parabolic pseudosphere [136, 230]. The size (height and extent) of this universal form is governed by the ratio of surface tension to in-plane elasticity. The inclusion of bending rigidity opposes this puckering. If the bending cost is small, the singularities at the tip and rim of the defect become smoother. The logarithmically diverging tip of the parabolic pseudosphere is replaced by the finite height of an *elliptic* pseudosphere [136], and the sharp rim is replaced by an exponential falloff with a length scale related to rigidity. Higher bending costs completely eliminate the buckling instability. The anisotropic elasticity of nematics singles out specific defect orientations (asters and vortices); and corresponding anisotropies in bending rigidity lead to different length scales for their shapes.

The rest of the manuscript is organized as follows: In Sec. 2.2, we describe the free energy of a nematic membrane using tensor contractions from differential geometry. This provides a compact formulation applicable to all deformations, including highly curved shapes. In Sec. 2.3, we describe vortex and aster defects, derive shape equations for radially symmetric configurations, and solve them to find the buckled defect shapes. Section 2.4 provides a summary and indications for future research. In Appendix 2.5, we study filament orientations in fixed geometries, which may provide other ways of measuring the nematic membrane parameters. In Appendix 2.6, we check the linear stability of the buckled defect shapes.

2.2 Elastic Free Energy of Nematic Membranes

Using differential geometry to describe a two-surface in three-space, we construct a power series expansion for the free energy by selecting a linearly independent set of scalar contractions of the surface tensors. For a surface described by an embedding vector $\vec{\boldsymbol{X}}(\sigma^1, \sigma^2)$, one constructs tangent vectors, $\vec{\boldsymbol{t}}_a = \partial_a \vec{\boldsymbol{X}}$, by taking derivatives of the embedding vector with respect to its two parameters. The metric tensor is then $g_{ab} = \vec{\boldsymbol{t}}_a \cdot \vec{\boldsymbol{t}}_b$. The covariant derivative is defined such that $\nabla_a g_{bc} = 0$. The curvature tensor is constructed from covariant derivatives of the tangent vectors as $K_{ab} = (\nabla_a \vec{\boldsymbol{t}}_b) \cdot \hat{\boldsymbol{n}}$, where $\hat{\boldsymbol{n}}$ is a surface normal. One must choose a side to define the sign of $\hat{\boldsymbol{n}}$. In the principle directions basis, $K_{ij} = \begin{pmatrix} 1/R_1 & 0 \\ 0 & 1/R_2 \end{pmatrix}$, where R_i are the radii of curvature [188].

A unit-magnitude tangent vector field $\vec{\boldsymbol{T}} = T^a \vec{\boldsymbol{t}}_a$ represents the nematic particles. At constant filament density, the magnitude $T^a T_a = 1$ is fixed and only its orientation changes [1]. Nematic symmetry implies invariance under $T^a \to -T^a$ [2]. A complete set of scalars up to second order in derivatives is

$$\begin{aligned}\mathcal{F}_{nematic} =& \sigma + \frac{K_1}{2}\left(\nabla_a T^a\right)^2 + \frac{K_3}{2}\left(\nabla_a T_\perp^a\right)^2 \\ &+ \frac{\kappa_\parallel}{2}\left(T^a K_{ab} T^b - H_\parallel\right)^2 \\ &+ \frac{\kappa_\perp}{2}\left(T_\perp^a K_{ab} T_\perp^b - H_\perp\right)^2 \\ &+ \frac{\kappa_\times}{2}\left(T^a K_{ab} T_\perp^b - H_\times\right)^2 \ . \end{aligned} \tag{2.1}$$

This free energy density must be integrated with a surface area element $dA = \sqrt{g}\ d^2\sigma$, where g is the determinant of the metric. The weighted antisymmetric tensor $\gamma_{ab} = \sqrt{g}\,[\epsilon_{ab}]$ rotates one-tensors by $\pi/2$, such that $T_\perp^a = \gamma^{ab} T_b$ [188]. Each term is manifestly positive, so stability demands that the moduli be positive. In the remainder, we consider reflection symmetric, non-chiral membranes without spontaneous curvatures $H_{\parallel,\perp,\times}$.

Unlike parameterizations used to study nematic membranes near the hexatic fixed line [141, 152], this set of scalars cleanly delineates the anisotropic bending energies that make nematic membranes unique. Creating more surface area costs σ [105, 134]. In-plane splay and bend cost K_1 and K_3, which are the two-dimensional analogs of the bulk nematic Frank constants [81, 160]. Membrane curvature in the direction of the local filament orientation costs $\kappa_\parallel$. Curvature perpendicular to the filaments costs $\kappa_\perp$. These out-of-plane bending terms are the anisotropic analogs of the the Canham[92]-Helfrich[102] bending rigidity. Saddle curves cannot be constructed from the other two out-of-plane bending terms and incur an independent energy cost of

---

[1] Relaxing $T^a T_a = 1$ would introduce independent $TKKT$ and $T_\perp KKT_\perp$ terms and several new gradient terms.

[2] Dropping the nematic symmetry requirement introduces four new spontaneous curvatures, two of which are chiral.

$\kappa_\times$. The square of the chiral scalar $TKT_\perp$ [141, 145] is non-chiral. The underlying membrane has a fluid character in that the particles can rearrange in the surface without stretching or shearing costs.

Compared to the *splay*, *bend*, and *twist* of bulk nematics, nematic membranes have additional freedom that comes from relaxing a constraint: instead of three fields constrained to a unit vector, the nematic membrane constrains only two fields to a unit vector and allows a third field to range freely in describing the membrane's local deviation from flatness [3].

In a system of motor proteins pulling on cytoskeletal filaments, K_1 would be proportional to motor density, which we assume to be uniform, and $\kappa_\perp$ would be determined primarily by the bare membrane's isotropic rigidity. Filament rigidity would influence both K_3 and $\kappa_{||}$. See Appendix 2.5 for comments on $\kappa_\times$.

Perturbative RG near the hexatic fixed line [152] shows that thermal fluctuations reduce weak anisotropy, i.e., the three quantities $\kappa_\times - \kappa_{||} - \kappa_\perp$, $\kappa_{||} - \kappa_\perp$, and $K_1 - K_3$ fade at long distances, so that only the hexatic membrane energy remains, and

$$\mathcal{F}_{hexatic} = \sigma + \frac{K_A}{2}(\nabla_a T_b)(\nabla^a T^b) + \frac{\kappa}{2}\left(K^a_a - H_0\right)^2 \ , \tag{2.2}$$

where $K_A = \frac{1}{2}(K_1 + K_3)$ and $\kappa = \frac{1}{2}(\kappa_{||} + \kappa_\perp)$. Under further rescaling, $\kappa \to 0$ and K_A is unrenormalized. Note that while the hexatic energy takes its name from the six-fold symmetry of triangular lattices, any n-atic symmetry with $n \geq 3$ restricts $K_1 = K_3$ and $\kappa_\perp = \kappa_{||} = 2\kappa_\times$. For polar ($n = 1$) or nematic ($n = 2$) membranes, the isotropic approximation is an important limiting case at one extreme of a phase diagram that deserves further attention.

Estimates of the thermal persistence length, ξ_T, of weakly anisotropic rigid membranes indicate an exponential form $\log \xi_T \propto \kappa$ [124, 152, 214]. Modest changes in κ can thus sweep the persistence length from small values up to thousands of times the short-distance cut-off [118]. Effects unique to the nematic membrane can then appear in patches of material smaller than this persistence length.

---

[3] Such constraints deserve further study in the spirit of Capovilla's and Guven's study of membranes with isotropic rigidity in Ref. [212].

2.3 Buckled Defects Shapes

In the nematic phase, the rod orientation varies slowly throughout most of the material. However, at particular defect points, the orientation may be undefined, because rods at neighboring locations point in all directions. The *topological charge* of a defect is the number of times that the orientation rotates through 2π as the coordinate angle θ sweeps through 2π. Different patterns appear for integer, half integer, and positive and negative charges. The defect depicted in Fig. 2-1 is radially symmetric, and is rotated by a uniform angle ξ with respect to the radial vectors.

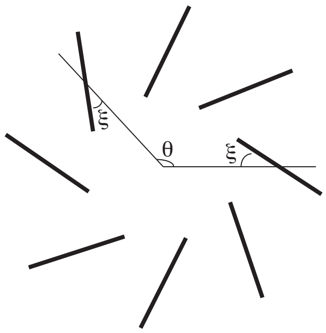

Figure 2-1: Rod orientations around a general uniform +1 topological defect. $\xi = 0$ corresponds to an aster, and $\xi = \pi/2$ to a vortex.

In the limit of isotropic rigidity, +1 defects with any radially uniform ξ have the same energy. The symmetry is removed by the anisotropic moduli in a nematic membrane, which distinguish asters ($\xi = 0$) and vortices ($\xi = \pi/2$). The energy of such a planar defect as a function of ξ is

$$E_{planar}(\xi) = \pi \left(K_1 \cos^2(\xi) + K_3 \sin^2(\xi) \right) \ln \frac{R}{a} + E_c(\xi), \tag{2.3}$$

where R is the size of the membrane, a is a short distance cutoff, and E_c is a core energy reflecting the defect's microscopic situation inside of the core radius a.

For $K_3 > K_1$, asters have lower energy than vortices and are stable against in-plane deformations. If $K_1 > 2\kappa_\perp$, the defect energy is further reduced by buckling out of flatness to align the filaments in the third dimension. (See Appendix 2.6 for linear stability analysis.) Buckling comes at the expense of creating more area, so surface tension sets the size of the deformation. Analogously, when $K_1 > K_3 > 2\kappa_{\|}$, vortices are stable and can reduce their core energy by tilting the surface around the defect.

To study this buckling, we minimize the nematic membrane energy, Eq. (2.1), around fixed aster and vortex arrangements. For a radially symmetric surface with no overhangs, we use the *polar Monge tangent* representation with embedding vector $\vec{\boldsymbol{X}}(r,\theta)$. The height above the Monge plane is found by integrating the tangent angle $\chi(r)$ from a base value, so that

$$\vec{\boldsymbol{X}}(r,\theta) = \begin{pmatrix} r\ \cos(\theta) \\ r\ \sin(\theta) \\ \int^r \tan(\chi(r'))dr' \end{pmatrix} . \tag{2.4}$$

This yields a metric with no derivatives and thus lower order shape equations. To handle shapes with overhangs, such as prolate vesicles [140], one can parameterize the shape by contour length instead of Monge radius.

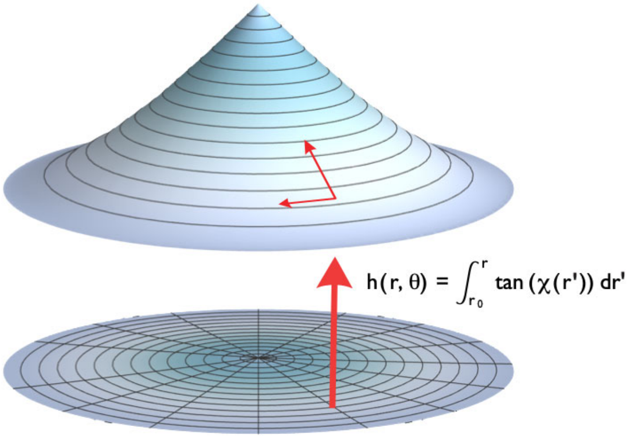

Figure 2-2: An illustration of the coordinate system.

The unit vector constraint is enforced by defining the angle ξ such that

$$T^a = \begin{pmatrix} \cos(\xi)\cos(\chi) \\ \sin(\xi)/r \end{pmatrix} . \tag{2.5}$$

With this parameterization, the nematic membrane free energy becomes

$$F_{nematic} = 2\pi \int dr \left(\sigma \frac{r}{\cos(\chi)} + \begin{bmatrix} \kappa_{\|}(\sin^2(\xi)\tan^2(\chi) + r^2\cos^2(\xi)\chi'^2) + \\ \kappa_{\perp}(\cos^2(\xi)\tan^2(\chi) + r^2\sin^2(\xi)\chi'^2) + \\ \bar{\kappa}_{\times}\sin^2(\xi)\cos^2(\xi)(\tan(\chi) - r\chi')^2 + \\ K_1(\cos(\xi) - r\sin(\xi)\xi')^2 + K_3(\sin(\xi) + r\cos(\xi)\xi')^2 \end{bmatrix} \frac{\cos(\chi)}{2r} \right), \tag{2.6}$$

where $\bar{\kappa}_{\times} = \kappa_{\times} - \kappa_{\|} - \kappa_{\perp}$. We could have written the energy directly in terms of $\bar{\kappa}_{\times}$ by switching from a $(TKT)^2$ to a $TKKT$ parameterization as permitted by the unit-vector constraint. Fixed aster or vortex configurations carry no energy cost from the term proportional to $\bar{\kappa}_{\times}$. Setting to zero the functional derivative of $F_{nematic}$ with respect to χ yields a *shape equation*, which for an aster ($\xi = 0$) becomes

$$0 = \sigma \frac{r\sin(\chi)}{\cos^2(\chi)} + \frac{\kappa_{\|}}{2}(-2\cos(\chi)\chi' + r\sin(\chi)\chi'^2 - 2r\cos(\chi)\chi'') + \frac{\kappa_{\perp}}{2}\left(1 + \frac{1}{\cos^2(\chi)}\right)\frac{\sin(\chi)}{r} - \frac{K_1}{2}\frac{\sin(\chi)}{r}. \tag{2.7}$$

For fixed vortices, the same shape equation holds after switching the coefficients $\kappa_{\perp} \leftrightarrow \kappa_{\|}$ and $K_1 \leftrightarrow K_3$.

For any membrane (hexatic or nematic) without stiffness ($\{\kappa\} = 0$), defects have a simple universal shape resulting from the competition between the in-plane misalignment cost and surface tension. The misaligned rods near the defect core can align by bending out of the plane into the third dimension, at the cost of increasing surface area. The optimum tangent angle is given by the simple formula

$$\cos(\chi) = \sqrt{\frac{2\sigma r^2}{K_1}} = \frac{r}{r_0}, \tag{2.8}$$

where $r_0 = \sqrt{K_1/2\sigma}$ is the distance outside of which surface tension dominates and flattens the surface. Integrating the angle gives the universal shape

$$h(r) = r_0\left(\operatorname{sech}^{-1}\left(\frac{r}{r_0}\right) - \sqrt{1 - \left(\frac{r}{r_0}\right)^2}\right), \tag{2.9}$$

which approaches vertical at $r = 0$ where the height is logarithmically divergent. This may be regulated by a cut-off, such as the membrane thickness. As a reference, at half the rim radius: $h(r_0/2) \approx 0.45\, r_0$. In a hexatic membrane $K_1 = K_3$, so asters and vortices have the same radius. In a nematic membrane, asters and vortices have different radii; the lower energy defect also has smaller size.

This shape, Eq. (2.9), is known as a *parabolic pseudosphere* or *antisphere*, because it has constant negative Gaussian curvature equal to $-1/r_0^2$ [136, 230]. It is also known as a *tractrisoid*, because it is half the surface of revolution generated by revolving a *tractrix* about its asymptote [187]. The tractrix is the path of an object being dragged by a string of constant length along a straight line that does not intersect the object. Leibniz likened this problem to a dog owner dragging his hound by its leash and named the solution *hundskurve*. The hundskurve has been studied by Huygens and others [84]. This construction makes it clear that the distance to the axis along the line tangent to any point on the surface is constant, i.e. the leash length is r_0. These shapes of constant negative curvature are also known in quantum gravity as solutions to classical Liouville theory [133].

This simple shape has singularities at the origin and at the rim $r = r_0$, which are modified by the membrane bending rigidities, $\kappa_\perp$ and $\kappa_\parallel$, respectively. Setting $\kappa_\parallel = 0$ removes all derivatives of χ from the shape equation, so a simple rearrangement provides the solution,

$$\cos(\chi) = \sqrt{\frac{2\sigma r^2 + \kappa_\perp}{K_1 - \kappa_\perp}} = \sqrt{\frac{\left(\frac{r}{r_1}\right)^2 + c}{1 + c}}\ , \tag{2.10}$$

where $r_1 = \sqrt{(K_1 - 2\kappa_\perp)/2\sigma}$ is the new rim radius, and $c = \kappa_\perp/(K_1 - 2\kappa_\perp)$ is related to the now finite slope at the tip. For sufficiently large K_1, the surface puckers out of the plane for $r < r_1$, with a profile

$$
\begin{aligned}
h(r) &= \int_r^{r_1} \tan\left[\pm\cos^{-1}\left(\sqrt{\frac{2\sigma r^2 + \kappa_\perp}{K_1 - \kappa_\perp}}\right)\right] dr && (2.11)\\
&= \pm r_1 \int_{\frac{r}{r_1}}^{1} \sqrt{\frac{1-u^2}{c+u^2}} du \ . && (2.12)
\end{aligned}
$$

For $K_1 < 2\kappa_\perp$ or for $r_1 < r$, this solution is not real, so $\chi = 0$ becomes the only solution to the shape equation.

Equation (2.12) is a complete elliptic integral of the second kind [222]. We change variables $u \to \sqrt{c}\sinh(u)$ to obtain

$$h(r) = \pm r_1\sqrt{1+c}\int \sqrt{1 - \frac{c\cosh^2(u)}{1+c}} du \ , \tag{2.13}$$

where the integration ranges from $\sinh^{-1}(r/(r_1\sqrt{c}))$ to $\sinh^{-1}(1/\sqrt{c})$. In the study of surfaces with constant Gaussian curvature, Eq. (2.13) is a familiar expression for an *elliptic* pseudosphere [136]. Figure 2-3 shows an example elliptic pseudosphere.

The bending rigidity cuts off the logarithmically diverging tip near the core. Near the origin, the elliptic pseudosphere is approximately cone-shaped with slope $\sqrt{1/c} = \sqrt{(K_1 - 2\kappa_\perp)/\kappa_\perp}$,

$$h(r) \to \pm\frac{r}{\sqrt{c}} \ . \tag{2.14}$$

If the r^2 term in Eq. (2.10) were not present, the shape would be a cone. Unlike the cone, pseudospheres have constant Gaussian curvature,

$$
\begin{aligned}
\frac{1}{R_1 R_2} &= \det\left[K_i^j\right] = \det\left[g^{ab}\hat{\boldsymbol{n}}\cdot\nabla_b\vec{\boldsymbol{t}}_c\right]\\
&= -\frac{1}{r_1^2(1+c)} , && (2.15)
\end{aligned}
$$

where $\hat{\boldsymbol{n}}$ is the unit vector proportional to $\vec{\boldsymbol{t}}_1 \times \vec{\boldsymbol{t}}_2$ and we have carried through the computation after inserting the coordinate tangent vectors for the elliptic pseudoshere,

$$
\begin{aligned}
\vec{t}_1 &= \left(\cos(\theta), \sin(\theta), \sqrt{\frac{1-\left(\frac{r}{r_1}\right)^2}{c+\left(\frac{r}{r_1}\right)^2}}\right) \\
\vec{t}_2 &= (-r\sin(\theta), r\cos(\theta), 0) \ .
\end{aligned}
\tag{2.16}
$$

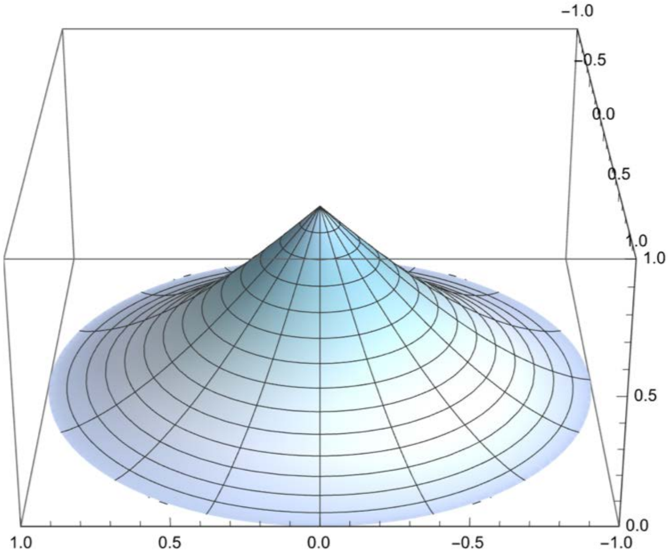

Figure 2-3: An example of buckled shape for $r_1 = 1$ and $c = 1$.

Even with finite $\kappa_\perp$ the above shape retains a cusp-like singularity at the origin. We may well question how the singularity is modified by inclusion of cut-offs and higher order terms. A simple short-distance cut-off, a, can be introduced as the radius of a hemispherical or similar cap over the singular point at the origin. The curvature energy density $\sim 1/a^2$ integrated over the cap's area $\sim a^2$ leads to a finite energy. We can then regard this as a benign singularity that adds a constant to the defect core energy E_c in Eq. (2.3).

Substituting Eq. (2.10) into the full shape equation, Eq. (2.7), leaves a term proportional to both $\kappa_\parallel$ and to r, so the elliptic pseudosphere is expected to remain valid as $r \to 0$ near the core. The situation at the rim is very different: Designating the distance from r_1 by $\epsilon = 1 - r/r_1$, one sees that $\chi \propto \sqrt{\epsilon}$ as $\epsilon \to 0^+$ and is zero immediately outside this radius. The abrupt rim would cause the energy proportional to $\kappa_\parallel$ to diverge, so when $\kappa_{||} > 0$, the defect shape must be different. Since χ tends to zero away from the core, we linearize the shape equation for small χ and χ' to

$$0 \approx \left((K_1 - 2\kappa_{\perp}) \frac{1}{r} - 2\sigma r \right) \chi + 2\kappa_{||}(\chi' + r\chi'') \ . \tag{2.17}$$

After changing variables to ϵ and redefining $\chi \rightarrow \chi(\epsilon)$ to be a function of ϵ, the linearized shape equation is

$$0 = \epsilon(\epsilon - 2)\chi - \frac{2\kappa_{||}(\epsilon - 1)}{K_1 - 2\kappa_{\perp}} (\chi' + (\epsilon - 1)\chi'') \ . \tag{2.18}$$

Note that the approximation is made for small χ and χ', and ϵ need not be small. For real-valued $\chi(\epsilon)$, this equation is solved by modified Bessel functions of the second kind with imaginary order. The order and argument both diverge with vanishing $\kappa_{||}$, as

$$\chi(\epsilon) \propto K\left[i\nu, \nu \frac{r}{r_1} \right] , \tag{2.19}$$

with

$$\nu = \sqrt{\frac{K_1 - 2\kappa_{\perp}}{2\kappa_{||}}} \ . \tag{2.20}$$

This solution decays exponentially and has no zeros for $r_1 \leq r$. Since our parameterization does not handle overhanging surfaces, χ is limited to the range $(-\pi/2, \pi/2)$. Thus, for a given value of ν, the amplitude must be such that the solution stays in this range. For ν of order one and larger, an amplitude of unity yields a χ that is sufficiently small for $r_1 \leq r$ that the linearized shape equation is valid. It approaches zero asymptotically, so the rim radius at which $\chi = 0$ shifts to infinity. The asymptotic form of Eq. (2.19) is [87, 95]

$$\chi \sim \frac{e^{-\sqrt{\frac{3}{2}}\nu \frac{r}{r_1}}}{\sqrt{\frac{r}{r_1}\nu}} \text{ , for } (\nu, r) \longrightarrow \infty \ , \tag{2.21}$$

which shows that bending rigidity introduces a new length scale

$$r_2 \equiv \sqrt{\frac{2}{3}\frac{r_1}{\nu}} = \sqrt{\frac{2\kappa_{\|}}{3\sigma}} \ . \tag{2.22}$$

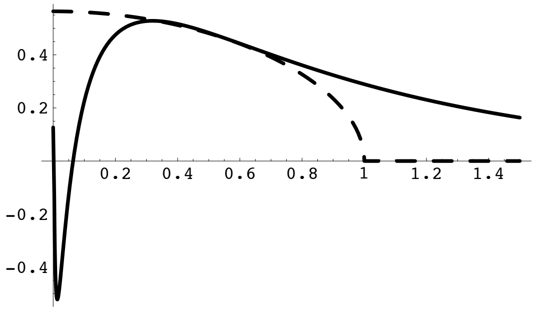

Figure 2-4: The tangent angle (not the height) as a function of radius in units of r_1. Solid curve: The Bessel function solution for $\chi(\epsilon)$ for $\nu = 1$. Dashed curve: $\cos^{-1}\left(\sqrt{\left((r/r_1)^2 + c\right)/(1+c)}\right)$ for $c = 2.5$ chosen to suggest matching in the crossover.

As shown in Fig. 2-4, this solution for χ oscillates sharply near the core, which invalidates the small χ' approximation. In this region, nonlinearities take over and the shape crosses over to the elliptic pseudosphere. As $\kappa_{\|}$ approaches zero, the Bessel function becomes flat for $r_1 < r$ and oscillates rapidly inside this radius, thus restoring the abrupt rim.

2.4 Conclusions and Outlook

We predict that topological defects can buckle nematic membranes into elliptic pseudospheres with exponentially decaying rims. Let us explore this possibility in the case of a freely suspended thin film of smectic-C liquid crystal. The observation that these films maintain orientational order at room temperature suggests that K_1 (and K_3) are at least of the order of $k_B T_{\text{room}} \approx 4 \times 10^{-14}$erg. If we assume a surface tension typical of *bulk* liquid crystal interfaces, $\sigma \sim 10$ ergs/cm^2, and ignore bending rigidities ($\{\kappa\} = 0$), then from $K \sim k_B T_{\text{room}}$, we would estimate a rim radius $r_0 = \sqrt{K/2\sigma} \approx 1/2$ nm, which is smaller than a typical film thickness and beyond the limits of this coarse grained model. To create larger (observable) defects requires either smaller surface tension or larger in-plane stiffness than this initial estimate. Some physical systems may allow this.

For example, studies of thin films of liquid crystal often observe a small surface tension, because the chemical potential for particles in the film is similar to the chemical potential in the meniscus surrounding the film [105]. This reservoir on the edge of the suspended film allows the film to increase its area at a low energetic cost. One might control the size of buckled defects by manipulating the surface tension via this reservoir.

In addition to having a surface tension smaller than our initial estimate, some materials have observed values of $\{K\}$ one or two orders of magnitude larger than room temperature. For example, scattering studies by Spector et al on thin films of smectic-C 8OSI found large values of $\{K\}$ and surface tension made small by the meniscus [146]. This particular study used a smectic-C tilt angle of 32.2° and found $K_1/K_3 = 4.6(\pm 0.4)$, $\kappa_{||}/K_3 = 3.4(\pm 0.3)$, $\kappa_{\times}/\kappa_{||} = 5.5(\pm 3.1)$, $\kappa_{\perp}/\kappa_{||} = 75(\pm 24)$, and $\kappa_{||} \approx 10^{-12}$ergs. Unfortunately, the large value of $\kappa_{||}/K_3$ prevents buckling. Since $K_1/K_3 > 1$, flat vortices should be stable relative to asters. For other tilt angles or other materials, one might hope to find lower values of $\kappa_{||}/K_3$ that allow buckling.

For sufficiently floppy films, buckled defects could be observable via specular reflection or by interferometry techniques used to measure the flatness of mirrors. Additionally, islands of smectic-C material may provide means of manipulating single defects with laser tweezers, although coupling between the island's multiple smectic layers may introduce additional affects [199].

While smectic-C 8OSI has sufficiently small surface tension and large in-plane stiffness, its bending rigidity suppresses buckling. That such shapes have not been observed so far in other materials may well be an indication of the importance of bending rigidity. Since typical lipid membranes have $\kappa \sim 5 k_B T_{\mathrm{room}}$, this is a severe constraint. We note, however, that for stiff rods (nanotubes, cytoskeletal filaments) embedded in membranes, the rigidities, $\kappa_{\|}$ and $\kappa_{\perp}$, and corresponding stiffnesses, K_1 and K_3, may well differ by orders of magnitude. The challenge remains to obtain estimates of these parameters for specific microscopic models, and come up with an appropriate system for the study of buckled defects. Observations of these shapes in nematic membranes may provide estimates of the ratios between $\kappa_\perp$, $\kappa_{||}$, K_1, K_3, and σ. Measurements of $\kappa_\times$ are possible via other shapes as described in Appendix 2.5.

If one could control the anisotropic bending rigidities individually, one might be able to sweep a nematic membrane through a sequence of regimes in which different types of defects are stable. For example, for $K_3 < K_1$, if one could hold $\kappa_{||}$ fixed while adjusting $\kappa_\perp$ one might observe buckled vortices when $2\kappa_\perp < K_1 - K_3 + 2\kappa_{||}$, and buckled asters when $K_1 - K_3 + 2\kappa_{||} < 2\kappa_\perp < K_1$, and buckled vortices again when $K_1 < 2\kappa_\perp$. By increasing $\kappa_{||}$ while keeping $\kappa_\perp$ in any of these regimes, one would flatten the preferred shape of vortices. Thus, it is possible for vortices and asters to prefer buckled or flat shapes independently.

In focusing on shapes of minimal energy, we have neglected thermal fluctuations. At long distances, thermal fluctuations reduce the differences between aster and vortex defects in *weakly* anisotropic membranes [152]. In future work, we would like to explore if this is still the case in *strongly* anisotropic membranes, or if thermal fluctuations can enhance the anisotropy.

Unlike bulk nematics, nematic sheets often appear with naturally periodic boundaries such as closed vesicles. By the Poincare-Brouwer theorem [180], a genus zero nematic vesicle must have topological charge of $+2$. In fact, defects can burst the vesicle [139, 156, 159]. This resembles Bryopsis sprouting branches out of defects in its tethered nematic cell wall – a topic to which we hope to return in the future.

2.5 Appendix: Nematic Membranes in Fixed Geometries

While $\kappa_\times$ did not contribute to the shape of $+1$ defects, it affects other geometries. Following de Gennes' molecular field argument [143], we impose the unit vector constraint via a Lagrange multiplier λ and seek energy minimizing filament configurations in fixed geometries. In a two-bein basis aligned with the principle directions, the curvature tensor is diagonal and $T^a = e^a_i T_i$, where e^a_i is a transformation to local coordinates in which $g_{ab} \to \delta_{ij}$ at each point [188]. In the principle two-bein,

$$T_i = \begin{pmatrix} \cos(\xi) \\ \sin(\xi) \end{pmatrix}. \tag{2.23}$$

In the following, there is no summation over i or $\bar{i} = (i+1) \mod (2)$. The functional derivative of Eq. (2.1) in the principle two-bein reads

$$\begin{aligned} H_i \equiv & \frac{\delta F}{\delta T_i} = -\lambda(\sigma^1, \sigma^2) T_i \\ =& T_i \left\{ \kappa_{\|} C_i^2 + \kappa_{\perp} C_{\bar{i}}^2 + \bar{\kappa}_{\times} T_{\bar{i}}^2 (C_1 - C_2)^2 \right\} \\ & - K_1 \partial_i \left(\nabla_k T_k \right)) - K_3 \epsilon_{ji} \partial_j \left(\epsilon_{kl} \nabla_k T_l \right) \\ =& T_i \left\{ \kappa_{\|} C_i^2 + \kappa_{\perp} C_{\bar{i}}^2 + \bar{\kappa}_{\times} T_{\bar{i}}^2 (C_1 - C_2)^2 \right\} \\ & - K_1 \partial_i \left(\partial_k \xi - A_k \right) T_{\perp k} \\ & - K_3 \epsilon_{ji} \partial_j \left(\partial_k \xi - A_k \right) T_k \,, \end{aligned} \tag{2.24}$$

where C_i are the principle curvatures and $A_i = \hat{e}_1 \cdot \partial_i \hat{e}_2$ is the spin connection. The three-vectors $\hat{e}_i = e^a_i \vec{\boldsymbol{t}}_a$ form an orthonormal basis in the principle two-bein. To setup the molecular field equation, one must carry out the derivatives and pullout an overall factor of T_i to obtain an expression for λ that is a function of index i. One obtains an equation for ξ by requiring λ to be a scalar, i.e., to have the same value for both $i = 1$ and $i = 2$. Solutions to this equation for ξ extremize the energy.

Considering first $K_1 = 0 = K_3$, the equation yields a simple solution for ξ,

$$\cos^2(\xi) = \frac{1}{2} \left(1 + \frac{\kappa_{\|} - \kappa_{\perp}}{\kappa_{\times} - \kappa_{\|} - \kappa_{\perp}} \frac{C_1 + C_2}{C_1 - C_2} \right) \,. \tag{2.25}$$

This is only valid with both components of T_i are non-zero, so $\xi = 0$ and $\xi = \pi/2$ must also be considered in the list of possible ξ values. One must check which candidate value for ξ minimizes the energy for particular values of $\{\kappa\}$ and the principle curvatures. In the following, we list a few special cases. When $\kappa \equiv \kappa_{\|} = \kappa_{\perp} \neq \kappa_{\times}/2$ and

$C_1 \neq C_2$, one has that $\xi = \pi/4$ minimizes the energy if

$$\frac{\kappa}{\kappa_\times} > -\frac{(C_1 - C_2)^2}{4C_1C_2} \; . \tag{2.26}$$

Otherwise, the filaments align with the least curved direction.

When $\kappa_\times = \kappa_{||} + \kappa_\perp$, so that $\bar{\kappa}_\times = 0$, the orientation can be found by minimizing the energy with respect to ξ directly, instead of the molecular field equation. The result for $K_1 = 0 = K_3$ and $C_1 < C_2$ is shown in Table 2.1.

Angle	Stability Criterion
$\xi \; = 0$	$C_1\kappa_{\vert\vert} > C_2\kappa_\perp$
$\xi \; = \pi/2$	$C_1\kappa_\perp > C_2\kappa_{\vert\vert}$
$\cos^2(\xi) \; = \frac{C_1\kappa_\perp - C_2\kappa_{\vert\vert}}{(C_1-C_2)(\kappa_\perp+\kappa_{\vert\vert})}$	$C_1\kappa_\perp < C_2\kappa_{\vert\vert}$, $C_1\kappa_{\vert\vert} < C_2\kappa_\perp$

Table 2.1: Stability criteria when $\bar{\kappa}_\times = 0$, and $K_1 = 0 = K_3$ and $C_1 < C_2$.

On a developable surface, i.e. $C_1 = 0$ and $C_2 \neq 0$, when $\kappa_\times \geq 2\min\left\{\kappa_{||}, \kappa_\perp\right\}$ the stable orientation is aligned with the uncurved direction. For smaller values of $\kappa_\times$, a special intermediate angle is the global minimum,

$$\cos^2(\xi) = \frac{2\kappa_{||} - \kappa_\times}{2\left(\kappa_{||} + \kappa_\perp - \kappa_\times\right)} \; . \tag{2.27}$$

Note that this only occurs when *both* parallel *and* perpendicular bending are more costly than $\kappa_\times/2$. This might result from rods that weaken the sheet or have a specific texture on the rod's surface.

For a developable surface, the spin connection is zero, so the covariant derivatives become regular partial derivatives. Thus, on a cylinder, far from boundaries, a constant orientation solves the full molecular field equation with the gradient terms included. This could allow experimental measurement of $(2\kappa_{||} - \kappa_\times)/(\kappa_{||} + \kappa_\perp - \kappa_\times)$.

In more general geometries, in-plane splay and bend compete with out-of-plane bending in a non-linear PDE, which, in principle, can be numerically integrated to fit model parameters to vectorized images of a real nematic membrane. Computing model parameters from such images in the presence of topological defects requires care.

2.6 Appendix: Stability of Buckled Defect Shapes

As discussed in Appendix 2.5, the relative strength of $\kappa_\times$ plays an important role in the stability of orientation patterns on curved shapes. Substituting the principle curvatures for the elliptic pseudosphere into Eq. (2.25) yields an equation for ξ that is not constant,

$$\cos^2(\xi) = \frac{2\kappa_\perp \left(\frac{r}{r_1}\right)^2 - \kappa_\times}{2(\kappa_\perp - \kappa_\times)} \ , \tag{2.28}$$

and thus not the perfect aster (or vortex) that we assumed when setting up the shape equation, Eq. (2.7). Since Eq. (2.25) was derived assuming $K_1 = 0 = K_3$, the question remains whether the buckled defect is stable to perturbations away from a perfect aster (or vortex).

To check this, we construct linearized evolution equations for small perturbations,

$$\frac{d}{dt}\begin{pmatrix} \Delta \\ \Xi \end{pmatrix} \propto -\frac{\delta F}{\delta(\Delta, \Xi)} \approx M \begin{pmatrix} \Delta \\ \Xi \end{pmatrix}, \tag{2.29}$$

where Δ represents deviations of the surface away from a pseudosphere, and Ξ represents deviations away from an aster ($\xi = 0$). Perturbations of the height field couple with perturbations of the angle field, so all four components of the two-by-two matrix of differential operators, M, are non-zero. The perturbations are functions of both radius and angle, and are generally not radially symmetric. To solve this, we write the perturbations in a Fourier basis,

$$\begin{pmatrix} \Delta(r,\theta,t) \\ \Xi(r,\theta,t) \end{pmatrix} = \sum_m \begin{pmatrix} \Delta_m(r) \\ \Xi_m(r) \end{pmatrix} e^{im\theta} e^{\lambda_m t} \ , \tag{2.30}$$

where each two-vector (Δ_m, Ξ_m) is independent. Substituting this solution into the evolution equation gives a separate set of coupled equations for each m-value.

Neglecting bending rigidity, and choosing units of energy such that $\sigma = 1$ and units of length such that $K_1 = 2\sigma$, we have for each value of m,

$$M^{(m)} = \left[\begin{array}{c|c} \frac{r(-K_3 m^2 r + 2(1-r^2)((2-4r^2)\partial_r + r(1-r^2)\partial_r^2))}{1-r^2} & \frac{im((2-K_3)r - (2-(2-K_3)r^2)\partial_r)}{\sqrt{1-r^2}} \\ \hline \frac{im(K_3 r + (1-r^2)(2-(2-K_3)r^2)\partial_r)}{r(1-r^2)^{3/2}} & -\frac{2m^2}{r^4} + K_3\partial_r^2 \end{array}\right]. \tag{2.31}$$

For $m = 0$, the equations decouple. Since these are perturbations, we must find real-valued solutions that vanish at the boundaries $r = 0$ and $r = 1$. The equation for Ξ has such a solution,

$$\Xi \propto \sin\left(r\sqrt{\frac{-\lambda_0}{K_3}}\right) , \tag{2.32}$$

if $\lambda_0 = -K_3\pi^2 n^2$ for integer n. This is always negative. The equation for Δ has the real-valued solution

$$\begin{aligned} \Delta \quad \propto \quad & r^{2a}\,{}_2F_1(a, a+\frac{3}{2}; 2a+\frac{3}{2}; r^2) \\ & + r^{2b}\,{}_2F_1(b, b+\frac{3}{2}; 2b+\frac{3}{2}; r^2) , \end{aligned} \tag{2.33}$$

where ${}_2F_1$ is the Gauss hypergeometric function and $a = (-1-\sqrt{1+2\lambda_0})/4$ and $b = (-1+\sqrt{1+2\lambda_0})/4$. Since the third argument exactly equals the sum of the first two, $0 < r < 1$ is the convergent domain for these functions. An ad hoc numerical study indicates that $\lambda_0 \to -\infty$ might extend this domain and allow the limit $\Delta(1) \to 0$. These functions also diverge at $r = 0$, and again a large negative λ_0 appears to mediate this because the function oscillates rapidly and might average to zero as $r \to 0$. We lack an analytic treatment of this asymptotic regime, so we turn to a numerical method below.

Considering $0 < m$ and substituting $u = r^2$, one sees that Eq. (2.31) consists of second-order ODEs with non-essential singularities at two points (the boundaries), so the equations can be transformed into hypergeometric differential equations [229]. By combining linearly independent solutions, one might construct real solutions that meet the boundary conditions for all values of m. After satisfying these constraints, one would obtain expressions for λ_m, which, when negative, indicate stable regions of parameter space. This approach is complicated even when rigidity is neglected.

Instead of taking this approach, we have checked stability numerically by discretizing the fields. We represent the deviations of the height and angle fields by a large column vector of field values at discrete steps in radius and polar angle. By representing the derivative operators as banded square matrices acting on this large vector, one obtains a matrix of numbers for any given set of parameter values. The largest non-zero eigenvalue of this matrix determines the stability of the shape. If the largest non-zero eigenvalue is negative, then that set of parameters suppresses perturbations and the shape remains stable.

We have carried out such a numerical procedure. Generally, the buckled aster is stable for $2\kappa_\perp < K_1 < K_3$ and any $0 < \kappa_\times$. The analogous statement holds for buckled vortices.

Chapter 3

Turing Patterns on Curved Interfaces

Diffusion-driven patterns appear on curved surfaces in many settings, initiated by unstable modes of an underlying Laplacian operator. On a flat surface or perfect sphere, the patterns are degenerate, reflecting translational/rotational symmetry. Deformations, e.g. by a bulge or indentation, break symmetry and can pin a pattern. We adapt methods of conformal mapping and perturbation theory to examine how curvature inhomogeneities select and pin patterns, and confirm the results numerically. The theory provides an analogy to quantum mechanics in a geometry-dependent potential and yields intuitive implications for cell membranes, tissues, thin films, and noise-induced quasipatterns.

3.1 Motivation

In Chapter 2, we studied orientational order on curved interfaces. As discussed in Chapter 1, such order arises in biological systems on many length scales, including rod-shaped molecules floating in cell membranes. These systems also exhibit pattern formation, which can often be modeled using Turing or Turing-like reaction-diffusion processes. For example, in bacteria, the MinCDE system of proteins acts as a measuring stick for detecting a cell's size and locating its midplane where the division ring forms during mitosis [245]. MinCDE also forms patterns *in vitro*, see Figure 3-1. When such patterns occur on cell membranes or multi-cellular tissues, how does curvature influence the patterning?

Many microscopic factors could be at play in real patterns, including the three-dimensional orientation of particles in the surface. While one would like a unified model that includes orientational order and chemical patterning, such a model will be complicated. As a step toward this larger goal, we ask how pattern formation proceeds on a curved surface. As discussed in Chapter 1, irregularly shaped transmembrane proteins can anchor machinery to curved regions of membranes. For example, the banana-shaped BAR domain has a radius of curvature of 11nm and plays many roles in cellular processes, including generating membrane tubules [200]. BAR can also *sense* curvature and cooperatively enhance processes in curved regions [206]. Endocytosis depends on a concert of molecular machines including clathrin triskilions and dynamin that create “pits” in the cell membrane and then pull pits into the cell to form vesicles of 60-140nm in diameter.

Similarly, actin has been observed to localize to curved regions in cells, which is relevant to lamellipodia and cell motility [268, 303]. However, it is still an open question as to what mechanisms select a the locations for these various patterns on the membrane [304]. While the *Bacillus Subtilis* cell in Figure 1-4 appears approximately spherical, most cells not perfect spheres. When rotational symmetry is broken by a deformation, how does this influence patterning?

In the following, I will show that membrane-bound diffusion *alone* can sense regions of curvature and localize patterns *without help from irregularly shaped molecules.*

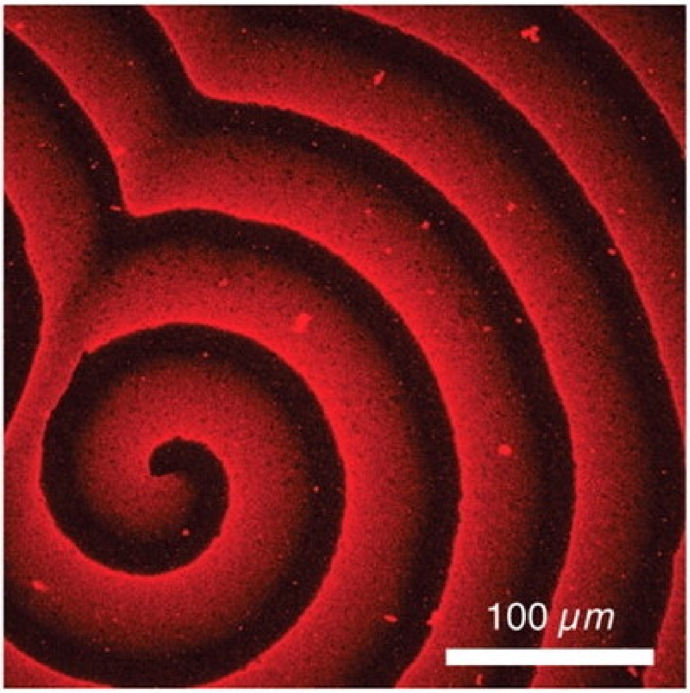

Figure 3-1: Spiral waves formed by Min proteins, showing only MinE. (Both MinD and MinE are 1 μM concentration.) Reprinted with permission from AAAS, "Spatial Regulators for Bacterial Cell Division Self-Organize into Surface Waves in Vitro" by Loose *et al.* in *Science* 2008.[237]

When beginning this work to study localization phenomena, I built simulations in COMSOL.[1] Based on the considerations outlined above, I had expected that curvature-sensing particles would be an essential ingredient. I had expected that diffusion would be mostly a bystander. When one looks at Turing's basic reaction-diffusion system described in Eqn. 1.7, more ink is dedicated to reaction rates than to the Laplacian.

Let us represent protein concentration by a field $\Phi(x, y, t)$. As a heuristic equation of motion, one might expect the proteins to seek regions where the membrane's radii of curvature R_i are close to the protein's preferred radius of R_0:

$$\frac{\partial \Phi}{\partial t} = \kappa' \left(\frac{1}{R_1} + \frac{1}{R_2} - \frac{\Phi}{R_0} \right) + D \Delta \Phi \,. \tag{3.1}$$

A diffusion term is "tacked on" at the end for stability.

---

[1] In 2008-10, the global financial crisis pulled me out of MIT and back into my company MetaCarta, which landed at Nokia in April of 2010 just three weeks after my wife gave birth to our first child. Later that year, I dove back into physics with the COMSOL simulations that eventually led to the paper in the next section.

Given the success of minimum energy shapes in the study of vesicle, it is natural to look at extending the Canham-Helfrich energy of Eqn. 1.6 with a location-dependent spontaneous curvature. That is, Helfrich's spontaneous curvature constant $H_0 = 1/R_0$ is now multiplied by the chemical concentration Φ that varies in space and time:

$$E = \oint_S dA \left[\sigma + \frac{\kappa}{2} \left(K^a_a - H_0 \Phi \right)^2 + D \left(\nabla_a \Phi \right) \left(\nabla^a \Phi \right) \right] . \tag{3.2}$$

Where again, we add diffusion $D(\nabla\Phi)^2$ for stability. Minimizing such an energy yields the same Langevin equation as Eqn. 3.1,

$$\frac{\partial \Phi}{\partial t} \propto -\frac{\delta E}{\delta \Phi} = \kappa H_0 \left(K^a_a - H_0 \Phi \right) + D \Delta \Phi . \tag{3.3}$$

However, I quickly found that pattern localization occurred with $H_0 = 0$ in simple simulations. Even with just one compound diffusing on a simulated membrane in a differential equation solver like COMSOL, concentrations in regions of high curvature and low curvature equilibrate differently. Inspired by this observation, I implemented two-component reaction diffusion systems, like the Thomas-Murray model, and found that pattern localization occurred generically *without* inserting a curvature sensing term like H_0.

Therefore, curvature sensing arises naturally in the Laplacian itself. The paper in the next section presented our analytical explanation of this phenomenon.[2]

As the simplest scalar differential operator, the Laplacian ∇^2 appears in many models of natural phenomena. Laplace found its eigenfunctions in rectangular coordinates in 1787 [18], and Fick used it to describe diffusion in 1855 [35]. Laplace's familiar $-k^2$ eigenvalues and $e^{i\vec{\boldsymbol{k}}\cdot\vec{\boldsymbol{x}}}$ eigenfunctions appear throughout scientific and engineering literature. The cylinder and sphere also have simple eigenvalues for the Laplacian, $-k^2 - s^2$ and $-l(l+1)$, respectively. The Laplacian is well-defined on less simple shapes, however its eigenvalues and eigenfunctions are generally not known in closed form. By considering surfaces that are small deviations away from simple geometries for which closed forms exist, we calculate corrections to the eigenvalues and eigenfunctions, and thus *also to diffusion.*

---

[2] I presented key parts this work at a Gordon Conference and the APS March Meeting in 2011. However, the launch of my second text-mining startup Diffeo delayed expanding the results and publication for several years. I am very grateful to my co-authors. European Physics Letters accepted the paper in 2019 just a few weeks before Salesforce completed the acquisition of Diffeo.

Ripples imposed on a cylinder or sphere cause diffusion to speed up in regions of negative Gaussian curvature, and to slow down where curvature is positive [244]. This geometric principle foreshadows our results and is useful guide, so let me emphasize the connection to Gaussian curvature. The celebrated "Einstein relation" was derived independently by three people around 1905 [57–59]:

$$D = \frac{RT}{6\pi N_{\text{A}} \eta r}$$

where R is the ideal gas constant, T is temperature, η is the dynamic viscosity of the fluid, r is the radius of the particle moving through the fluid, and N_{A} is Avogadro's number. M.J. Perrin used this expression for the rate of diffusion to measure Avogadro's number as 7.05×10^{23} and publish his famous book "Brownian Movement and Molecular Reality"[60], for which he won the Nobel Prize in 1926. The granules in Perrin's experiment moved in flat Euclidean space, so D was the same at each point in his chamber. However, when the experiment is *lifted* onto a curved surface the mean-square-displacement (MSD) of a diffusing particle is changed, such that the *short-time* mean-squared-displacement is larger (diffusion faster) in regions of negative Gaussian curvature, and smaller (diffusion slower) in regions of positive Gaussian curvature. See Figure 3-2

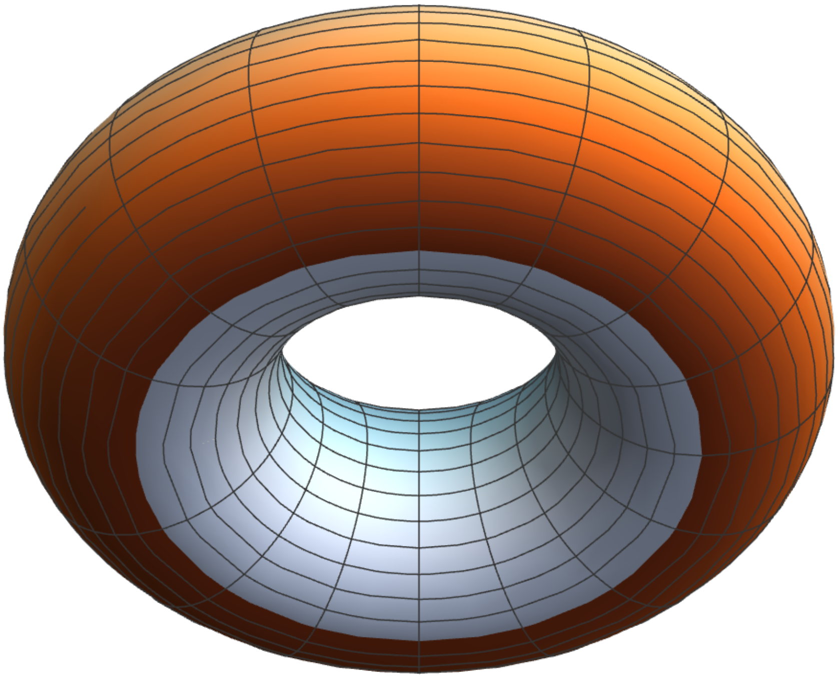

Figure 3-2: This torus illustrates different values of Gaussian curvature. The red outer region has positive Gaussian curvature where the MSD of a diffusing particle is shorter, so diffusion is slower. The interior neck region has negative Gaussian curvature and longer MSD, so faster diffusion. See Ref. [244] for further discussion.

Remarkably, this change to the MSD is an *intrinsic* property of the surface. This is not obvious from the picture. It requires a careful calculation to find that the leading order correction from surface curvature to the short-time mean-square-displacement of a diffusing particle is proportional to the Gaussian curvature [244]:

$$\left\langle s^2 \right\rangle_t = 4Dt - \frac{4}{3}\frac{1}{R_1 R_2}(Dt)^2 + \ldots$$

In the following, we will expand this idea in three ways. First, we show how this modifies the eigenfunctions and eigenvalues of the Laplacian on various geometries. Second, our procedure for computing these modifications provides a general tool set for understanding diffusion on curved surfaces. Third, we show how this location-dependent diffusion modifies reaction diffusion systems such that deformations can anchor patterns. Our approach connects these results to diffusion and biological pattern formation.

Just as we've discussed in previous chapters, we can locate the surface using an embedding vector,

$$\vec{\boldsymbol{X}}(\sigma^1, \sigma^2) = \begin{pmatrix} x(\sigma^1, \sigma^2) \\ y(\sigma^1, \sigma^2) \\ z(\sigma^1, \sigma^2) \end{pmatrix} \in \mathbb{R}^3 \,. \tag{3.4}$$

I emphasize this structure of the embedding vector, because in this chapter, we will construct a special parameterization σ^a called "conformal" coordinates. To motivate this, let me briefly outline the steps that I initially took that revealed the need for this.

Our agenda is to start with a surface shape that admits closed form eigenfunctions of the Laplacian, such as a cylinder, and then *perturb the geometry* into a slightly different shape whose eigenvalues and eigenfunctions we approximate using those of the unperturbed shape. When first writing these expressions, one naturally writes σ^a as a selection of the lab frame coordinates. For example, for a nearly flat patch, we can follow Monge and parameterize the surface by (x, y). For a cylinder, cylindrical coordinates (ϕ, z) are natural, or for a sphere, (ϕ, θ). However, in this introduction section, we will briefly illustrate that the conformal coordinates are easier to use than the lab frame coordinates.

Just as in quantum mechanics, we can use the eigenfunctions of any normal operator as a basis for the function space.[3] As is commonly done, the Laplacian's eigenfunctions are a convenient choice. Since the Laplacian is manifestly self-adjoint, it is certainly normal, even if we cannot write its eigenfunctions in closed form. Let us denote these eigenfunctions by $\Phi_k(\sigma^1, \sigma^2)$ and expand them in terms of the unperturbed eigenfunctions, $\phi_k^{(0)}$.

From the embedding vector, we compute tangent vectors and then a metric induced by our choice of parameters. Denote the metric G_{ab}. To use perturbation theory, we require that this new metric is close to the unperturbed metric and can be written as a expansion in some small parameter ϵ:

---

[3] A normal operator commutes with its adjoint, i.e. $H^\dagger H = H H^\dagger$. The adjoint operator is its transpose conjugate, which in matrix notation is $H^\dagger_{jk} = H^*_{kj}$. Self-adjoint means that $H = H^\dagger$.

$$G_{ab} = g_{ab} + \epsilon G^{(1)}_{ab} + \epsilon^2 G^{(2)}_{ab} + \ldots$$

Any other quantity of interest can also be written as an analogous expansion.

Denote the Laplacian on the perturbed shape as Δ^G. This is a more nuanced object. We want to write it as Δ^g plus corrections. We can organize those corrections as follows:

$$\Delta^G = \frac{1}{\underbrace{\sqrt{g}\,{}^{\mathrm{A}}\Omega}_{=\sqrt{G}}} \partial_a \overbrace{\sqrt{g}\left(g^{ab} - T^{ab}\right)}^{\sqrt{G}\reflectbox{G}^{ab}} \partial_b = \frac{1}{{}^{\mathrm{A}}\Omega}\left(\Delta^g - \nabla_a T^{ab} \partial_b\right) . \tag{3.5}$$

We have defined two new quantities: T^{ab} and ${}^{\mathrm{A}}\Omega$.

${}^{\mathrm{A}}\Omega$ is the ratio of area elements. The area element $\mathrm{d}A = \sqrt{G}\,\mathrm{d}\sigma^1\,\mathrm{d}\sigma^2$, so when we use the same parameters for both the undeformed and deformed shapes, then ${}^{\mathrm{A}}\Omega$ equals the ratio of the square roots of the determinants of the metrics:

$${}^{\mathrm{A}}\Omega \equiv \frac{\mathrm{d}A^G}{\mathrm{d}A^g} = \frac{\sqrt{G}}{\sqrt{g}}$$

This ratio ${}^{\mathrm{A}}\Omega$ is useful analytically because the surface parameters $\mathrm{d}\sigma^a$ are the same in the numerator and denominator, so they cancel. This will not be the case for conformal scale factor ${}^{\mathrm{C}}\Omega$ introduced below.

The second object, T^{ab}, is the "one-tensor inner product correction" that appears in formulae like this:

$$U_a W^a = U_a W_b \reflectbox{G}^{ab} = U_a W_b g^{ab} - U_a W_b T^{ab}$$

Note that $\reflectbox{G}^{ab}$ is the matrix inverse of G_{ab}. We must use such a new symbol to denote the inverse metric of the deformed manifold when writing it in terms of tensors defined on the undeformed manifold.

We can directly apply Rayleigh-Schrödinger perturbation theory to the Laplacian in Eqn. 3.5 to obtain corrections to the eigenfunctions and eigenvalues. However, as explained in Appendix C, the first-order corrections are typically zero in the lab frame coordinates, so one must go to second-order, which is more complicated.

Conformal coordinates allows *first-order* perturbation theory to extract the key results. This is the benefit of using the conformal surface coordinate, which we denote v on the cylinder and Θ on the sphere. We construct this new surface parameter *from* one of the lab frame coordinate. For example, in cylindrical coordinates, our conformal coordinate $v \approx z$ plus small corrections. The benefit of constructing this new surface parameter is that it provides a *flat* metric with a location-dependent factor that rescales all directions *equally* at each point on the shape. Denoting this location-dependent scale factor by ${}^{\mathrm{C}}\Omega$, the Laplacian on the deformed shape becomes:

$$\Delta^G = \frac{1}{{}^{\mathrm{C}}\Omega^2}\Delta^0 \tag{3.6}$$

where Δ^0 is the *un*perturbed Laplacian in the *new* surface parameters, so we call it "conformally flat." In these coordinates, $T^{ab} = 0$. This is the source of the power of our conformal approach. I'm indebted to Jemal Guven for teaching me this approach. In this chapter, any reference to $\Omega \equiv {}^{\mathrm{C}}\Omega$. Where necessary, we use the pre-superscript "C" and "A" to distinguish between the conformal scale factor and the related but different ratio of area elements in the lab frame coordinates. Further details in Appendix C.

The remainder of this chapter is organized as follows. Section 3.2 is the paper that we published in European Physics Letters in 2019 [308]. Section 3.3 expands the development of the conformal mapping approach that efficiently extracts first-order corrections to diffusion from curved shapes. I comment on future work in Chapter 4.

3.2 Pinning of Diffusional Patterns by Non-Uniform Curvature

In 1952, Turing coined the term “morphogen” in a seminal paper that showed how combining diffusion with generalized reactions can create spatial and temporal patterns even though separately each leads to uniform, static concentrations [78]. Such reaction-diffusion (RD) patterns are but one example of diffusion-driven instabilities that have since been studied on scales ranging from tens of nanometers on neurons [253], microns in cells [246] and active fluids [251, 257, 264, 273, 303, 306], millimeters in hydrodynamics [243], centimeters in zoology [116], to meters in ecology [252]. Diffusion-driven patterns are known to determine morphology [248] in model organisms like zebrafish [241, 278] and complex organs like the eye [265]. Recent theoretical progress in patterning [293, 294] encourages further study.

Substrate curvature plays a role in pattern formation in many systems, including cell membranes [263] and thin films [250]. The importance of surface curvature on collective behavior has recently been explored in liquid crystals [295], flocking [301], and wave propagation [305]. Closer to our work, the geometric dependence of pattern formation has recently been studied in various models of protein [290, 291] and molecular bonding [302].

Recent studies of Turing patterns have explored the effects of curvature on highly symmetric shapes such as spheres, cylinders, toroids [287, 307], and ellipsoids [299] where the Laplacian is known in closed form.[18] Inhomogeneities in curvature, such as protrusions or cavities, reduce such symmetries and can pin or modify the patterns. To understand how nonuniform curvature can entrain and modify patterns, we study perturbations to the Laplacian, and its eigenmodes. To our knowledge, the intimate link between pinning of patterns and the spectrum of the Laplacian has not been pursued.

We follow a two prong strategy. First, we identify the *onset* of instabilities, by linearizing evolution equations expressed in terms of the appropriate ‘modes’, e.g., Fourier, cylindrical, or spherical harmonics. Modes with the largest positive real part grow fastest and are harbingers of the final patterns molded by nonlinearities. The modes are eigenfunctions of the diffusion (Laplacian) operator on the relevant manifold. Symmetries of the manifold, reflected in degeneracies of the eigenfunctions, must be broken in the final patterns. Previous work on the Laplacian on Riemannian manifolds focused on its determinant [86, 148, 163, 232] and short-time behavior appropriate to field theory [126, 179, 244]. We focus instead on how non-uniform curvature breaks degeneracies, pinning eigenfunctions to inhomogeneities. To do this, we utilize conformal mappings and perturbation theory. There is no guarantee, however, that patterns resulting from non-linear evolution are similarly entrained, so the second step in our study explores patterns with simulations. We implemented the Thomas-Murray RD equations [116] on COMSOL Multiphysics® [285]. We conclude with suggestions for experiments.

We first consider a cylinder with axially symmetric deformations described in cylindrical polar coordinates as $\rho = R(z)$. The surface line element is

$$\mathrm{d}s^2 = \left(1 + R_z^2\right)\mathrm{d}z^2 + R^2\,\mathrm{d}\varphi^2\ , \tag{3.7}$$

where R_z denotes the derivative with respect to z. The Laplacian of a scalar ϕ is

$$\Delta\phi \;=\; \frac{1}{\sqrt{g}}\partial_a\left(\sqrt{g}g^{ab}\partial_b\phi\right)\ , \tag{3.8}$$

where g_{ab} is the metric of the underlying geometry; g is the determinant of the metric. Conformal mapping simplifies analysis through mapping to a flat geometry. We introduce a conformal axial coordinate v, such that the line element acquires the conformally flat form

$$\mathrm{d}s^2 = \Omega^2(v)\left(\mathrm{d}v^2 + R_0^2\,\mathrm{d}\varphi^2\right)\ , \tag{3.9}$$

where R_0 is the asymptotic radius and Ω is the conformal factor. In the conformal coordinates, $\sqrt{g} = \Omega^2 R_0$, and thus the Laplacian on the deformed geometry takes the simple form $\Delta^G = \Omega^{-2}\Delta^0$, where Δ^0 is the Laplacian in the conformally flat coordinates. Since the behavior of Δ^0 is well understood, and Ω is determined by the equality of Eqs. 3.7 and 3.9, this conformal mapping provides a tractable method of understanding Δ^G.

Solutions for v and Ω for arbitrary $R(z)$ are in the supplement. To develop perturbation theory, we set $R = R_0(1+\epsilon h(z))$, in which case $v \approx z$ and $\Omega \approx 1 + 2\epsilon h(v)$ to lowest order, such that the eigenfunctions ϕ_k of Δ^G, with eigenvalues λ, satisfy

$$-\Delta^0\phi_k + 2\lambda\epsilon h(v)\phi_k = -\lambda\phi_k \,. \tag{3.10}$$

In analogy with quantum mechanics, one can interpret the deformation as giving rise to a potential in the conformal coordinates, whose magnitude is dependent on the eigenvalue λ. (This differs from da Costa's geometric potential, which comes from confining a particle to a surface [115].) For physical phenomena described by the Laplacian, this mapping can be interpreted as the replacement of the diffusion operator $-D\Delta$ on a deformed geometry, with a spatially-dependent diffusion coefficient $\tilde{D}(v) \equiv D/\Omega^2$ in the conformally-related homogeneous geometry. This provides an intuitive picture of how diffusion is modified by curvature.

The undistorted cylinder of length L with periodic boundary conditions has eigenfunctions and eigenvalues

$$\begin{aligned}\phi_{sk}^{(0)} &= \frac{e^{is\varphi}}{\sqrt{2\pi R_0}}\frac{e^{i2\pi kz/L}}{\sqrt{L}}\,,\\ \lambda_{sk}^{(0)} &= -\frac{s^2}{R_0^2} - \left(\frac{2\pi k}{L}\right)^2 \equiv -\bar{s}^2 - \bar{k}^2\,,\end{aligned} \tag{3.11}$$

with integers s and k. Consider an axially-symmetric bump on the cylinder, shaped like a Gaussian of standard deviation σ and height v_0. We apply Rayleigh-Schrödinger perturbation theory to Eqn. 3.10 to calculate eigenvalue corrections to first order in $\epsilon \equiv v_0/R$, which simplify for the case $s = 0$ to

$$\lambda_{0k}^{\pm} = -\bar{k}^2\left(1 \mp \frac{2\epsilon\sigma\sqrt{2\pi}}{L}e^{-2\bar{k}^2\sigma^2}\right) + \mathcal{O}\left(\epsilon^2\right). \tag{3.12}$$

The positive/negative sign (on $\lambda_{0k}^{\pm}$) is set by the mode: positive for cosine (symmetric) modes, and negative for sine (antisymmetric) modes. The sign of ϵ depends on the orientation of the ridge-like deformation: positive for a bulge and negative for a constriction. Thus, to first order, a ridge breaks the degeneracy in the eigenvalues of a Laplacian on the cylinder, causing the eigenvalues of sine (cosine) modes to become more negative in the case of an outward (inward) ridge.[4] This correction is largest for $2\pi/\bar{k} = 4\pi\sigma$, when the wavelength is approximately twice the width of the ridge. This is a general trait of deformations, explored later for a rippled cylinder. The ridge can be positioned anywhere along the cylinder, and the modes will shift with the ridge.

Modifications to the Laplacian spectrum affect any physical system involving diffusion. For example, consider a two-component RD system:

$$\partial_t \begin{pmatrix} \Psi_1(\mathbf{x},t) \\ \Psi_2(\mathbf{x},t) \end{pmatrix} = \overbrace{\begin{pmatrix} R_1(\Psi_1,\Psi_2) \\ R_2(\Psi_1,\Psi_2) \end{pmatrix}}^{\text{Reactions}} + \overbrace{\begin{pmatrix} \nu_1 & 0 \\ 0 & \nu_2 \end{pmatrix} \Delta^G \begin{pmatrix} \Psi_1 \\ \Psi_2 \end{pmatrix}}^{\text{Diffusion}} . \tag{3.13}$$

After linearization, small deviations around a uniform stable fixed point of the reactions, $(\Psi_1, \Psi_2)^*$, evolve as

$$\begin{pmatrix} \Psi_1(\mathbf{x},t) \\ \Psi_2(\mathbf{x},t) \end{pmatrix} = \begin{pmatrix} \Psi_1 \\ \Psi_2 \end{pmatrix}^* + \sum_k \begin{pmatrix} u_{1k} \\ u_{2k} \end{pmatrix} e^{t\omega(k)} \phi_k(\mathbf{x}) \ ,$$

with $\omega(k)$ satisfying eigenvalue equation, $\mathbf{M}(\lambda) = \mathbf{R} + \lambda\boldsymbol{\nu}$,

$$\left[\begin{pmatrix} R_{1,1} & R_{1,2} \\ R_{2,1} & R_{2,2} \end{pmatrix}^* + \begin{pmatrix} \nu_1\lambda_k & 0 \\ 0 & \nu_2\lambda_k \end{pmatrix} \right] \begin{pmatrix} u_{1k} \\ u_{2k} \end{pmatrix} = \omega(k) \begin{pmatrix} u_{1k} \\ u_{2k} \end{pmatrix} .$$

While the diffusion and stable reaction matrices separately posses negative eigenvalues, Turing showed that their sum can have positive eigenvalues ($\omega_+(k) > 0$) signaling finite-wavelength instabilities [78]. The possibly degenerate modes, k^*, with largest eigenvalue evolve to the final pattern. On a cylinder with a ridge, the degeneracy between sine and cosine modes is broken: an outward (inward) ridge leads to sine (cosine) growing faster.

---

[4] The words following Eqn. 3.12 were correct in [308]; however, the $\mp$ sign inside the parentheses in Eqn. 3.12 was incorrectly flipped. Here it is corrected. This agrees with the general principle that negative Gaussian curvature has shorter path lengths [244], so diffusion is faster on the shoulders of the outward ridge. For the constriction, this is reversed and diffusion is faster in the bottom of the valley at the origin where the Gaussian curvature is most negative. The sine modes sample the shoulders, and the cosine modes sample the origin. See Eqn. 3.46 for full derivation.

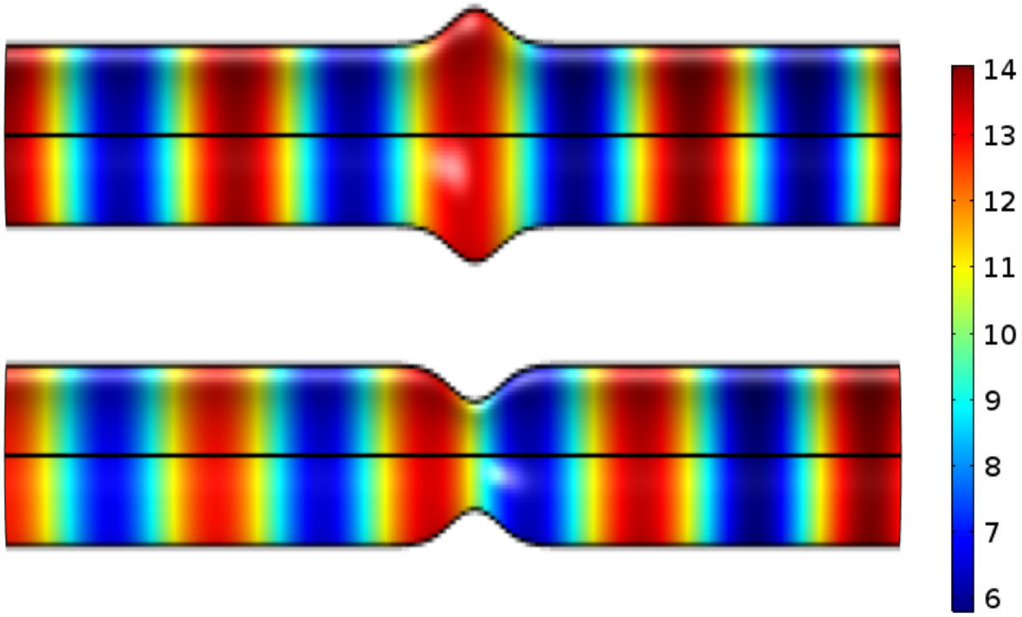

Figure 3-3: Patterns from the Thomas-Murray RD model in Eqn. (3.14) are entrained to a Gaussian-shaped ridge, switching in phase between inward and outward deformations. Red (blue) indicates a high (low) concentration of chemicals. Vertical dimension magnified 3x. Parameters: $\nu_1 = 1$, $\nu_2 = 10$, $u_{10} = 92$, $u_{20} = 64$, $\alpha = 1.5$, $K = 0.1$, $\gamma = 2$, and $\rho = 18.5$. Unless specified otherwise, other figures have these parameters. (See Sec. 3.3.1.1 for details.)

This linear analysis indicates only the onset of instabilities. To understand the patterns formed after nonlinearities stabilize the dynamics, we conducted finite element simulations of the Thomas-Murray model [116]:

$$\begin{aligned}\dot{\Psi}_1 &= \nu_1\Delta^G\Psi_1 + \gamma\left(\Psi_1 - u_{10} - \frac{\rho\Psi_1\Psi_2}{1+\Psi_1+\Psi_1^2/K}\right)\\ \dot{\Psi}_2 &= \nu_2\Delta^G\Psi_2 + \gamma\left(\alpha\left(\Psi_2 - u_{20}\right) - \frac{\rho\Psi_1\Psi_2}{1+\Psi_1+\Psi_1^2/K}\right) .\end{aligned} \tag{3.14}$$

We used COMSOL Multiphysics®[285], which approximates the Laplacian by finite differences on a mesh and computes the fully non-linear reaction terms. (Supplement includes .mph file.) It should be noted that, although periodic boundary conditions are enforced in the numerical calculations, the computational methods using by COM-

SOL have a tendency to pin the resulting Turing patterns in a specific configuartion, even on a flat cylinder. Despite this, as shown in Fig. 3-3, density maxima of Turing patterns on a deformed cylinder are entrained by a ridge. An inward (outward) ridge selects the sine (cosine) mode.

This conformal mapping approach enables studies of other geometries, including bumps on spheres (below), drums (supplement), and rippled cylinders. An axially symmetric rippled cylinder, $h(z) = \cos\left[(2\pi m/L)z\right] \equiv \cos(\bar{m}z)$, gives a Schrödinger-like equation at $\mathcal{O}(\epsilon)$ (cf. Eqn. 3.10):

$$\left[-\Delta^0 - 2\epsilon\lambda_{sk}^{(0)}\cos(\bar{m}v)\right]\phi_k = k^2\phi_k\,. \tag{3.15}$$

This Schrödinger equation describes a particle moving in a weak periodic potential, whose properties are well understood in the context of solid-state physics [195]. At leading order, this perturbation gives rise to a broken degeneracy (band-gap) at $k = m/2$ with magnitude $4\epsilon\lambda_{sk}^{(0)}$. Our analysis predicts that when an RD system governs surface concentrations, the effective diffusion rate will increase in troughs and slow down on ridges. Hence, diffusion is enhanced (diminished) where Gaussian curvature is negative (positive). This agrees with the short-time analysis of diffusion on Riemannian manifolds, where the leading order correction to diffusion is proportional to Gaussian curvature [126, 179, 244]. [5] For Turing patterns, steady-state regions of high concentration switch sharply from ridges to troughs as the most unstable wavelength is dialed past twice the ripple wavelength, see Fig. 3-4. Note that Eqn. 3.15 predicts a broken degeneracy only when the most unstable wavelength is commensurate with the ripple wavelength. However, in numerical simulations (presumably due to higher-order effects), we observe pinning for a range of wavelengths close to commensurability, although the patterns become unpinned for sufficiently incommensurate wavelengths.

---

[5] One can compare this slowing of diffusion in regions of negative curvature with general relativity, which tells us that time runs slower where space-time is more curved. Clocks run fastest in free space far from masses. Indeed, clocks on Earth run 56 microseconds slower per day compared with the Moon.[334, 335] Viewers of the movie Interstellar will recall Miller's Planet, where clocks advance only one hour for every seven years on Earth [277].

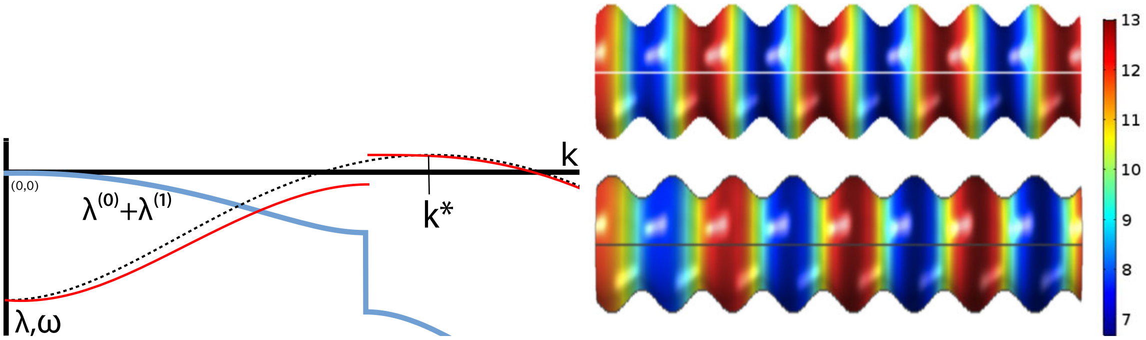

Figure 3-4: (Left) three functions of wave-number: (blue) Laplacian eigenvalues on a rippled cylinder, including a band gap at the edge of the Brillouin zone (BZ) at $m/2$; (black dotted) Turing spectrum on a non-rippled cylinder; (red) Turing spectrum on a rippled cylinder. For the case shown with $k^* > m/2$, the sine mode is selected; (cosine selected if $k^* < m/2$). (Right) Numerical confirmation: Concentration patterns in the Thomas-Murray model switch from troughs to ridges as the unstable chemical wavelength, k^*, is dialed past twice the ripple wavelength by changing $\gamma = 1.125$ (upper) to $\gamma = 0.975$ (lower). Vertical dimension magnified 3x. Supplement includes video of sweeping m (Mathematica & COMSOL files).

An axially-symmetric distorted sphere, described by $R(\theta)$, has line element

$$\mathrm{d}s^2 = \left(R^2 + R'^2\right)\mathrm{d}\theta^2 + R^2 \sin^2\theta \,\mathrm{d}\varphi^2 \ ,$$

where prime denotes derivatives. Mapping to conformally flat coordinates:

$$\mathrm{d}s^2 = \Omega^2 \left(\mathrm{d}\Theta^2 + \sin^2\Theta \,\mathrm{d}\varphi^2\right) \ .$$

The Laplacian eigenvalue equation in conformal coordinates becomes (see supplement, Eqn. 3.16)

$$\left[-\Delta^0 + k^2\left(R_0^2 - R^2\frac{\sin^2\theta}{\sin^2\Theta}\right)\right]\Phi = k^2 R_0^2 \Phi \,, \tag{3.16}$$

where Δ^0 is the Laplacian on a round sphere. Setting $R = R_0\left(1 + \epsilon h(\theta)\right)$, we expand in powers of ϵ. To $\mathcal{O}(\epsilon)$, $\theta = \Theta$, and Eqn. 3.16 reduces to

$$\left[-\Delta^0 - 2\epsilon k^2 R_0^2 h\right]\Phi = k^2 \Phi \,. \tag{3.17}$$

Using Eqn. 3.17, we study how deformations modify the Laplacian eigenfunctions $Y_\ell^m(\theta,\phi)$. The perturbation depends only on θ, breaking rotational symmetry by fixing polar orientation of eigenmodes while preserving azimuthal symmetry. This can potentially entrain Turing patterns, although there are competing influences from nonlinear effects and incommensurability of length scales as seen in Fig. 3-5. In fact, in numerical simulations, we often found that the initial patterning predicted by linear stability analysis would stabilize to more complex patterns. In contrast, on a cylinder, initial patterning tends to persist indefinitely. We attribute this to differing degrees of degeneracy. The spherical eigenmodes, Y_ℓ^m, have $2\ell + 1$ degeneracy. Thus, near the most unstable eigenmode, there are 2ℓ additional unstable modes that can contribute to non-linear pattern formation. In contrast, a cylinder presents only a twofold degeneracy.

As evident from Eqn. 3.17, eigenfunction modifications are sensitive to the sign of h. An inward (outward) bump causes an increase (decrease) in diffusion. Non-linear effects in the Thomas-Murray model are known to stabilize spotted patterns instead of the single most unstable spherical harmonic, see Ref. [170]. However, during the initial development of Turing patterns, the most unstable Y_ℓ^m is visible, and the mode selected by a deformed sphere differs from that of an uniform sphere, see Fig. 3-5.

Including extrinsic noise in RD systems leads to temporally fluctuating *quasi-patterns* for a broader range of parameters than those required for a Turing instability [238, 252, 266, 293]. We have investigated how curvature influences such *noise-induced transient* patterns. We add uncorrelated white noise $\eta(\mathbf{x}, t)$ of zero mean and variance $\mathcal{D}$ to Eqn. 3.13. In the linearly stable regime, this noise leads to eigenfunction fluctuations with a power spectrum $P(\lambda)$ proportional to $\mathcal{D}\left[\det\mathbf{M}(\lambda)\right]^{-1}$. On a uniform surface, time averaged fluctuations are translationally invariant, $\langle|\mathbf{\Psi}(x)|^2\rangle = \mathbf{\Psi}_0^2$. Deformations break this symmetry, leading to average fluctuations on a cylinder of the form

$$\langle|\mathbf{\Psi}(x)|^2\rangle \propto \sum_k \frac{\cos^2(\bar{k}x)}{\det\mathbf{M}(\lambda_{0k}^+)} + \frac{\sin^2(\bar{k}x)}{\det\mathbf{M}(\lambda_{0k}^-)} + \mathcal{O}\big(\epsilon^2\big)\,. \tag{3.18}$$

On spheres, the spherical harmonics replace the Fourier modes. Figure 3-6 shows

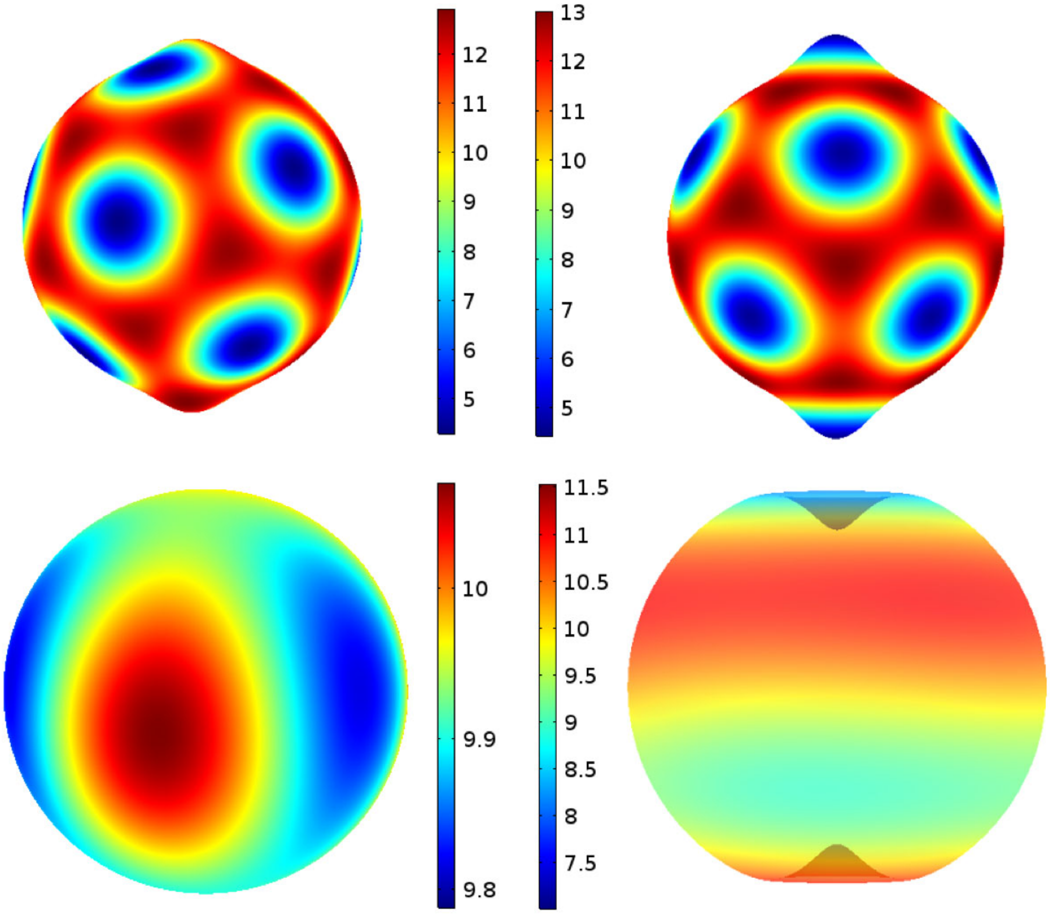

Figure 3-5: Sufficiently large bumps entrain spotted patterns (top pair). Initial patterning on an undeformed sphere shows Y_5^5 (bottom-left); the inward bumps of a "pinched sphere" amplify lower harmonics, causing Y_3^0 to appear (bottom-right).

numerical verification that such deformations fix the phase of fluctuations and create non-uniform time-averaged intensities. Such behavior is expected to hold generically for quasi-patterns induced by intrinsic noise [238, 252, 266, 293], where the power spectrum describing fluctuations is qualitatively similar.

If these effects can be realized in manufactured or experimental systems they could enable systematic manipulation of patterns. For example, collagen vitrigel (CV) for corneal endothelial regenerative treatment [279] could be molded in a hemispherical or eggcrate geometry and used to support zebrafish chromatophores, which were recently cultured for *in vitro* studies [278] to explore RD models [241]. Mice hair follicle patterning is also driven by an RD system involving WNT growth factor [218], and

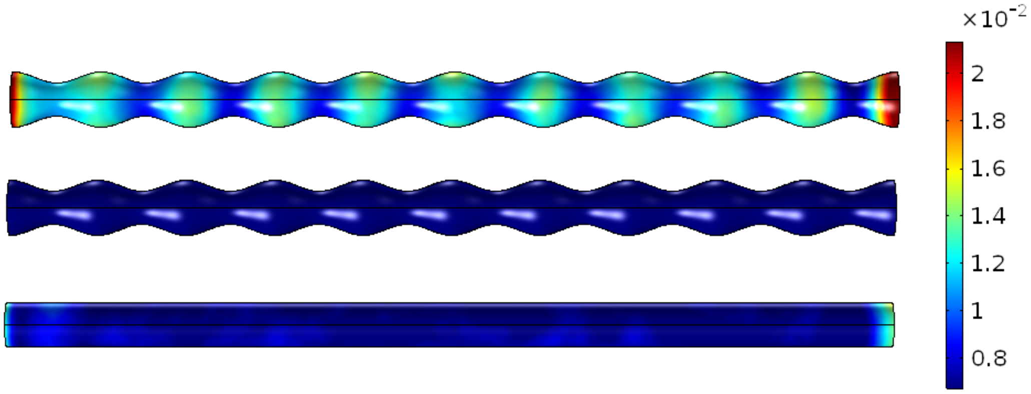

Figure 3-6: Noise-induced quasipatterns appear when geometric ripples split degenerate eigenmodes of an RD system below threshold. Deformations pin the time-averaged intensity of fluctuations in RD quasipatterns (top); compare this with the same intensity of extrinsic noise on a flat surface (bottom). For all two figures, $\nu_2 = 6$ and $K = 0.15$.

might be cultured on molded CV using established *in vitro* techniques [131]. Zebrafish stripes and hair follicles have spacing on the order of hundred microns. Three orders of magnitude smaller, cytoskeletal suspensions exhibit patterns [251, 257, 306] that may realize our results. For example, a pinched sphere might be constructed in the recently studied encapsulations of actomyosin in giant unilamellar vesicles [303]. A recent review of such active fluids suggests that coupling to RD systems looks like a fruitful direction for research [264].

Even in a system as simple as a cylinder with a ridge, geometry can dramatically affect pattern formation. Our approach to the Laplacian on curved surfaces opens a new route to analytical understanding of patterns in real systems, taking advantage of intuition and tools from quantum mechanics. Future directions include pattern formation in the presence of advection [273], and on time-varying shapes. Our approach can also be applied to scenarios involving interactions between the surface and boundary physics. In particular, it would be interesting to examine the effect of nonuniform surface curvature when additional reaction-diffusion processes take place at the boundary [258]. Our mathematical methods apply to any process described by the Laplacian, and may also find application in soap films [185], or Marangoni flows from surface tension gradients [226].

JRF acknowledges support from the Hertz Foundation. JG acknowledges support from CONACyT grant 180901. MK acknowledges support from DMR-1708280.

3.3 Perturbation Theory

The paper in the previous section was published with a two-page supplement describing the construction of conformally flat coordinates for cylinders, spheres, and drums with one axis of rotational symmetry [308]. Here, I expand the calculations to explain the perturbation theory and illustrate the overall approach in more detail.

3.3.1 Deformed Cylinder

By constructing a conformal mapping from the lab frame coordinates to a related surface of constant curvature, analysis of the Laplacian eigenfunctions on the deformed surface can be made more tractable.

Consider a cylinder with radius R_0. Using cylindrical polar coordinates, radially-symmetric deformations from this geometry can be described by a position-dependent radius, $R(z) = R_0\,(1 + h(z))$. The coordinate z has dimensions of length and ranges $z \in [0, L]$. The embedding vector,

$$\vec{\boldsymbol{X}}(\varphi, z) = \begin{pmatrix} R(z)\cos(\varphi) \\ R(z)\sin(\varphi) \\ z \end{pmatrix},$$

where $\varphi \in [0, 2\pi)$. We refer to changes in tube radius as a function of z as “longitudinal” variations:

$$R_0 \to R_0\,(1 + h(z)) \implies G_{ab}(\varphi, z) = \begin{pmatrix} R_0^2\,(1+h)^2 & 0 \\ 0 & 1 + R_0^2 h_z^2 \end{pmatrix} \tag{3.19}$$

This parameterization of the perturbed metric depends only on h, and it depends indirectly on z through h being written as a function of z. Where h_z denotes a first derivative with respect to z. We also sometimes include a comma for clarity by writing $h_{,z}$ and $h_{,zz}$ to denote first and second derivatives with respect to z.

When $h = 0$, then the metric returns to the non-curved metric of the cylinder:

$$G_{ab} \xrightarrow{h=0} g_{ab} = \begin{pmatrix} R_0^2 & 0 \\ 0 & 1 \end{pmatrix} .$$

To prepare to change coordinates from z to a conformally flat coordinate v, we introduce a few tools. The radial perturbation h has a simple relationship with z illustrated in Figure 3-7. The tangent angle χ is related to the change in height as a function of z by

$$\tan\chi = \frac{\partial h}{\partial z} = h_{,z} \,. \tag{3.20}$$

However, an essential point is that h is a measurable quantity that a model can parameterize in many ways. For example, we could parameterize h, z, and χ as functions of arclength s.

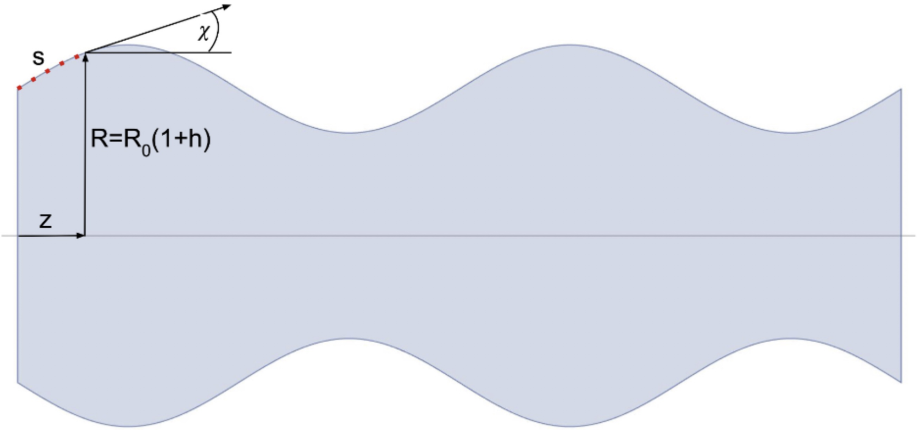

Figure 3-7: Illustration of three lengths and an angle that can be measured on a cylindrically symmetric shape.

Instead, we will now define a new parameter v that is not directly measurable with a measuring stick in the lab. To arrive at this coordinate, we will examine the measurement of path lengths on the surface. The infinitesimal line element on the surface is:

$$\begin{aligned}
\mathrm{d}s_2^2 &= G_{ab}\,\mathrm{d}\sigma^a\,\mathrm{d}\sigma^b \\
&= \left(1 + R_0^2 h_z^2\right)\mathrm{d}z^2 + R_0^2\left(1+h\right)^2\mathrm{d}\varphi^2 \\
&= \left(1+h\right)^2\left(\underbrace{\frac{1+R_0^2h_z^2}{\left(1+h\right)^2}\,\mathrm{d}z^2}_{\mathrm{d}v^2} + R_0^2\,\mathrm{d}\varphi^2\right).. \qquad (3.21)
\end{aligned}$$

The third line shows a rearrangement that motivates the definition of the new coordinate v. We put a subscript 2 on this line element $\mathrm{d}s_2$ to distinguish it from the arclength coordinate s that is measured parallel to the axis of symmetry. The general line element $\mathrm{d}s_2$ travels in both surface parameters.

We will map this to a conformally flat cylinder, whose line element is given by

$$\mathrm{d}s_2^2 = \Omega^2(v)\left(\mathrm{d}v^2 + R_0^2\,\mathrm{d}\varphi^2\right)\,. \qquad (3.22)$$

First, note that prefactor for $\mathrm{d}z$ has a simple expression in terms of the tangent angle χ:

$$\sqrt{1+R_0^2h_{,z}^2} = \sqrt{1+\tan^2\chi} = \frac{1}{\cos\chi}$$

While not independent, comparing expressions in terms of h and χ can help maintain intuition while moving to conformal coordinates.

The equality between the two line elements Eqns. 3.21 and 3.22 implies the relationship

$$\begin{aligned}
v &= \int_0^z \left(1+R_0^2h_z^2\right)^{\frac{1}{2}}\frac{\mathrm{d}z'}{1+h(z')} + C \\
&= \int_0^z \frac{R_0\,\mathrm{d}z'}{R\cos\chi} + C\,. \qquad (3.23)
\end{aligned}$$

The condition $v \sim z$ at $z = 0$ implies that $C = 0$. To first order in h and its gradients,

$$v \approx z - \int_0^z h(z')\,\mathrm{d}z' \ . \tag{3.24}$$

The conformal factor is given by Eqn. 3.21 and 3.22 as

$$\Omega^2 = (1+h)^2 \ , \tag{3.25}$$

where h can be expressed as a function of v or z.

Going the other direction in the derivation:

$$\begin{aligned} \frac{\mathrm{d}z}{\cos\chi} &= (1+h)\,\mathrm{d}v = \frac{R}{R_0}\,\mathrm{d}v \\ \Longrightarrow \quad z(v) &= \int_0^z \mathrm{d}z = \int_0^v (1+h)\cos\chi\,\mathrm{d}v = \int_0^v \frac{R}{R_0}\cos\chi\,\mathrm{d}v \end{aligned} \tag{3.26}$$

where the integration constant is zero for the same reason as above.

Similarly, the function $h(v)$ is not the same as $h(z)$. Other useful expression for understanding $h(v)$ comes from computing the radius as

$$\begin{aligned} R(v) &= \int_0^v \tan\chi \overbrace{(1+h)\cos\chi\,\mathrm{d}v}^{\mathrm{d}z} \\ \Longrightarrow \quad R'(v) &= \sin\chi \frac{R}{R_0} \end{aligned} \tag{3.27}$$

which has the solution:

$$R(v) = R_0 \exp\left(\frac{1}{R_0}\int_1^v \sin\chi\,\mathrm{d}v\right) . \tag{3.28}$$

We can also rearrange this to get another expression:

$$\begin{aligned} R_0 h_{,v} &= \sin\chi(1+h) \\ \Longrightarrow \quad \frac{R_0 h_{,v}}{1+h} &= \sin\chi \, , \end{aligned} \tag{3.29}$$

which combines with Eqn. 3.26 to give:

$$z(v) = \int_0^v \sqrt{(1+h(v))^2 - R_0^2 h_{,v}^2}\, \mathrm{d}v \ , \tag{3.30}$$

which we use in parametric plots in the following.

In upcoming sections, we will study a Gaussian bump and sinusoidal ripple. As a preliminary, here, we show that we can use either v or z as a coordinate for roughly approximating such a geometry. As shown in Figure 3-8, it is close to z but can grow faster or slower depending on the deformation.

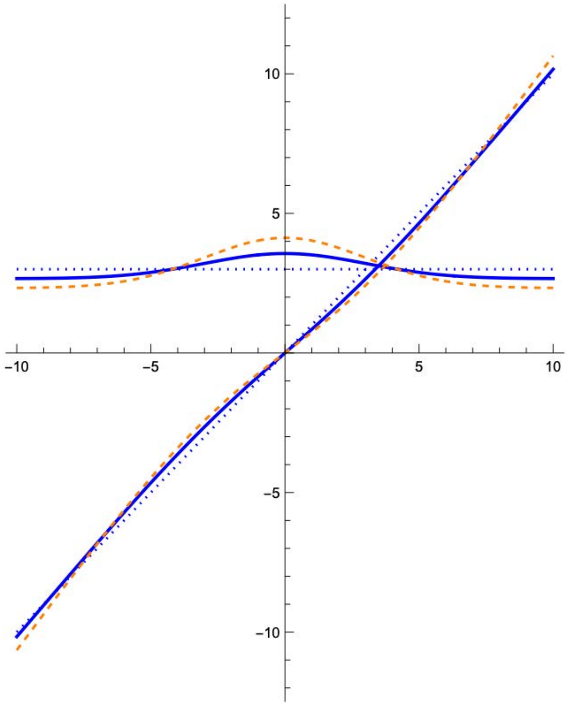

Figure 3-8: Illustration of the conformal coordinate $v(z)$ as a function of z on three different cylinders of initial radius $R_0 = 3$ and $L = 20$. The two straight blue dotted lines are guides to the eye: the horizontal dotted line is located at the undeformed cylinder radius of $R_0 = 3$, and the diagonal dotted line has a slope of one. The two deformed cylinders have a Gaussian bump centered at $z = 0$ with $\sigma = 3$. The solid blue line shows shows a bump with amplitude $\epsilon = 0.3$, and dashed orange line $\epsilon = 0.6$. The corresponding diagonal lines show the $v(z)$ curves. The solid blue diagonal line is $v(z)$ for the lower amplitude bump. Note that these plots use $h = \exp\{-z^2/(2\sigma^2)\} - M$, where M is a constant that keeps the surface area of the cylinder the same as the undeformed cylinder, see Eqn. 3.40.

A key point here is that we can use *either* v or z as a coordinate. To illustrate this, Figure 3-9 shows four bumps, two expressed as $\exp\{-z^2/(2\sigma^2)\}$ and two as $\exp\{-v^2/(2\sigma^2)\}$. For the purposes of modeling biological interfaces with diffusing materials, either coordinate v or z can be used to fit a Gaussian shape to approximate a real "bump" or "constriction." The price that must be paid for the analytical simplicity of v is that it cannot be measured directly on a sample, and instead must be computed using measurements of z and h or χ.

Our goal here is to understand general mechanisms of pattern localization. Comparison with laboratory measurements or simulations will involve stabilization by nonlinear terms and boundary effects, so approximate shapes will satisfy our needs here.

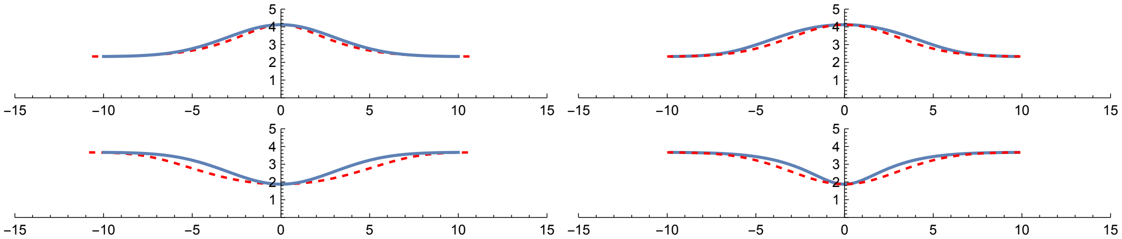

Figure 3-9: These parametric plots show show $\exp\left\{-z^2/(2\sigma^2)\right\}$ on the left and $\exp\left\{-v^2/(2\sigma^2)\right\}$ on the right. The dashed redlines are $R(v)$, and the solid blue lines are $R(z)$. The horizontal axes count both v and z. These use the same numerical values as the higher amplitude orange dashed line in Fig. 3-8. The lower two have $\epsilon \to -\epsilon$ to make an inward constriction.

Further note that far from the bump, the slope of $v(z)$ returns to one as follows:

$$\frac{\mathrm{d}v}{\mathrm{d}z} \xrightarrow{z\to\infty} \frac{1}{1+\frac{M}{L}}\,,$$

where M is a constant offset in h that enables keeping the cylinder area constant, which we compute in Eqn. 3.40.

Similarly, a rippled cylinder expressed as $h(v) = \cos(\bar{p}v)$ works just as well as if we expressed it as $h(z) = \cos(\bar{p}z)$. See Figure 3-10.

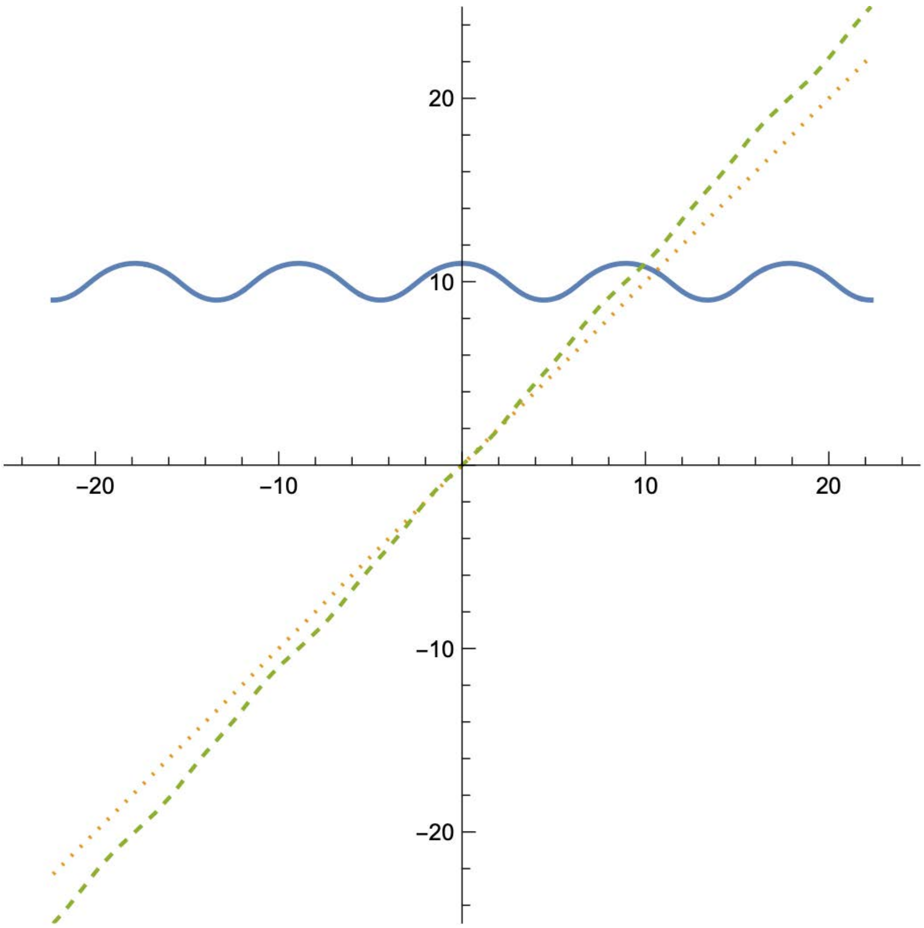

Figure 3-10: Ripple in v. The horizontal axis is the lab frame coordinate z along the axis of the cylinder. The solid line is what is seen in the lab frame when we express the deformation as a function of the conformal coordinate, v. The dotted line has slope of one to guide the eye, and the dashed line is the value of the conformal parameter v. This is plotted parametrically in v using Eqn. 3.30. $\epsilon = 0.1, k = 5, R_0 = 10, L = 50$.

What does the embedding vector look like in terms of coordinates (φ, v)?

$$\vec{\boldsymbol{X}}(\varphi, v) = \begin{pmatrix} R_0(1 + h(v)) \cos\varphi \\ R_0(1 + h(v)) \sin\varphi \\ z(v) \end{pmatrix} = \begin{pmatrix} R_0(1 + h(v)) \cos\varphi \\ R_0(1 + h(v)) \sin\varphi \\ \int^v (1 + h) \cos\chi dv' \end{pmatrix},$$

so the tangent vectors are:

$$\vec{\boldsymbol{t}}_{\varphi} = R_0(1+h)\begin{pmatrix} -\sin\varphi \\ \cos\varphi \\ 0 \end{pmatrix}$$

$$\vec{\boldsymbol{t}}_{v} = \begin{pmatrix} R_0 h'(v)\cos\varphi \\ R_0 h'(v)\sin\varphi \\ z'(v) \end{pmatrix} = (1+h)\begin{pmatrix} \sin\chi\cos\varphi \\ \sin\chi\sin\varphi \\ \cos\chi \end{pmatrix}.$$

The normal vector:

$$\hat{\boldsymbol{n}} = \frac{\vec{\boldsymbol{t}}_{\varphi} \times \vec{\boldsymbol{t}}_{v}}{\left|\vec{\boldsymbol{t}}_{\varphi} \times \vec{\boldsymbol{t}}_{v}\right|} = \begin{pmatrix} \cos\chi\cos\theta \\ \cos\chi\sin\theta \\ -\sin\chi \end{pmatrix}.$$

This gives a perturbed metric:

$$\begin{aligned} G_{ab}(\varphi, v) &= \begin{pmatrix} R_0^2(1+h(v))^2 & 0 \\ 0 & R_0^2 h_{,v}^2 + z_{,v}^2 \end{pmatrix} \\ &= \begin{pmatrix} R_0^2(1+h)^2 & 0 \\ 0 & (1+h)^2\sin^2\chi + (1+h)^2\cos^2\chi \end{pmatrix} \\ &= (1+h)^2 \begin{pmatrix} R_0^2 & 0 \\ 0 & 1 \end{pmatrix}, \end{aligned}$$

and its inverse is

$$\Game^{ab}(\varphi, v) = \frac{1}{(1+h)^2}\begin{pmatrix} \frac{1}{R_0^2} & 0 \\ 0 & 1 \end{pmatrix}.$$

The area element is:

$$dA = \mathrm{d}\varphi\,\mathrm{d}v\,\sqrt{G} = \mathrm{d}\varphi\,\mathrm{d}v\;R_0(1+h)^2 \tag{3.31}$$

To compute Christoffel symbols, we compute derivatives of this metric:

$$G_{ab,c}(\varphi, v) = \begin{cases} G_{ab,\varphi} = 0 \\ G_{ab,v} = 2h_{,v}(1+h)\begin{pmatrix} R_0^2 & 0 \\ 0 & 1 \end{pmatrix} \end{cases} .$$

From these, the Christoffel symbols in the (φ, v) coordinates are:

$$\begin{aligned} \Gamma^c_{ab} &= \frac{1}{2}G^{cd}\left(G_{ac,b} + G_{cb,a} - G_{ab,c}\right) \\ &= \frac{\sin\chi}{R_0}\begin{pmatrix} \begin{pmatrix} 0 \\ -R_0^2 \end{pmatrix} & \begin{pmatrix} 1 \\ 0 \end{pmatrix} \\ \begin{pmatrix} 1 \\ 0 \end{pmatrix} & \begin{pmatrix} 0 \\ 1 \end{pmatrix} \end{pmatrix} . \end{aligned}$$

As a result, the curvature tensor:

$$\begin{aligned} K_{ab}(\varphi, v) &= \hat{\boldsymbol{n}} \cdot \nabla_a \vec{\boldsymbol{t}}_b \\ &= (1+h)\begin{pmatrix} -R_0\cos\chi & 0 \\ 0 & \chi_{,v} \end{pmatrix} . \end{aligned}$$

Therefore, the mean curvature is $K^a_a = (\chi_{,v} - \cos\chi/R_0)/(1+h)$. The Gauss curvature is:

$$\det\left[K_{ab}\right] = -\frac{\partial_v \cos\chi}{(1+h)^2 R_0} . \tag{3.32}$$

The perturbed Laplacian in these special conformal coordinates (φ, v) is:

$$\begin{aligned} \Delta^0(\varphi, v) &= \frac{1}{\sqrt{G(\epsilon)}}\partial_a \sqrt{G(\epsilon)}\rotatebox{180}{G}^{ab}\partial_b \\ &= \frac{1}{(1+h)^2}\left(\partial_v^2 + \frac{1}{R_0^2}\partial_\varphi^2\right) . \end{aligned}$$

NB: Δ^0 is not the same as $\Delta^{(0)}$ with the superscript zero *in parentheses*, which we sometimes use to denote the unperturbed Laplacian, because Δ^0 has the structure of the unperturbed Laplacian but the coordinates are changed to use the conformal coordinate v.

Compare this conformally flat Laplacian with the the Laplacian in the lab frame coordinate z:

$$\Delta^G(\varphi, z) = \frac{1}{R_0\,(1+h)\sqrt{1+R_0^2 h_{,z}^2}}\left(\partial_z \frac{R_0(1+h)}{\sqrt{1+R_0^2 h_{,z}^2}}\partial_z + \frac{\sqrt{1+R_0^2 h'^2}}{R_0(1+h)}\partial_\phi^2\right),$$

where $h = h(z)$ in this expression, so we explicitly write the partial derivative w.r.t. to the lab frame z coordinate instead of just writing h'.

Since $h = h(v)$, we can separate variables and denote the eigenfunctions of the perturbed Laplacian in conformal coordinates as $\phi_k(v; s)e^{is\varphi}/\sqrt{\pi R_0}$, where the functions ϕ are parameterized by the angular wavenumber s:

$$\begin{aligned}\hat{\Delta}^0 \frac{e^{is\varphi}}{\sqrt{\pi R_0}}\phi_k(v; s) &= \lambda_{sk}\frac{e^{is\varphi}}{\sqrt{\pi R_0}}\phi_k(v; s) \\ &= \frac{1}{(1+h)^2}\left(\partial_v^2 + \frac{1}{R_0^2}\partial_\varphi^2\right)\frac{e^{is\varphi}}{\sqrt{\pi R_0}}\phi_k(v; s) \\ &= \frac{e^{is\varphi}}{\sqrt{\pi R_0}}\frac{1}{(1+h)^2}\left(\partial_v^2 - \frac{s^2}{R_0^2}\right)\phi_k(v; s)\,. \end{aligned} \tag{3.33}$$

Define $\tilde{\lambda}_{sk} \equiv \lambda_{sk} + s^2/R_0^2$. We will expand $\tilde{\lambda}_{sk}$ perturbatively. Comparing this to the unperturbed eigenvalue, $\tilde{\lambda}_{sk}^{(0)} = -k^2$.

Rearranging:

$$\begin{aligned} \phi_k'' &= \overbrace{(1+h)^2}^{{}^{\mathrm{c}}\Omega^2}\tilde{\lambda}_{sk}\phi_k \\ \implies \phi_k'' \underbrace{-(2h+h^2)\tilde{\lambda}_{sk}}_{V}\,\phi_k &= \tilde{\lambda}_{sk}\phi_k\,, \end{aligned} \tag{3.34}$$

The term in underbraces is like a momentum-dependent potential. We will examine the first order term in small h, just as in Eqn. 3.10.

Operator perturbation theory (OPT) is reviewed in Appendix D. To apply OPT to first order, replace $\tilde{\lambda}_{sk}$ and ϕ_k with ansätze series for small ϵ:

$$\tilde{\lambda}_{sk} = \tilde{\lambda}_{sk}^{(0)} + \tilde{\lambda}_{sk}^{(1)} + \ldots \tag{3.35}$$

$$\phi_k = \phi_k^{(0)} + \sum_{k'} \phi_{k'}^{(0)} c_{k'k}^{(1)} + \ldots . \tag{3.36}$$

Carrying out derivatives and integrating:

$$\begin{aligned} 0 &= \int dA^0 \phi_{k'}^{(0)*} \left(\partial_v^2 - \left(\tilde{\lambda}_{sk}^{(0)} + \tilde{\lambda}_{sk}^{(1)} \right) - \left(\tilde{\lambda}_{sk}^{(0)} + \tilde{\lambda}_{sk}^{(1)} \right) 2h \right) \phi_k^{(0)} \qquad (3.37) \\ &\quad + \int dA^0 \phi_{k'}^{(0)*} \left(\partial_v^2 - \left(\tilde{\lambda}_{sk}^{(0)} + \tilde{\lambda}_{sk}^{(1)} \right) - \left(\tilde{\lambda}_{sk}^{(0)} + \tilde{\lambda}_{sk}^{(1)} \right) 2h \right) \sum_{k''} \phi_{k''}^{(0)} c_{k''k}^{(1)} \\ &= \left(\tilde{\lambda}_{sk}^{(0)} \delta_{k'k} - \left(\tilde{\lambda}_{sk}^{(0)} + \tilde{\lambda}_{sk}^{(1)} \right) \delta_{k'k} - \left(\tilde{\lambda}_{sk}^{(0)} + \cancel{\tilde{\lambda}_{sk}^{(1)}} \right) 2h_{k'k} \right) \\ &\quad + \left(\tilde{\lambda}_{s'k'}^{(0)} c_{k'k}^{(1)} - \left(\tilde{\lambda}_{sk}^{(0)} + \cancel{\tilde{\lambda}_{sk}^{(1)}} \right) c_{k'k}^{(1)} - \left(\tilde{\lambda}_{sk}^{(0)} + \tilde{\lambda}_{sk}^{(1)} \right) \sum_{k''} \cancel{c_{k''k}^{(1)} 2h_{k'k''}} \right) \\ \implies 0 &= - \tilde{\lambda}_{sk_\pm}^{(1)} \delta_{s's} \delta_{k'_\pm k_\pm} - \tilde{\lambda}_{sk_\pm}^{(0)} 2h_{k'_\pm k_\pm} + \left(\tilde{\lambda}_{s'k'_\pm}^{(0)} - \tilde{\lambda}_{s_\pm k_\pm}^{(0)} \right) c_{k'_\pm k_\pm}^{(1)} , \qquad (3.38) \end{aligned}$$

where we have put a strike through second-order terms. On the last line, we denote the ± modes separately in anticipation of the potential $V(v)$ splitting the sine and cosine modes.

3.3.1.1 Cylinder Ridge: Splits the Modes

With those preliminaries in hand, let's compute the mode splitting mentioned in Section 3.2 in Eqn. 3.12. We estimated how a ridge-like deformation selects even or odd modes that can pin a diffusion-driven pattern. We now recapitulate this calculation more carefully.

To consider a bump geometry, take the conformal coordinate $v \in [-L/2, L/2]$ and set

$$h(v) = \epsilon \left(\exp\left(-v^2/(2\sigma^2) \right) - M \right)$$

where we will choose an offset M that keeps the surface area of the cylinder constant, so-called "isoperimetric." For a cylinder of finite length, M, can just be a constant defined by:

$$0 = \int \mathrm{d}v\, h(v) \tag{3.39}$$

$$\implies M = \sqrt{2\pi}\frac{\sigma}{L}\operatorname{erf}\left(\frac{L}{2\sqrt{2}\sigma}\right) . \tag{3.40}$$

Take $\epsilon = v_0/R_0$ as a small parameter. Note that the Gaussian is not normalized, so that its height is controlled only by ϵ. We must ensure that its height remains less than the radius, so that the perturbed shape does not intersect itself.

With this choice of M,

$$\frac{\mathrm{d}v}{\mathrm{d}z} \xrightarrow{z\to\infty} \frac{1}{1 + \epsilon\frac{\sigma}{L}\operatorname{erf}\left(\frac{L}{2\sqrt{2}\sigma}\right)}$$

so when $\sigma << L$, the slope returns to 1.

Inserting this choice of h into Eqn. 3.34 and expanding to first order in ϵ:

$$0 = \left(\partial_v^2 - \tilde{\lambda}_{sk} \overbrace{-2\tilde{\lambda}_{sk}\epsilon e^{-v^2/(2\sigma^2)}}^{V(v)}\right)\phi_k . \tag{3.41}$$

The quantity $V(v)$ is our momentum-dependent potential.

We're interested in chemical concentrations, so want real-valued eigenfunctions:

$$\phi^{(0)}_{s_\pm k_\pm} = \begin{cases} \dfrac{\cos(s\theta)}{\sqrt{\pi R_0}}\sqrt{\dfrac{2}{L}}\cos\left(\dfrac{2\pi k}{L}v\right) = \phi^{(0)}_{s_+k_+} \\ \dfrac{\cos(s\theta)}{\sqrt{\pi R_0}}\sqrt{\dfrac{2}{L}}\sin\left(\dfrac{2\pi k}{L}v\right) = \phi^{(0)}_{s_+k_-} \\ \dfrac{\sin(s\theta)}{\sqrt{\pi R_0}}\sqrt{\dfrac{2}{L}}\cos\left(\dfrac{2\pi k}{L}v\right) = \phi^{(0)}_{s_-k_+} \\ \dfrac{\sin(s\theta)}{\sqrt{\pi R_0}}\sqrt{\dfrac{2}{L}}\sin\left(\dfrac{2\pi k}{L}v\right) = \phi^{(0)}_{s_-k_-} \end{cases} \tag{3.42}$$

where the second column of v-dependent sines and cosines are the $\phi^{(0)}_{k_\pm}$:

$$\phi^{(0)}_{k_\pm} = \begin{cases} \sqrt{\frac{2}{L}} \cos\left(\frac{2\pi k}{L} v\right) & \text{denoted } + \\ \sqrt{\frac{2}{L}} \sin\left(\frac{2\pi k}{L} v\right) & \text{denoted } - \end{cases} \tag{3.43}$$

These are orthonormal when integrated over the cylinder from $v = -L/2$ to $L/2$ using area element in Eqn. 3.31.

To use Eqn. 3.38, we need the integral $h_{k'_\pm k_\pm}$,

$$\begin{aligned} h_{k'_\pm k_\pm} &= \langle k'_\pm | h(v) | k_\pm \rangle \\ &= \epsilon \begin{cases} \int \mathrm{d}v \left(e^{-v^2/(2\sigma^2)} - M\right) \frac{2}{L} \cos\left(v \frac{2\pi k'}{L}\right) \cos\left(v \frac{2\pi k}{L}\right) \\ \int \mathrm{d}v \left(e^{-v^2/(2\sigma^2)} - M\right) \frac{2}{L} \sin\left(v \frac{2\pi k'}{L}\right) \sin\left(v \frac{2\pi k}{L}\right) \end{cases} \\ &= \epsilon \sqrt{2\pi} \frac{\sigma}{L} \left(A(k'-k) \exp\left\{-2\pi^2 (k'-k)^2 \frac{\sigma^2}{L^2}\right\} \pm A(k'+k) \exp\left\{-2\pi^2 (k'+k)^2 \frac{\sigma^2}{L^2}\right\} \right) . \end{aligned} \tag{3.44}$$

where the endpoints of integration are ±$L/2$. The prefactor $A(k)$ is the real part of an error function, which goes to one rapidly as L becomes larger than σ:

$$\begin{aligned} A(k) &= \frac{1}{2} \left(\operatorname{erf}\left(\frac{L}{2\sqrt{2}\sigma} + \frac{ik\pi\sigma}{\sqrt{2}L} \right) + \operatorname{erf}\left(\frac{L}{2\sqrt{2}\sigma} - \frac{ik\pi\sigma}{\sqrt{2}L} \right) \right) \\ &\xrightarrow{\sigma << L} 1 \end{aligned}$$

Going forward, we will drop the $A(k)$ as negligible. One can imagine the bump being far removed from the ends of the real physical cylinder, so that patterns can shift gradually over many wavelengths and thus become unconstrained by the boundaries.

Setting $k' = k$ in Eqn. 3.38 gives the leading order eigenvalue correction is:

$$\tilde{\lambda}^{(1)}_{sk_\pm} = \mp \tilde{\lambda}^{(0)}_{sk} 2\epsilon \sqrt{2\pi} \frac{\sigma}{L} e^{-2\bar{k}^2 \sigma^2} . \tag{3.45}$$

Recall that $\bar{k} = 2\pi k/L$. Note that without the M offset, this integral would make a leading order correction to the zero-mode of $\sqrt{2\pi}\sigma/L$.

This provides the result mentioned in explanation of our numerical simulation in Fig. 3-3. The perturbed eigenvalue estimated through this conformal mapping combined with Rayleigh-Schrödinger perturbation theory is:

$$\begin{aligned}\lambda_{sk_{\pm}}^{0+1} &= -\bar{s}^2 - \bar{k}^2\left(1 \mp 2\epsilon\sqrt{2\pi}\frac{\sigma}{L}e^{-2\bar{k}^2\sigma^2}\right) + \ldots \\ &= -\bar{s}^2 - \bar{k}^2 \pm 2\bar{k}^2\epsilon\sqrt{2\pi}\frac{\sigma}{L}e^{-2\bar{k}^2\sigma^2} + \ldots \end{aligned} \tag{3.46}$$

For $0 < \epsilon$, the cosine mode (+ sign) is less negative than the sine mode (–). This is the same as Eqn. 3.12.

To find the maximum value of the first order correction, take the derivative of $\lambda_{sk_{\pm}}^{(1)}$ w.r.t. k and set equal to zero. The correction is largest for k^*:

$$k^* = \pm\frac{L}{2\sqrt{2\pi}\sigma}\,. \tag{3.47}$$

The corrected spectrum, $\lambda_{sk_{\pm}}^{(0+1)}$, is plotted for select values in Fig. 3-11. On the ridge deformation, cosine modes diffuse slower than sine modes. That is, the cosine modes' eigenvalues are *less negative.* The cosine modes sample the peak, where Gaussian curvature is positive, and the sine modes sample the rim, where the Gaussian curvature is negative.

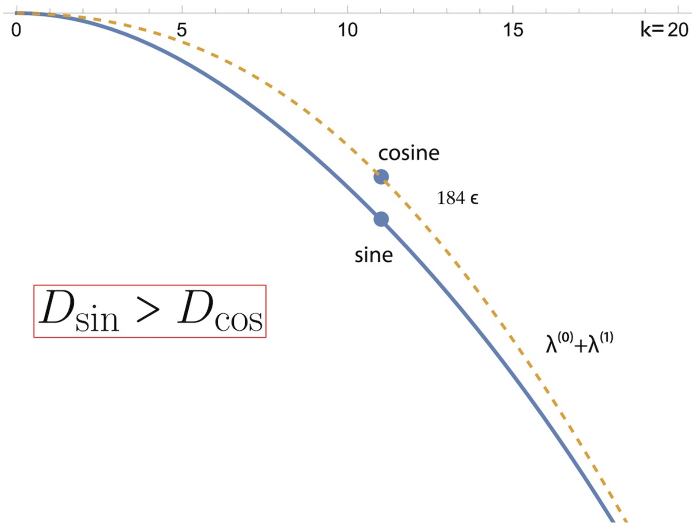

Figure 3-11: Mode Splitting for Outward Bump $0 < \epsilon$: The horizontal axis is the wavenumber, k, and the vertical axis is the eigenvalue $\lambda_{sk}^{(0+1)}$ at $s = 0$, $L = 1000$, and $\sigma = 10$, the mode splitting is largest at $k^* = 11$ and the cosine mode's eigenvalue is 184ϵ larger (less negative) than the sine mode's, for an outward bump. This means that the effective diffusion coefficient for the sine mode is larger than for cosine. These lines are produced with $\epsilon = 0.6$ and the difference between the $\lambda_{sk_\pm}^{(1)}$ made more visible by magnifying the vertical axis 20x.

See COMSOL simulation for this geometry in Figure 3-3.

3.3.1.2 Cylinder Ridge: First-Order Eigenfunction

The first-order corrections to the eigenfunctions are found by considering the off-diagonal elements of Eqn. 3.38:

$$c_{k'_\pm k_\pm}^{(1)} = 2\frac{\bar{k}^2}{\bar{k}'^2 - \bar{k}^2}\,{}^{\mathrm{c}}\Omega_{k'_\pm k_\pm}^{(1)}$$

Fortunately, the bump is an even function, so overlaps of sines and cosines are zero, i.e. ${}^{\mathrm{c}}\Omega_{k'_+ k_-}^{(1)} = 0$. Thus, these modes are already separated and not degenerate.

Eqn. 3.38 provides no information about the self-corrections, $c_{k_\pm k_\pm}^{(1)}$. As in Rayleigh-Schrödinger perturbation theory for Euclidean space, we can constrain these diagonal elements using the orthogonality relation. While we may not be able to find a close form $\phi_k(v; s)$ that solves Eqn. 3.33 for any particular $h(v)$, we still expect that they form an orthonormal basis:

$$\begin{aligned}
\delta_{s's}\delta_{k'_\pm k_\pm} = \langle s'k'_\pm | s k_\pm \rangle = \int & \overbrace{\mathrm{d}\varphi\,\mathrm{d}v\,\sqrt{G(\varphi,v)}}^{\mathrm{d}A}\,\frac{e^{-is'\varphi}}{\sqrt{R_0}}\phi^*_{k'_\pm}(v;s')\frac{e^{is\varphi}}{\sqrt{R_0}}\phi_{k_\pm}(v;s) \\
\implies \delta_{k'k} &= \int \mathrm{d}v\,(1+h)^2\phi^*_{k'_\pm}\phi_{k_\pm} \\
&= \int \mathrm{d}v\,(1+h)^2 \\
&\left(\sum_{k''}\left(\delta_{k''_\pm k'_\pm} + c^{(1)*}_{k''_\pm k'_\pm} + \ldots\right)\phi^{(0)*}_{k''_\pm}\right)\left(\sum_{k'''}\left(\delta_{k'''_\pm k_\pm} + c^{(1)}_{k'''_\pm k_\pm} + \ldots\right)\phi^{(0)}_{k'''_\pm}\right).
\end{aligned}$$

Unlike the Euclidean version shown in Eqn. D.13 in the appendix, here, the first two orders are modified by the presence of the conformal factor $(1+h)^2$ These new identities are:

$$0 = c^{(1)*}_{k_\pm k'_\pm} + c^{(1)}_{k'_\pm k_\pm} + {}^{\mathrm{C}}\Omega^{(1)}_{k'_\pm k_\pm} \tag{3.48}$$

$$0 = c^{(2)*}_{k_\pm k'_\pm} + c^{(2)}_{k'_\pm k_\pm} + {}^{\mathrm{C}}\Omega^{(2)}_{k'_\pm k_\pm} \tag{3.49}$$

$$0 = c^{(2<n)*}_{k_\pm k'_\pm} + c^{(2<n)}_{k'_\pm k_\pm}.$$

The third line states that all of the higher order recursion relations are unchanged from Euclidean space. From this, $\mathrm{Re}\left\{c^{(1)}_{k_\pm k_\pm}\right\} = {}^{\mathrm{C}}\Omega^{(1)}_{k_\pm k_\pm}$.

Therefore, a cosine-cosine mode on the *un*perturbed cylinder becomes:

$$\begin{aligned}
\phi^{(0+1)}_{s_+k_+} =& \frac{\cos(s\theta)}{\sqrt{\pi}R_0}\sqrt{\frac{2}{L}}\times \\
&\left(\cos\left(\bar{k}v\right)\left(1+\epsilon e^{-2\bar{k}^2\sigma^2}\right) + \epsilon 2\sqrt{2\pi}\frac{\sigma}{L}\sum_{\bar{k}'\neq\bar{k}}\frac{\bar{k}^2}{\bar{k}'^2-\bar{k}^2}\cos\left(\bar{k}'v\right)\left(e^{-(\bar{k}'-\bar{k})^2\sigma^2/2} + e^{-(\bar{k}'+\bar{k})^2\sigma^2/2}\right)\right) + \mathcal{O}(\epsilon^2)
\end{aligned} \tag{3.50}$$

Two examples are shown in Figure 3-12.

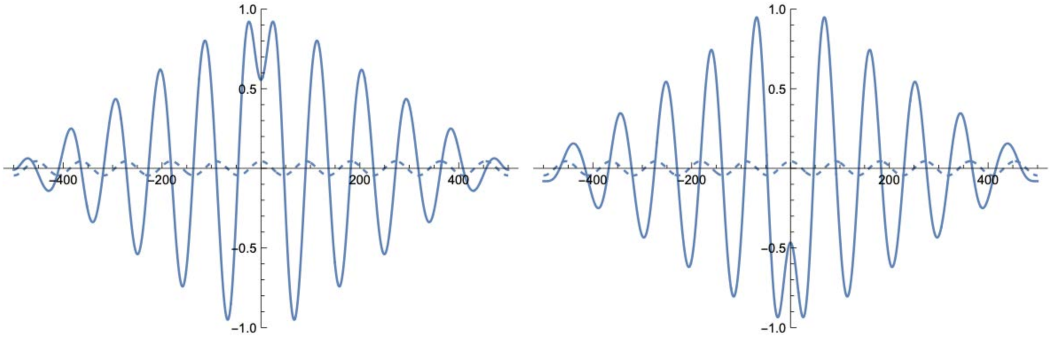

Figure 3-12: For, $\epsilon = 0.6$, $L = 1000$, $\sigma = 10$, $k = k^* = 11$. The left shows an inward constriction and the right shows an outward ridge. The dashed lines show the unmodified mode, which is normalized. The perturbed mode is not normalized. The relative magnitude of the mode near the bump compared to far from the bump shows how much the mode is localized at the bump.

The sine modes are *not modified* by the perturbation, because they exactly cancel as follows. The $c^{(1)}_{k'_-k_-}$ are even functions of k', and $\sin\left(\bar{k}'v\right)$ is odd. Therefore,

$$c^{(1)}_{-k'_-k_-}\sin\left(-\bar{k}'v\right) = -c^{(1)}_{k'_-k_-}\sin\left(\bar{k}'v\right)$$

so the summation over $\bar{k}'$ exactly cancels.

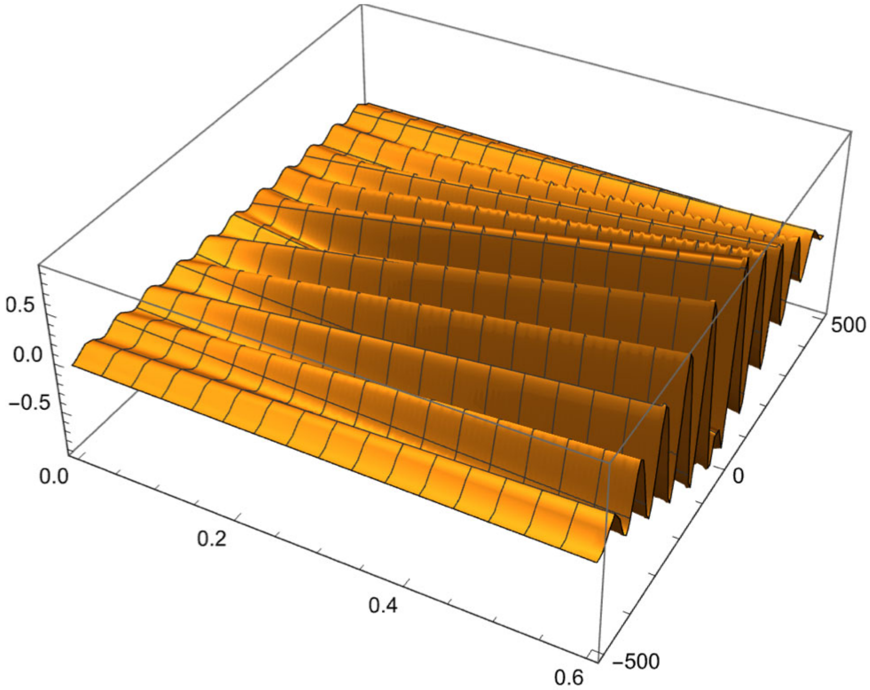

Figure 3-13: Turning on the localization: This shows the amplitude of the perturbed mode in Fig. 3-12 turning on gradually as ϵ sweeps from zero up to 0.6.

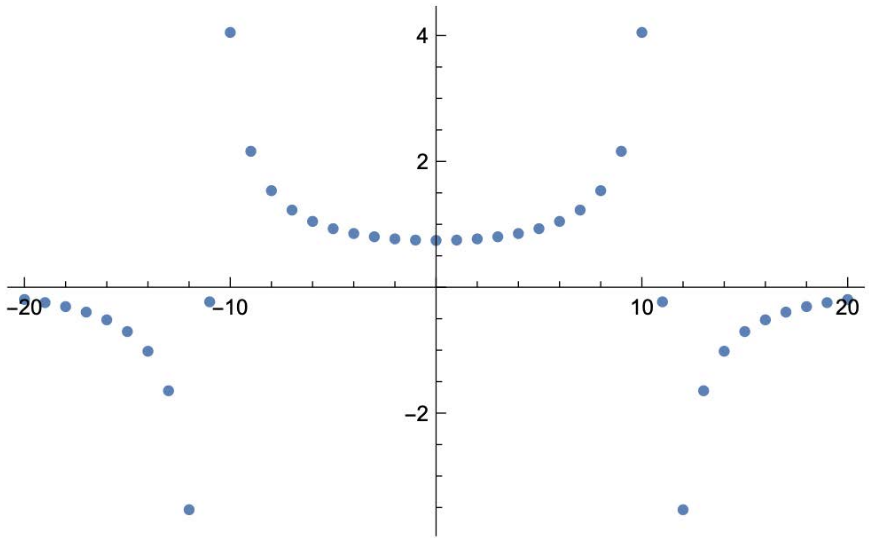

Figure 3-14: This shows the amplitude of first-order corrections for the perturbed mode in Fig. 3-12.

3.3.1.3 Cylinder with Ripples

The Fourier transform of the Gaussian bump involves modes of many wavelengths. Consider a deformation of a single wavelength. Periodic potentials arise in the study of crystal lattices. Their simplicity was discovered independently in the late 1800s by Gaston Floquet[49], George W. Hill[52], and Alexander M. Lyapunov[53]. Approximately forty years later, Felix Bloch[66] applied these ideas to the quantum mechanics of crystal lattices. We summarize these tools in Appendix Section D.3.

Consider a rippled cylinder perturbation in the conformal coordinate v mentioned in Eqn. 3.15:

$$h(v) = \cos\left(\frac{2\pi m}{L} v\right) = \cos(\bar{m} v) \tag{3.51}$$

Referring to our one-dimensional eigenvalue equation, our Eqn. 3.41 now becomes:

$$0 = \left(\partial_v^2 - \tilde{\lambda}_{sk} - 2\tilde{\lambda}_{sk}\epsilon\cos(\bar{m}v)\right)\phi_k \, .$$

The ripple does not need an offset M, because this integral is already zero:

$$0 = \int \mathrm{d}v\, h(v) = \int_{-L/2}^{L/2} \epsilon \cos(\bar{m}v)\,.$$

The cylinder's unperturbed eigenfunctions apply here. However, given the periodic potential, it is more straightforward to start with the complex eigenfunctions $\phi_k(v)^{(0)} = \exp\big(i\bar{k}v\big)/\sqrt{L}$ and directly apply the analysis of a one-dimensional crystal described in Appendix D.3. The difference here will be that the potential carries with it a factor of $\lambda_k^{(0)} = -k^2$.

The first-order recursion relations derived in Eqn. 3.38 apply here with the new definition of the integral $h_{k'_\pm k_\pm}$:

$$\begin{aligned} h_{k'_\pm k_\pm} &= \epsilon \int_0^L \mathrm{d}v\, e^{-i\bar{k}'v} \cos(\bar{m}v) e^{i\bar{k}v} \\ &= \frac{\epsilon}{2} \left(\delta_{-k'+m+k} + \delta_{-k'-m+k}\right) \end{aligned} \tag{3.52}$$

We have allowed periodic boundary conditions, so other than discretizing the modes to have wavelengths commensurate with the length, the boundaries do not eliminate either sines or cosines.

Now our potential is:

$$\begin{aligned} \mathcal{V}_{k'k} &= \tilde{\lambda}_k^{(0)} 2h_{k'_\pm k_\pm} \\ &= -\bar{k}^2 \epsilon \left(\delta_{-k'+m+k} + \delta_{-k'-m+k}\right) \end{aligned} \tag{3.53}$$

Setting $k' = k$ shows that for most k there is no first-order correction. However, we expect degeneracy near the edges of the Brilliouin Zone (BZ), where the eigenfunction corrections become singular:

$$\begin{aligned} c_{sk_\pm}^{(1)} &= \frac{\tilde{\lambda}_k^{(0)} 2h_{k'_\pm k_\pm}}{\tilde{\lambda}_{k'}^{(0)} - \tilde{\lambda}_k^{(0)}} \\ &= \epsilon \frac{\bar{k}^2}{\bar{k}'^2 - \bar{k}^2} \left(\delta_{-k'+m+k} + \delta_{-k'-m+k}\right) \end{aligned}$$

This leads to a non-symmetric, momentum-dependent Bragg-like matrix at the edge of the BZ is shown in Figure 3-15 and mathematically here:

$$\mathcal{V}_{k'k}\big|_{\mathrm{BZ}} = \begin{bmatrix} \lambda^{(0)}_{k-m} & \mathcal{V}_{k-m,k} \\ \mathcal{V}_{k+m,k} & \lambda^{(0)}_{k} \end{bmatrix} = \begin{bmatrix} \lambda^{(0)}_{k-m} & \epsilon\lambda^{(0)}_{k}/2 \\ \epsilon\lambda^{(0)}_{k-m}/2 & \lambda^{(0)}_{k} \end{bmatrix} \tag{3.54}$$

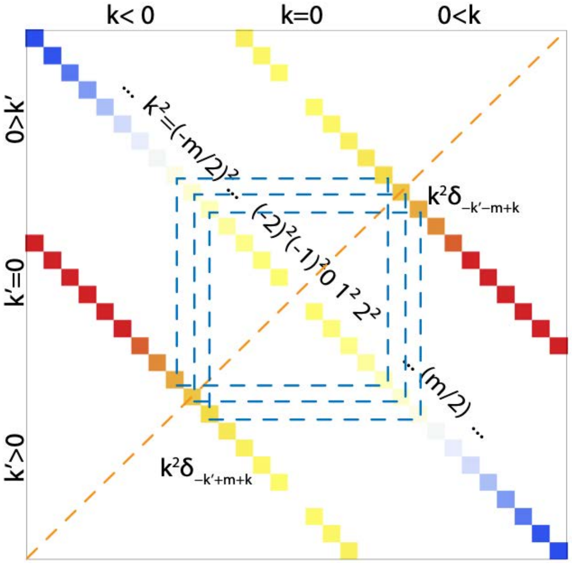

Figure 3-15: Illustration of the Bragg-like matrix for our momentum-dependent periodic potential ($\epsilon = 1$). This shows just one harmonic, so a single cosine. Other periodic ripple profiles could be decomposed into a superposition of multiple harmonics. For large L, these off-diagonal stripes will be well-separated. The three blue dashed squares show examples of the 2×2 Bragg matrix just below the BZ, exactly on the BZ, and just above it.

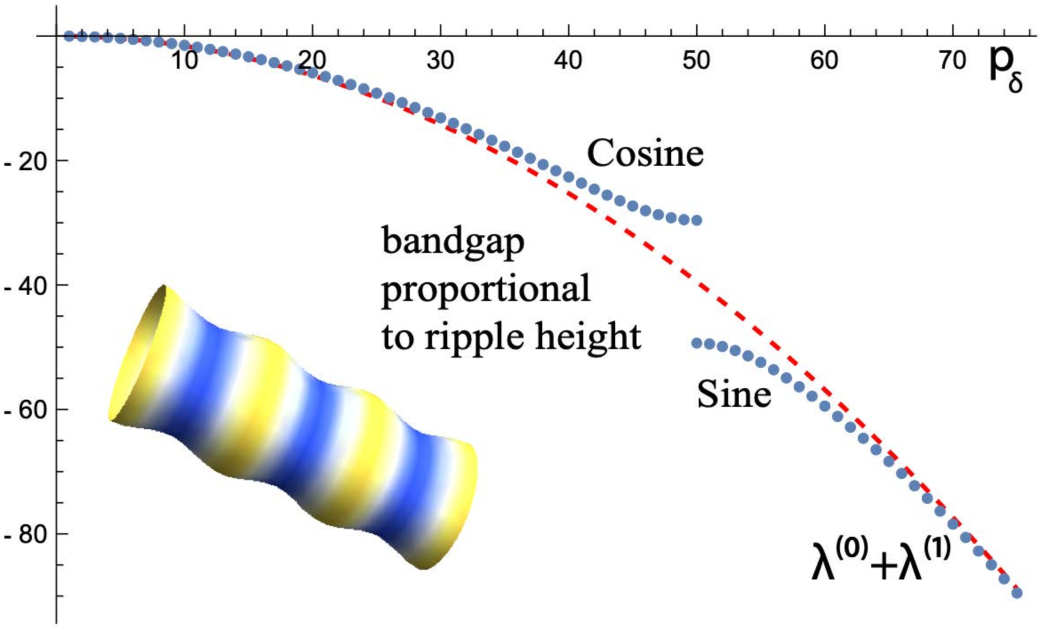

Figure 3-16: Diffusion Band Gap: the spectral band gap familiar from solid-state physics appears in this new context. The horizontal axis is the k labeling the eigenfunctions, and the vertical axis is the corresponding eigenvalue. $m = 100$, $\epsilon = 0.5$, $L = 50$

Just as in Appendix D.3, near the BZ edge, we can define p_δ by

$$k = \frac{m}{2} + p_\delta\,,$$

so for positive $0 < p_\delta$, we can pull the larger of the unperturbed eigenvalues out of $\lambda^{(0+1)}(+)$, and the smaller out of $\lambda^{(0+1)}(-)$, to obtain:

$$0 < p_\delta \implies \begin{cases} \lambda_k^{(0+1)}(+) = \underbrace{\lambda_k^{(0)}}_{-\bar{k}^2} \quad \underbrace{+\epsilon\bar{k}\bar{k}' \overbrace{\left(-\frac{mp_\delta}{\bar{k}\bar{k}'} + \sqrt{1 + \left(\frac{mp_\delta}{\bar{k}\bar{k}'}\right)^2}\right)}^{F_+(k)}}_{\lambda_k^{(1)}} \\ \lambda_k^{(0+1)}(-) = \underbrace{\lambda_{k-m}^{(0)}}_{-(\bar{k}-\bar{m})^2} \quad \overbrace{-\epsilon\bar{k}\bar{k}' \underbrace{\left(-\frac{mp_\delta}{\bar{k}\bar{k}'} + \sqrt{1 + \left(\frac{mp_\delta}{\bar{k}\bar{k}'}\right)^2}\right)}_{F_+(k)}}^{\lambda_{k-pN}^{(1)}} \end{cases} . \qquad (3.55)$$

Note the function $F_+(k)$ comes from Bloch's analysis and equals one at $p_\delta = 0$. Here, our momentum dependent potential $\bar{k}\bar{k}'$ replaces the Fourier coefficient of the crystal's potential, $\tilde{V}_{pN}$.

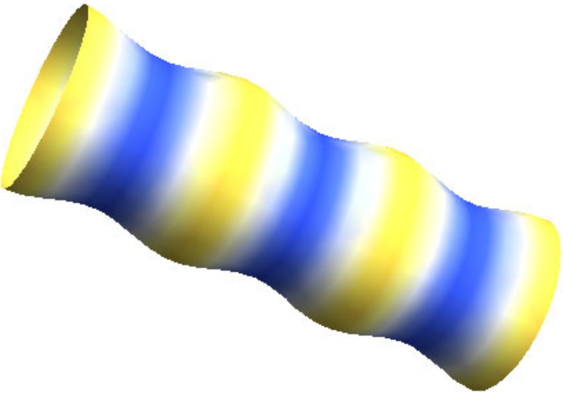

Figure 3-17: Near the edge of the BZ, eigenfunctions have wavelengths approximately twice the ripple wavelength. The sine mode has extrema in the troughs of the ripples, and the cosine mode on the peaks.

3.3.2 Conformal Mapping of a Deformed Sphere

Consider a rippled two-sphere in three-space with non-constant radius $R(\theta,\varphi)$:

$$\vec{\boldsymbol{X}}(\theta,\varphi) = R(\theta,\varphi)\begin{pmatrix}\sin\theta\cos\varphi \\ \sin\theta\sin\varphi \\ \cos\theta\end{pmatrix} \Longrightarrow G_{ab} = \begin{pmatrix} R^2 + R_\theta^2 & R_\theta R_\varphi \\ R_\theta R_\varphi & R^2\sin^2\theta + R_\varphi^2 \end{pmatrix},$$

where $\varphi \in [0,2\pi)$ and $\theta \in [0,\pi]$. The subscripts mean partial derivatives, e.g. $R_\theta \equiv \partial_\theta R$.

The general line element on such an unsymmetric sphere is:

$$\begin{aligned} \mathrm{d}s_2^2 &= G_{ab}\,\mathrm{d}\sigma^a\,\mathrm{d}\sigma^b \\ &= (R^2 + R_\theta^2)\,\mathrm{d}\theta^2 + 2R_\theta R_\varphi\,\mathrm{d}\theta\,\mathrm{d}\varphi + (R^2\sin^2\theta + R_\varphi^2)\,\mathrm{d}\varphi\ . \end{aligned} \tag{3.56}$$

The cross-terms make it challenging to construct a conformal mapping to back to an unperturbed sphere. Therefore, we specialize to perturbations independent of φ,

$$R(\theta,\varphi) \to R(\theta) = R_0\,(1 + h(\theta)) \tag{3.57}$$

See Figure 3-18 for the relationship between the shapes $R(\theta, \varphi)$ and arclength from the pole, s, and tangent angle relative to the reference plane.

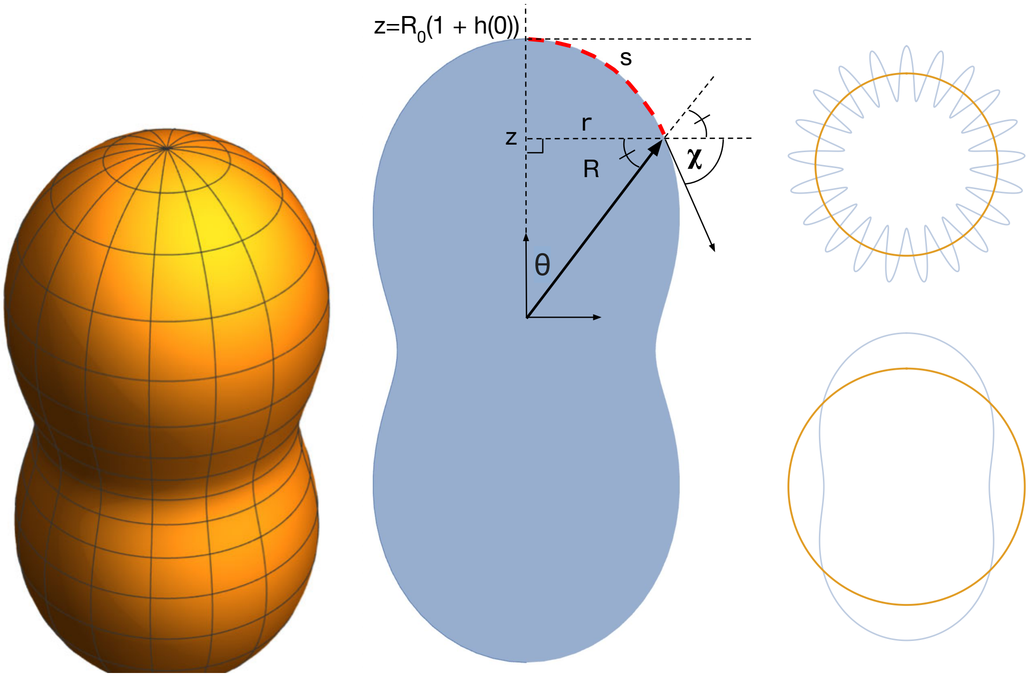

Figure 3-18: Like the deformed cylinder, a sphere has several lengths and angles that can be measured in the lab. The examples on the right show $h = 0.3\cos(p\theta)$ for $p = 21$ and $p = 2$. The orange circles are the undeformed reference shape.

In these coordinates, the line element is given by

$$\mathrm{d}s_2^2 = \left(R^2 + R_\theta^2\right)\mathrm{d}\theta^2 + R^2 \sin^2\theta \, \mathrm{d}\varphi^2 \; . \tag{3.58}$$

Recall that $\mathrm{d}s_2$ is the general line element and only equal to the arclength s for points on the same line of longitude. To map this to a conformally-flat sphere, we wish to define a new coordinate that we denote Θ:

$$\mathrm{d}s_2^2 = \Omega^2\left(\mathrm{d}\Theta^2 + \sin^2\Theta \, \mathrm{d}\varphi^2\right) . \tag{3.59}$$

The key property here is that all coordinates are rescaled by the same function Ω.

Equating the expressions for the line elements in the two coordinate systems gives

$$\sin^2\theta \;\Theta'^2 = \sin^2\Theta\left(1 + \frac{R'^2}{R^2}\right) . \tag{3.60}$$

Comparing the two expressions for the line element gives,

$$\Omega\,\mathrm{d}\Theta = \mathrm{d}\theta\, R\sqrt{1+\frac{R_\theta^2}{R^2}}\,, \tag{3.61}$$

and,

$$\Omega \sin\Theta = R\sin\theta\,. \tag{3.62}$$

Using the latter to eliminate Ω from the former and expanding for $h \sim \epsilon << 1$

$$\begin{aligned}\frac{\mathrm{d}\Theta}{\sin\Theta} &= \frac{\mathrm{d}\theta}{\sin\theta}\sqrt{1+\frac{R'^2}{R^2}}\\ &\approx \frac{\mathrm{d}\theta}{\sin\theta}\left(1+\frac{R_0^2 h_\theta^2}{R_0^2(1+h)}+\mathcal{O}(h^4)\right).\end{aligned} \tag{3.63}$$

This implies that $\Theta = \theta + \mathcal{O}(\epsilon^2)$. Further, $\Omega = R + \mathcal{O}(\epsilon^2)$.

The Laplacian eigenvalue equation in conformal coordinates becomes:

$$\begin{aligned}\Delta^G\Phi_k &= \lambda_k\Phi_k\\ \implies \frac{1}{\Omega^2}\Delta^0\Phi_k &= \lambda_k\Phi_k\\ \implies \Delta^0\Phi_k &= \Omega^2\lambda_k\Phi_k\\ &= \left(R_0(1+h)+\mathcal{O}(h^2)\right)^2\lambda_k\Phi_k\\ &\approx R_0^2(1+2h)\lambda_k\Phi_k\\ \implies \left[\Delta^0 - 2R_0^2 h\lambda_k\right]\Phi_k &\approx R_0^2\lambda_k\Phi_k\end{aligned} \tag{3.64}$$

Substituting $\lambda_k = -k^2$ yields Eqn. 3.17 in the published paper presented in Section 3.2. Here we provide more detail. As we noted in the previous section, the additional term on the LHS of Eqn. 3.64 breaks the polar symmetry in the eigenfunctions, effectively "fixing" the resulting polar orientation of the eigenfunctions, although azimuthal symmetry is preserved.

To examine modified spectrum and eigenfunctions, consider a radial deformation:

$$h = \epsilon \cos(p\theta) + M\,, \tag{3.65}$$

where M must be small like ϵ for the deformation to remain small. As with the cylinder, we will choose M to keep the area constant:

$$A = \int_0^{2\pi} \mathrm{d}\varphi \int_0^{\pi} \mathrm{d}\theta \sin\theta R_0^2 (1+h)^2 \tag{3.66}$$

A straightforward calculation yields:

$$\begin{aligned} M &= -1 + \epsilon \frac{\textsc{Odd}(p)}{p^2-1} + \sqrt{1 - \frac{\epsilon^2 \textsc{Even}(p)}{(p^2-1)^2} + \frac{\epsilon^2 p^4 (5-2p^2)}{(p^2-1)^2((2p)^2-1))}} \\ &= \epsilon \frac{\textsc{Odd}(p)}{p^2-1} - \epsilon^2 \frac{\textsc{Even}(p)}{(p^2-1)^2} + \epsilon^2 \frac{p^4(5-2p^2)}{(p^2-1)^2((2p)^2-1))} + \mathcal{O}(\epsilon^3) \end{aligned} \tag{3.67}$$

The conformally flat line element in Eqn. 3.59 corresponds to this metric, inverse metric and area element:

$$\begin{aligned} G^0_{ab} &= \Omega^2 \begin{pmatrix} 1 & 0 \\ 0 & \sin^2\Theta \end{pmatrix}, \\ \Game^{ab^0} &= \frac{1}{\Omega^2} \begin{pmatrix} 1 & 0 \\ 0 & \frac{1}{\sin^2\Theta} \end{pmatrix}, \\ \sqrt{G}\,\mathrm{d}\Theta\,\mathrm{d}\varphi &= \Omega^2 \sin\Theta\,\mathrm{d}\Theta\,\mathrm{d}\varphi\ . \end{aligned} \tag{3.68}$$

These are desirable, because the (surface) Laplacian in these coordinates is:

$$\begin{aligned} \Delta^G &= \frac{1}{\sqrt{G}} \partial_a \sqrt{G} \Game^{ab} \partial_b \\ &= \frac{1}{\Omega^2} \left(\frac{1}{\sin\Theta} \partial_\Theta \sin\Theta \partial_\Theta + \frac{1}{\sin\Theta} \partial_\varphi^2 \right) \\ &= \frac{1}{\Omega^2} \Delta^0\,, \end{aligned} \tag{3.69}$$

where the Δ^0 is the Laplacian on an undeformed sphere of unit radius, which has the familiar spherical harmonics as eigenfunctions:

$$\Delta^0 Y_l^m = -l(l+1) Y_l^m \equiv \lambda_{lm}^{(0)} \Phi_{lm}^{(0)} \, .$$

The indices l, m now replace the k in our schematic eigenvalue equation Eqn. 3.16.

As we are in pursuit of chemical concentrations, we form real-valued linear combinations of the Y_l^m. These are odd and even in φ, which we denote with $\pm$:

$$Y_l^{m\pm}(\theta, \varphi) = \sqrt{\frac{2l+1}{4\pi} \frac{(l-m)!}{(l+m)!}} P_l^m(\cos\theta) \times \begin{cases} \cos(m\varphi) \\ \sin(m\varphi) \end{cases} \tag{3.70}$$

where P_l^m are the associated Legendre polynomials.

Using these as our function basis, let's apply perturbation theory. Using the Rayleigh-Schrödinger ansätze in Eqn. 3.36, we arrive at the same expression as Eqn. 3.38 with the first-order matrix element of ${}^{\mathrm{c}}\Omega$ now being:

$$\begin{aligned} {}^{\mathrm{c}}\Omega^{(1)}_{l'm'_\pm lm_\pm} =& \int \mathrm{d}\theta \, \mathrm{d}\varphi \, \overbrace{\sin\theta}^{\sqrt{g^{(0)}}} \, \overbrace{Y_{l'}^{m'_\pm}}^{\phi^{(0)}_{l'm'_\pm}} \, \overbrace{2R_0^2 h}^{{}^{\mathrm{c}}\Omega^{(1)}} \, \overbrace{Y_l^{m_\pm}}^{\phi^{(0)}_{lm_\pm}} \\ =& 2R_0^2 \delta_{m'_\pm m_\pm} \sqrt{\frac{2l'+1}{4\pi} \frac{(l'-m)!}{(l'+m)!}} \sqrt{\frac{2l+1}{4\pi} \frac{(l-m)!}{(l+m)!}} \\ & \times \int_0^\pi \mathrm{d}\theta \, \sin\theta P_{l'}^m(\cos\theta) P_l^m(\cos\theta) \left(\epsilon \cos(p\theta) + M\right) \, , \end{aligned}$$

where we've resolved the φ integral because h is independent of φ and inserted the perturbation discussed above. Therefore, the eigenvalue corrections at first order are:

$$\lambda_{lm}^{(0+1)} = -\frac{l(l+1)}{R_0} \left(1 + {}^{\mathrm{c}}\Omega^{(1)}_{lm_\pm lm_\pm}\right) \, . \tag{3.71}$$

While the ${}^{\mathrm{c}}\Omega^{(1)}_{lm_\pm lm_\pm}$ appears to depend on m, the numerical values turn out to be independent of m, so this does not split the $2l+1$ degenerate modes labeled by index $m_\pm$. This is obvious from the fact that our perturbation is independent of φ. As a result, while we can approach axisymmetric perturbations analytically, their influence on the nonlinear evolution of Turing patterns is more complex, as we discussed in the previous section.

3.3.3 Conformal Mapping of Deformed Planar Drum

The technique of using conformal mapping to understand how deformations modify the Laplacian can be applied to a variety of surfaces. To elaborate on the procedure that we used for deformed spheres and cylinders, we show the steps of the calculation for a circularly symmetric deformation on a planar drum. Consider a height function, $h(r)$. The line element on this surface is given by

$$\mathrm{d}s^2 = \left(1 + h_r^2\right)\mathrm{d}r^2 + r^2\,\mathrm{d}\varphi^2\,, \tag{3.72}$$

We assume a reparameterization of the surface geometry $(r,\varphi) \to (u,\varphi)$ so that the line element assumes the manifestly conformally flat form

$$\mathrm{d}s^2 = \Omega^2(u)\left(\mathrm{d}u^2 + u^2\,\mathrm{d}\varphi^2\right)\,. \tag{3.73}$$

Setting these two line elements equal to each other, we obtain the two relations

$$\begin{gathered}\left(1 + h_r^2\right)\mathrm{d}r^2 = \Omega^2(u)\,\mathrm{d}u^2\,,\\ r^2 = u^2\Omega^2\,.\end{gathered} \tag{3.74}$$

Rearranging, one obtains a relationship between u and r,

$$u = Cr\exp\int_0^r \left[\left(1 + h_r^2\right)^{\frac{1}{2}} - 1\right]\frac{\mathrm{d}r}{r}. \tag{3.75}$$

Provided our bump possesses a tangent plane at $r = 0$, the relationship $r \sim u$ at $r = 0$ sets the constant of integration to $C = 1$, which gives an exact relationship that can be expanded in powers of h_r. To $\mathcal{O}(h_r^2)$,

$$r = u\left(1 - \frac{1}{2}\int_0^u \frac{\mathrm{d}u}{u}h_u^2\right), \tag{3.76}$$

where we have inverted the equation to obtain $r(u)$. As $u \to \infty$, this relationship becomes linear,

$$r = u\left(1 - \frac{\Gamma}{2}\right),$$

where $\Gamma \equiv \int_0^\infty \mathrm{d}u\, h_u^2/u$.

From Eqn. 3.74, we also obtain Ω, and hence the relationship between the Laplacian defined on the curved coordinates, Δ^G, and conformally flat coordinates, Δ^0,

$$\Delta^G \phi(v,\varphi) = k^2 \phi(v,\varphi) \to \Delta^0 \phi(u,\varphi) = \frac{r(u)k^2}{u^2}\phi(u,\varphi)\,. \tag{3.77}$$

Using Eqn. 3.76 and the definition of Γ, we can express this in a more telling form,

$$\left[-\Delta^0 + V(u)\right]\phi = k^2(1-\Gamma)\phi, \tag{3.78}$$

where

$$V(u) = -k^2 \int_u^\infty \frac{\mathrm{d}u}{u} h_u^2\,. \tag{3.79}$$

Similar to the cases of the deformed sphere and cylinder, we can express the effect of a deformation as the addition of an eigenvalue-dependent potential. As an example, if one considers a planar drum with a circularly symmetric Gaussian bump, Eqn. 3.79 shows that this leads to a Gaussian potential in conformal coordinates.

3.4 Conclusion

We have shown that diffusion on curved interfaces can sense curvature. This clearly should affect pattern formation via Turing-type instabilities. What other aspects of natural interfaces might this help explain? We will suggest one possibility in the next chapter.

Chapter 4

Outlook

In the previous chapters, we showed how curvature affects ordering in biologically relevant ways. Despite the tremendous progress since 1892, when Pearson named biophysics, there are still many biological *laws of motion* to uncover [54]. In this chapter, I will highlight two particular areas of future work. Section 4.1 comments on ingredients that may lead to a minimal model of the role of geometry in the origin of life. Section 4.2 describes simulations of orientational order in growing solids.

4.1 Filaments on Neck Geometries

Consider the remarkable *in vitro* system in Figure 4-1. With just three ingredients plus water, Szwedziak *et al* demonstrated membrane neck constriction. The three ingredients are (1) lipids that form a lipid liposome membrane, (2) prokaryotic tubulin homologue FtsZ forms the visible filaments, and (3) the prokaryotic actin homologue FtsA adheres the filaments to the membrane. No molecular motors are present. The constrictions evidently result from the minimum energy configuration of the proteins inside the liposome.

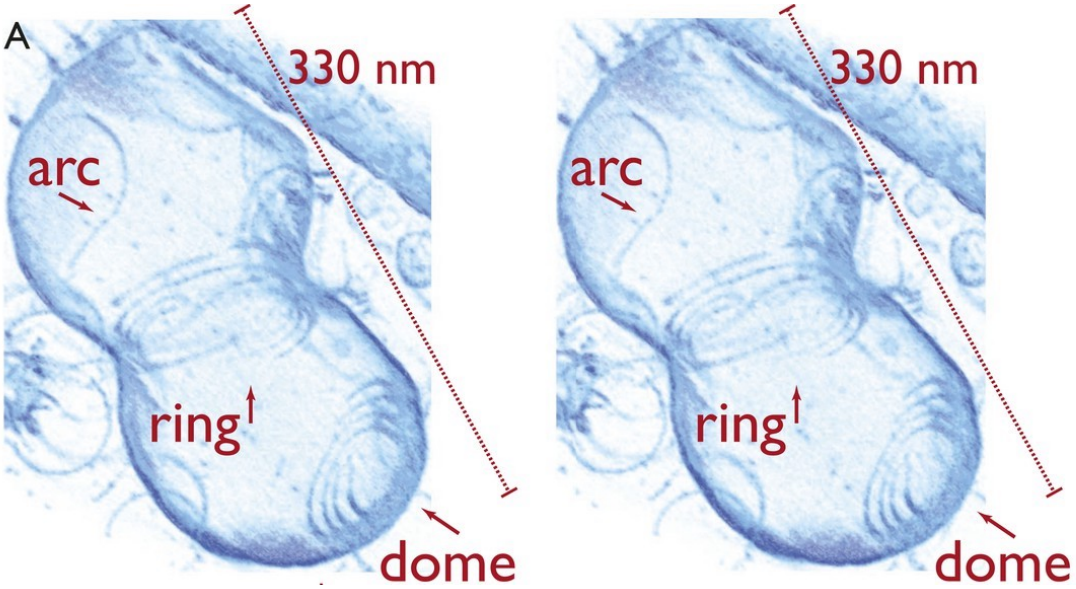

Figure 4-1: This remarkable stereo image shows a membrane constriction produced *in vitro*. Reproduced from "Architecture of the ring formed by the tubulin homologue FtsZ in bacterial cell division" by Szwedziak *et al* in *eLife* 2014.[276].

Inspired by this, one can ask: What are the minimal geometric ingredients for filaments to drive division of vesicles? In Sec. 2.5, we calculated that filaments can assume a variety of minimum energy orientations on cylinders. If the cylinder can deform to develop ridges or necks, which geometric couplings might suppress or enhance the deformation?

Is it possible that diffusion of the particles in the curving membrane contributes to their localization? Or are spontaneous curvatures required?

In setting up Eqn. 2.1 for our nematic membrane, we carefully avoided polar terms. These include spontaneous curvatures, some of which break chiral symmetry, which distinguishes between the two sides of the membrane and thus between the inside and outside of the vesicle. These spontaneous curvatures could be good effective descriptions for the static shapes shown in Fig. 4-1.

With the various updates to the Canham-Hilfrich model from oriented fields, perhaps it's time to revisit Seifert's phase diagram and extend it to include more anisotropies. It may still be possible to address parts of this question using the nice arclength parameterization that Siefert, Berndl, and Lipowski used in their 1991 paper to produce Figure 1-2.[140] See Figure 3-18 for an illustration.

Such an extended phase diagram may help distinguish between curvature-sensing by diffusion versus particle shape.

4.2 Self-Directed Growth of Living Solids

Living systems grow through active processes that drive the shape evolution of the boundaries between living and non-living matter. Many lifeforms develop body plans during an early stage of growth. For example, vertebrates establish a body plan during gestation of the fetus. In contrast, other lifeforms develop their shape gradually over time.

Recently, Hoffman *et al* extended the results of our Chapter 2 to the *active* matter context where hydrodynamic flows continue driving the buckled membrane to create protrusions and droplets [327]. This illustrates how defect structures can drive morphodynamical processes.

Botanical woody trees are another example of life that develops its shape over time. Woody trees are living solids whose eventual shape emerges through many small iterations of cell reproduction in a thin two-dimensional layer of cells known as the *cambium*.

Are woody trees predominantly a biological phenomenon whose essential features depend on complex details of biochemistry and interactions between many types of cells? Indeed, biologists have identified many details in the structures of plants, see Figure 4-3. In contrast to this, I will present initial evidence of that the branching shapes of woody trees may result from a simple, universal growth process.

This section is structured as follows. Section 4.2.1 briefly reviews previous research on branching systems. Section 4.2.2 shows pictures of wood from real botanical trees that motivate the present work. Section 4.2.3 explains a simulation that extends a widely used model of *isotropic* surface growth to incorporate *anisotropy* from spins that influence growth. That motivates a new model that I call “self-directed solids” (SDS). Section 4.2.4, shows SDS in 1+1D, and Section 4.2.5 shows 2+1D.

4.2.1 Review of Previous Branching Models

The arrangment leafs and petals of plants have obvious repeating patterns and spirals, which have attracted wonder since antiquity. This study of "phyllotaxis" receives comment in literature across essentially all time periods of human history.

In the Renaissance, Leonardo da Vinci observed that the cross-sectional area of daughter branches equals the parent's cross-sectional area, see Figure 4-2.

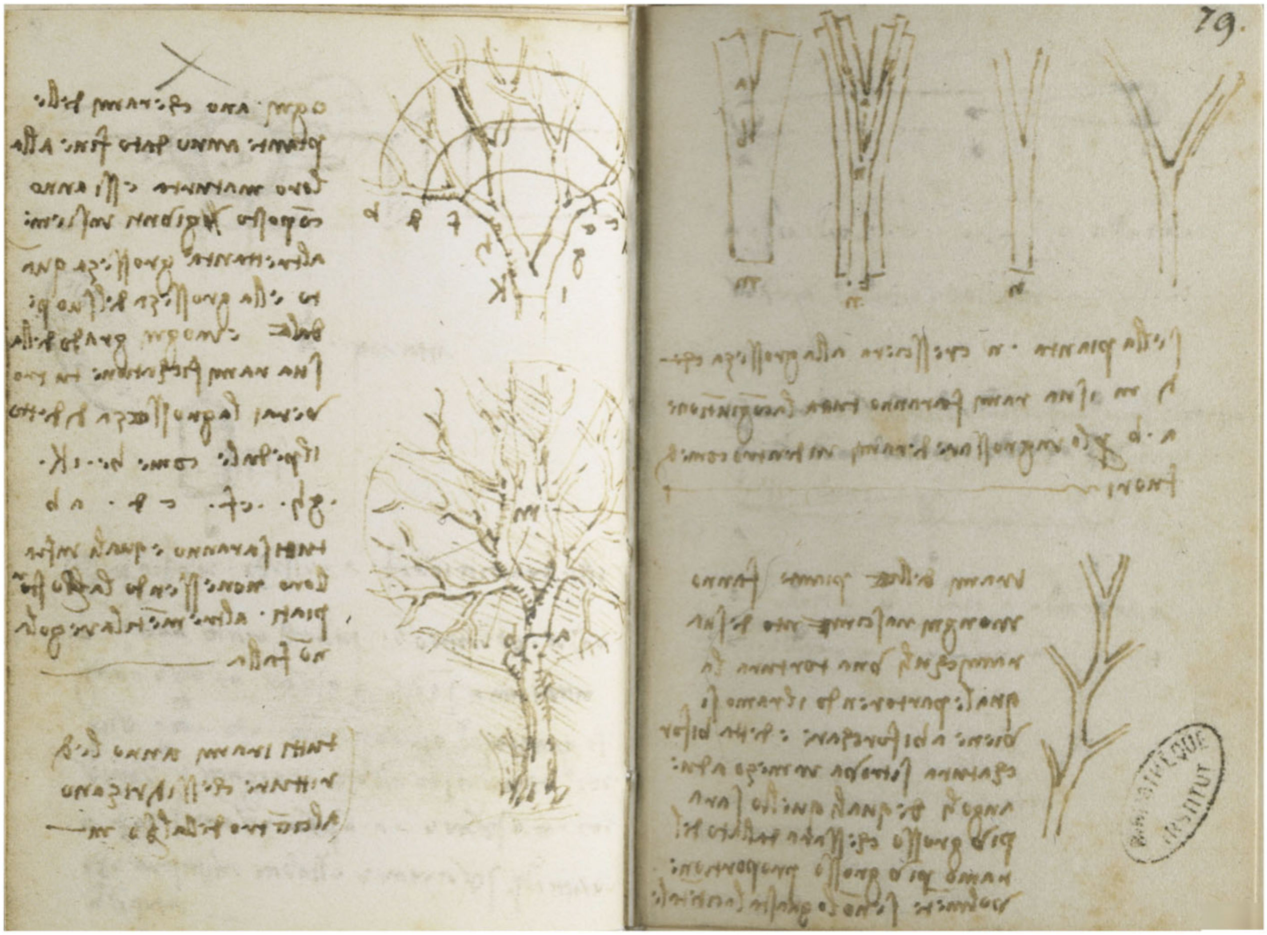

Figure 4-2: "All the branches of a tree at every stage of its height when put together are equal in thickness to the trunk [below them]. All the branches of a water [course] at every stage of its course, if they are of equal rapidity, are equal to the body of the main stream." passage 394 in J.P. Richter's "The literary works of Leonardo da Vinci" [50], which comes from pages 78v – 79r in the *Paris Manuscript M*[4], see also Plate XXVII in Ref. [50]. [See 274, Minamino & Tateno] for an analysis of how closely real botanical trees obey da Vinci's Tree Rule.

As mentioned in Chapter 1, many scholars saw Turing's instability as a likely cornerstone to understanding morphogenesis. However, it took time to develop connections between his simple idea and real systems. Lindenmayer's L-systems [89, 90] and Gierer & Meinhardt's [99] are different approaches to morphogenesis built on Turing. Each initiated a subfield.

Building on Lindenmayer's L-systems computer scientists have developed programs for generating realistic-looking leaf patterns and whole tree branching patterns [132, 202, 210, 228, 300]. While instructive, these models use many free parameters to offer control knobs that allow a user to configure resulting shapes. This is useful for programmatic generation of scenes in movies and video games. Here, we focus on a minimal model to understand how such shapes emerge from the smallest number of ingredients.

As described in Chapter 1, Hans Meinhardt expanded the study of Turing patterns by considering many different systems of nonlinear equations that generate patterns after the onset of a Turing-type instability.[1] In 1976, Meinhardt proposed models for patterns of veins in leafy plants.[107] In 1977, Mitchison offered an explanation based on reaction-diffusion modeling for the long-standing puzzle of why Fibonacci sequences appear so frequently in the spirals of flowers and plants [110]. Subsequent work in leaf patterning has focused on capturing finer details of veins in real plants and biological understanding of hormones like *auxin* [114]. Levitov connected these Fibonacci sequences of phyllotaxis to the physics of soft growth [130, 137, 138, 168, 224].

Leaf venation has also been explored from the perspective of the mechanics of materials. Couder *et al* showed that leaf patterns emerge from a tensorial structure of the mechanical stress field in thin sheets [178]. Bends, folds, and creases in soft thin shells is an active area of on-going work [254, 259], and is relevant to the explosion of interest in soft robotics [282]. These approaches often focus on understanding parameters and conditions for control material samples that are typically a few centimeters or smaller.

Diffusion limited aggregation (DLA) is a well-studied minimal model that exhibits branching and statistical self-similarity. However, “the large-scale structure of a DLA cluster is dominated by non-local effects.” [175] Here, we focus on minimal *local* growth rules of anisotropic growth.

---

[1] Like Prusinkiewicz & Lindenmayer's "Algorithmic Beauty of Plants,"[132], Meinhardt's models are now available in a popular book, "Algorithmic Beauty of Sea Shells."[240]

Another physical model of branching comes from the study of branching and annihilating random walks (BARW), which grew out of understanding diffusion-limited chemical reactions that violate detailed balance [155]. This line of thought starts with the assumption of branching and coalescing of paths. We might hope to eventually develop a formal connection between the models presented below and BARW. Indeed, BARW has inspired models of branching organs in animals [296].

Neurons also exhibit branching patterns, see for example Ref. [176] from the Les Houches summer school “Branching in Nature, Dynamics and Morphogenesis of Branching Structures, from Cell to River Networks.”

Data on the metabolic rates of animals suggest that they follow a power-law relationship with body mass with a 3/4 exponent:

$$Y = Y_0 M^{3/4} \,.$$

West, Brown, & Enquist at the Sante Fe Institute proposed an explanation of this data based on the hierarchical branching structure of vascular networks [166, 172]. Subsequently, they extended this idea to propose a fractal self-similar structure for branching in woody trees [171]. However, follow-on work has suggested that space filing and hydro-mechanical constraints may better fit available data from real trees.[249]

It seems that most biophysics researcher have not focused on the *grain* patterns of wood. A notable exception is Eric Kramer, whose work has connected wood grain polarity with *auxin* [197, 216, 236].

Wood grain patterns exhibit topological defects. These defect structures evolve as the living solid grows (see photos below). Moving defects in biological systems are an increasingly hot topic in biophysics [338, 341]. Thus far, that work has focused on cell membranes and mammalian tissues.

4.2.2 Observations of Wood

The hormone *auxin* plays a key role in the development of the *cambium*, which is the thin layer of living cells that form a two-dimensional sheath of cells in the outer layers of woody plants, see Figure 4-3.

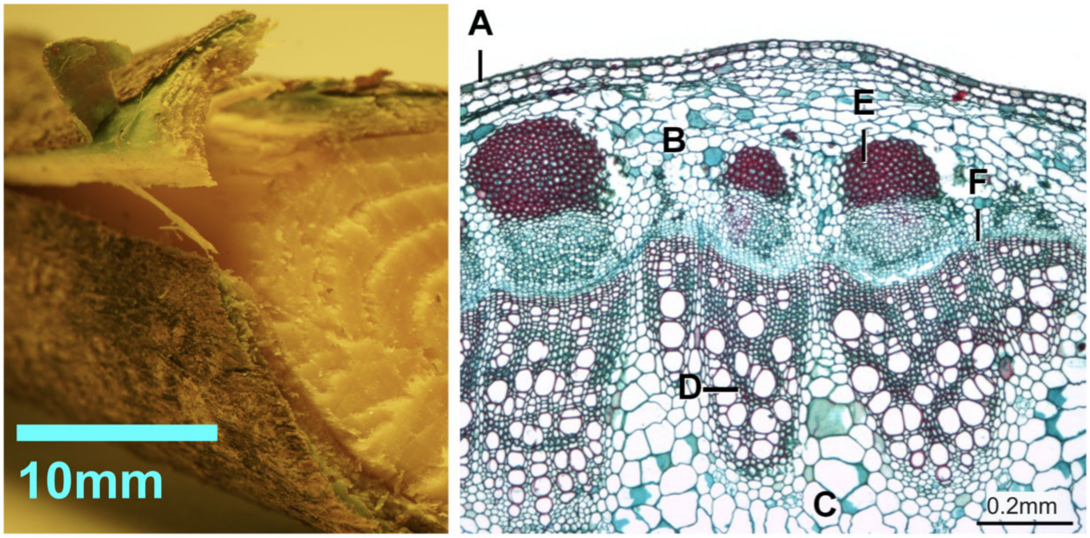

Figure 4-3: Left: pulling back outer layers of a Lilac branch from my garden. Right: Helianthus stem in section showing A-Epidermis, B-Cortex, C-Pith, D-Xylem, E-Phloem fibers, F-Vascular cambium. Scale=0.2mm. "Cells of the vascular cambium (F) divide to form phloem on the outside, located beneath the bundle cap (E), and xylem (D)." This vascular cambium is in bundles of phloem and xylem together, and is starting to connect the bundles at point F. (Reproduced by Wikipedia, image made by Jon Houseman and Matthew Ford.)

Wood grains show a history of the iterative growth of a living solid. In this history, one readily observes topological defects in the wood grain, as required by Poincaré's 1885 theorem [51]. In the notch of any branch, one can remove the bark to find negative topological defects, see Figure 4-4. From boiling off the bark of a half-dozen branches from various species, I have found –1 topological defects in most cases where the two branches are of roughly equal diameter. When a child branch is much smaller than its parent branch, I have found pairs of –1/2 topological defects arranged symmetrically. In some cases, a turbulent proliferation of defects appears, see the Silver Maple (bottom-right Fig. 4-4). This may accompany its finer grain compared to the larger grains of the Basswood on the left. From looking at the region surrounding this turbulence, one readily identifies a total topological charge of –1. From examining the scars on bark on many living trees, I believe that this total charge of -1 is found at essentially all branching points — again, this is required by Poincaré's "cowlick" theorem [51].

The tip of the diverging branch is a $+1$ topological defect escaping into the third dimension, analogous to bulk liquid crystals [96, 98, 101]. Thus, each branch consists of a pair of $+1$ and -1 defects. This is reminiscent of the Berezinskii-Kosterlitz-Thouless (BKT) [97, 100] transition. However, here, the $+1$ defect escapes rapidly into the third dimension as the tip grows. The -1 defect remains anchored at the notch and grows much more slowly.

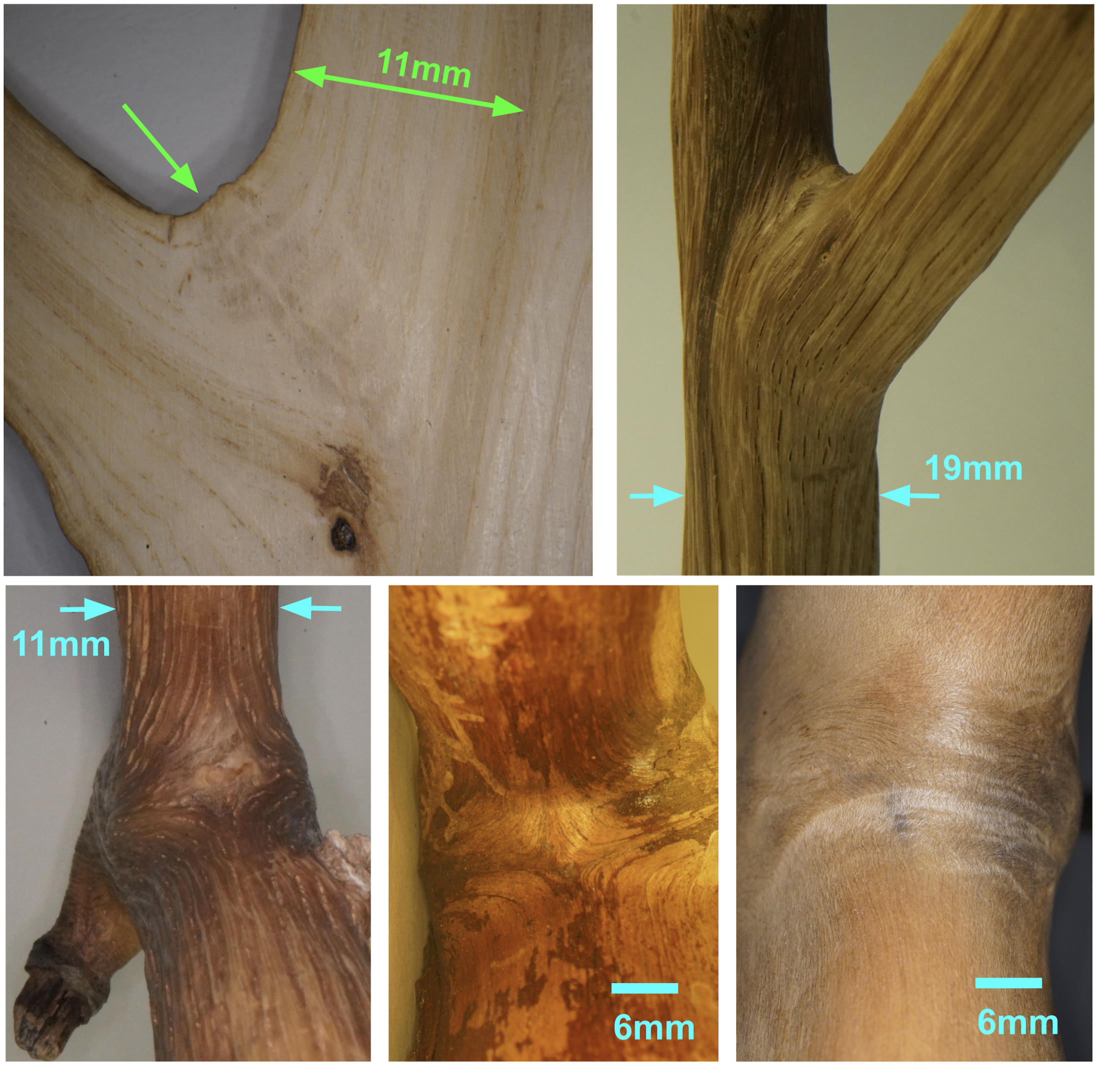

Figure 4-4: (Top) basswood branch with bark soaked off in hot water, one finds $+1$ topological defects in the notches of branches. The defect core traces a line through the layers of growth that is visible in a cross-section on the top-left. (Bottom) From left to right: Basswood, White Pine, and Silver Maple branches have different grain sizes, and all exhibit defect structures in the notches.

Tip growth is faster than lateral growth. This asymmetry is fundamental to the emergent morphologies of woody plants. Denote the tip growth speed as $g_{||}$. It is parallel to the aligned long axis of the cells. Denote the lateral growth speed as $g_{\perp}$ along the surface normal. Growth rates clearly vary in time with available sunlight, water, and nutrients. Growth rates could depend on many other factors, including maturity (or diameter) of a beam or proximity to other features along the beam. However, setting those complexities aside, assume constant $g_{||}$ and $g_{\perp}$. Denote the *aspect ratio* $\alpha = g_{||}/g_{\perp}$. The +1 defect of the tip advances at $g_{+} = g_{||}$. However, the −1 defect of the notch advances in a more subtle way. In this simplified model, we can estimate g_{-}. As shown in the right-most subfigure of Figure 4-5, *both sides* of the notch "zipper" the gap at a rate of $g_{\perp}$. Thus, the −1 defect advances along the dashed line at a speed of

$$\sin\frac{\theta}{2} = \frac{g_{\perp}}{g_{-}} \implies g_{-} = \frac{g_{\perp}}{\sin\theta/2} \tag{4.1}$$

In this mean-field-like model, when a tip begins to diverge from a parent beam, the angle of divergence θ has a critical angle θ_c below which the tip fails to escape and lateral growth overtakes the tip:

$$\sin\theta_c = \frac{g_{\perp}}{g_{||}} = \frac{1}{\alpha}\,. \tag{4.2}$$

This is only an estimate, because if a +1 defect were to diverge *at* this critical angle, then both defects would stay at the same radius from the center of the parent beam and also pull apart from each other. More likely, the soft matter nature of the cambium would allow the defects to annihilate.

One might also estimate the critical angle based on thermal fluctuations of the surface, and thus hope to find a formula for the critical aspect ratio as a function of noise strength, $\alpha(\eta)$. However, a usefully accurate estimate of this form has yet to be put forward.

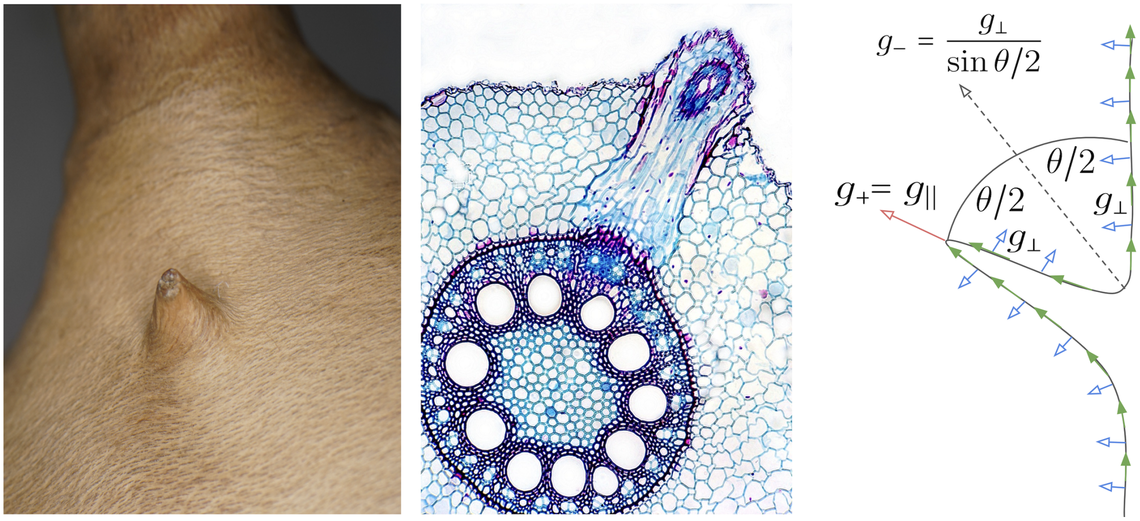

Figure 4-5: (Left) Woody spike emerging below a −1/2 defect in Silver Maple, a dicot. The other −1/2 defect is on the other side of this small branch growing out of a larger branch. (Center) Cross section of Maize (Zea mays), a monocot, about 800 µm diameter. A lateral root is bursting out of the parent root. Root tips can diverge at any location. In contrast, shoots that form leaves and stems typically emerge only from the apical meristem. Image by John Bebbington FRPS. (Right) Diagram of tip geometry.

Plant hormones clearly influence branching. The full picture surely involves the interplay of gene networks and the activity of asymmetric growth. However, I will show that a simple cellular automaton with a constant aspect ratio can product branched growth.

Nonequilibrium growth of solids has been studied for decades. Many different systems have been found to be within the basin of attraction of the KPZ universality class [123]. Given the highly curved nature of these self-directed solids, in Subsection 4.2.6 we lift the KPZ growth equation into a covariant form and augment it with an orientational field, $\vec{s}$. An initial look at all terms allowed by symmetries suggests a dizzying number of possible couplings. Therefore, at this stage, we present initial results from three types of simulations aimed at gaining intuition.

To model this $2 + 1$-dimensional growth process, we introduce a simple off-lattice automaton that exhibits asymmetry such that growth along an oriented axis is faster than lateral growth. This model exhibits a transition between growing spheres and long pillars. The spheres arise from isotropic growth when the spins are ignored or scrambled by noise. When the noise does not overwhelm the asymetry, anisotropic growth generates long pillars, possibly with long-range order. These two states may be analogous to the two phases of the flocking transition: disordered motion with birds scrambling in all directions (spheres) and ordered motion with a single flock direction (pillars) [153, 154]. Interestingly, the finite size of real flocks allows them to twist and turn. This is our dominant visual experience of flocks in nature. However, the mostly thoroughly studied aspects of flocking models and field theories focus on the bulk rather than the boundary of flocks [169].

This model of self-directed growth also generates visually interesting images at finite-size. In between the sphere and pillar growth modes, the model produces *branched* objects that resemble botanical trees. These forms may be statistically self-similar, and thus fractal.

Each of these three simulations is a simple automaton that fills in sites in a 2D or 3D space. These models live in a two-parameter space of aspect ratio, α, and temperature or noise, η. Setting $\alpha = 1$ produces isotropic growth at all values of noise strength η. As aspect ratio α is increased above 1, interesting morphologies unfolds.

Anisotropic automatons:

1. 2+1D anisotropic restricted-solid-on-solid (ARSOS) with an orientation $\vec{s}$ at each site that causes faster growth when local alignment is higher. RSOS models are on-lattice and the isotropic form has been thoroughly studied as a member of the KPZ universality class. This anisotropic variant exhibits a transition from stable to unstable growth. At low aspect ratio, growth "heals" misalignments and the surface width is reduced. When α is above a critical value, pillars form and the surface width diverges such that the RSOS automaton becomes invalid.

2. 1+1D self-directed solid (SDS) is an "over lattice" automaton consisting of "cells" positioned in $\mathbb{R}^2$ that produce "child" cells a short distance away. Each cell carries an orientation vector, $\vec{s}$, that determines where child cells are deposited. The child's orientation angle is set by averaging neighbors plus noise. An underlying square lattice enables self-avoidance and keeps the density approximately uniform by allowing cells to avoid depositing cells on top of existing cells. Even in this two-dimensional space, a rich phase space of morphologies and topolog-

ical defects arises.

3. 2+1D self-directed solid (SDS) extends the previous automaton to $\mathbb{R}^3$. Instead of a single angle describing $\vec{s}$, each cell now carries an "attitude" defined by three angles that evolve as cell lineages propagate in space. Like the previous two models, this is parameterized by aspect ratio α and noise strength η. A similar array of morphologies arise with important differences from greater freedom in $\mathbb{R}^3$. Branching does not resemble botanical woody trees until a third automaton rule is added to favor growth sites in the tangent plane of the emerging solid. With this third rule, -1 and pairs of $-1/2$ topological defects become visible, and resemble those in real tree branches.

4.2.3 2+1D Anisotropic Restricted Solid-on-Solid (ARSOS)

To make an initial connection with the extensive literature on nonequilibrium surface growth, consider the following *asymmetric* extension to the standard restricted-solid-on-solid (RSOS) model. The standard RSOS model considers a columns above a flat plane. A column is picked at random and the height increment $h_{ij} \to h_{ij} + 1$ if the nearest-neighbor columns are not lagging behind, i.e. $h_{nn} - h_{ij} \leq 1$.[151] Note that the standard RSOS condition is restricted to looking downward toward the reference plane. The standard RSOS condition generates hills of unit slope. We augment this model in three ways:

1. **Spins:** Each site now carries a unit spin vector, $\vec{s}$. The spin direction is computed by averaging existing neighbor sites plus noise and then frozen in place when the site is deposited. We denote noise by η.

2. **Spin Alignment Coupling:** Instead of always depositing allowed sites like standard RSOS, in ARSOS we randomly skip some growth opportunities where *neighboring spins are misaligned.* This backoff probability is controlled by a coupling parameter that we denote "α." Further details below.

3. **Floppy Condition:** To allow steep domain wall crevices to form, we replace

the standard RSOS condition with “floppy RSOS” that allows for a threshold number of neighboring cells to be filled. For 2+1D implemented on a cubic lattice, the total number of possible neighbors is $3^3 - 1 = 26$. We found that requiring between six and nine neighbors generated growth that resembled standard RSOS, and typically used a floppy RSOS threshold of seven neighbors. Unlike standard RSOS, this allows the supporting sites to come from any side, not just from “below,” i.e. from the direction of the reference plane.

The simplest spin alignment rule we considered is a polar model:

1. For a candidate growth site located at $\vec{\boldsymbol{x}} = (x, y, h(x, y))$, compute “alignment”, A as the magnitude of the vector sum of the nearest-neighboring sites' unit vectors divided by the number of neighbors:

$$A = \frac{1}{N} \left| \sum_{nn}^{N} \vec{\boldsymbol{s}} \right|$$

2. Compute the site's growth probability as

$$P(\vec{\boldsymbol{x}}) = \frac{1 + A\alpha}{1 + \alpha} .$$

3. Draw a random number between zero and one. If the draw is less than $P(\vec{\boldsymbol{x}})$, then proceed with depositing a new spin at that site, otherwise skip it and allow it to be revisited later.

When the coupling constant is turned off $\alpha = 0$, the surface grows like standard RSOS and the spin field is convected down slopes. This makes pretty pictures in which valleys are filled via sedimentation flows, and the spin field evolves to passively indicate where the sedimentation is occurring.

We also explored nematic alignment rules using the largest eigenvalue of the Oseen–de Gennes tensor. Given a random initial configuration of spins, the spins on the growing surface evolve differently for nematic versus polar alignment rules. We observed pairs of integer defects in polar spins, and pairs of half-integer defects in nematics. However, we focused on the formation of domain walls, and both polar and nematic alignment rules produced qualitatively similar crevices.

As shown in Figure 4-6, this model exhibits a transition. When the coupling constant α is above a threshold, areas of misalignment get frozen in place and grow much slower than aligned areas. This leads to runaway growth of aligned regions, such that the RSOS model becomes invalid.

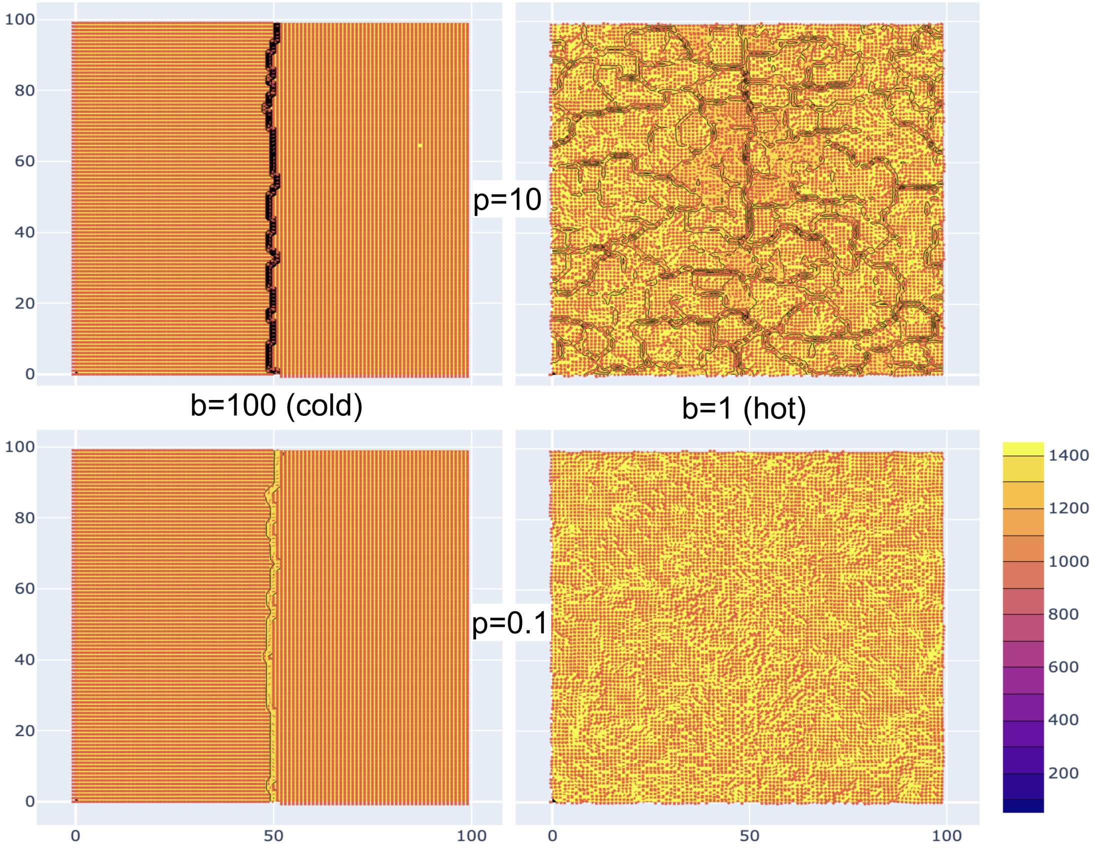

Figure 4-6: Anisotropic RSOS of a Spin Wave. These nematic test cases have a $\pi/2$ spin wave frozen at the boundaries: left spins pinned pointing inward and right spins pointing up. The initial height profile is a cosine wave in the horizontal direction, so there are “hills” on the left and right edges that are 80 height steps above the “valley” in the center. The left column shows low temperature (b=100), and the right shows high temperature (b=1). The bottom row shows small coupling of growth rate to alignment (p=0.1), and the top row shows stronger coupling (p=10). **upper-left:** at low temperature and high enough coupling constant, growth quickly moves the spin wave to a crevice that falls behind and the surface width diverges. In all other cases, even if crevices form, they lag behind only a small amount and the surface remains stable. **lower-left:** at lower coupling, the misaligned spins focus in a crevice that lags the rest of the surface by a small amount. **upper-right:** at high temperature and coupling, a network of crevices form between domains of mostly aligned spins. **lower-right:** at high temperature and low coupling, the surface becomes approximately uniform in height and the spin field evolves on a flat substrate.

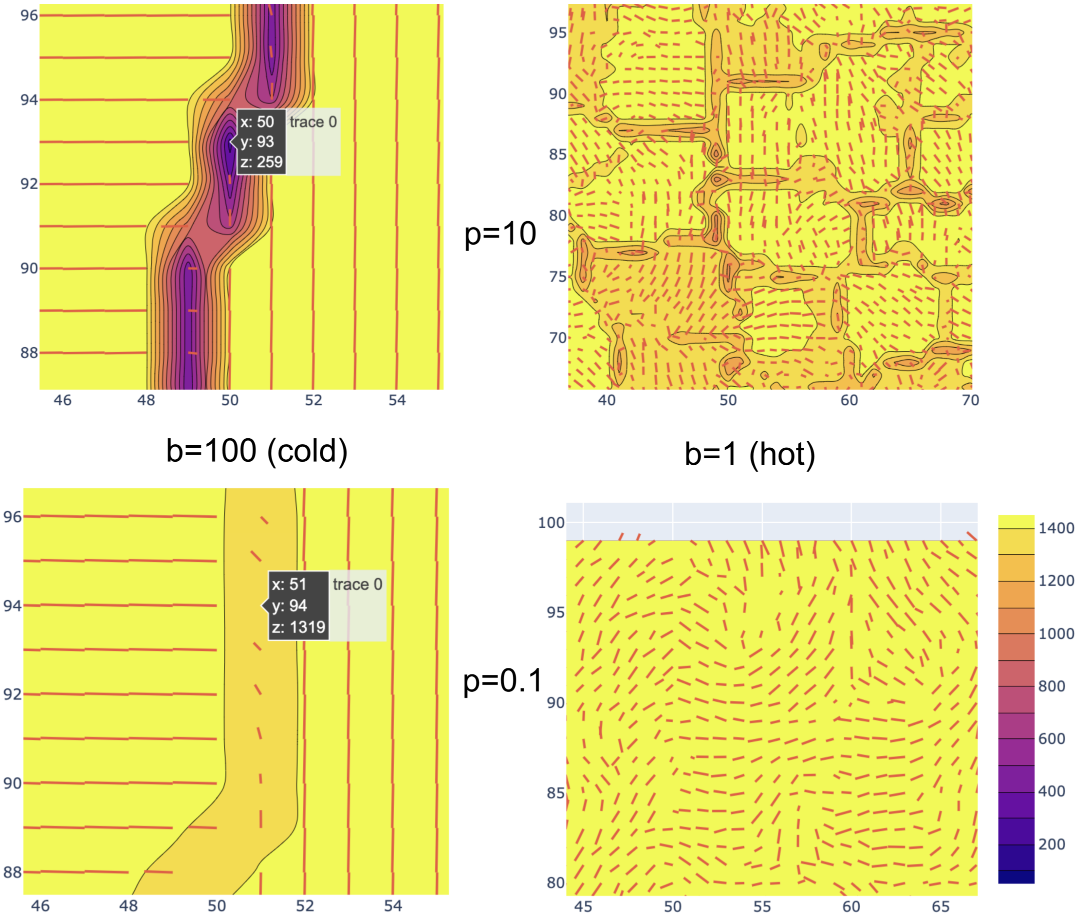

Figure 4-7: Anisotropic RSOS of a Spin Wave (zoom). The same four cases as Fig. 4-6 zoomed in to show details. The deep crevices in the upper-left will fall farther and farther behind. This is analogous to the branch points with –1 topological defects in the SDS models below.

My study of 2+1D ARSOS suggests that when the noise is turned off, the threshold for α is zero. That is, at zero temperature, any amount of coupling leads to domain wall formation and a surface width that diverges. At finite temperature, a small enough coupling gets washed away by the noise, so our simulations suggest that the threshold becomes finite at finite temperature.

While this observation of a transition in the ARSOS model is helpful, there are limitations to the ARSOS model. Once a domain wall falls behind, it can continue growing up, however it does not move laterally. This prevents regions from healing over the domain wall, as anticipated in Appendix B. Therefore, we set ARSOS aside and move on to Self-Directed Solid models, which are off-lattice.

4.2.4 1+1D Self-Directed Solid (SDS)

In my initial attempts at growing a more general oriented solid *on-lattice*, all of the automatons that I tried ended up locked to the lattice directions. Cube-like trees were easy to grow; natural trees not. Moving off-lattice, I tried growing long ellipsoids in free space. Each cell could deposit child cells as adjacent ellipsoids. By giving a higher growth probability to child sites near the head or tail of the long axis, it was clear that anisotropic growth resulted. However, detecting collisions required spatial indexing. While r-trees are efficient [309], the computational cost of controlling density increased with larger aspect ratios. To explore large growths of very elongated ellipsoids, I had to either spend a lot of compute cycles or have pile ups of cells in high density regions where collision detection was inadequate.

Here, we present a better off-lattice model. I call this "over-lattice" because a lattice is present; however, cells are not positioned on the vertices of the lattice. Instead, cells are located at points in $\mathbb{R}^d$, and their density is tracked in the grid cells of a lattice. For 1+1D, the lattice is a square lattice in the plane, and for 2+1D a cubic lattice in $\mathbb{R}^3$. Instead of ellipsoids, each cell is a just a point that carries a unit spin vector. This means that each cell exists in a single lattice plaquette or voxel. Instead of using a general r-tree index to find neighboring cells, the lattice grid sites provide a sufficient index. When a cell is created, its position $\vec{\boldsymbol{x}}$ is marked on the corresponding grid coordinate $\textsc{Int}(\vec{\boldsymbol{x}})$. When deciding whether to deposit a new child cell at $\vec{\boldsymbol{x}}_c$, it is easy to check whether it falls in a lattice site that is already populated by an existing cell. All lengths are measured in units of the lattice spacing.

There are many algorithms for selecting child sites that result in qualitatively similar growth morphologies. Since we want to assign higher growth likelihood to child sites in the direction of the parent's spin vector, a particularly efficient procedure uses a priority queue of parent cells with open child sites. We call this priority queue the "open edge." Cells in the "open edge" are analogous to the *cambium* of a woody tree.

1. When depositing a cell at $\vec{\boldsymbol{x}}$ compute the locations of four candidate child sites

   and assign each site the following odds of growth:

   - $\vec{\boldsymbol{x}} + \vec{\boldsymbol{s}}$, odds = α
   - $\vec{\boldsymbol{x}} - \vec{\boldsymbol{s}}$, odds = α for nematic growth or odds = 1 for polar
   - $\vec{\boldsymbol{x}} + \vec{\boldsymbol{s}}_{\perp}$, odds = 1, and
   - $\vec{\boldsymbol{x}} - \vec{\boldsymbol{s}}_{\perp}$, odds = 1,

   where $\vec{\boldsymbol{s}}_{\perp}$ is perpendicular to the spin.

2. Remove any child locations that land in lattice sites that are already filled, unless the cell in that filled lattice site is the parent, in which case allow the growth, because the diagonal of the square plaquettes is longer than one.

3. Register the parent cell in the priority queue with a priority equal to the highest odds of its candidate child locations.

At each iteration of the algorithm, consider the sum of all priorities in the queue, denoted M. Roll a metaphorical M-sided dice to get a number $0 \leq m < M$, and count m steps down the ordered priorities in the queue. Pop that parent cell and grow a new cell at its highest odds child location, unless its lattice site has already been colonized. If the parent cell still has open child sites, put it back in the queue.

In 1+1D, each spin is a defined by a single angle θ. We will consider more general attitudes in the next section on 2+1D. A simulation is initialized with a single first cell. When depositing a new child cell, its angle is determined by averaging over all of the existing cells in its one-hop lattice neighborhood. In 1+1D, this is a 3x3 region. To mimic the effect of thermal noise, an additional noise angle is added to θ before depositing the cell. Noise is parameterized by η. We used Vicsek-style noise from the Vicsek *et al* flocking model in which the noise angle is a uniform draw from $[-\eta/2, \eta/2]$ [154]. Other approaches to drawing a random angle, such as from a Gaussian mapped on to $[-\pi/2, \pi/2]$, appear to result in qualitatively similar morphologies.

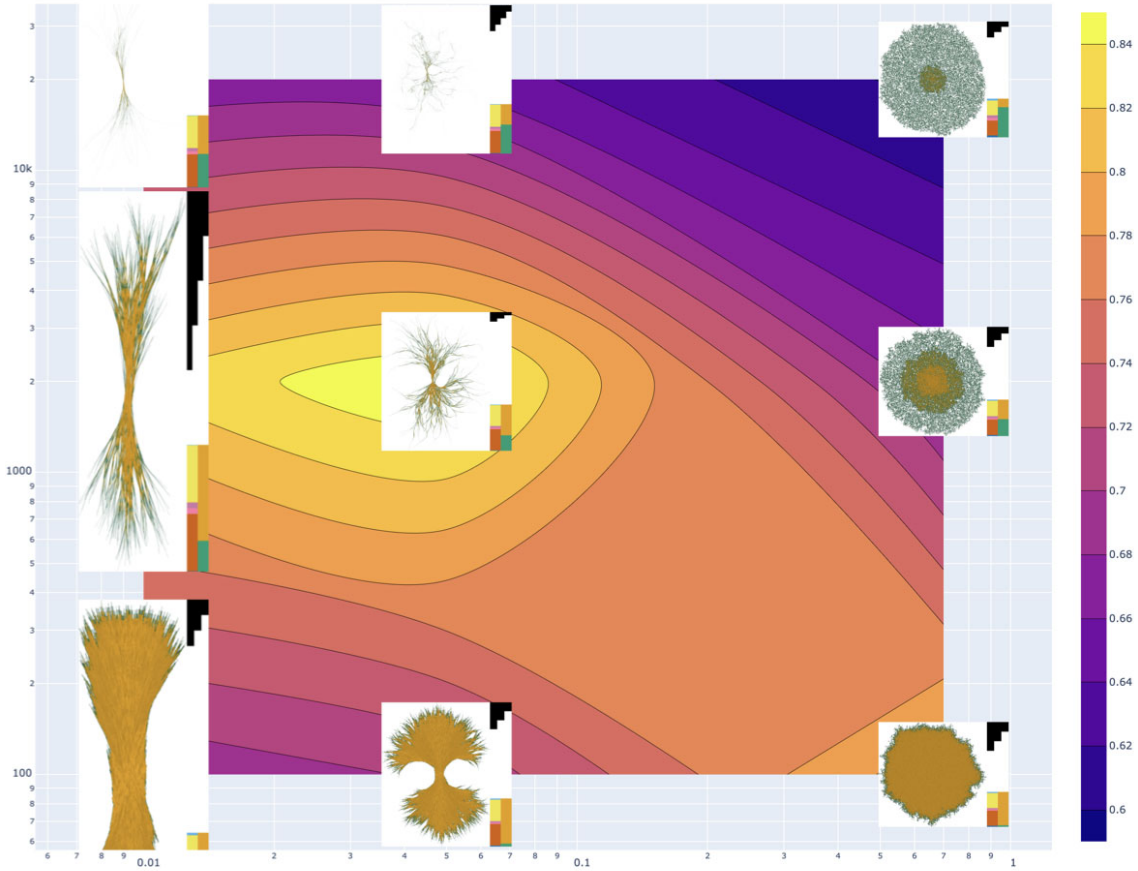

Figure 4-8: Various Morphologies at mass=1e7. This illustrates observed morphologies as a function of noise η on the horizontal axis versus aspect ratio α on the vertical axis. *Green* indicates a site that has open child sites, which we call "cambium" in analogy to woody trees. *Orange* indicates a site with no open child sites, which we call "wood." The colored contour plot back drop is discusssed below.

I should emphasize that Figure 4-8 is a draft and could change when the shapes are grown to larger sizes using more compute cycles. For example, as the outer tendrils of cells escape further, the region where box counting can detect self-similarity over many scales may become an *annulus*. Here, we use the full shape for box counting. However, we can already see that the core is becoming solid with a box counting dimension of 2, and the outer most radius is pushed by just a few tendrils with a box counting dimension of 1. Developing a principled theory of box counting for this context is an area for future work.

With these simple rules, three distinct morphologies emerge. See draft phase diagram in Figure 4-8. At high temperatures, large η scrambles the spins and isotropic growth generates a "ball" with a layer of active growth sites expands outwards uniformly in all directions. The surface of the ball changes as α is increased. At low α, the active layer is thin, and most of the ball is wood. At high α, the ball's surface becomes diffuse with a thick cambium of active growth. The roughness of these balls' surfaces is likely in the KPZ universality class, at least at low α, although I have not confirmed this quantitatively.

When α is close to one, the ball morphology persists down to low temperature, i.e. small η. Like the 2+1D ARSOS model, at $\eta = 0$, any amount of anisotropy, $1 < \alpha$, results in a new morphology, which we call a "pole," see left side of Fig. 4-8. While growth occurs in all directions, the ends of the pole grow much faster than the sides. The direction of the pole is set by the initial seed.

Between ball and pole shapes, a branching shape emerges. We refer to these as "trees" or more precisely "smashed trees" because they cannot escape into an actual third dimension until the next section. With high α and a little noise, but not too much, long slender fibers grow outward. These fibers branch off of each other and re-connect, forming a web. Voids in the web eventually fill in. However, the outer radius of the structure grows faster than the thickness of these in-filling trunks near the origin. As a result, the region of active growth is very large. Within this region of active growth, we observe self-similarity. Figure 4-9 shows an example from this branching morphology.

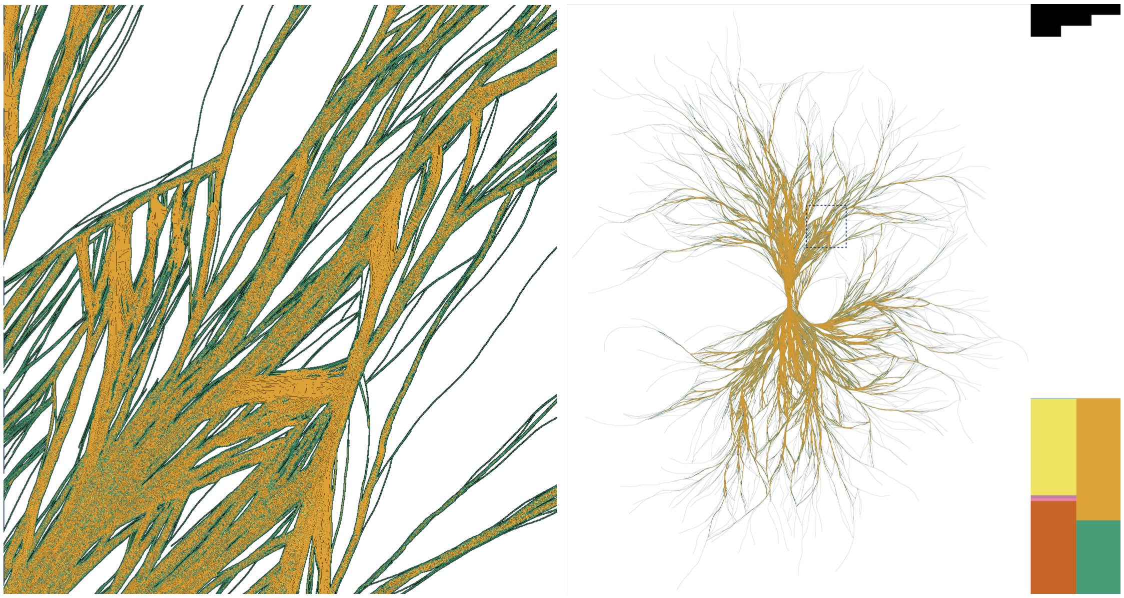

Figure 4-9: Branches diverge and coalesce on many scales. (left) zoom in on a portion of the shape on the right. (right) full view of 17,061,445 cells grown at $a = 2000$ and $\eta = 0.05$ using Vicsek-style noise. The black stair steps are a scale bar. The number of steps indicates the power of ten, so the largest step is 10^3 lattice sites. The stack bar chart shows that wood sites (orange) out number cambium sites (green) 58% versus 42% in this snapshot. The inner stacked bar chart indicates that there are roughly as many $+1$ defects as -1 defects. Eventually, all of this interstities shown here will fill in with wood; however, by that time, the farthest tendrils will have reached even farther.

Concepts of statistical self-similarity and fractals have been studied extensively in nonequilibrium growth of surfaces [150, 161].

Before Mandelbrot's famous 1967 paper on coastlines,[88] mathematicians had found many examples of non-differentiable curves and surfaces, such as the Sierpi'nski triangle and Koch's snowflake, see G. Edgar's "Classics on Fractals" for translations of original papers [191]. However, these were often viewed as mere curiosities. In the same time period that Wilson and coworkers were establishing the importance of scale invariance in field theory and inventing the renormalization group [103], Mandelbrot and coworkers were finding scale invariance in mathematical geometry. In 1982, the same year as Meinhardt's book on reaction-diffusion patterning [120]. Mandelbrot's landmark book on "The Fractal Geometry of Nature" drew significant attention to the idea that scale-invariance applied to observable structures around us [119].

Box-counting is a widely used technique for estimating the fractal dimensions of spatial patterns [189, 256]. The idea is that a spatial pattern generated by a scale-invariant process will have regions of open space and filled space such that if one covers the shape with a grid of boxes of side-length ϵ then some of the boxes will be filled and others empty. Counting the filled boxes provides an estimate of the "fractal dimension," D_f,

$$D_f = \lim_{\epsilon \to 0} \frac{\log N}{\log 1/\epsilon} \tag{4.3}$$

There are many possible definitions of "fractal dimension," so care must be taken in ascribing detailed meaning to exactly which physical quantity is exhibiting scale invariance, see E. Stanley's chapter "Form: An Introduction to Self-Similarity and Fractal Behavior" in Ref. [122].

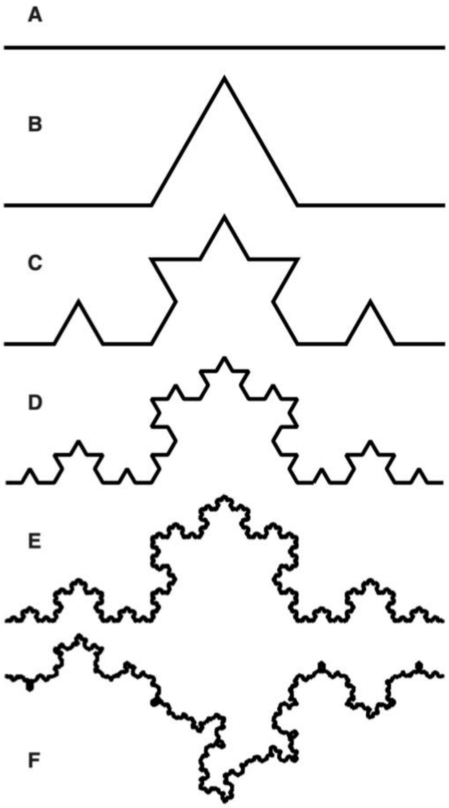

Figure 4-10: Concept of Statistical Self-Similarity: Figure from Bouda, Caplan, & Saiers: "Construction of the Koch curve, following Falconer (2003). Each interval (A) is divided evenly into three and the middle section is replaced by the complementary two sides of an equilateral triangle (B). The process is repeated for each newly created interval, yielding the second (C), third (D), and nth iterations. The Koch curve is the limit approached as $n \to \infty$. The limit curve can be subdivided into four quarters, each an exact copy of the whole, scaled down by a factor of three. The curve is thus self-similar with a similarity dimension of $\log(4)/\log(3)$. Even with n = 10 (E), zooming in on the pinnacle of the curve by a factor of three yields an image visually indistinguishable from the largest magnification five times over, meaning the curve is approximately self-similar over a finite range of scales. Following the same construction, but randomly choosing the side of the old interval on which each new pair of intervals is placed, yields one of many "statistically self-similar" curves (F). These cannot be divided into sets of identical copies; rather, their parts are scaled random variations on the whole and they only conform to a fractal dimension on average."[283]

Declaring that any given natural data set "is fractal" has become a meme in science, and many are likely not fractal. For example, measuring the shapes of plant roots or tree branches typically produces data over less than 5 doublings, 2^5, which does not exhibit a sufficiently constant slope over enough box sizes to confidently assert self-similarity [283, 325]. Further, the box counting procedure for *statistically* self-similarity differs from exact self-similarity in an important practical way. In counting the boxes covering an exactly self-similar shape, one easily minimizes N by aligning the grid with large edges in the pattern. In statistically self-similar shapes, one must search for the grid offset and rotation that minimizes N.[283] We have implemented such a pattern search algorithm, based on Bouda *et al*'s proposal. However, as noted above, the annular nature of these growing structures suggests that more theoretical work is needed.

Applying this algorithm to the balls, poles, and trees shown in Figure 4-8, we find that balls tends to $D_f \approx 2$ and poles tend to $D_f \approx 1$. However, their jagged edges may have interesting scaling properties. The tree morphology exhibits roughly constant slopes over several doublings, suggesting that they possess scale invariance, see Figure 4-11.

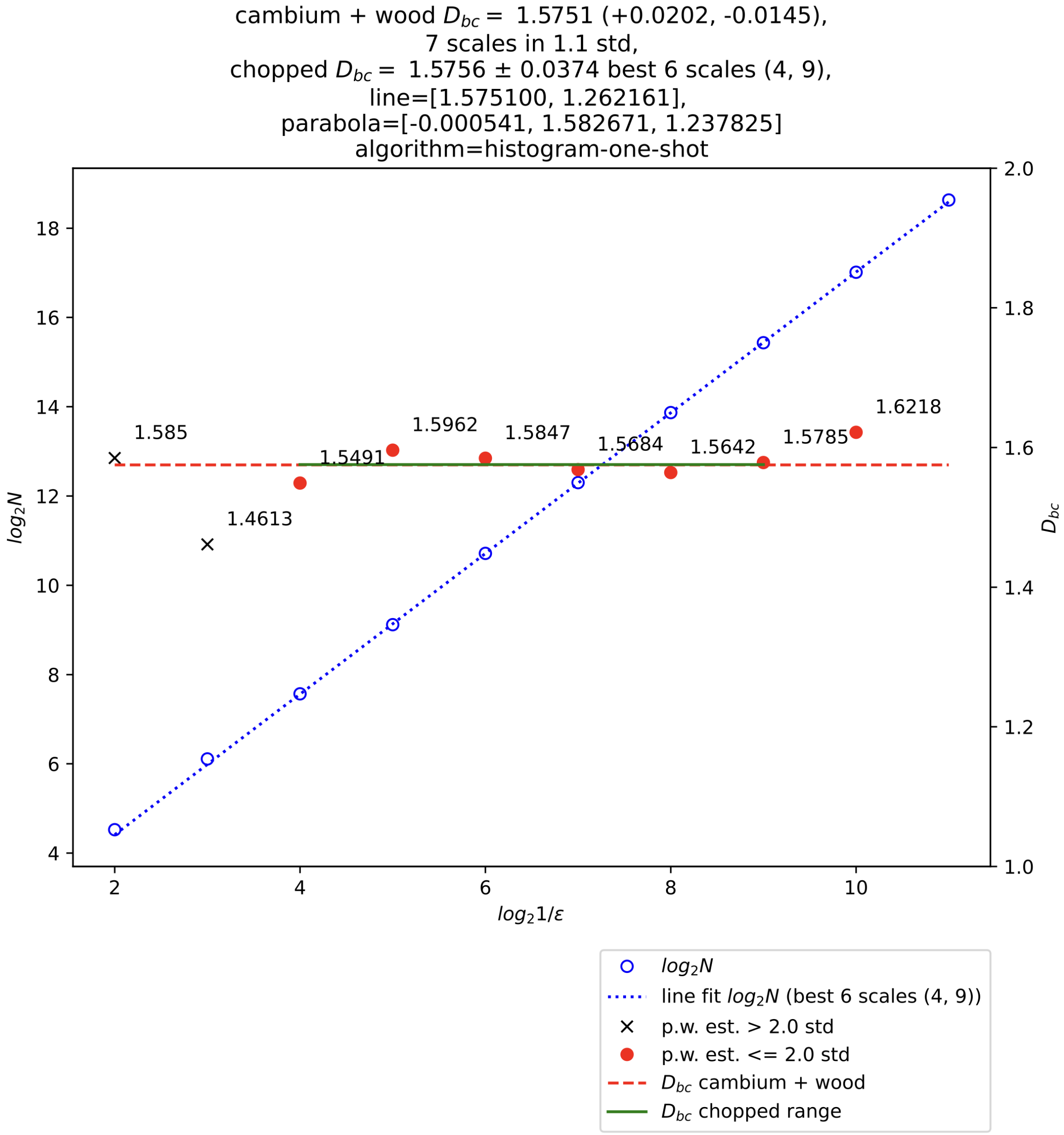

Figure 4-11: Estimating Self-Similarity and Fractal Dimension: Branched shapes in the middle region of Fig. 4-8 exhibit self-similarity over several scales. This plot comes from the shape in Fig. 4-9. ϵ is the side length of boxes in a grid. The blue-dashed line counts the number of boxes N that contain part of the shape at a given ϵ. The horizontal axis is $\log_2 1/\epsilon$. The blue circles mark reductions in ϵ by half. Right axis shows the slope of this line. Red dots are slopes of individual segments of the blue-dashed line within 2 σ of the average slope. Black x markers have been dropped. The green range shows seven segments used in the best fit.

4.2.5 2+1D Self-Directed Solid (SDS)

The self-directed solid model extends naturally to $\mathbb{R}^3$ with the important modification that spins now become general attitude matrices parameterized by *three* angles. Like a rocket in flight, the direction of flight requires two angles and the orientation of the object around the axis defined by the direction of flight requires a third angle. Averaging such rotation matrices is easily accomplished using quaternions to represent the rotations [183, 260].

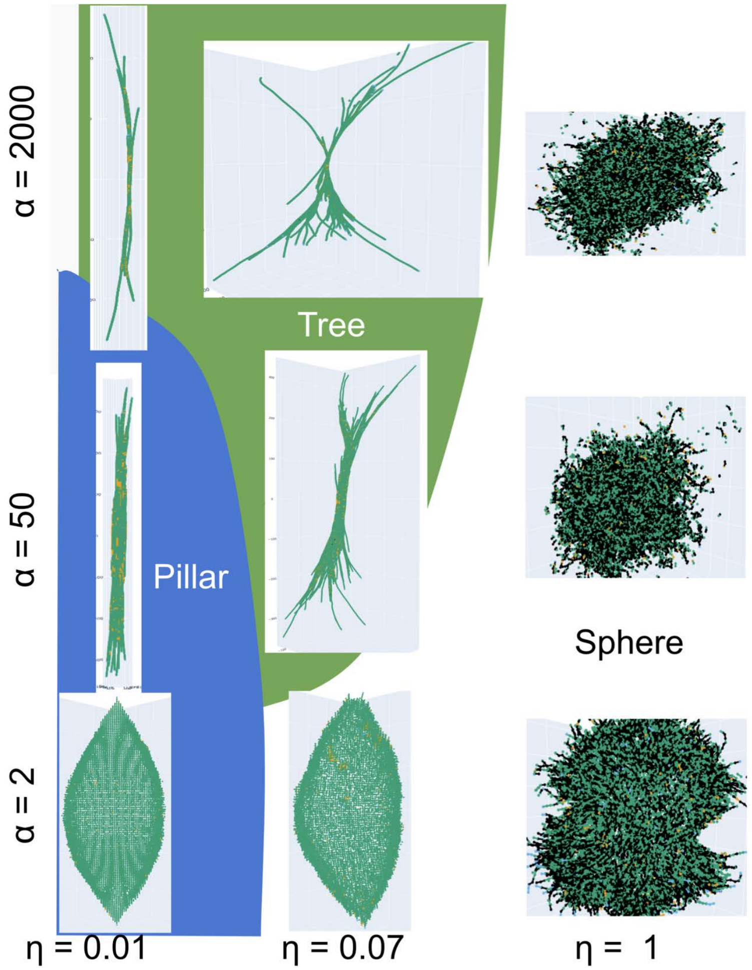

Figure 4-12: Proposed Draft of Phase Diagram for 2+1D self-directed growth: Like the morphologies found in 1+1D (Fig. 4-12, the 2+1D SDS model generates pillars and trees and spheres. (Left) very small noise $\eta = 0.01$. (Middle) small noise $\eta = 0.07$. (Right) high noise $\eta = 1$. I have sketched possible boundaries lines between the three modes of growth.

Figure 4-12 shows a 3x3 grid of example morphologies, which I have grouped into these categories:

1. **Pillars:** At $\eta = 0$ and $2 \leq \alpha$, a pillar maintains its order and grows to an arbitrarily large shape while maintaining its length-to-width aspect ratio equal to α. At very small but positive $0 < \eta$, it appears that there is a region of small α for which the pillar is maintained and noise does not disrupt the long-time aspect ratio. The lateral disturbances from noise are smaller than the lateral growth rate, so branches may nucleate but are subsequently overtaken and absorbed by the pillar.

2. **Spheres:** At high noise a lateral disturbances can escape, however, its persistence length is so short that it quickly turns back and reconnects with the object. It is likely that the thickness of this layer of branches meandering and reconnecting grows faster than the core, like we see in 1+1D; however, our computational tools for exploring this are not yet well developed.

3. **Trees:** With η small but not too small, and higher α, lateral disturbances escape and form branches that have large enough persistence length that they appear to not reconnect with the main trunk. I have labelled this region "Tree" in Fig. 4-12. It remains to be seen whether this mode of growth is truly distinct from spheres.

Figure 4-12 shows a guess at approximate boundaries between these modes of growth. It is not clear whether these boundaries continue to exist for arbitrarily large growths, and their exact locations are just guesses. Does the line separating pillars and trees reach either axis? It seems likely, and this motivates developing an analytical understanding.

Our implementation uses integer values of $1 \leq \alpha$. At $\alpha = 1$, the growth expands randomly in all directions.

It appears possible that the 2+1D tree morphology could exhibit statistical self-similarity. Measuring this will require more data. Before rewriting this automaton in a faster programming language, we may be able to make more headway analytically using the tools suggested in the next section.

As shown in Fig. 4-4, botanical trees exhibit defects with topological charge of –1 in the notches of branches. As shown in Fig. 4-5 pairs of –1/2 defects also appear in botanical trees. From my limited observations, it seems that such pairs of –1/2 defects arise around *small* branches coming out of larger trunks. It seems possible that they may eventually merge to form a –1 defect as the branch grows.

It is possible to zoom in on the branch points and examine them visually. However, extracting a winding number around possible defects is noisy. To get a better look at the surface textures around the notch of a branch, I initialized a simulation with two strands of cells: first a trunk and second a strand that follows the trunk for a distance and then arcs away. By setting the temperature low, the initialized shape is preserved and growth proceeds in the "pillar" mode with two pillars touching. The result is shown in Figure 4-13.

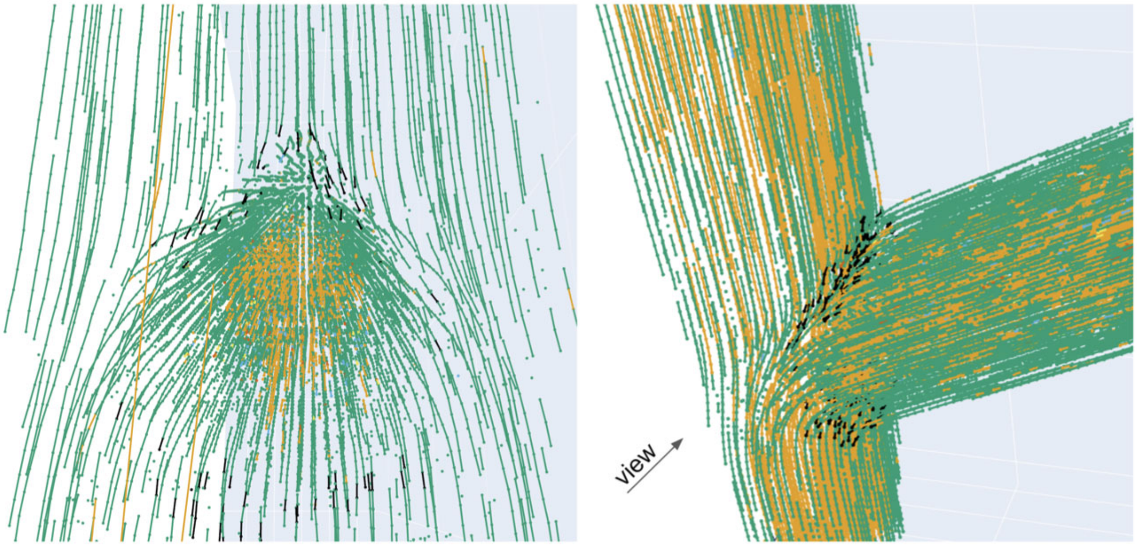

Figure 4-13: –1 defect appears at branch: (Right) Surface pattern in the shape of a –1 topological defect appears in the notch of this branch. The "view" angle shown on the right is the camera position for the image on the left. (Left) Looking through the trunk with wood cells hidden. This was grown at $\alpha = 50$ and low temperature, $\eta = 0.01$, so new branches do not emerge and disrupt our view.

Regarding color coding in these images, these follow the color coding of the 1+1D model: the green markers and lines connecting them represent cells that have open child sites for growth, and are thus "cambium." The orange sites correspond to "wood." While it was practical to categorize defect sites in the planar model, it has not yet proven practical here. The black-colored segments in these images are new. They correspond to highly curved segments, which were not tracked in the 1+1D model.

When examining these close up defects, I found that adding a new growth rule was helpful, which can be called "tangent plane adhesion (TPA)." In areas where neighboring spins are misaligned, like the notch of a branch, the averaging process can encounter a near-zero pivot and effectively generate a random direction and splinter. This also happens in the 1+1D model; however, it is more pronounced in averaging the larger number of degrees of attitude freedom in 2+1D, see Ref. [260] on averaging of attitudes.

To ameliorate this, the TPA rule sets a new cell's orientation to the weighted average of the local average orientation and the orientation pointing in the nearest open direction of the local tangent plane:

$$\mathbf{q}(\vec{\boldsymbol{x}}) = A\mathbf{q}_{nn} + (1 - A)\mathbf{O}\,,$$

where $\mathbf{q}(\vec{\boldsymbol{x}})$ is the attitude (quaternion) for a new cell being deposited at site $\vec{\boldsymbol{x}}$. The measure of agreement amongst neighboring sites $A \in [0, 1]$ comes from the averaging process over nearest-neighbors, which also computes their average attitude $\mathbf{q}_{nn}$. The $\mathbf{O}$ points toward an open spot in the tangent plane. Identifying the local tangent plane can be noisy at tip locations. At cambium cells with sufficient neighboring wood, the local normal vector is accurately computed from the discrete density gradient, and the tangent plane can be defined from that normal vector. Activating this TPA rule appeared to not qualitatively change the phase diagram in Fig. 4-12, so it is turned off there. It is activated for Fig. 4-13 and has two effects: splintering is much less likely and more highly bent cells appear.

I have attempted to examine pairs of $-1/2$ defects by examining a spike growing out of a plane. However, *mounding* of wood like in the Silver Maple shown in Fig. 4-5 does not happen in this toy model. Without such mounding, the junction between the plane and stalk stays sharp and it is difficult to discern where a $-1/2$ defect is located; even if the far-field orientations imply that it is there.

Microscopic mechanisms with nematic order at microscopic scales have been observed to form polar order at larger scales through "polarity sorting" in assays of actin filaments [321], perhaps something analogous happens in wood.

Before attempting to push these models farther, it would be helpful to have more instructions from nature. Perhaps wood cells cultured in the lab can reproduce aspects of the planar shapes.

In parallel, an analytical understanding of relevant couplings might inspire a better choice of rules for an automaton.

4.2.6 Covariant Model of Surface Growth

Motivate by these simulations, I will briefly describe elements of field theory that may help understand the morphologies analytically.

The Canham-Helfrich model Eqn. 1.6 is most often expressed in a reparameterization-invariant form,[2] because the highly curved shapes of membranes require that one pay attention to the coordinates. In contrast, surface growth is often expressed in terms of a Monge height field, $h(x, y, t)$, which is not reparameterization invariant. For example, the KPZ equation is typically written,[123]

$$\dot{h} = c + \frac{\lambda}{2}(\partial h)^2 + \nu \Delta h + \eta_h + \ldots \tag{4.4}$$

This expansion in small h has been very productive for analytical study [123].

A reparameterization invariant form of the KPZ equation is:

$$\dot{\vec{\boldsymbol{X}}} = \hat{\boldsymbol{n}} \left(\lambda \sqrt{g} + \nu K^a_a + \eta + \ldots \right) , \tag{4.5}$$

where the embedding vector $\vec{\boldsymbol{X}}$ locates the surface in the laboratory frame, $\mathbb{R}^3$. To extract Eqn. 4.4 from Eqn. 4.5, one simply inserts the Monge embedding vector $\vec{\boldsymbol{X}} = (x, y, h(x, y, t)$ and expands in small h.

Shape equations of this form has been studied by several authors [158, 215, 234]. The surface normal vector $\hat{\boldsymbol{n}}$ and curvature tensor K^b_a can be computed from the embedding vector. In principle, one could include tangential flows $F^a \vec{\boldsymbol{t}}_a$ on the right-hand side of Eqn. 4.5; however, when considering only the shape of the evolving surface, such tangential flows are extraneous.

---

[2] Another name for "reparameterization invariant" is "covariant."

Examining Eqn. 4.5, let's highlight the meaning of these covariant terms. It is well known that the mean curvature $K^a_a \sim \Delta h$ is the gradient of the surface area. Given an energy proportional to the surface area, a functional derivative yields this term:

$$\mathcal{H}_A = \nu \oint_{\text{SHAPE}} \mathrm{d}A = \nu \oint_{\text{SHAPE}} \mathrm{d}\sigma^1\, \mathrm{d}\sigma^2 \sqrt{g} \implies \frac{\delta \mathcal{H}_A}{\delta \overrightarrow{\boldsymbol{X}}} = \nu K^a_a \hat{\boldsymbol{n}}\,. \tag{4.6}$$

The $\lambda\hat{\boldsymbol{n}}$ term comes from varying the *volume* enclosed by the surface, which can be written:

$$V(t) = \frac{1}{3} \oint_{\text{SHAPE}} \mathrm{d}A\, \hat{\boldsymbol{n}} \cdot \vec{X} \implies \frac{\delta V}{\delta \overrightarrow{\boldsymbol{X}}} = \frac{2}{3}\sqrt{g}\hat{\boldsymbol{n}} \tag{4.7}$$

where the surface normal, $\hat{\boldsymbol{n}}$, the embedding vector, $\vec{X}$, and the area element dA, each depend on time. In constructing such an integral, one must take care to include all of the surface that enclose the shape. See Appendix A.5 for a derivation. See also Guven 2006 for treatment of Laplace pressure using this expression.[215]

One can combine these two terms to define a "KPZ Hamiltonian,"[158]

$$\mathcal{H}_{KPZ} = \int_{\text{shape}} \mathrm{d}A \left(\frac{3\lambda}{2} \hat{\boldsymbol{n}} \cdot \overrightarrow{\boldsymbol{X}} + \nu \right) \tag{4.8}$$

$$\implies \dot{\overrightarrow{\boldsymbol{X}}} = \frac{\delta \mathcal{H}}{\delta \overrightarrow{\boldsymbol{X}}} = \hat{\boldsymbol{n}} \left(\lambda \sqrt{g} + \nu K^a_a \right)\,. \tag{4.9}$$

This is unbounded as the volume goes to infinity ($h \to \infty$), so Eqn. 4.4 does not have $\exp(\beta \mathcal{H}_{KPZ})$ as the equilibrium distribution of h.[158]

Nonetheless, using Eqn. 4.8 as a guide, we seek to include the orientation field $\overrightarrow{\boldsymbol{s}}$ in the Hamiltonian. Even in a limit where $\overrightarrow{\boldsymbol{s}}$ is constant magnitude, there are many independent scalar contractions, because there are now two special directions at each point: the surface normal $\hat{\boldsymbol{n}}$ and the spin $\overrightarrow{\boldsymbol{s}}$.

Assume that once solidified in the bulk, spins only contribute through the λV term. That means that frozen spins in the bulk influence the value of λ. At the surface, spin misalignment contributes new terms from contracting surface indices and ambient space vector indices, such as $\hat{\boldsymbol{n}} \cdot \vec{\boldsymbol{s}}$ and $\vec{t}_a \cdot \nabla^a \vec{s}$ and $\vec{\partial} \cdot (\hat{\boldsymbol{n}} \times \vec{s})$. Writing a Langevin equation of motion for $\dot{\vec{\boldsymbol{s}}}$ and $\dot{\vec{\boldsymbol{X}}}$ allows even more terms than can be obtained from a functional derivative of such an energy integral.

Decomposing surface spins into tangential and normal components at each point:

$$\vec{\boldsymbol{s}} = S^a \vec{t}_a + S^n \hat{\boldsymbol{n}} \,. \tag{4.10}$$

The tangential component is a one-tensor and the normal component is a scalar. Decompose the ambient derivative into

$$\vec{\boldsymbol{\partial}} = \vec{\boldsymbol{t}}_a \nabla^a + \hat{\boldsymbol{n}} \partial_n \,, \tag{4.11}$$

where the normal derivative $\hat{\boldsymbol{n}} \cdot \vec{\boldsymbol{\partial}}$ provides the missing piece of the ambient space gradient at each point on the surface, see Ref. [262]. These normal derivatives appear in the generalized Cole-Hopf transform solution for including a spin field in the Monge form of the KPZ evolution, see Appendix B.

To build an effective Hamiltonian or Langevin equation, there's no *a priori* reason to expect that terms like $(S^n)^2$ and $S_a S^a$ would have the *same* coupling constant even though they both appear in the magnitude of $\vec{\boldsymbol{s}} \cdot \vec{\boldsymbol{s}}$. Indeed, a glance at the elongated fibers of natural wood says that they surely contribute with different coefficients. Similarly, S^n and $-S^n$ should result in different contributions, because the inside and outside of the surface are different.

To Be Continued...

4.3 Conclusion

Why pursue a deeper understanding of these diverging and coalescing branches?

One reason is manufacturing. Additive manufacturing or 3D printing recently emerged as an alternative to traditional subtractive manufacturing. Trees build themselves *in place*. Such *in situ* manufacturing could offer a third choice. Recent efforts to create lab-grown wood are heading in this direction [318, 324]. I hope that *in-place manufacturing* will enable us to stop cutting down forests for building materials and toilet paper.

While our simulations suggest scale invariance, it is not clear whether this will persist to infinitely large trees. Real trees are limited by the weight of water in Earth's gravity [196, 267]. Perhaps a tree growing in microgravity would grow to unlimited size with a fractal dimension constant over many more scales. While photosynthesis on Earth relies on transpiration with the atmosphere, perhaps anisotropic growth could arise in other lifeforms, such as fungi that could function as chemoautotrophs elsewhere in our solar system, such as the moon [316]. Active matter has much to contribute to our progress in space [332].

If these structures represent a universality class, then it might shed light on why trees are ubiquitous on Earth. Such living solids may appear on remote exoplanets. If so, perhaps an image of a tree would be recognized in messaging to extraterrestrial intelligence [223].

Appendix A

Differential Geometry

Continuing from the brief section on differential geometry in Section 1.1, this appendix provides several derivations and tools from differential geometry. Many good references exist for understanding differential geometry of surfaces, including Refs [61, 106, 181, 188, 262, 288, 289, 320].

As discussed in Sec. 1.1, we start with an embedding vector, $\vec{\boldsymbol{X}}(\sigma^1, \sigma^2) \in \mathbb{R}^3$. That's a function of two parameters that returns a Euclidean three vector. One constructs tangent vectors by taking derivatives w.r.t. the surface paramters:

$$\vec{t}_a \equiv \frac{\partial \vec{X}}{\partial \sigma^a} \equiv \partial_a \vec{X} \equiv \vec{X}_{,a} \,,$$

The surface normal vector can be computed from the cross product of the tangent vectors.

$$\vec{\boldsymbol{n}} = \vec{\boldsymbol{t}}_1 \times \vec{\boldsymbol{t}}_2$$

A nicer arrangement uses the antisymmetric tensor ϵ^{ab}, which is a constant:

$$\vec{\boldsymbol{n}} = \frac{1}{2}\epsilon^{ab}\vec{\boldsymbol{t}}_a \times \vec{\boldsymbol{t}}_b \tag{A.1}$$

This is unnormalized. $\hat{\boldsymbol{n}} = \vec{\boldsymbol{n}}/|\vec{\boldsymbol{n}}|$.

The metric is simply $g_{ab} = \vec{\boldsymbol{t}}_a \cdot \vec{\boldsymbol{t}}_b$. The covariant derivative satisfies the requirement that $\nabla_a g_{bc} = 0$. In Sec. 1.1, we briefly explained the Christoffel symbols that enable explicit construction of ∇_a. Here, we present an intuitive motivation for the metric tensor g_{ab}.

Since we're focused on describing a surface under observation in a three-dimensional lab frame, we often have vectors in $\mathbb{R}^3$ that are *on* the surface. To represent these in terms of the surface parameters, we write:

$$\vec{\boldsymbol{v}} = v^a \vec{\boldsymbol{t}}_a + v^n \hat{\boldsymbol{n}} . \tag{A.2}$$

The one-tensor v^a is the tangential component for the surface parameters σ^a. If the vector is tangent to the surface, then the scalar field describing its component out of the tangent plane is zero, $v^n = 0$. Note that this coordinate systems functions perfectly well, even though its three basis change at every point on the surface. For example, dot products in the ambient space become:

$$\begin{aligned} \vec{\boldsymbol{v}} \cdot \vec{\boldsymbol{u}} &= \left(v^a \vec{\boldsymbol{t}}_a + v^n \hat{\boldsymbol{n}}\right) \cdot \left(u^b \vec{\boldsymbol{t}}_b + u^n \hat{\boldsymbol{n}}\right) \\ &= v^a \underbrace{\vec{\boldsymbol{t}}_a \cdot \vec{\boldsymbol{t}}_b}_{g_{ab}} u^b + v^n \hat{\boldsymbol{n}} \cdot \hat{\boldsymbol{n}} u^n \\ &= v^a g_{ab} u^b + v^n u^n . \end{aligned}$$

The metric tensor arose naturally out of representing our three-vectors in terms of the surface coordinates.

Focusing on tangent vectors, the upper- and lower-position of indices indicates whether a quantity "co"varies with the coordinates σ^a or "contra"varies with the derivatives ∂_a. To convert between the two, we can write $v_a \equiv g_{ab} v^b$ and notice that the inner product continues to hold,

$$\begin{aligned} \vec{\boldsymbol{v}} \cdot \vec{\boldsymbol{u}} &= v^a g_{ab} \overbrace{g^{bc} g_{cd}}^{\delta^b_d} u^d \\ &= v_a g^{ab} u_b . \end{aligned}$$

if we *define* the matrix inverse of the metric: $g^{ab} \equiv [g_{ab}]^{-1}$. The Kronecker delta δ_a^b is just the two-by-two identity matrix.

The three-vector gradient operator $\vec{\boldsymbol{\partial}} \equiv \hat{\boldsymbol{x}}\partial_x + \hat{\boldsymbol{y}}\partial_y + \hat{\boldsymbol{z}}\partial_z$ can be projected into the surface to obtain a covariant derivative in the surface: $\nabla_a = \vec{\boldsymbol{t}}_a \cdot \vec{\nabla}$. We can also write the ambient

$$\vec{\boldsymbol{\partial}} = \vec{\boldsymbol{t}}^a \nabla_a + \hat{\boldsymbol{t}}\partial_n \,, \tag{A.3}$$

where ∂_n is the directional derivative along the normal direction defined at each point on the surface. The directional derivative of a function is computed by contracting the regular lab gradient with the vector in that direction, e.g. $\vec{w}$. For example, consider the directional derivative of a vector valued function $\vec{\boldsymbol{s}}$:

$$\partial_{\vec{w}}\vec{s} = w^i \partial_i \vec{s}(\vec{r}) \,, \tag{A.4}$$

where the index i ranges over the Euclidean coordinates of the lab.

The covariant derivative acts on functions defined on the surface. If the function is a scalar, then the covariant derivative is simply equal to the partial derivatives w.r.t. the σ^a coordinates: $\nabla_a \phi = \partial_a \phi$. When applied to a tensor, it acquires a correction for the motion of the tangent vector, which vary from point to point.

$$\nabla_a v_b = \partial_a v_b + \Gamma^c_{ab} v_c \ ,$$

where the Γ^c_{ab} is called a Christoffel symbol.

As mentioned near Eqn. 1.3, Gauss resolved a question raised by Euler when he introduced his second fundamental form or “curvature tensor” for a two-dimensional surface. Recall that this was decades before Riemann generalized these ideas to n-dimensional manifolds.

$$K_{ab} = \hat{n} \cdot \nabla_a \vec{t}_b \,. \tag{A.5}$$

We will explore this tensor in the next section.

A.1 Gauss-Codazzi-Weingarten and Similar Identities

The basic constructions of differential geometry in the previous section imply several further identities. Many similar identities can be computed for *time varying* manifolds. See the recent texts by Grinfeld [262], and the standard text by MTW on *Gravitation*.[174] Here, we provide the simpler, constant-time identities.

The constant magnitude of the unit normal vector:

$$\begin{aligned} 1 &= \hat{\boldsymbol{n}} \cdot \hat{\boldsymbol{n}} \\ \Longrightarrow\ 0 &= \nabla_a (\hat{\boldsymbol{n}} \cdot \hat{\boldsymbol{n}}) \\ &= 2\hat{\boldsymbol{n}} \cdot \nabla_a \hat{\boldsymbol{n}}\,, \end{aligned} \tag{A.6}$$

so the gradient of the unit normal is also purely tangential.

By definition, a unit normal is orthogonal to the tangent vectors, so:

$$\begin{aligned} 0 &= \vec{t}_b \cdot \hat{\boldsymbol{n}} \\ \Longrightarrow\ 0 &= \nabla_a (\vec{t}_b \cdot \hat{\boldsymbol{n}}) \\ &= (\nabla_a \vec{t}_b) \cdot \hat{\boldsymbol{n}} + \vec{t}_b \cdot (\nabla_a \hat{\boldsymbol{n}}) \\ &= K_{ab} + \vec{t}_b \cdot (\nabla_a \hat{\boldsymbol{n}}) \\ &\Longrightarrow\ \nabla_a \hat{\boldsymbol{n}} = -K_a^b \vec{t}_b\ . \end{aligned} \tag{A.7}$$

This set of equations is called the Gauss Equations.

Additional identities can be found by computing the tangential and normal projections of two derivatives applied to $\hat{\boldsymbol{n}}$:

$$\begin{aligned}
\nabla_a \nabla_b \hat{\boldsymbol{n}} &= -\nabla_a K_b^c \vec{t}_c \\
&= -K^c_{b;a} \vec{t}_c + K_{ac} K_b^c \hat{\boldsymbol{n}} \\
\Longrightarrow \hat{\boldsymbol{n}} \cdot \nabla_a \nabla_b \hat{\boldsymbol{n}} &= K_{ac} K_b^c \\
\Longrightarrow \hat{\boldsymbol{t}}_a \cdot \nabla_b \nabla_c \hat{\boldsymbol{n}} &= K_{ab;c} \qquad \text{(A.8)}
\end{aligned}$$

A.2 Principle Two-Bein

We used the principle two-bein in Sec. 2.5. This is the two-dimensional analog of the four-bein or *vier bein* in German.

The principle two-bein defines orthonormal unit vectors in the tangent space of the surface, $\hat{\boldsymbol{e}}_i = e_i^a \overrightarrow{\boldsymbol{t}}_a$. By selecting a two-bein aligned with the principle directions of curvature, we obtain a coordinate system that diagonalizes the curvature tensor:

$$\begin{aligned}
K_{ab} &= \hat{\boldsymbol{n}} \cdot \nabla_a \vec{t}_b \\
&= \hat{\boldsymbol{n}} \cdot \nabla_a \left(e_b^i \hat{\boldsymbol{e}}_i \right) \\
&= e_b^i \left(\hat{\boldsymbol{n}} \cdot \nabla_a \hat{\boldsymbol{e}}_i \right) \\
&= \begin{pmatrix} c_1 & 0 \\ 0 & c_2 \end{pmatrix} .
\end{aligned}$$

In a two-bein, the Christoffel symbols are converted into the simpler *spin connection*, $\omega_{aij} = A_a \epsilon_{ij}$, where the angle A_a is defined by the covariant derivative of the two-index object, e_a^i:

$$\nabla_a e_{ib} = -A_a \epsilon_{ij} e_b^j \ . \qquad \text{(A.9)}$$

Any tensor expressed in the embedding coordinates, e.g. T_a, can be re-expressed in two-bein coordinates, $T_i = e_i^a T_a$, so the covariant derivative becomes:

$$\begin{aligned}\nabla_a T_b = \nabla_a T_i e_b^i &= e_b^i \nabla_a T_i + T_i \nabla_a e_b^i \\ &= e_b^i \partial_a T_i - T^i A_a \epsilon_{ij} e_b^j \\ &= \left(e_b^i \partial_a - A_a \epsilon^{ij} e_{bj} \right) T_i \ . \end{aligned} \tag{A.10}$$

A.3 Scalar Laplacian

The Laplacian for scalar functions is constructed from appling the covariant derivative twice:

$$\begin{aligned}\Delta\phi &\equiv g^{ab} \nabla_a \nabla_b \phi \\ &= g^{ab} \nabla_a \partial_b \phi \\ &= \frac{1}{\sqrt{g}} \partial_a \sqrt{g} g^{ab} \partial_b \phi \,, \end{aligned} \tag{A.11}$$

where one can verify the final line by writing $\partial_a v^b = \nabla_a v^b - \Gamma^b_{ac} v^c$. This identity can be written:

$$\frac{1}{\sqrt{g}} \partial_a \sqrt{g} g^{ab} = g^{ab} \nabla_a = \nabla_a g^{ab} \tag{A.12}$$

There is extensive mathematical literature on this Laplacian, as well as vector Laplacians and other variants. This simple definition suffices for our purposes.

A.4 Geometric Identities

Covariant derivatives do not commute. Riemann gave us

$$\begin{aligned} T_{a;[bc]} \equiv T_{a;bc} - T_{a;cb} \equiv \nabla_b \nabla_c T_a - \nabla_c \nabla_b T_a &= T_d R^d_{abc} \\ &= T_d G \left(g^d_b g_{ac} - g^d_c g_{ab} \right) \\ &= G \left(T_b g_{ac} - T_c g_{ab} \right) \,, \end{aligned} \tag{A.13}$$

where the second line is the simplified form of the Riemann tensor on a two-dimensional surface, where it has only one independent degree of freedom, which is equal to the Guassian curvature, $G = \det\{K_{ab}\} = -\frac{1}{2}\gamma_{ab}\gamma_{cd}K^{ac}K^{bd}$. Therefore,

$$\begin{aligned} g^{ab}\nabla_b \nabla_c T_a &= g^{ab} \left(\nabla_c \nabla_b T_a + T_d G (g^d_b g_{ac} - g^d_c g_{ab}) \right) \\ &= \nabla_c \nabla_a T_a + T_d G (g^d_c - g^d_c \, \mathrm{trace}(g)) \\ &= \nabla_c \nabla_a T_a - T_c G \,, \end{aligned} \tag{A.14}$$

so the contracted commutator is:

$$[\nabla_a, \nabla_b] T^a = -T_b G \,. \tag{A.15}$$

Another set of identities comes from explicitly separating the symmetric and antisymmetric parts of the commutator:

$$\begin{aligned} \nabla_a \nabla_b T_c &= \left(\frac{\nabla_a \nabla_b + \nabla_b \nabla_a}{2} + \frac{\nabla_a \nabla_b - \nabla_b \nabla_a}{2} \right) T_c \\ &= \frac{\nabla_a \nabla_b + \nabla_b \nabla_a}{2} T_c + G \frac{T_b g_{ac} - T_c g_{ab}}{2} \,. \end{aligned}$$

Contracting with an antisymmetric tensor gives:

$$\begin{aligned}\gamma^{ab}\nabla_a\nabla_b T_c &= \cancel{\gamma^{ab}\frac{\nabla_a\nabla_b + \nabla_b\nabla_a}{2}}T_c + G\frac{\gamma^{ab}T_b g_{ac} - T_c\cancel{\gamma^{ab}g_{ab}}}{2}\\ &= \frac{G}{2}T_{c\perp}\,.\end{aligned}$$

A.5 Functional Derivatives

Given a functional of the embedding vector,

$$F(\overrightarrow{\boldsymbol{X}}) = \oint_{\text{SHAPE}} \mathrm{d}A\,\mathcal{F}(\overrightarrow{\boldsymbol{X}})\,,$$

one can compute its functional derivative.

$$\begin{aligned}\frac{\delta F}{\delta\overrightarrow{\boldsymbol{X}}} &= \left(\frac{\partial}{\partial\overrightarrow{\boldsymbol{X}}} + \nabla_a\frac{\partial}{\partial(\nabla_a\overrightarrow{\boldsymbol{X}})} + \nabla_a\nabla_b\frac{\partial}{\partial(\nabla_a\nabla_b\overrightarrow{\boldsymbol{X}})} + \nabla_a\nabla_b\nabla_c\frac{\partial}{\partial(\nabla_a\nabla_b\nabla_c\overrightarrow{\boldsymbol{X}})} + \ldots\right)\mathcal{F}\\ &= \left(\frac{\partial}{\partial\overrightarrow{\boldsymbol{X}}} + \nabla_a\frac{\partial}{\partial\vec{t}_a} + \nabla_a\nabla_b\frac{\partial}{\partial(K_{ab}\hat{\boldsymbol{n}})} + \nabla_a\nabla_b\nabla_c\frac{\partial}{\partial(\nabla_a\overrightarrow{\boldsymbol{K}}_{bc})} + \ldots\right)\mathcal{F} \qquad \text{(A.16)}\end{aligned}$$

The integration in F is consumed by resolving delta functions from the partial derivatives. The second line shows the partial derivatives replaced with their symbols from differential geometry. One fruitful approach to making progress is to assume that these objects are independent of each other, and then impose their relationships via Lagrange multipliers. See Guven Ref. [193].

As an example, consider the functional derivative of the area:

$$\begin{aligned}
\frac{\delta}{\delta \overrightarrow{\boldsymbol{X}}}\mathcal{F} &= \frac{\delta}{\delta \overrightarrow{\boldsymbol{X}}}\int dA \\
&= \frac{\delta}{\delta \overrightarrow{\boldsymbol{X}}}\int d\sigma^2\sqrt{\det\{g\}} \\
&= \nabla_c \frac{\partial}{\partial \vec{t}_c}\int d\sigma^2\sqrt{\det\{[\vec{t}\cdot\vec{t}]\}} \\
&= \nabla_c \int d\sigma^2 \frac{1}{\sqrt{\det\{g\}}}\frac{1}{2}\frac{\partial}{\partial \vec{t}_c}\det\{[\vec{t}\cdot\vec{t}]\} \\
&= \nabla_c \int d\sigma^2 \frac{1}{\sqrt{\det\{g\}}}\frac{1}{2}\det\{g\}\,\mathrm{Tr}\left\{[\vec{t}\cdot\vec{t}]^{-1}\frac{\partial}{\partial \vec{t}_c}[\vec{t}\cdot\vec{t}]\right\} && \text{(A.17)} \\
&= \nabla_c \int d\sigma^2 \frac{1}{\sqrt{g}}\frac{1}{2}\,g\,g^{ab}2\delta_{ac}\vec{t}_b \\
&= \nabla_a \int dA g^{ab}\vec{t}_b \\
&= K^a_a\hat{\boldsymbol{n}} && \text{(A.18)}
\end{aligned}$$

where Eqn. A.17 uses the Jacobi's formula.

Consider a Hamiltonian that includes a bulk volume and the surface:

$$H_{\text{TOTAL}} = \underbrace{C_1\text{Volume}}_{H_{\text{BULK}}} + \underbrace{\oint_{\text{SHAPE}} dA\,\mathcal{H}_s}_{H_{\text{SURFACE}}}\,. \tag{A.19}$$

To compute the volume from an embedding vector,

$$V(t) = \frac{1}{d+1}\int_{\text{shape}} dA\,\hat{\boldsymbol{n}}\cdot\overrightarrow{\boldsymbol{X}} \tag{A.20}$$

where $d = 2$. This is a direct consequence of the divergence theorem, because $\vec{\boldsymbol{\partial}}\cdot\overrightarrow{\boldsymbol{X}} = d+1$ [215]. The surface normal, $\hat{\boldsymbol{n}}$, and the area element dA, each depend on the embedding vector, $\overrightarrow{\boldsymbol{X}}$, which may depend on time.

The unnormalized surface normal vector is:

$$\begin{aligned}
\vec{\boldsymbol{n}} &= \vec{\boldsymbol{t}}_1 \times \vec{\boldsymbol{t}}_2 = \epsilon_{klm} t_1^k t_2^l \hat{\boldsymbol{e}}^m \\
&= -\vec{\boldsymbol{t}}_2 \times \vec{\boldsymbol{t}}_1 = -\epsilon_{klm} t_2^k t_1^l \hat{\boldsymbol{e}}^m \\
\implies \vec{\boldsymbol{n}} &= \frac{\vec{\boldsymbol{t}}_1 \times \vec{\boldsymbol{t}}_2 - \vec{\boldsymbol{t}}_2 \times \vec{\boldsymbol{t}}_1}{2} \\
&= \frac{1}{2} \epsilon^{de} \epsilon_{klm} t_d^k t_e^l \hat{\boldsymbol{e}}^m
\end{aligned}$$

Here, we have used $\hat{\boldsymbol{e}}^m$ to denote the m-th component of the lab frame coordinate vectors, which are constant. The magnitude of this vector is:

$$\begin{aligned}
\sqrt{4 \vec{\boldsymbol{n}} \cdot \vec{\boldsymbol{n}}} &= \sqrt{\left(\epsilon^{ab} \epsilon_{ijk} t_a^i t_b^j \hat{\boldsymbol{e}}^k\right) \cdot \left(\epsilon^{cd} \epsilon_{pqr} t_c^p t_d^q \hat{\boldsymbol{e}}^r\right)} \\
&= \sqrt{\epsilon^{ab} \epsilon^{cd} \epsilon_{ijk} \epsilon_{pqk} t_a^i t_b^j t_c^p t_d^q} \\
&= \sqrt{\epsilon^{ab} \epsilon^{cd} \left(\delta_{ip} \delta_{jq} - \delta_{iq} \delta_{jp}\right) t_a^i t_b^j t_c^p t_d^q} \\
&= \sqrt{\epsilon^{ab} \epsilon^{cd} \left(g_{ac} g_{bd} - g_{ad} g_{bc}\right)} \\
&= \sqrt{4 \det g} \, .
\end{aligned}$$

The last line uses the formula for the determinant of an $n \times n$ matrix,

$$\det M = \frac{1}{n!} \epsilon^{ab} \epsilon^{cd} M_{ac} M_{bd} \, .$$

This yields $|\vec{\boldsymbol{n}}| = \sqrt{g}$ and therefore,

$$\hat{\boldsymbol{n}} = \frac{1}{2\sqrt{g}} \epsilon^{de} \epsilon_{klm} t_d^k t_e^l \hat{\boldsymbol{e}}^m \, . \tag{A.21}$$

The functional derivative of the bulk component is:

$$
\begin{aligned}
\frac{\delta}{\delta \vec{\boldsymbol{X}}} H_{\text{BULK}} &= \frac{C_1}{3} \oint_{\text{SHAPE}} dA \left(\frac{\partial}{\partial \vec{\boldsymbol{X}}} + \nabla_a \frac{\partial}{\partial \left(\nabla_a \vec{\boldsymbol{X}} \right)} + \nabla_a \nabla_b \frac{\partial}{\partial \left(\nabla_a \nabla_b \vec{\boldsymbol{X}} \right)} + \ldots \right) \hat{\boldsymbol{n}} \cdot \vec{\boldsymbol{X}} \\
&= \frac{C_1}{3} \oint_{\text{SHAPE}} d\sigma^2 \frac{\partial}{\partial \vec{\boldsymbol{X}}} \sqrt{g} \hat{\boldsymbol{n}} \cdot \vec{\boldsymbol{X}} + \frac{C_1}{3} \oint_{\text{SHAPE}} d\sigma^2 \nabla_a \frac{\partial}{\partial t^i_a} \sqrt{g} \overbrace{\frac{1}{2\sqrt{g}} \epsilon^{de} \epsilon_{klm} t^k_d t^l_e \hat{\boldsymbol{e}}^m}^{\hat{\boldsymbol{n}}} \cdot \vec{\boldsymbol{X}} \\
&= \frac{C_1}{3} \underbrace{\oint_{\text{SHAPE}} d\sigma^2 \sqrt{g} \hat{\boldsymbol{n}}}_{\text{=0 for a closed object}} + \frac{C_1}{3} \epsilon^{da} \hat{\boldsymbol{e}}^i \epsilon_{ilm} \nabla_a \left(t^l_d e^m_n X^n \right) \\
&= \frac{C_1}{3} \hat{\boldsymbol{e}}^i \epsilon_{ilm} \left(\cancel{\epsilon^{da} K^l_{ad}} e^m_n X^n + \epsilon^{da} t^l_d \cancel{(\nabla_a e^m_n)} X^n + \epsilon^{da} t^l_d \underbrace{e^m_n \nabla_a X^n}_{t^m_a} \right) \\
&= C_1 \frac{2}{3} \sqrt{g} \hat{\boldsymbol{n}} \, . \qquad \text{(A.22)}
\end{aligned}
$$

As noted in Ref. [158], this Hamiltonian is unbounded as the volume goes to infinity ($h \to \infty$), so $\exp(\beta \mathcal{H}_{KPZ})$ does not describe an equilibrium distribution.

Appendix B

Note on Cole-Hopf Solutions to the KPZ Equation

As pointed out by Kardar, Parisi, and Zhang in 1986, Ref. [123], the KPZ equation can be linearized by a Cole-Hopf transformation, and the resulting diffusion equation can be solved in the deterministic limit by the diffusion kernel solution:

$$\begin{aligned}
W &= \exp\left[\frac{\lambda h\left(\vec{\boldsymbol{x}},t\right)}{2\nu}\right] \\
\dot{W} &= \nu\Delta W + \frac{\lambda}{2\nu}\eta \\
\frac{\lambda\dot{h}}{2\nu}W &= \nu\partial_i\frac{\lambda h_{,i}}{2\nu}W + \frac{\lambda}{2\nu}\eta \\
\frac{\lambda\dot{h}}{2\nu}W &= \nu\frac{\lambda h_{,ii}}{2\nu}W + \nu\left(\frac{\lambda h_{,i}}{2\nu}\right)^2 W + \frac{\lambda}{2\nu}\eta\,,
\end{aligned} \tag{B.1}$$

which is Eqn. 4.4 after dividing through by the common factor. In the deterministic limit, i.e., without the noise, Eqn. B.1 can be solved from an arbitrary initial condition using the diffusion kernel:

$$\begin{aligned}
W(\vec{\boldsymbol{x}},t) &= A\left(\vec{\boldsymbol{x}},t\right)\exp\left[\frac{\lambda h(\vec{\boldsymbol{x}},t)}{2\nu}\right] \\
&= \int\frac{d^d\vec{\boldsymbol{x}}'}{(4\pi\nu t)^{d/2}}A\left(\vec{\boldsymbol{x}}',t=0\right)\exp\overbrace{\left[-\frac{(\vec{\boldsymbol{x}}-\vec{\boldsymbol{x}}')^2}{4\nu t}+\frac{\lambda h(\vec{\boldsymbol{x}}',t=0)}{2\nu}\right]}^{-\Phi(\vec{\boldsymbol{x}},\vec{\boldsymbol{x}}',h(\vec{\boldsymbol{x}}',0))},
\end{aligned} \tag{B.2}$$

where we've defined Φ as the argument to the exponential and included an arbitrary additional field $A\left(\vec{\boldsymbol{x}},t\right)$ in the diffusion kernel to show that it does not contribute to the derivatives in time and space:

$$\begin{aligned}
\dot{W} &= -\frac{d}{2}\frac{W}{t} + \int \frac{d^d\vec{\boldsymbol{x}}'}{(4\pi\nu t)^{d/2}} A\left(\vec{\boldsymbol{x}}',0\right) \frac{(\vec{\boldsymbol{x}}-\vec{\boldsymbol{x}}')^2}{4\nu t^2} e^{-\Phi} \\
\partial_i W &= \int \frac{d^d\vec{\boldsymbol{x}}'}{(4\pi\nu t)^{d/2}} A\left(\vec{\boldsymbol{x}}',0\right) \frac{-(x_i - x_i')}{2\nu t} e^{-\Phi} \\
\implies \partial_i\partial_i W &= \int \frac{d^d\vec{\boldsymbol{x}}'}{(4\pi\nu t)^{d/2}} A\left(\vec{\boldsymbol{x}}',0\right) \left(-\frac{d}{2\nu t} + \frac{\left(\vec{\boldsymbol{x}}-\vec{\boldsymbol{x}}'\right)^2}{4\nu^2 t^2}\right) e^{-\Phi} \\
&= -d\frac{W}{2\nu t} + \frac{1}{\nu}\int \frac{d^d\vec{\boldsymbol{x}}'}{(4\pi\nu t)^{d/2}} A\left(\vec{\boldsymbol{x}}',0\right) \frac{\left(\vec{\boldsymbol{x}}-\vec{\boldsymbol{x}}'\right)^2}{4\nu t^2} e^{-\Phi}\,, \qquad \text{(B.3)}
\end{aligned}$$

and therefore even with the arbitrary additional field, Eqn. B.2 is still a solution to Eqn. B.1 without noise. In fact, the additional field $A\left(\vec{\boldsymbol{x}},t\right)$ could be a vector or tensor. To see the long time behavior of this solution, note that $e^{-\Phi}$ is strongly peaked if ν is small, so we can estimate W using the saddle point approximation. When ν is small enough, the maximum value of the integrand can be estimated:

$$\max_{\vec{\boldsymbol{x}}'} A\left(\vec{\boldsymbol{x}}',0\right) e^{-\Phi(\vec{\boldsymbol{x}}')} \approx A\left(\vec{\boldsymbol{x}}',0\right) e^{-\Phi(\vec{\boldsymbol{x}}')}\Big|_{\min_{\vec{\boldsymbol{x}}'}\Phi}\,, \qquad \text{(B.4)}$$

and these minima of Φ occur at maxima in the initial height profile, $h(\vec{\boldsymbol{x}}_0,0)$, which occur at the peaks of initial mounds, which we denote $\{\vec{\boldsymbol{x}}_0\}$. Note that in this limit of slow enough diffusion, the additional field A does not influence the height. Under these evolution equations, the value of the auxiliary field at later times is approximately fixed by the values of the auxiliary at $t = 0$,

$$A(\vec{\boldsymbol{x}},t) \approx A(\vec{\boldsymbol{x}}_0,0)\,, \qquad \text{(B.5)}$$

so the height field controls the long time behavior of the additional field by spreading its value at the peaks in the height profile toward neighboring points. This suggests that adjacent regions will compete and eventually the higher region will overtake the lower region, stochastically. Our ARSOS simulations do not capture this movement of the domain walls, even at low coupling.

As pointed out by Kardar in Ref. [173], the amplitude in W could be a texture on the surface, which we denote by a vector field of "spins" $\vec{\boldsymbol{s}}$ here:

$$\vec{\boldsymbol{W}} = \vec{\boldsymbol{s}}(\vec{\boldsymbol{x}},t)\exp\left[\frac{\lambda h}{2\nu}\right] \tag{B.6}$$

We will set $|\vec{\boldsymbol{s}}| = 1$ below in order to regain the KPZ equation and an additional equation for the spins.

$$\partial_t \vec{\boldsymbol{W}} = \nu\Delta\vec{\boldsymbol{W}} + \frac{\lambda}{2\nu}\eta_h \vec{\boldsymbol{W}} \tag{B.7}$$

$$\begin{gathered}
\partial_t \exp\left[\frac{\lambda h}{2\nu}\right]\vec{\boldsymbol{s}} = \nu\Delta\exp\left[\frac{\lambda h}{2\nu}\right]\vec{\boldsymbol{s}} + \frac{\lambda}{2\nu}\eta_h \exp\left[\frac{\lambda h}{2\nu}\right]\vec{\boldsymbol{s}} \\
\frac{\lambda\partial_t h}{2\nu}\vec{\boldsymbol{W}} + \exp\left[\frac{\lambda h}{2\nu}\right]\partial_t \vec{\boldsymbol{s}} = \\
\nu\left(\frac{\lambda\Delta h}{2\nu}\vec{\boldsymbol{W}} + \frac{\lambda\partial_i h}{2\nu}\frac{\lambda\partial_i h}{2\nu}\vec{\boldsymbol{W}} + \exp\left[\frac{\lambda h}{2\nu}\right](\partial_i h)(\partial_i \vec{\boldsymbol{s}}) + \exp\left[\frac{\lambda h}{2\nu}\right]\Delta\vec{\boldsymbol{s}}\right) + \frac{\lambda}{2\nu}\eta_h \vec{\boldsymbol{W}}
\end{gathered} \tag{B.8}$$

The unit vector constraint means that any single derivative of $\vec{\boldsymbol{s}}$ is orthogonal to $\vec{\boldsymbol{s}}$:

$$1 = s^2 \implies 0 = \vec{\boldsymbol{s}} \cdot \partial\vec{\boldsymbol{s}} \tag{B.9}$$

Dotting Eqn. B.8 with $\vec{\boldsymbol{s}}$ and dividing through by the common factor yields:

$$\partial_t h = \nu\Delta h + \frac{\lambda}{2}(\partial_i h)^2 + \frac{2\nu^2}{\lambda}s_i\Delta s_i + \eta_h\,. \tag{B.10}$$

Multiplying Eqn. B.10 by $\vec{\boldsymbol{W}}\lambda/2\nu$ and subtracting it from Eqn. B.8 yields:

$$\partial_t \vec{\boldsymbol{s}} = \nu\left(\Delta\vec{\boldsymbol{s}} - \vec{\boldsymbol{s}}\left(s_i\Delta s_i\right)\right) + \lambda(\partial_i h)(\partial_i \vec{\boldsymbol{s}}) \tag{B.11}$$

This equation of motion for the spins is convenient in that it preserves the length of $\vec{\boldsymbol{s}}$ at unity. The new term is a directional derivative of $\vec{\boldsymbol{s}}$ in the direction of the surface gradient,

$$\vec{\boldsymbol{\partial}} h = \begin{pmatrix} h_{,x} \\ h_{,y} \\ 0 \end{pmatrix} \approx \hat{z} - \hat{n}\sqrt{g}\,. \tag{B.12}$$

At first, such a term appears to treat "up" as a special direction, because $\hat{z} - \sqrt{g}\hat{n}$ is not reparameterization invariant. However, this problem is resolved when one writes the spin function in the same surface coordinates.

In the Monge representation, the surface coordinates are the coordinates of the Cartesian plane, (x, y), and therefore $\vec{\boldsymbol{s}} = \vec{\boldsymbol{s}}(x, y, t)$ and $\partial_z \vec{\boldsymbol{s}} = 0$ by construction. Using this, the new term in Eqn. B.11 becomes,

$$\begin{aligned} (\partial_i h)(\partial_i \vec{\boldsymbol{s}}) &= \hat{z}\cancel{\partial_z \vec{\boldsymbol{s}}} - \left(\sqrt{g}\hat{n}\right)_a \partial_a \vec{\boldsymbol{s}} \\ &= -\left(\sqrt{g}\hat{n}\right)_a \partial_a \vec{\boldsymbol{s}} \\ &= -\sqrt{g}\partial_{\hat{n}} \vec{\boldsymbol{s}} \\ &\approx \partial_{\hat{n}} \vec{\boldsymbol{s}}\,, \end{aligned} \tag{B.13}$$

i.e. a directional derivative of the spins along the surface normal, which *is* reparameterization invariant. This foreshadows other terms that could be relevant in general evolution equations for spins on a growing surface, such as $\hat{\boldsymbol{n}} \cdot \vec{\boldsymbol{s}}$ and $\vec{\boldsymbol{K}}^{a}_{a} \cdot \vec{\boldsymbol{s}}$.

Appendix C

Discussion of OPT in non-flat coordinates

In the introduction to Chapter 3, I briefly explained that conformal coordinates avoid a challenge that one encounters when applying perturbation theory to curved diffusion problems using lab frame coordinates as surface parameters. This appendix provides more detail on that challenge.

In Chap. 3, we use $\Omega \equiv {}^{\mathrm{C}}\Omega$ to refer to the conformal scale factor. It's important to note that ${}^{\mathrm{A}}\Omega$ means something similar and importantly different. ${}^{\mathrm{A}}\Omega$ is the ratio of volume elements between the deformed and undeformed shapes *in same surface parameters.*

In Chap. 3, we use the operator perturbation theory (OPT) developed by Lord Rayleigh for sound waves[55] and further developed by Schrödinger for quantum mechanics. In Appendix D, we recite the standard development of OPT with Euclidean support, which we use in Sec. 3.3.1.3. OPT is widely used for modeling interactions as a simple part plus small corrections:

$$\dot{\Phi} = H_{\text{COMPLICATED}}(\Phi) = H_{\text{SIMPLE}}(\Phi) + \epsilon V(\Phi) + \mathcal{O}(\epsilon^2)$$

Φ is usually an experimentally accessible quantity of interest, such as the probability amplitude in quantum mechanics.

One chooses the simple part H_{SIMPLE} to have nice eigenfunctions, such as the Laplacian in Euclidean coordinates with its sine and cosine eigenfunctions, e.g. $\phi_k^{(0)} = \cos(k\theta)$. Then, one can use these eigenfunctions as a function *basis* for representing Φ. Further, one can propose that Φ also has a simple part plus corrections:

$$\Phi = \sum_k C_k^{(0)} \phi_k^{(0)} + \epsilon \sum_k C_k^{(1)} \phi^{(1)} + \epsilon^2 \sum_k C_k^{(2)} \phi^{(2)} + \dots .$$

The crucial insight made by John William Strutt, 3rd Baron Rayleigh, was that one can seek a solution for the corrections in terms of the *lower* order terms. That is, one can compute $\phi^{(1)}$ in terms of $\phi^{(0)}$, and generally $\phi^{(n+1)}$ using only $\phi^{(n)}$ and lower terms. These recursion relations allow a controlled perturbation expansion.

The crucial step of computing the coefficients $C_k^{(n)}$ involves an computing an inner product in the function space spanned by the basis functions $\phi_k^{(0)}$. The usual inner product of two functions is an integral over the volume. Using Dirac's bra-ket notation, this integral is:

$$\langle j | k \rangle = \int_{\mathcal{M}} dV \phi_j^*(\sigma) \phi_k(\sigma) ,$$

where $\mathcal{M}$ denotes the supporting space and dV is the volume element of $\mathcal{M}$. Appendix D summarizes OPT when the supporting space is familiar Euclidean space, i.e. $\mathcal{M} = \mathbb{R}^d$. However, $\mathcal{M}$ could be more general, such as a Riemannian manifold.

If the manifold $\mathcal{M}$ supporting the Hilbert space is Riemannian rather than Euclidean, then the integration measure changes from $dV = d^d x$ to $dV = \sqrt{g} d^d \sigma$, where g is the determinant of the manifold's metric g_{ab} and σ^a are local coordinates. See Appendix A for explanation of the metric tensor. This new volume element modifies the inner product, and therefore also matrix elements of operators and orthogonality of eigenfunctions, like Eqn. D.2.

Here, we will mostly stay in two dimensions, so the "volume" element is the area element, dA:

$$\text{area} = \int \underbrace{\mathrm{d}\sigma^1\,\mathrm{d}\sigma^2\,\sqrt{\det g}}_{dA}\ .$$

Next, consider a modification to the surface that changes the embedding vector by a small amount $\vec{\boldsymbol{X}}(0) \longrightarrow \vec{\boldsymbol{X}}(\epsilon)$, where ϵ is a small parameter that we will use extensively for bookkeeping.

Essential Point: Any quantity defined on the modified shape can be written in terms of its counterpart on the original shape plus small corrections proportional to ϵ, ϵ^2, ...

This new surface located by $\vec{\boldsymbol{X}}(\epsilon)$ will have a metric that we denote by G_{ab}. If the modification is small enough, then the surface parameters σ^a will continue to cover the new manifold. We assume that the perturbation is such that the same coordinate charts continue to parameterize the perturbed manifold, so the σ^a *do not change*. For example, cylindrical coordinates $\sigma^a = (\phi, z)$ continue to describe a rippled cylinder unless the deformation becomes so unruly as to make the surface no longer a single-valued function of those coordinates.

In the following, we define tensors only on the original manifold, so for raising/lowering indices, we only ever use the original manifold's metric, $g^{(0)}_{ab}$, and its matrix inverse, called the inverse metric, $g^{ab(0)} \equiv [g_{ab}]$.

Since the coordinate charts do not change, the Hilbert space of functions remains valid and the basis functions $\left\{\phi^{(0)}_k\right\}$ are still a basis on the modified surface. Before considering changes to the spectrum of any particular operator, we consider corrections to the basis functions, which we write $\phi^{(n)}_k$. Here, we will make use of Dirac's bra-ket notation from quantum mechanics, which allows us to refer to the abstract eigenfunction $|k\rangle$ without reference to a particular set of physical coordinates. The projection of $|k\rangle$ on to specific coordinates is written $\phi_k \equiv \langle\sigma^a|k\rangle \equiv \phi_k(\sigma^a)$.

This notation makes it easy to write the matrix elements of an operator as a bra-ket. The simplest example is a bra-ket of 1, which is just the overlap of eigenfunctions.

This is easily computed by inserting a resolution of the identity, $1 = \int dA \left|\sigma^a\right\rangle \left\langle\sigma^a\right|$,

$$\left\langle j^{(0)} \middle| 1 \middle| k^{(0)} \right\rangle^{(0)} = \int dA^{(0)} \left\langle j^{(0)} \middle| \sigma^a \right\rangle \left\langle \sigma^a \middle| k^{(0)} \right\rangle \tag{C.1}$$

$$= \int d\sigma \sqrt{g}\, \phi_j^{(0)*} \phi_k^{(0)} \tag{C.2}$$

$$= \delta_{jk}\,. \tag{C.3}$$

The superscript (0) means *un*perturbed manifold. The Kronecker delta, δ_{jk}, is zero or one for normalized eigenfunctions. We need not raise/lower the indices on this Kronecker delta, because they are eigenvalue labels – not labels for the coordinates on the curved surface.

Superscript numbers in parenthesis, (n), indicate quantities proportional to ϵ^n. The unperturbed metric is $g_{ab}^{(0)}$ and corrections to it are written $g_{ab}^{(n)}$. The metric G_{ab} is the fully modified metric, i.e. sum of all $g_{ab}^{(n)}$ including $n = 0$. For simplicity, we sometimes drop the (0) on the unperturbed metric, $g_{ab} \equiv g_{ab}^{(0)}$, and also on its covariant derivative $\nabla_a \equiv \nabla_a^{(0)}$. Any other quantity written without a superscript (n) means the object on the fully modified manifold, i.e. the sum of all corrections including $n = 0$. For clarity, when we mean covariant derivatives for the perturbed metric, we will write a superscript G, like ∇_a^G or Δ^G

The framework of Rayleigh-Schrödinger perturbation theory constructs an ansatz for each perturbed quantity in terms of unperturbed quantities, see Appendix D. Specifically, the ansatz for the fully perturbed basis function $|k\rangle$ is written as a superposition of *un*perturbed basis functions, $|j^{(0)}\rangle$:

$$|k\rangle = \sum_{n=0}^{\infty} \left|k^{(n)}\right\rangle$$

$$= \sum_{n=0}^{\infty} \sum_j \left|j^{(0)}\right\rangle \underbrace{\left\langle j^{(0)} \middle| k^{(n)} \right\rangle}_{\equiv c_{jk}^{(n)}}\,. \tag{C.4}$$

The second line inserts a partition of unity $1 = \sum_j |j^{(0)}\rangle\langle j^{(0)}|$.

Projecting these onto particular coordinates:

$$\phi_k = \sum_{n=0}^{\infty} \sum_j \phi_j^{(0)} c_{jk}^{(n)} \,, \tag{C.5}$$

where the coefficients, $c_{jk}^{(n)}$, are computed from overlapping the n-th order correction with the unperturbed basis functions. This is an integration over the *un*perturbed manifold:

$$\begin{aligned} c_{jk}^{(n)} &\equiv \left\langle j^{(0)} \middle| k^{(n)} \right\rangle \\ &= \int dA^{(0)} \phi_j^{(0)*} \phi_k^{(n)} \,. \end{aligned} \tag{C.6}$$

Each object with a superscript (1) is carrying an ϵ^1, and (2) carries ϵ^2, etc. Lord Rayleigh's insight was that n-order correction $\phi_k^{(n)}$ in Eqn. C.6 could be constructed inductively through recursion relations that build the nth order correction from the $(n-1)$th order corrections; see Appendix D for details.

In a moment, we will find that a modification to the shape can rescale the basis functions, i.e. have non-zero $c_{kk}^{(n)}$, even at first order. To see this, we will use the perturbative ansatz to expand the orthogonality relation for basis vectors on the perturbed manifold. This can be compared to the Euclidean analog in Eqn. D.13:

$$\begin{aligned} \delta_{jk} = \langle j|k\rangle &= \int dA\, \phi_j^* \phi_k \\ &= \int dA \left(\mathop{\sum\!\!\!\!\!\!\!\int}_{j'} \left(\delta_{j'j} + c_{j'j}^{(1)*} + \ldots \right) \phi_{j'}^{(0)*} \right) \left(\mathop{\sum\!\!\!\!\!\!\!\int}_{k'} \left(\delta_{k'k} + c_{k'k}^{(1)} + \ldots \right) \phi_{k'}^{(0)*} \right) \\ &= \mathop{\sum\!\!\!\!\!\!\!\int}_{j'k'} \left(\delta_{j'j} + c_{j'j}^{(1)*} + \ldots \right) \left(\delta_{k'k} + c_{k'k}^{(1)} + \ldots \right) \int dA \phi_{j'}^{(0)*} \phi_{k'}^{(0)*} \left(1 + \left(\sqrt{\frac{G}{g}} \right)^{(1)} + \ldots \right) \\ &= \mathop{\sum\!\!\!\!\!\!\!\int}_{j'k'} \left(\delta_{j'j} + c_{j'j}^{(1)*} + \ldots \right) \left(\delta_{k'k} + c_{k'k}^{(1)} + \ldots \right) \left(\delta_{j'k'} + {}^{\mathrm{A}}\Omega_{j'k'}^{(1)} + \ldots \right) , \end{aligned} \tag{C.7}$$

where the $\sum\!\!\!\!\!\!\!\int$ symbol indicates that the labels of the basis functions could be partially discrete and partially continuous. In the following, we will usually suppress this notation. Any repeated primed index, like j' or k', implies summation and/or integration.

We defined the ratio of volume measures:

$$
{}^{\mathrm{A}}\Omega \equiv \sqrt{\frac{dV(\epsilon)}{dV(0)}} = \sqrt{\frac{G}{g}}\,. \tag{C.8}
$$

Its matrix elements at a given order are:

$$
\begin{aligned}
{}^{\mathrm{A}}\Omega^{(n)}_{jk} &\equiv \left\langle j^{(0)} \middle| \left(\sqrt{\frac{G}{g^{(0)}}}\right)^{(n)} \middle| k^{(0)} \right\rangle^{(0)} \\
&= \int d\sigma \sqrt{g}\, \phi^{(0)*}_{j} \left(\sqrt{\frac{G}{g^{(0)}}}\right)^{(n)} \phi^{(0)}_{k} \\
&= \int d\sigma\, \phi^{(0)*}_{j} \left(\sqrt{G}\right)^{(n)} \phi^{(0)}_{k}\,.
\end{aligned} \tag{C.9}
$$

Note the cancellation of unperturbed $\sqrt{g}$ on the penultimate line. These integrals are often straightforward to compute.

In Eqn. C.7, each order in ϵ must equal zero independently,

$$
\begin{aligned}
\delta_{jk} =& \epsilon^{0}\delta_{jk} + \underbrace{\left(c^{(1)*}_{kj} + c^{(1)}_{jk} + {}^{\mathrm{A}}\Omega^{(1)}_{jk}\right)}_{\sim\epsilon^{1}} \\
&+ \underbrace{\left(c^{(2)*}_{kj} + c^{(2)}_{jk} + {}^{\mathrm{A}}\Omega^{(2)}_{jk} + c^{(1)*}_{j'j}\, c^{(1)}_{j'k} + c^{(1)*}_{k'k}\, {}^{\mathrm{A}}\Omega^{(1)}_{jk'} + c^{(1)}_{j'j}\, {}^{\mathrm{A}}\Omega^{(1)}_{j'k}\right)}_{\sim\epsilon^{2}} + \ldots \\
&+ \sum_{m_1+m_2+m_3=n} \underbrace{c^{(m_1)*}_{j'j}\, c^{(m_2)}_{k'k}\, {}^{\mathrm{A}}\Omega^{(m_3)}_{j'k'}}_{\sim\epsilon^{n}} + \ldots\,.
\end{aligned} \tag{C.10}
$$

Note that repeated primed indices implies summation, e.g. over j'. Each order of $0 < N$ must equal zero independently, which leads to useful simplifications below. In computing these terms, one must remember that $c^{(0)}_{jk} = \delta_{jk} = {}^{\mathrm{A}}\Omega^{(0)}_{jk}$.

Thus, changing the shape can rescale the eigenfunctions. This should be expected, because volume changes in Euclidean space also rescale the eigenfunctions.

$$
\mathrm{Re}\left(c^{(1)}_{kk}\right) = -\frac{1}{2}\, {}^{\mathrm{A}}\Omega^{(1)}_{kk}\,. \tag{C.11}
$$

This does not specify the imaginary part, so we can choose it to be zero as an arbitrary phase factor. These rescalings would affect any orthonormal function basis, regardless of whether it was associated with a particular normal operator. Note that this is in contrast to regular quantum mechanics with Euclidean support, where one can always arrange the corrections such that $c^{(1)}_{kk} = 0$.

The general term from Eqn. C.10 can be rearranged:

$$0 = \underbrace{c^{(n)*}_{kj} + \sum_{m=1}^{n-1} c^{(n-m)*}_{j'j} c^{(m)}_{j'k} + c^{(n)}_{jk}}_{\text{familiar from quantum mechanics}} + \underbrace{\sum_{m_1=1}^{n} {}^{\mathrm{A}}\Omega^{(m_1)}_{j'k'} \sum_{m_2=0}^{n-m_1} c^{(n-m_1-m_2)*}_{j'j} c^{(m_2)}_{k'k}}_{\text{from modifying geometry}} \tag{C.12}$$

The Laplacian for the *perturbed* manifold is easily seen to be Hermitian. The Laplacian on the new manifold located by $\vec{\boldsymbol{X}}(\epsilon)$ with metric G_{ab} is

$$\Delta^G = \frac{1}{\sqrt{G}} \partial_a \sqrt{G} \rotatebox[origin=c]{180}{G}^{ab} \partial_b \,,$$

where we have defined the upside-down G symbol, $\rotatebox[origin=c]{180}{$G^{ab}, to be the *matrix inverse* of the new shape's metric tensor, G_{ab}:

$$\rotatebox[origin=c]{180}{G}^{ab} \equiv \left[G_{ab}\right]^{-1} \tag{C.13}$$

Recall that we define tensors only on the unperturbed manifold, so $\rotatebox[origin=c]{180}{$G^{ab} is not the same as $g^{ac} G_{cd} g^{db} \neq \rotatebox[origin=c]{180}{$G^{ab}. (Recall that $g_{ab} \equiv g^{(0)}_{ab}$.) See appendix for how to construct this representation of the scalar Laplacian, Sec. A.3. We will focus on the *scalar* Laplacian. The Laplacian operator for higher rank tensors, such as the *vector* Laplacian, is a separate subject, see for example Ref. [284].

Its matrix elements are computed via a bra-ket on the perturbed manifold:

$$\begin{aligned} \left\langle \Delta^G \right\rangle^G_{jk} &= \int dV(\epsilon) \phi^{(0)*}_j \rotatebox[origin=c]{180}{G}^{ab} \nabla_a \partial_b \phi^{(0)}_k \\ &\doteq -\int dV(\epsilon) \left(\partial_a \phi^{(0)*}_j\right) \rotatebox[origin=c]{180}{G}^{ab} \left(\partial_b \phi^{(0)}_k\right) \,, \end{aligned} \tag{C.14}$$

where the overdot on the equals symbol indicates an integration by parts in which we dropped the boundary term and used the defining property of the covariant derivative: $\nabla^G_a \sqrt{G} = 0$. The last line is manifestly equal to its transpose conjugate. However, this same operator integrated over the *un*perturbed manifold is not guaranteed to be Hermitian:

$$\begin{aligned}
\left\langle \Delta^G \right\rangle^{(0)}_{jk} &= \int dV^{(0)} \phi^{(0)*}_j ⅁^{ab} \nabla^G_a \partial_b \phi^{(0)}_k \\
&\doteq -\int d\sigma \left(\nabla^G_a \sqrt{g^{(0)}} \phi^{(0)*}_j \right) ⅁^{ab} \left(\partial_b \phi^{(0)}_k \right) ,
\end{aligned}$$

which is not equal to its transpose conjugate unless $\nabla^G_a \sqrt{g^{(0)}}$ just happens to equal zero. Note that we're being careful to distinguish between the covariant derivatives on the perturbed and unperturbed manifolds, which we denote ∇^G_a and $\nabla_a \equiv \nabla^g_a$, respectively.

Rescaling the Laplacian by ${}^{\mathrm{A}}\Omega$ fixes this:

$$\begin{aligned}
\left\langle {}^{\mathrm{A}}\Omega \Delta^G \right\rangle^{(0)}_{jk} &= \int \underbrace{d\sigma \sqrt{g^{(0)}}}_{dV^{(0)}} \phi^{(0)*}_j \underbrace{\sqrt{\frac{G}{g^{(0)}}}}_{{}^{\mathrm{A}}\Omega} \underbrace{\frac{1}{\sqrt{G}} \partial_a \sqrt{G} ⅁^{ab} \partial_b}_{\hat{\Delta}} \phi^{(0)}_k \\
&= \int d\sigma \phi^{(0)*}_j \partial_a \sqrt{G} ⅁^{ab} \partial_b \phi^{(0)}_k \\
&\doteq -\int d\sigma \left(\partial_a \phi^{(0)*}_j \right) \sqrt{G} ⅁^{ab} \left(\partial_b \phi^{(0)}_k \right) . \qquad \text{(C.15)}
\end{aligned}$$

which is the same as Eqn. C.14 and manifestly self-adjoint.

If the perturbation leaves the volume measure unchanged, then the volume measure is simply carried through all the calculations of Sec. D, and Eqns. D.17 remain valid with the implicit change that the matrix elements, $H^{(n)}_{jk}$, now depend on the more nuanced volume measure of the manifold instead of Euclidean space. Similarly, other relations derived for Euclidean space would remain unchanged.

However, if the perturbation changes the volume measure, then it must be expanded in our bookkeeping parameter, ϵ,

$$dV(\epsilon) \equiv d\sigma \sqrt{G} = dV^{(0)} \sqrt{\frac{G}{g^{(0)}}} = dV^{(0)} \, {}^{\mathrm{A}}\Omega(\epsilon) ,$$

as we defined earlier.

For any surface, the scalar Laplacian's eigenfunctions, $\phi_k(\sigma^1, \sigma^2)$, are defined by

$$\Delta\phi_k = \lambda_k\phi_k\,, \tag{C.16}$$

where λ_k is the eigenvalue labeled by parameter k, which represents a collection of parameters, one for each spatial dimension. When the space is compact, these parameters are discrete and can be enumerated by the integers. When the space is non-compact, these parameters are real valued. The compact case is generally more physically relevant. While the Laplacian is less well-understood in non-compact spaces, it can be a useful abstraction. The Laplacian's eigenvalues are always negative real numbers. While the plane waves $\phi_k = e^{i\vec{\boldsymbol{k}}\cdot\vec{\boldsymbol{x}}}$ are most familiar, this is true for *any* surface, even when the eigenfunctions are not known in closed form.

We can rewrite Δ^G in terms of Δ^g plus corrections:

$$\Delta^G = \underbrace{\frac{1}{\sqrt{g}\,{}^{\mathrm{A}}\Omega}}_{=\sqrt{G}}\partial_a \overbrace{\sqrt{g}\left(g^{ab} - T^{ab}\right)}^{\sqrt{G}\Game^{ab}}\partial_b = \frac{1}{{}^{\mathrm{A}}\Omega}\left(\Delta^g - \nabla_a T^{ab}\partial_b\right)\,. \tag{C.17}$$

Here, we have used Eqn. A.12 and defined the "one-tensor product correction":

$$T^{ab} = -\left({}^{\mathrm{A}}\Omega\Game^{ab} - g^{ab}\right)\,. \tag{C.18}$$

This construction has two useful properties: first, each term is manifestly self-adjoint. Less useful arrangements lead to terms with matrix elements in the basis of the unperturbed Laplacians eigenfunctions that are not equal to their transpose conjugate. Second, the objects T^{ab} and ${}^{\mathrm{A}}\Omega$ are easily calculated. The ratio of volume measures, ${}^{\mathrm{A}}\Omega$, is equal to one plus corrections at each order in ϵ. The one-tensor product product correction, T^{ab}, is only perturbative, starting at ϵ^1. Using this expression for the Laplacian, we wish to write its eigenvalues and eigenfunctions in terms of their counterparts on the original manifold plus small corrections proportional to ϵ, ϵ^2, ...

Note that T^{ab} has broader applicability than just the Laplacian. Consider one-tensor fields on the manifold. Denote two such fields as S_a and V_a. The inner product of these fields is $\text{Ɗ}^{ab} S_a V_b$. When integrated over the entire manifold, this is:

$$F = \int dA \, \text{Ɗ}^{ab} S_a V_b = \int d\sigma \sqrt{G} \text{Ɗ}^{ab} S_a V_b \, .$$

The difference between this quantity on the perturbed and unperturbed manifold is:

$$F - F^{(0)} = \int d\sigma \overbrace{\left(\sqrt{G} \text{Ɗ}^{ab} - \sqrt{g} g^{ab} \right)}^{-\sqrt{g} T^{ab}} S_a V_b \, . \tag{C.19}$$

In the following, we focus on the Laplacian.

To compute corrections to the Laplacian's spectrum of eigenvalues, we write the new eigenvalue equation analogous to Eqn. C.16 for Δ^G from Eqn. C.17:

$$\lambda_k \phi_k = \Delta^G \phi_k = \frac{1}{{}^{\mathrm{A}}\Omega} \left(\Delta^g - \nabla_a T^{ab} \partial_b \right) \phi_k \, . \tag{C.20}$$

To proceed, move ${}^{\mathrm{A}}\Omega$ to the left side, multiply from the left with an arbitrary basis function $\phi_j^{(0)}$, and integrate over the entire *un*perturbed manifold:

$$0 = \int dA^{(0)} \phi_j^{(0)^*} \left(\Delta^g - \nabla_a T^{ab} \partial_b - \lambda_k \, {}^{\mathrm{A}}\Omega \right) \phi_k \, . \tag{C.21}$$

Next, we apply the framework of Rayleigh-Schrödinger perturbation theory by constructing ansätze according to the standard pattern for each perturbed quantity, λ_k, T^{ab}, ${}^{\mathrm{A}}\Omega$, see Appendix D. For example,

$${}^{\mathrm{A}}\Omega = 1 + {}^{\mathrm{A}}\Omega^{(1)} + {}^{\mathrm{A}}\Omega^{(2)} + {}^{\mathrm{A}}\Omega^{(3)} + \dots \, ,$$

where ${}^{\mathrm{A}}\Omega^{(n)} \propto \epsilon^n$. Grouping expanded terms of Eqn. C.21 order by order in ϵ, each collection of nth-order terms proportional to ϵ^n must cancel independently.

Since the coordinate charts have not changed in Eqn. C.21, we can replace the wavefunctions with Eqn. C.5 and integrate by parts in the second term to obtain:

$$\begin{aligned}0 &= \int dA\phi_j^{(0)*}\left(\Delta^g - \nabla_a T^{ab}\partial_b - \lambda_k\, {}^{\mathrm{A}}\Omega\right)\overbrace{\left(\sum_{n=0}^{\infty}\sum_{j'} c_{j'k}^{(n_2)}\phi_{j'}^{(0)}\right)}^{\langle\vec{\boldsymbol{r}}|k\rangle} \\ &= \sum_{j'}\sum_{n=0}^{\infty}\underbrace{c_{j'k}^{(n_2)}}_{\sim\epsilon^n}\left(\underbrace{\lambda_{j'}^{(0)}\delta_{jj'}}_{\text{first}} + \underbrace{T_{jj'}}_{\text{second}} - \underbrace{\lambda_k\, {}^{\mathrm{A}}\Omega_{jj'}}_{\text{third}}\right).\end{aligned} \tag{C.22}$$

The second and third terms are the fully perturbed objects, so we must organize Eqn. C.22 into groups of equal order in ϵ^n. One obtains different parts of the recursion relations for $j = k$ and $j \neq k$.

Note that the "second" term in Eqn. C.22 switched signs compared to the previous line, because we have defined matrix elements our one-tensor product corrections after taking an integration by parts:

$$T_{jk} = \int dA^{(0)}\left(\partial_a\phi_j^{(0)*}\right)T^{ab}\left(\partial_b\phi_k^{(0)}\right).$$

At zeroth order in Eqn. C.22, the first and third terms cancel trivially. The second term is only perturbative and does not contribute at zeroth order.

Expanding Eqn. C.22 to second order:

$$\begin{aligned}0 = &\int dA\phi_j^{(0)*}\left(\Delta^g - \nabla_a T^{ab}\partial_b - \lambda_k\, {}^{\mathrm{A}}\Omega\right)\left(\phi_k^{(0)} + c_{j'k}^{(1)}\phi_{j'}^{(0)} + c_{j'k}^{(2)}\phi_{j'}^{(0)}\right) \\ = &c_{jk}^{(1)}\left(\lambda_j^{(0)} - \lambda_k^{(0)}\right) - \lambda_k^{(1)}\delta_{jk} + T_{jk}^{(1)} - \lambda_k^{(0)}\, {}^{\mathrm{A}}\Omega_{jk}^{(1)} \\ &+ c_{jk}^{(2)}\left(\lambda_j^{(0)} - \lambda_k^{(0)}\right) - \lambda_k^{(2)}\delta_{jk} + T_{jk}^{(2)} - \lambda_k^{(0)}\, {}^{\mathrm{A}}\Omega_{jk}^{(2)} + c_{j'k}^{(1)}\left(T_{jj'}^{(1)} - \lambda_k^{(0)}\, {}^{\mathrm{A}}\Omega_{jj'}^{(1)}\right) - \lambda_k^{(1)}\left({}^{\mathrm{A}}\Omega_{jk}^{(1)} + c_{jk}^{(1)}\right)\end{aligned} \tag{C.23}$$

The first-order terms yield these two relations:

$$\begin{aligned}c_{jk}^{(1)}\left(\lambda_k^{(0)} - \lambda_j^{(0)}\right) &= T_{jk}^{(1)} - \lambda_k^{(0)}\, {}^{\mathrm{A}}\Omega_{jk}^{(1)}, \\ \lambda_k^{(1)} &= T_{kk}^{(1)} - \lambda_k^{(0)}\, {}^{\mathrm{A}}\Omega_{kk}^{(1)},\end{aligned} \tag{C.24}$$

The second-order terms must cancel separately, yielding these two relations:

$$\begin{aligned} c_{jk}^{(2)}\left(\lambda_k^{(0)} - \lambda_j^{(0)}\right) &= T_{jk}^{(2)} - \lambda_k^{(0)}\, {}^{\mathrm{A}}\Omega_{jk}^{(2)} + c_{j'k}^{(1)}\left(T_{jj'}^{(1)} - \lambda_k^{(0)}\, {}^{\mathrm{A}}\Omega_{jj'}^{(1)}\right) - \lambda_k^{(1)}\left({}^{\mathrm{A}}\Omega_{jk}^{(1)} + c_{jk}^{(1)}\right), \\ \lambda_k^{(2)} &= T_{kk}^{(2)} - \lambda_k^{(0)}\, {}^{\mathrm{A}}\Omega_{kk}^{(2)} + c_{j'k}^{(1)}\left(T_{kj'}^{(1)} - \lambda_k^{(0)}\, {}^{\mathrm{A}}\Omega_{kj'}^{(1)}\right) - \lambda_k^{(1)}\left({}^{\mathrm{A}}\Omega_{kk}^{(1)} + c_{kk}^{(1)}\right), \end{aligned} \tag{C.25}$$

A simple two-dimensional manifold for our purposes is the flat 2-torus, or a cylinder with periodic boundary conditions connecting the ends – known as Born–von Karman boundary conditions. This differs from a 2-torus embedded in three-dimensions, which has non-zero Gaussian curvature. We will introduce Gaussian curvature to the flat torus, but only through small perturbations. The unperturbed flat torus has zero Gaussian curvature, and cannot be embedded in three-space – although it can be embedded in four-space.

Consider a flat torus with tube radius R_0 and length L with embedding vector,

$$\vec{\boldsymbol{X}}(\phi, u) = \begin{pmatrix} R_0\cos(\phi) \\ R_0\sin(\phi) \\ uL \end{pmatrix} \implies g_{ab} = \begin{pmatrix} R_0^2 & 0 \\ 0 & L^2 \end{pmatrix},$$

where $\phi \in [0, 2\pi)$ and $u \in [0, 1]$. We refer to changes in tube radius as a function of u as "longitudinal" variations:

$$R_0 \to R_0\left(1 + \epsilon r(u)\right) \implies G_{ab} = R_0^2 \begin{pmatrix} (1+\epsilon r)^2 & 0 \\ 0 & \left(\frac{L}{R_0}\right)^2 + \epsilon^2 r'^2 \end{pmatrix} \tag{C.26}$$

For a perturbative expansion, we take ϵ smaller than $1/r$ and $1/r'$. Also, we consider the length to be of similar size as the radius, $L \sim R_0$.

The Laplacian is:

$$
\begin{aligned}
\Delta^G &= \frac{1}{\sqrt{G(\epsilon)}}\partial_a\sqrt{G(\epsilon)}\Game^{ab}\partial_b \\
&= \frac{1}{R_0^2\left(1+\epsilon r\right)\sqrt{\left(\frac{L}{R_0}\right)^2+\epsilon^2 r'^2}}\sum_{a,b=1}^{2}\partial_a\begin{pmatrix} \frac{\sqrt{\left(\frac{L}{R_0}\right)^2+\epsilon^2 r'^2}}{1+\epsilon r} & 0 \\ 0 & \frac{1+\epsilon r}{\sqrt{\left(\frac{L}{R_0}\right)^2+\epsilon^2 r'^2}} \end{pmatrix}\partial_b \\
&= \frac{1}{R_0^2}\left(\frac{1}{\left(1+\epsilon r\right)^2}\partial_\phi^2+\frac{\epsilon r'}{\left(\frac{L}{R_0}\right)^2+\epsilon^2 r'^2}\left(\frac{1}{1+\epsilon r}-\frac{\epsilon r''}{\left(\frac{L}{R_0}\right)^2+\epsilon^2 r'^2}\right)\partial_u+\frac{1}{\left(\frac{L}{R_0}\right)^2+\epsilon^2 r'^2}\partial_u^2\right) \\
&\xrightarrow{\epsilon\to 0}\left(\frac{1}{R_0^2}\partial_\phi^2+\frac{1}{L^2}\partial_u^2\right).
\end{aligned}
$$

Thanks to the periodic boundary conditions connecting the ends of the tube, the unperturbed eigenfunctions are:

$$
\phi_{sk}^{(0)} = \frac{e^{is\phi}}{\sqrt{2\pi R_0}}\frac{e^{i2\pi k u}}{\sqrt{L}} \ ,
$$

where the k-component would have been restricted to only a sine wave for non-periodic Dirichlet boundary conditions. The unperturbed eigenvalues are:

$$
\lambda_{sk}^{(0)} = -\overbrace{\frac{s^2}{R_0^2}}^{\equiv\bar{s}^2} - \overbrace{\left(\frac{2\pi k}{L}\right)^2}^{\equiv\bar{k}^2} \ ,
$$

where we have defined barred variables that absorb the inverse-length dependent factors.

Following the rescaling prescription described in Eqn. C.15, we compute the matrix elements of the perturbed Laplacian density, ${\scriptstyle\mathrm{A}}\Omega\hat{\Delta}^{G}$, using unperturbed basis functions. This is equivalent to integrating over the perturbed manifold:

$$
\begin{aligned}
\left\langle s'k' \middle| {}^{\mathrm{A}}\Omega\hat{\Delta}^{G} \middle| sk \right\rangle &= \lambda_{sk}^{(0)}\mathbb{I}_{s'k'sk} - T_{s'k'sk} \\
&= \int_0^{2\pi}\int_0^1 d\phi\; du\sqrt{g^{(0)}}\phi_{s'k'}^{(0)*}\underbrace{\sqrt{\frac{G(\epsilon)}{g^{(}0)}}}_{{}^{\mathrm{A}}\Omega}\hat{\Delta}^{G}\phi_{sk}^{(0)} \\
&= \int_0^{2\pi}\int_0^1 d\phi\; du\; \phi_{s'k'}^{(0)*}\underbrace{\left(\partial_a\sqrt{G(\epsilon)}\reflectbox{D}^{ab}\partial_b\right)}_{\Delta^g-\nabla_a T^{ab}\partial_b}\phi_{sk}^{(0)} \\
&\dot{=} -\int_0^{2\pi}\int_0^1 d\phi\; du\; \left(\partial_a\phi_{s'k'}^{(0)*}\right)\left(\sqrt{G(\epsilon)}\reflectbox{D}^{ab}\right)\left(\partial_b\phi_{sk}^{(0)}\right),
\end{aligned}
$$

where the overdot indicates an integration by parts in which our periodic boundary conditions ensure that the boundary component is zero. Computing the derivatives of the eigenfunctions and completing the angular integral in $\tilde{H}_{s'k'sk}$:

$$
= -\frac{\delta_{s's}}{LR_0}\int_0^1 du\; e^{i2\pi(k-k')u}\left(s's\frac{\sqrt{\left(\frac{L}{R_0}\right)^2+\epsilon^2r'^2}}{1+\epsilon r}+(2\pi k')(2\pi k)\frac{1+\epsilon r}{\sqrt{\left(\frac{L}{R_0}\right)^2+\epsilon^2r'^2}}\right) \tag{C.27}
$$

$$
\begin{aligned}
&= -\delta_{s's}\int_0^1 du\; e^{i2\pi(k-k')u} \\
&\qquad\left(\begin{array}{rllllll}
\frac{s^2}{R_0^2} & (1 & -\epsilon r & +\epsilon^2\left(r^2+\left(\frac{R_0}{L}\right)^2\frac{r'^2}{2}\right) & -\epsilon^3\left(r^3+\left(\frac{R_0}{L}\right)^2\frac{r'^2r}{2}\right) & +\ldots) \\
+\frac{(2\pi k')(2\pi k)}{L^2} & (1 & +\epsilon r & -\epsilon^2\left(\frac{R_0}{L}\right)^2\frac{r'^2}{2} & -\epsilon^3\left(\frac{R_0}{L}\right)^2\frac{r'^2r}{2} & +\ldots)
\end{array}\right).
\end{aligned} \tag{C.28}
$$

This agrees with the unperturbed eigenvalues at zeroth order:

$$
\left\langle s'k' \middle| \left({}^{\mathrm{A}}\Omega\hat{\Delta}^{G}\right)^{(0)} \middle| sk \right\rangle = \left(-\bar{s}^2-\bar{k}^2\right)\underbrace{\delta_{s's}\delta_{k'k}}_{\mathbb{I}_{s'k'sk}},
$$

where $\mathbb{I}_{s'k'sk}$ is the identity operator.

The simplest case is a deformation consisting of a single wavelength. This makes our problem identical to the analysis of periodic potentials that is widely used in the quantum mechanics of crystal lattices, see Sec. D.3.

Following the standard approach for periodic potentials, represent $r(u)$ as a superposition of the longitudinal basis functions, i.e. a Fourier series,

$$r(u) = \sum_{p=-\infty}^{\infty} \tilde{r}_{pN} e^{i2\pi pNu} \,,$$

where $\tilde{r}_{-pN} = \tilde{r}^*_{pN}$ and N is the number of periods of $r(u)$ that fit within L. If r has only the periodicity of the boundary conditions, then $N = 1$; however, we typically assume that many wavelengths fit within L. We define $\bar{p} \equiv 2\pi pN/L$. The important feature of periodic deformations is that while a general deformation $r(u)$ would involve many modes, the periodic ripple only activates its harmonics. Below, we will take just a single value of p, to examine a perfect sinusoidally rippled cylinder.

Before considering how the ripple affects the modes, we must address the zero mode. In general, changing the area of a manifold shifts the spectrum. To remove this trivial shift, we could rescale all lengths to maintain constant area:

$$\begin{aligned} G_{ab} &\longrightarrow \left(\frac{\int \sqrt{g^{(0)}} d\sigma}{\int \sqrt{G} d\sigma} \right)^2 G_{ab} \\ &= \left(\frac{2\pi L R_0}{2\pi \int_0^1 du\, R_0^2 (1 + \epsilon r) \sqrt{\left(\frac{L}{R_0}\right)^2 + \epsilon^2 r'^2}} \right)^2 G_{ab} \\ &= \left(1 - 2\epsilon \underbrace{\int_0^1 r\, du}_{\text{average of } r} + \epsilon^2 \int_0^1 \left(3r^2 - \frac{R_0^2 r'^2}{L^2} \right) du + \ldots \right) G_{ab} \,. \end{aligned} \tag{C.29}$$

By arranging our perturbation to be *symmetric* about the average embedding vector, it has no zero mode ($\tilde{r}_0 = 0$) and also no first-order change in area. By arranging our representation of the perturbation to have no zero mode, we need not worry about removing a trivial shift from the spectrum.

At first order, Eqn. C.28 gives this matrix element:

$$T^{(1)}_{s'k'sk} = \delta_{s's} \sum_{p=-\infty}^{\infty} \epsilon \tilde{r}_{pN} \left(-\bar{s}^2 + \bar{k}\bar{k}' \right) \delta_{k-k',pN} \,. \tag{C.30}$$

The difference in signs of the angular and longitudinal wavenumbers originates in the structure of $\sqrt{G}\Game^{ab}$, so it is a general feature of the cylinder with a radially symmetric deformation. The Kronecker delta function is zero for all values of k and k' unless their difference equals pN, i.e. a harmonic of the ripple.

The second-order corrections from Eqn. C.28 are:

$$\tilde{T}^{(2)}_{s'k'sk} = \delta_{s's} \sum_{p_1,p_2=-\infty}^{\infty} \epsilon^2 \tilde{r}_{p_1N}\tilde{r}_{p_2N}\delta_{k-k'+p_1N+p_2N}\bar{p}_1\bar{p}_2 \left(\bar{s}^2\left(1+\frac{R_0^2}{L^2}\right)-\frac{R_0^2}{L^2}\bar{k}\bar{k}'\right) . \qquad \text{(C.31)}$$

where the $\bar{p}_1$ and $\bar{p}_2$ come from the two copies of the Fourier transformed ripple inside r'^2. The delta function comes from the area integral over the modes and requires that $k - k' + p_1N + p_2N = 0$.

Similarly, the matrix elements of ${}^{\mathrm{A}}\Omega$ are:

$$\begin{aligned}
\langle s'k'|{}^{\mathrm{A}}\Omega|sk\rangle &= \int_0^{2\pi}\int_0^1 d\phi\; du\sqrt{g^{(0)}}\phi^{(0)*}_{s'k'}\sqrt{\frac{G(\epsilon)}{g^{(0)}}}\phi^{(0)}_{sk} \\
&= \delta_{s's}\int_0^1 du\frac{e^{i2\pi(k-k')u}}{LR_0}\left(LR_0 + \epsilon LR_0 r + \epsilon^2\frac{R_0^3r'^2}{2L} + \epsilon^3\frac{R_0^3rr'^2}{2L} + \ldots\right) \\
&= \underbrace{\delta_{s's}\delta_{k'k}}_{{}^{\mathrm{A}}\Omega^{(0)}_{s'k'sk}} + \underbrace{\sum_{p=-\infty}^{\infty}\epsilon\tilde{r}_{pN}\delta_{s's}\delta_{k-k',pN}}_{{}^{\mathrm{A}}\Omega^{(1)}_{s'k'sk}} + \underbrace{\frac{R_0^2}{L^2}\sum_{p_1,p_2=-\infty}^{\infty}\epsilon^2\tilde{r}_{p_1N}\tilde{r}_{p_2N}\delta_{k-k'+p_1N+p_2N}\bar{p}_1\bar{p}_2}_{{}^{\mathrm{A}}\Omega^{(2)}_{s'k'sk}} + \ldots .
\end{aligned} \qquad \text{(C.32)}$$

Combining these terms at first order cancels the angular wavenumber, and the effective potential matrix elements to first order are:

$$\begin{aligned}
\mathcal{V}^{(1)}_{s'k'sk} &= T^{(1)}_{s'k'sk} - \lambda^{(0)}_{sk}\,{}^{\mathrm{A}}\Omega^{(1)}_{s'k'sk} \\
&= \delta_{s's}\sum_{p=-\infty}^{\infty}\epsilon\tilde{r}_{pN}\left(-\bar{s}^2+\bar{k}\bar{k}'\right)\delta_{k-k'+pN} - \left(-\bar{s}^2-\bar{k}^2\right)\sum_{p=-\infty}^{\infty}\tilde{r}_{pN}\delta_{s's}\delta_{k-k',pN} \\
&= \sum_{p=-\infty}^{\infty}\underbrace{\epsilon\tilde{r}_{pN}\left(\bar{k}\bar{k}'+\bar{k}^2\right)}_{\equiv\epsilon\tilde{V}_{pN}}\delta_{s's}\delta_{k-k',pN} .
\end{aligned} \qquad \text{(C.33)}$$

The term with the underbrace is the analogue of $\tilde{V}_{pN}$ Fourier transformed potential in the one-dimensional crystal, see appendix Eqn. D.36.

By construction, $\tilde{r}_0 = 0$, so the diagonal elements of both $T^{(1)}_{s'k'sk}$ and ${}^{\mathrm{A}}\Omega^{(1)}_{s'k'sk}$

are zero. Thus, there is no first-order correction to the eigenvalues except near the boundaries of Brillouin zones (BZs), $\bar{k} = \frac{\bar{p}N}{2} + \bar{p}_\delta$. See the stripes in Fig. C-1.

For a given value of k, the full Hamiltonian matrix *at first order* has four non-zero elements near the edge of a BZ identified by harmonic p. Just as in the one-dimensional crystal, this forms a 2×2 matrix. The diagonal elements are the unperturbed eigenvalues $\lambda_{s,k}$ and $\lambda_{s,k-pN}$. The potential $\mathcal{V}$ from Eqn. C.33 contributes the two off-diagonal matrix elements at $\pm pN$. Rewritting the wavenumbers in terms of distance from the edge of the BZ: $k = p(N/2) + p_\delta$ and $k' = k - pN = -p(N/2) + p_\delta$. In this notation, the upper-right matrix element corresponds to $+p$:

$$\begin{aligned}\mathcal{V}^{(1)}_{sk'sk}(+p) &= \epsilon\tilde{r}_{pN}\frac{4\pi^2}{L^2}\left(\left(\frac{pN}{2}+p_\delta\right)\left(-\frac{pN}{2}+p_\delta\right)+\left(\frac{pN}{2}+p_\delta\right)^2\right)\delta_{s's}\delta_{k-k',pN}\\ &= \epsilon\tilde{r}_{pN}\left(\frac{\bar{p}}{2}+\bar{p}_\delta\right)2\bar{p}_\delta\delta_{s's}\delta_{k-k',pN}\,,\end{aligned}$$

where we've absorbed the $2\pi/L$ into the $\bar{p} \equiv 2\pi pN/L$ and $\bar{p}_\delta \equiv 2\pi p_\delta/L$. The lower-left matrix element is corresponds to $-p$:

$$\begin{aligned}\mathcal{V}^{(1)}_{sk'sk}(-p) &= \epsilon\tilde{r}_{-pN}\frac{4\pi^2}{L^2}\left(\left(\frac{-pN}{2}+p_\delta\right)\left(-\frac{-pN}{2}+p_\delta\right)+\left(\frac{-pN}{2}+p_\delta\right)^2\right)\delta_{s's}\delta_{k-k',-pN}\\ &= \epsilon\tilde{r}_{-pN}\left(\frac{-\bar{p}}{2}+\bar{p}_\delta\right)2\bar{p}_\delta\delta_{s's}\delta_{k-k',-pN}\,,\end{aligned}$$

This matrix does *not* produce a band gap. The off-diagonal elements have magnitude proportional to the distance from the BZ edge. It is *zero* at the BZ edge, so regular non-degenerate perturbation theory carries through without singularities. Contrast Figure C-1 here with the analogous Bragg matrix in conformal coordinates Fig. 3-15 and for a one-dimensional crystal Fig. D-1.

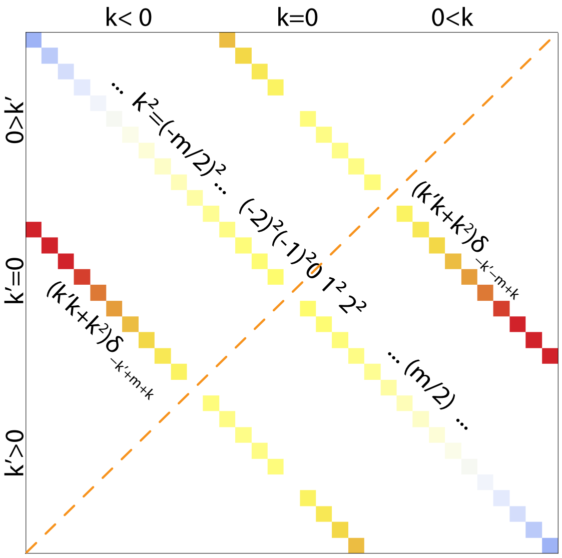

Figure C-1: Illustration of the Bragg-like matrix *in the lab frame z surface parameter* ($\epsilon = 1$). In these coordinates, the momentum-dependent potential has the inconvenient challenge of being zero on the anti-diagonal, hence the utility of the conformal coordinates.

The first-order eigenfunction corrections are:

$$\begin{aligned} c^{(1)}_{s'k'sk} &= \sum_p \frac{\mathcal{V}^{(1)}_{sk'sk}(p)}{-k'^2 + k^2} \\ &= \frac{\epsilon}{2} \sum_{p=-\infty}^{\infty} \tilde{r}_{pN} \left(1 + \frac{\bar{p}_\delta}{\frac{\bar{p}}{2}}\right) \delta_{s's}\delta_{k-k',pN} \end{aligned} \tag{C.34}$$

In the lab frame coordinate z, the ϵp_δ makes the deformation doubly small at first order in ϵ. Let's look at second-order. Using Eqn. C.25:

$$\begin{aligned} \lambda^{(2)}_{sk} =& T^{(2)}_{sksk} - \lambda^{(0)}_{sk}\,{}^{\mathrm{A}}\Omega^{(2)}_{sksk} + c^{(1)}_{s'k'sk}\left(T^{(1)}_{sks'k'} - \lambda^{(0)}_{sk}\,{}^{\mathrm{A}}\Omega^{(1)}_{sks'k'}\right) - \cancel{\lambda^{(1)}_{sk}}\left({}^{\mathrm{A}}\Omega^{(1)}_{sksk} + c^{(1)}_{sksk}\right) \\ =& \sum_{p_1,p_2=-\infty}^{\infty} \epsilon^2 \tilde{r}_{p_1N}\tilde{r}_{p_2N}\delta_{p_1N+p_2N}\bar{p}_1\bar{p}_2\left(\overbrace{\left(\bar{s}^2\left(1 + \frac{R_0^2}{L^2}\right) - \frac{R_0^2}{L^2}\bar{k}^2\right)}^{\text{from } T^{(2)}_{sksk}} - \overbrace{\frac{R_0^2}{L^2}\left(-\bar{s}^2 - \bar{k}^2\right)}^{\text{from } \lambda^{(0)}_{sk}\,{}^{\mathrm{A}}\Omega^{(2)}_{sksk}}\right) \\ &+ \sum_{s'}\sum_{k'} \underbrace{\sum_{p_1=-\infty}^{\infty} \epsilon\tilde{r}_{p_1N}\left(\bar{k}'\bar{k} + \bar{k}^2\right)\delta_{s's}\delta_{k-k',p_1N}}_{c^{(1)}_{s'k'sk}} \underbrace{\sum_{p_2=-\infty}^{\infty} \epsilon\tilde{r}_{p_2N}\delta_{s's}\delta_{k-k'+p_2N}\left(-\bar{s}\bar{s}' + \bar{k}\bar{k}' - (-\bar{s}^2 - \bar{k}^2)\right)}_{T^{(1)}_{sks'k'} - \lambda^{(0)}_{sk}\,{}^{\mathrm{A}}\Omega^{(1)}_{sks'k'}} \\ =& \epsilon^2 \sum_{p=-\infty}^{\infty} |\tilde{r}_{pN}|^2 \left(-\bar{p}^2\bar{s}^2\left(1 + 2\frac{R_0^2}{L^2}\right) + 4\bar{k}^2\left(\bar{k} - \frac{\bar{p}}{2}\right)^2\right). \end{aligned} \tag{C.35}$$

Note that when $s = 0$, this correction to the eigenvalue $\lambda_{sk}^{(2)} \sim \epsilon^2 \bar{p}_\delta^2$.

Using Eqn. C.25 again, for $s'k' \neq sk$ the matrix elements of the potential at second order are:

$$\left(\lambda_{sk}^{(0)} - \lambda_{s'k'}^{(0)}\right) c_{s'k'sk}^{(2)} = \underbrace{\tilde{T}_{s'k'sk}^{(2)} - \lambda_{sk}^{(0)}\, {}^{\mathrm{A}}\Omega_{s'k'sk}^{(2)}}_{A_{s'k'sk}} \quad + \underbrace{\left(\tilde{T}_{s'k's''k''}^{(1)} - \lambda_{sk}^{(0)}\, {}^{\mathrm{A}}\Omega_{s'k's''k''}^{(1)}\right) c_{s''k''sk}^{(1)}}_{B_{s'k'sk}} + c_{kj}^{(1)*} \cancel{\lambda_{sk}^{(1)}} \,. \tag{C.36}$$

Using Eqn. C.31 and Eqn. C.32 for $T_{s'k'sk}^{(2)}$ and ${}^{\mathrm{A}}\Omega_{s'k'sk}^{(2)}$ in term A in Eqn. C.36 gives:

$$\begin{aligned} A_{s'k'sk} =& \delta_{s's} \sum_{p_1, p_2 = -\infty}^{\infty} \epsilon^2 \tilde{r}_{p_1 N} \tilde{r}_{p_2 N} \delta_{k-k'+p_1 N+p_2 N} \bar{p}_1 \bar{p}_2 \left(\bar{s}^2 \left(1 + \frac{R_0^2}{L^2}\right) - \frac{R_0^2}{L^2} \bar{k}\bar{k}'\right) \\ & - (-\bar{s}^2 - \bar{k}^2) \frac{R_0^2}{L^2} \sum_{p_1, p_2 = -\infty}^{\infty} \epsilon^2 \tilde{r}_{p_1 N} \tilde{r}_{p_2 N} \delta_{k-k'+p_1 N+p_2 N} \bar{p}_1 \bar{p}_2 \\ =& \delta_{s's} \epsilon^2 \sum_{p=-\infty}^{\infty} \tilde{r}_{pN} \tilde{r}_{-k+k'-pN} \bar{p}(-\bar{k} + \bar{k}' - \bar{p}) \left(\bar{s}^2 \left(1 + 2\frac{R_0^2}{L^2}\right) + \frac{R_0^2}{L^2} (\bar{k}^2 - \bar{k}\bar{k}')\right) . \end{aligned} \tag{C.37}$$

The term B in Eqn. C.36 is not the same as $c_{sks'k'}^{(1)} c_{s'k'sk}^{(1)}$. It is:

$$\begin{aligned} B_{s'k'sk} =& \sum_{s''k''} \overbrace{\delta_{s''s'} \sum_{p_1=-\infty}^{\infty} \epsilon \tilde{r}_{p_1 N} \delta_{k'-k''+p_1 N} \left(\left(-\bar{s}'^2 + \bar{k}'\bar{k}''\right) - (-\bar{s}^2 - \bar{k}^2)\right)}^{\left(T_{s'k's''k''}^{(1)} - \lambda_{sk}^{(0)}\, {}^{\mathrm{A}}\Omega_{s'k's''k''}^{(1)}\right)} \\ & \times \underbrace{\sum_{p_2=-\infty}^{\infty} \epsilon \tilde{r}_{p_2 N} \frac{\bar{k}''\bar{k} + \bar{k}^2}{-\bar{k}^2 - \bar{k}''^2} \delta_{s''s} \delta_{k-k'', p_2 N}}_{c_{s''k''sk}^{(1)}} \\ =& \epsilon^2 \delta_{s's} \sum_{p=-\infty}^{\infty} \tilde{r}_{pN} \tilde{r}_{-k'+k-pN} \quad \underbrace{\left(\bar{k}'(\bar{k}' + \bar{p}) + \bar{k}^2\right)}_{\text{from } T_{s'k's''k''}^{(1)} - \lambda_{sk}^{(0)}\, {}^{\mathrm{A}}\Omega_{s'k's''k''}^{(1)}} \quad \underbrace{\frac{(\bar{k}' + \bar{p})\bar{k} + \bar{k}^2}{-\bar{k}^2 - (\bar{k}' + \bar{p})^2}}_{\text{from } c_{s''k''sk}^{(1)}} . \end{aligned}$$

Adding these together:

$$\begin{aligned}\left(\lambda^{(0)}_{sk} - \lambda^{(0)}_{s'k'}\right) c^{(2)}_{s'k'sk} =& \delta_{s's}\epsilon^2 \sum_{p=-\infty}^{\infty} \tilde{r}_{pN}\tilde{r}_{-k+k'-pN}\bar{p}(-\bar{k}+\bar{k}'-\bar{p})\left(\bar{s}^2\left(1+2\frac{R_0^2}{L^2}\right)+\frac{R_0^2}{L^2}(\bar{k}^2-\bar{k}\bar{k}')\right) \\ &+ \epsilon^2\delta_{s's}\sum_{p_1=-\infty}^{\infty}\tilde{r}_{p_1N}\tilde{r}_{-k'+k-p_1N} \quad \underbrace{\left(\bar{k}'(\bar{k}'+\bar{p}_1)+\bar{k}^2\right)}_{\text{from } T^{(1)}_{s'k's''k''}-\lambda^{(0)}_{sk}\,{}^{\mathrm{A}}\Omega^{(1)}_{s'k's''k''}} \quad \underbrace{\frac{(\bar{k}'+\bar{p}_1)\bar{k}+\bar{k}^2}{-\bar{k}^2-(\bar{k}'+\bar{p}_1)^2}}_{\text{from } c^{(1)}_{s''k''sk}} \\ =& \delta_{s's}\epsilon^2\sum_{p=-\infty}^{\infty}\tilde{r}_{pN}\tilde{r}_{-k+k'-pN}C(k,k',p)\,, \end{aligned} \tag{C.38}$$

where the momentum-dependent term $C(k,k',p)$ is:

$$\begin{aligned} C(k,k',p) =& \bar{p}(-\bar{k}+\bar{k}'-\bar{p})\left(\bar{s}^2\left(1+2\frac{R_0^2}{L^2}\right)+\frac{R_0^2}{L^2}(\bar{k}^2-\bar{k}\bar{k}')\right) \\ &+ \left(\bar{k}'(\bar{k}'+\bar{p})+\bar{k}^2\right)\frac{(\bar{k}'+\bar{p})\bar{k}+\bar{k}^2}{-\bar{k}^2-(\bar{k}'+\bar{p})^2}\,. \end{aligned} \tag{C.39}$$

Consider a single ripple of at some fixed wavelength p_0N. The Fourier transform as a single value with two delta functions:

$$\tilde{r}_{pN} = \tilde{r}_{p_0N}\left(\delta_{p,p_0}+\delta_{p,-p_0}\right)\,. \tag{C.40}$$

Note that its complex conjugate is:

$$\tilde{r}_{-pN} = \tilde{r}^*_{pN} = \tilde{r}^*_{p_0N}\left(\delta_{p,p_0}+\delta_{p,-p_0}\right)\,. \tag{C.41}$$

Using this, we can resolve the sum over p in Eqn. C.38:

$$\left(\lambda^{(0)}_{sk} - \lambda^{(0)}_{s'k'}\right) c^{(2)}_{s'k'sk} = \delta_{s's}\epsilon^2\sum_{p=-\infty}^{\infty}\tilde{r}_{p_0N}\left(\delta_{pN,p_0N}+\delta_{pN,-p_0N}\right)\tilde{r}^*_{p_0N}\left(\delta_{-k+k'-pN,p_0N}+\delta_{-k+k'-pN,-p_0N}\right)C(k,k',p)\,. \tag{C.42}$$

The first pair of delta functions is only non-zero if $pN = \pm p_0N$. The second pair of delta functions is only non-zero if $pN = k' - k \pm p_0N$. If $p = p_0$, then either (a) $p_0N = k' - k + p_0N$ implies $k' = k$, but that's forbidden by the construction of Eqn. C.25, or (b) $p_0N = k' - k - p_0N$ implies $k' - k = 2p_0N$. Similarly, $p = -p_0$, then either (a) $-p_0N = k' - k - p_0N$ implies $k' = k$, but that's forbidden, or (b) $-p_0N = k' - k + p_0N$ implies $k' - k = -2p_0N$. Thus, the corrections can only be nonzero when $k' = k \pm 2p_0N$.

This is the edge of a BZ at $k = p_0N$. Consider $k = p_0N + p_\delta$ and thus $k' = -p_0N + p_\delta$. Is the coefficient $C(k, k', p)$ nonzero at these values? If so, then we have a degeneracy.

$$
\begin{aligned}
&C(p_0N + p_\delta, -p_0N + p_\delta, p_0) \\
=&\bar{p}_0(-\bar{p}_0 - \bar{p}_\delta - \bar{p}_0 + \bar{p}_\delta - \bar{p}_0)\left(\bar{s}^2\left(1 + 2\frac{R_0^2}{L^2}\right) + \frac{R_0^2}{L^2}((\bar{p}_0 + \bar{p}_\delta)^2 - (\bar{p}_0 + \bar{p}_\delta)(-\bar{p}_0 + \bar{p}_\delta))\right) \\
&+ \left((-\bar{p}_0 + \bar{p}_\delta)(-\bar{p}_0 + \bar{p}_\delta + \bar{p}_0) + (\bar{p}_0 + \bar{p}_\delta)^2\right)\frac{(-\bar{p}_0 + \bar{p}_\delta + \bar{p}_0)(-\bar{p}_0 + \bar{p}_\delta) + (-\bar{p}_0 + \bar{p}_\delta)^2}{-(\bar{p}_0 + \bar{p}_\delta)^2 - (-\bar{p}_0 + \bar{p}_\delta + \bar{p}_0)^2} \\
=&3\bar{p}_0^2\left(\bar{s}^2\left(1 + 2\frac{R_0^2}{L^2}\right) + \frac{R_0^2}{L^2}2\bar{p}_0(\bar{p}_0 + \bar{p}_\delta)\right) \\
&+ \left(\bar{p}_\delta^2 + \bar{p}_0\bar{p}_\delta + 2\bar{p}_\delta^2\right)(-\bar{p}_0 + \bar{p}_\delta)\frac{-\bar{p}_0 + 2\bar{p}_\delta}{-(\bar{p}_0 + \bar{p}_\delta)^2 - \bar{p}_\delta^2}\,.
\end{aligned}
\tag{C.43}
$$

This is not zero at $p_\delta = 0$, which means that there is a second-order degeneracy. One could employ the technology of Van Vleck to pursue this, see Sec. D.2.1.

Clearly, the conformal mapping approach presented in Chapter 3 is significantly more tractable than this approach.

Appendix D

Operator Perturbation Theory with Euclidean Support

In this appendix, we document perturbation theory for operators on functions defined in Euclidean space. We start with non-degenerate Rayleigh-Schrödinger perturbation theory, and then continue with degenerate perturbation theory to first and second order.

The general context is a physical system described by scalar functions defined over some region of space. The physical quantities of interest could be chemical concentrations, pressures, probability amplitudes, etc. To study time evolution, ground states or some process of interest in the system, when defines "operators" that act on these scalar quantities. To make analytical progress in understanding the system, one often must pick particularly simple operators, and then consider *small deviations* away from this simplified picture.

A now-standard approach to such perturbation theory was introduced by John W. Strutt (a.k.a. Lord Rayleigh) in the second volume of his study of acoustics published in 1896.[55] Schrödinger generalized the approach in analyzing his quantum wave equation.[65]

D.1 Non-Degenerate Perturbations

We start with an Hermitian operator, $\hat{H}^{(0)}$, which we call the unperturbed Hamiltonian. Assume that we know its eigenfunctions $|k^{(0)}\rangle$ and corresponding eigenvalues $\lambda_k^{(0)}$.

Consider a *perturbed* Hamiltonian that includes a convergent series of perturbations:

$$\hat{H}(\epsilon) \equiv \hat{H}^{(0)} + \epsilon\hat{H}^{(1)} + \epsilon^2\hat{H}^{(2)} + \epsilon^3\hat{H}^{(3)} + \dots ,$$

where ϵ is a small parameter that we use for bookkeeping. The *perturbed* Hamiltonian has its own eigenfunctions and eigenvectors:

$$\hat{H}(\epsilon)\,|k\rangle = \lambda_k\,|k\rangle \ . \tag{D.1}$$

We define the Hamiltonian by its action on functions defined in Euclidean space, $\mathbb{R}^d$. As a Hermitian operator, its eigenfunctions provide an orthogonal set that span this function space. By the notation $|k\rangle$, we mean the normalized form of these functions. If either k or j is from a discrete set, then

$$\langle k|j\rangle \equiv \int \phi_k^*\phi_j d^dx^i = \delta_{kj} \ , \tag{D.2}$$

where d^dx^i indicates the d-dimensional integration. If both k and j are part of a continuous set, then the Kronecker delta is replaced by a Dirac delta distribution. The analogous relation holds for the unperturbed eigenfunctions, which are defined in the same Euclidean space.

This defines the standard bra-ket notation, which we also use to construct matrix elements of operators:

$$H_{jk} = \langle j|\hat{H}|k\rangle = \int \phi_j^*\left(\hat{H}\phi_k\right) d^dx^i \ . \tag{D.3}$$

"Hermitian" means that $\hat{H}$ is self-adjoint: $\hat{H} = \hat{H}^\dagger$, or in matrix notation: $H_{jk} = H_{kj}^*$.

“Normal” means that an operator commutes with its adjoint: $\hat{H}\hat{H}^{\dagger} = \hat{H}^{\dagger}\hat{H}$. Self-adjoint operators are clearly a subset of normal operators. The spectral theorem states that the eigenfunctions of a normal operator provide an orthogonal basis spanning the Hilbert space of functions on which the operator acts. We make frequent use of this property of the eigenfunctions.

The Rayleigh-Schrödinger approach uses the bookkeeping parameter to construct an *ansatz* for the eigenfunctions and eigenvalues of the *perturbed* Hamiltonian in terms of their *un*perturbed values via a convergent series of corrections:

$$\begin{aligned} |k\rangle &= \left|k^{(0)}\right\rangle + \epsilon\left|k^{(1)}\right\rangle + \epsilon^2\left|k^{(2)}\right\rangle + \epsilon^3\left|k^{(3)}\right\rangle + \ldots \\ \lambda_k &= \lambda_k^{(0)} + \epsilon\lambda_k^{(1)} + \epsilon^2\lambda_k^{(2)} + \epsilon^3\lambda_k^{(3)} + \ldots . \end{aligned} \tag{D.4}$$

Given a particular perturbation, one solves for these corrections by inserting the perturbative ansatz into Eqn. D.1 and projecting back onto the unperturbed eigenbasis:

$$\begin{aligned} 0 &= \left\langle j^{(0)}\middle|\hat{H}(\epsilon) - \lambda_k\middle|k\right\rangle \\ &= \int \phi_j^{(0)*}\left(\hat{H}(\epsilon)\phi_k\right) d^d x^i \ . \end{aligned} \tag{D.5}$$

Grouping terms order by order in ϵ, we have:

$$\begin{aligned} 0 =& \epsilon^0\left(\left(\hat{H}^{(0)} - \lambda_k^{(0)}\right)\left|k^{(0)}\right\rangle\right) + \\ &+ \epsilon^1\left(\left(\hat{H}^{(0)} - \lambda_k^{(0)}\right)\left|k^{(1)}\right\rangle + \left(\hat{H}^{(1)} - \lambda_k^{(1)}\right)\left|k^{(0)}\right\rangle\right) + \\ &+ \epsilon^2\left(\left(\hat{H}^{(0)} - \lambda_k^{(0)}\right)\left|k^{(2)}\right\rangle + \left(\hat{H}^{(1)} - \lambda_k^{(1)}\right)\left|k^{(1)}\right\rangle + \left(\hat{H}^{(2)} - \lambda_k^{(2)}\right)\left|k^{(0)}\right\rangle\right) + \\ &+ \epsilon^3\left(\left(\hat{H}^{(0)} - \lambda_k^{(0)}\right)\left|k^{(3)}\right\rangle + \left(\hat{H}^{(1)} - \lambda_k^{(1)}\right)\left|k^{(2)}\right\rangle + \left(\hat{H}^{(2)} - \lambda_k^{(2)}\right)\left|k^{(1)}\right\rangle + \left(\hat{H}^{(3)} - \lambda_k^{(3)}\right)\left|k^{(0)}\right\rangle\right) + \\ &\ldots \\ &+ \epsilon^n\sum_{m=0}^{n}\left(\hat{H}^{(m)} - \lambda_k^{(m)}\right)\left|k^{(n-m)}\right\rangle + \ldots \end{aligned} \tag{D.6}$$

Each order in ϵ must equal zero independently. Eqns. D.6 underspecify the correction terms in the ansatz. Normalization provides an additional constraint. Following the usual procedure, one takes the unperturbed eigenfunctions as a basis and writes the corrections as superpositions of these basis functions:

$$\left|k^{(n)}\right\rangle = \sum\!\!\!\!\!\!\int_{k'} c^{(n)}_{k'k} \left|k'^{(0)}\right\rangle \ , \tag{D.7}$$

where we sum over discrete eigenvalues and integrate over continuous portions of the spectrum. Note that $c^{(0)}_{k'k} = \delta_{k'k}$. Eqn. D.7 defines $c^{(n)}_{k'k}$ coefficients. Below, we will use $c^{(n)}_{kk}$ to normalize the eigenkets.

Substituting this representation of $|k^{(n)}\rangle$ into Eqn. D.6 gives:

$$0 \ = \ \sum_{m=0}^{n} \left(\hat{H}^{(m)} - \lambda^{(m)}_{k}\right) \sum\!\!\!\!\!\!\int_{k'} c^{(n-m)}_{k'k} \left|k'^{(0)}\right\rangle \ . \tag{D.8}$$

To solve for the $c^{(n)}_{k'k}$ and $\lambda^{(n)}_{k}$, we form the inner product of Eqn. D.8 with an arbitrary unperturbed eigenfunction, $\phi^{(0)}_{j}$, i.e. we multiply from the left with $\langle j^{(0)}|$. This gives a recursion relation for the $c^{(n)}_{k'k}$ and $\lambda^{(n)}_{k}$ that depends on all lower order perturbations to the Hamiltonian, $\hat{H}^{(m\leq n)}$:

$$0 \ = \ \sum_{m=0}^{n} \sum\!\!\!\!\!\!\int_{k'} \left(H^{(m)}_{jk'} - \lambda^{(m)}_{k}\delta_{jk'}\right) c^{(n-m)}_{k'k} \ . \tag{D.9}$$

We have introduced the notation $H^{(n)}_{jk}$ for the (j,k) matrix element of the n-th order correction to the operator with respect to the unperturbed eigenfunctions,

$$\begin{aligned} H^{(n)}_{jk} &= \left\langle j^{(0)} \middle| \hat{H}^{(n)} \middle| k^{(0)} \right\rangle \\ &= \int \phi^{(0)*}_{j} \left(\hat{H}^{(n)} \phi^{(0)}_{k}\right) dx^{i} \ . \end{aligned}$$

The steps above have expanded the inner product $\left\langle j^{(0)} \middle| \hat{H}(\epsilon) \middle| k \right\rangle$ using the perturbative ansatz.

This procedure works because at each value of n, the highest order corrections to the eigenvalues, $\lambda^{(n)}_{k}$, and eigenfunctions, $c^{(n)}_{kj}$, are coupled *only* to the unperturbed eigenvalues and eigenfunctions. This allows the following rearrangement:

$$\left(\lambda_k^{(0)} - \lambda_j^{(0)}\right) c_{jk}^{(n)} + \lambda_k^{(n)}\delta_{jk} = H_{jk}^{(n)} + \sum_{m=1}^{n-1} \sum\!\!\!\!\!\!\!\int_{k'} \left(H_{jk'}^{(m)} - \lambda_k^{(m)}\delta_{jk'}\right) c_{k'k}^{(n-m)} . \tag{D.10}$$

Considering $j = k$ and $j \neq k$ separately:

$$j = k \implies \qquad \lambda_k^{(n)} = H_{kk}^{(n)} + \sum_{m=1}^{n-1} \sum\!\!\!\!\!\!\!\int_{k'} H_{kk'}^{(m)} c_{k'k}^{(n-m)} \tag{D.11}$$

$$j \neq k \implies \left(\lambda_k^{(0)} - \lambda_j^{(0)}\right) \quad c_{jk}^{(n)} = H_{jk}^{(n)} + \sum_{m=1}^{n-1} \sum\!\!\!\!\!\!\!\int_{k'} \left(H_{jk'}^{(m)} - \lambda_k^{(m)}\delta_{jk'}\right) c_{k'k}^{(n-m)} . \tag{D.12}$$

The Hermiticity of the Hamiltonian ensures that the $\lambda_k^{(n)}$ are real. However, the $H_{jk}^{(n)}$ could be complex and therefore also the $c_{jk}^{(n)}$.

Note that Eqn. D.12 provides no constraint on the $c_{kk}^{n>0}$. Expanding the orthogonality relation gives:

$$\delta_{jk} = \langle j|k\rangle = \left(\sum\!\!\!\!\!\!\!\int_{j'} \left(\delta_{j'j} + \epsilon c_{j'j}^{(1)*} + \ldots\right) \left\langle j'^{(0)}\right|\right) \left(\sum\!\!\!\!\!\!\!\int_{k'} \left(\delta_{k'k} + \epsilon c_{k'k}^{(1)} + \ldots\right) \left|k'^{(0)}\right\rangle\right) . \tag{D.13}$$

Grouping terms order by order in ϵ:

$$\begin{aligned}
\delta_{jk} &= \epsilon^0 \delta_{jk} + \\
&+ \epsilon^1 \left(c_{kj}^{(1)*} + c_{jk}^{(1)}\right) + \\
&+ \epsilon^2 \left(c_{kj}^{(2)*} + \sum\!\!\!\!\!\!\!\int_{j'} c_{j'j}^{(1)*} c_{j'k}^{(1)} + c_{jk}^{(2)}\right) + \\
&\ldots \\
&+ \epsilon^n \left(c_{kj}^{(n)*} + \sum_{m=1}^{n-1} \sum\!\!\!\!\!\!\!\int_{j'} c_{j'j}^{(n-m)*} c_{j'k}^{(m)} + c_{jk}^{(n)}\right) + \ldots ,
\end{aligned} \tag{D.14}$$

where repeated indices imply summation. The first term cancels the l.h.s., and each order in ϵ must equal zero independently. For $n = 1$, we see that $c_{jk}^{(1)}$ is completely antihermitian; its Hermitian part is zero. For off-diagonal elements of $c_{jk}^{(1)}$, this antihermiticity is evident in Eqns. D.17.

The real part of $c_{kk}^{(1)}$ is constrained to zero by Eqn. D.14, and the imaginary part is unconstrained:

$$c_{kk}^{(1)} \equiv \left\langle k^{(1)} \middle| k^{(0)} \right\rangle = i\alpha \ ,$$

with α real. This amounts to a phase change at first order:

$$\begin{aligned} |k\rangle &= \left|k^{(0)}\right\rangle + \epsilon \left|k^{(1)}\right\rangle + \ldots \\ &= \left|k^{(0)}\right\rangle \left(1 + \epsilon c_{kk}^{(1)}\right) + \epsilon \sum\!\!\!\!\!\!\!\int_{j \neq k} c_{k'k} \left|k'^{(0)}\right\rangle + \mathcal{O}(\epsilon^2) \\ &= \left|k^{(0)}\right\rangle e^{i\alpha\epsilon} + \epsilon \sum\!\!\!\!\!\!\!\int_{j \neq k} c_{k'k} \left|k'^{(0)}\right\rangle + \mathcal{O}(\epsilon^2) \ , \end{aligned}$$

where the higher order terms differ between the last two lines. Since the phase of $|k\rangle$ is arbitrary, we can choose $\alpha = 0$ without loss of generality. That is, we can choose $c_{kk}^{(1)} = 0$

For values of $n \geq 2$, the Hermitian part is not zero:

$$2 \times \text{Herm}\left(c_{kj}^{(n)}\right) = c_{kj}^{(n)*} + c_{jk}^{(n)} = -\sum_{m=1}^{n-1} \sum\!\!\!\!\!\!\!\int_{j'} c_{j'j}^{(n-m)*} c_{j'k}^{(m)} \ . \tag{D.15}$$

For $n = 2$, we have:

$$\begin{aligned} c_{kj}^{(2)*} + c_{jk}^{(2)} &= -\sum\!\!\!\!\!\!\!\int_{j'} c_{j'j}^{(1)*} c_{j'k}^{(1)} \\ &= -\sum\!\!\!\!\!\!\!\int_{j'} \frac{H_{j'j}^{(1)*} H_{j'k}^{(1)}}{\left(\lambda_j^{(0)} - \lambda_{j'}^{(0)}\right)\left(\lambda_k^{(0)} - \lambda_{j'}^{(0)}\right)} \ . \end{aligned}$$

For $j = k$, this means:

$$\text{Re}\left(c_{kk}^{(2)}\right) = -\frac{1}{2} \sum\!\!\!\!\!\!\!\int_{j}{}' \frac{\left|H_{jk}^{(1)}\right|^2}{\left(\lambda_k^{(0)} - \lambda_j^{(0)}\right)^2} \ ,$$

where the prime on the sum-integral means that the pole at $j = k$ is explicitly avoided by our choice of $c_{kk}^{(1)} = 0$. We can again use the arbitrary phase of $|k\rangle$ to choose the imaginary part of $\text{Im}(c_{kk}^{(2)}) = 0$.

From these, one can extrapolate to get a second identity:

$$\begin{aligned} 2 \times \mathrm{Herm}\left(c_{kj}^{(n)}\right) = c_{kj}^{(n)*} + c_{jk}^{(n)} &= -\sum_{m=1}^{n-1} c_{j'j}^{(n-m)*} c_{j'k}^{(m)} \\ &= \sum_{m_1+\ldots+m_p=n} \sum\!\!\!\!\!\!\!\int_{j'} \ldots \sum\!\!\!\!\!\!\!\int_{j^{(p)}} (-1)^p \, c_{jj'}^{(m_1)} c_{j'j''}^{(m_2)} \ldots c_{j^{(p)}k}^{(m_p)}, \end{aligned} \tag{D.16}$$

where the sum goes over all sets of two or more integers $\{m_1, ..., m_p\}$ that sum to n.

The complete set of corrections for $n = 1, 2, 3$ is:

$$\begin{aligned} n = 1 \implies &\begin{cases} \lambda_k^{(1)} &= H_{kk}^{(1)} \\ c_{jk}^{(1)} &= H_{jk}^{(1)} \Big/ \left(\lambda_k^{(0)} - \lambda_j^{(0)}\right), \quad j \neq k \\ c_{kk}^{(1)} &= 0, \qquad\qquad\qquad\qquad j = k \end{cases} \\ n = 2 \implies &\begin{cases} \lambda_k^{(2)} &= H_{kk}^{(2)} + \displaystyle\sum_{k' \neq k} \frac{H_{kk'}^{(1)} H_{k'k}^{(1)}}{\lambda_k^{(0)} - \lambda_{k'}^{(0)}} \\ c_{jk}^{(2)} &= \left(H_{jk}^{(2)} + \displaystyle\sum_{k' \neq k} \left(H_{jk'}^{(1)} - H_{kk}^{(1)} \delta_{jk'} \right) \frac{H_{k'k}^{(1)}}{\lambda_k^{(0)} - \lambda_{k'}^{(0)}} \right) \Big/ \left(\lambda_k^{(0)} - \lambda_j^{(0)}\right), \quad j \neq k \\ c_{kk}^{(2)} &= -\displaystyle\sum_{j \neq k} \left| H_{jk}^{(1)} \right|^2 \Big/ \left(\lambda_k^{(0)} - \lambda_j^{(0)}\right)^2, \qquad j = k \end{cases} \end{aligned} \tag{D.17}$$

D.2 Degenerate Perturbation Theory

These perturbative expansions fail if any of the sums over states connect states with equal, or nearly equal, eigenvalues $\lambda_j^{(0)} \approx \lambda_k^{(0)}$, because Eqn. D.12 multiplies the correction by the difference between the eigenvalues. Such a connection only occur if *particular* off-diagonal matrix elements, $H_{jk}^{(n)}$, or combinations of these elements, are non-zero. The exact eigenfunctions for the full Hamiltonian are non-singular, so the infinity that results from dividing by $(\lambda_j^{(0)} - \lambda_k^{(0)})$ is a non-physical artifact of our procedure. It arises from an inadequate choice of function basis. By construction, the perturbative framework assumes that as $\epsilon \to 0$, each perturbed eigenfunction approaches a distinct unperturbed eigenfunction. This infinity in our perturbation expansion indicates that a set of eigenfunctions of $\hat{H}^{(0)}$ have the same eigenvalue, and that our perturbed eigenfunctions approach a linear combination of these degenerate eigenfunctions rather than a distinct member of the set.

To avoid this infinity, one must find the linear combinations of $\phi_k^{(0)}$ that represent the $\epsilon \to 0$ limit of the exact eigenfunctions, and must use these in the function basis instead. To discover these new basis functions, one must diagonalize a submatrix of the full Hamiltonian. That is, one must exactly solve a subset of the problem instead of seeking an approximate solution. This procedure amounts to a transformation that removes the problematic off-diagonal elements.

Fortunately, symmetries often make many zero elements in $H_{jk}^{(n)}$, so degeneracies are often isolated in small submatrices that are easily diagonalized. In the simplest case, a perturbation connects a state to only one other state that has nearly equal eigenvalue. This defines a two-by-two submatrix, which is easily diagonalized. For example, this arises from a periodic perturbation to the free particle Hamiltonian in one dimension with globally periodic boundary conditions, see Sec. D.3.1 or a standard textbook on quantum mechanics, e.g. [see 149, Shankar].

Such a degeneracy can happen at any order. An n-th order degeneracy occurs when two eigenvalues are equal at $(n-1)$-th order are connected by n-th order matrix elements. Given the structure of the recursion relation in Eqn. D.12, such a connection can involve just one matrix or a chain of up to n matrices multiplied together. Even in the simplified case of having only $H_{jk}^{(1)}$ and no higher order perturbations, a second order degeneracy may require eliminating the numerator of

$$\sum_{k' \neq k} \frac{H_{jk'}^{(1)} H_{k'k}^{(1)}}{\left(\lambda_k^{(0)} - \lambda_{k'}^{(0)}\right)\left(\lambda_k^{(0)} - \lambda_j^{(0)}\right)} \; . \tag{D.18}$$

If $\lambda_k^{(0)} = \lambda_j^{(0)}$, then the second-order corrections are valid only if no intermediate states connect these eigenvalues, i.e. either or both of $H_{jk'}^{(1)}$ and $H_{k'k}^{(1)}$ are zero for all k' [127]. When intermediate states exist, we must diagonalize this entire submatrix to construct a new set of degenerate eigenfunctions. This submatrix can be so large as to prevent exact solution.

D.2.1 Second-Order Degenerate Perturbation Theory

Fortunately, [67, Van Vleck] introduced a method of *approximate* diagonalization that enables perturbation theory up to third and even higher order. The Van Vleck transformation has been developed and applied in chemistry [71, 82], see Professor Field's lecture notes for MIT course 5.76 [157]. Here, we document two derivations of the Van Vleck transformation using our notation, starting first with a generalization of the derivation presented in [127, Schiff].

We restrict attention to discrete sets of degenerate eigenfunctions. Given a set of g_s degenerate eigenfunctions $\left\{\phi_s^{(0)}\right\}$, we seek the linear combinations that match the perturbed eigenfunctions. Van Vleck's direct approach to obtaining these linear combinations is to restate our perturbative ansatz to explicitly include these linear combinations at the zeroth order. Denoting eigenfunctions in the degenerate subspace by $s, s', s'', \ldots$:

$$\phi_s = \sum_{s'} a_{s's}\phi_{s'}^{(0)} + \epsilon \mathop{\sum\!\!\!\!\!\!\!\int}_k{}' c_{ks}^{(1)}\phi_k^{(0)} + \epsilon^2 \mathop{\sum\!\!\!\!\!\!\!\int}_k{}' c_{ks}^{(2)}\phi_k^{(0)} + \ldots \tag{D.19}$$

where the prime on the sum-integral indicates that that the degenerate states are excluded, $k \neq s$. Compared to Eqn. D.7 and Eqn. D.4, the only difference is that part of $c_{k'k}^{(0)} = \delta_{k'k}$ has been replaced by the $g_s \times g_s$ non-diagonal matrix $a_{s's}$, which constructs linear combinations of the degenerate unperturbed eigenfunctions. The ansatz for eigenfunctions outside the degenerate subspace remains unchanged.

To solve for $a_{s's}$, we repeat the steps for non-degenerate perturbations, see Sec. D.1. Substituting this new ansatz into Eqn. D.6 and grouping terms order by order gives the ϵ^n equation:

$$\left(\hat{H}^{(0)} - \lambda_s^{(0)}\right) \mathop{\sum\!\!\!\!\!\!\!\int}_k{}' c_{ks}^{(n)} \left|k^{(0)}\right\rangle + \left(\hat{H}^{(n)} - \lambda_s^{(n)}\right) \sum_{s'} a_{s's} \left|s'^{(0)}\right\rangle \;=\; -\sum_{m=1}^{n-1} \left(\hat{H}^{(m)} - \lambda_s^{(m)}\right) \mathop{\sum\!\!\!\!\!\!\!\int}_k{}' c_{ks}^{(n-m)} \left|k^{(0)}\right\rangle \tag{D.20}$$

We form two inner products with Eqn. D.20. One with an arbitrary unperturbed eigenfunction from the degenerate subspace, $\phi_{s''}^{(0)}$, and another with an arbitrary unperturbed eigenfunction from outside the degenerate subspace, $\phi^{(0)}_{k'}$, respectively:

$$\begin{aligned}
\cancel{\left(\lambda^{(0)}_{s''} - \lambda^{(0)}_s\right)} c^{(n)}_{s''s} + \sum_{s'} \left(H^{(n)}_{s''s'} - \lambda^{(n)}_s \delta_{s''s'}\right) a_{s's} &= -\sum_{m=1}^{n-1} \sum\!\!\!\!\!\!\int_k{}' \left(H^{(m)}_{s''k} - \cancel{\lambda^{(m)}_s \delta_{s''k}}\right) c^{(n-m)}_{ks} \quad \text{(D.21)} \\
\left(\lambda^{(0)}_{k'} - \lambda^{(0)}_s\right) c^{(n)}_{k's} + \sum_{s'} \left(H^{(n)}_{k's'} - \cancel{\lambda^{(n)}_s \delta_{k's'}}\right) a_{s's} &= -\sum_{m=1}^{n-1} \sum\!\!\!\!\!\!\int_k{}' \left(H^{(m)}_{k'k} - \lambda^{(m)}_s \delta_{k'k}\right) c^{(n-m)}_{ks} \quad \text{(D.22)}
\end{aligned}$$

Considering the $n = 1$ equations makes the r.h.s. zero. By definition, $a_{ks} = 0$. Since this is a second-order degeneracy, we have already diagonalized the first-order perturbation within the degenerate subspace, i.e. $H^{(1)}_{s''s} = 0$ for $s'' \neq s$. Thus, Eqn. D.21 gives:

$$\begin{aligned}
0 &= \sum_{s'} \left(H^{(1)}_{s''s'} - \lambda^{(1)}_s \delta_{s''s'}\right) a_{s's} \\
&= \left(H^{(1)}_{s''s''} - \lambda^{(1)}_s\right) a_{s''s} \\
&\quad \Longrightarrow H^{(1)}_{ss} = \lambda^{(1)}_s \ , \qquad \text{(D.23)}
\end{aligned}$$

which is expected, because the first-order perturbation has already been diagonalized and $\lambda^{(0)}_{s''} = \lambda^{(0)}_s$. Considering Eqn. D.22 where k is chosen to be outside the degenerate subspace we have:

$$\sum_{s'} H^{(1)}_{ks'} a_{s's} = -\left(\lambda^{(0)}_k - \lambda^{(0)}_s\right) c^{(1)}_{ks} \ . \tag{D.24}$$

For $n = 2$, Eqn. D.21 gives:

$$\sum_{s'} \left(H^{(2)}_{s''s'} - \lambda^{(2)}_s \delta_{s''s'}\right) a_{s's} = -\sum\!\!\!\!\!\!\int_k{}' H^{(1)}_{s''k} c^{(1)}_{ks} \ . \tag{D.25}$$

Using Eqn. D.24 to replace $c^{(1)}_{ks}$, we have:

$$0 = \sum_{s'} \left(H^{(2)}_{s''s'} - \lambda^{(2)}_{s'} \delta_{s''s'} + \sum\!\!\!\!\!\!\int_k{}' \frac{H^{(1)}_{s''k} H^{(1)}_{ks'}}{\lambda^{(0)}_k - \lambda^{(0)}_{s''}} \right) a_{s's} \ , \tag{D.26}$$

This is a secular equation for our unknown matrix $a_{s's}$. The eigenvectors of this matrix,

$$A_{s's} = H^{(2)}_{s's} + \sum_k{}' \frac{H^{(1)}_{s'k} H^{(1)}_{ks}}{\lambda^{(0)}_k - \lambda^{(0)}_{s'}} \ , \tag{D.27}$$

provide the linear combinations of degenerate eigenfunctions that diagonalize the degenerate block of total Hamiltonian up to second order. The eigenvalues of this matrix are the $\lambda^{(2)}_s$. This approach can be taken to higher orders by considering $n \geq 2$ in Eqns. D.21 and D.22

The derivation in Crawford & Kemble [82, 157] highlights that the new ansatz, Eqn. D.19, represents a unitary transformation on our Hamiltonian. Denoting this transformation by $\hat{T}(\epsilon) = \exp\left(i\epsilon\hat{S}\right)$, with $\hat{S}$ a Hermitian matrix, we have:

$$\begin{aligned}
\hat{G}(\epsilon) \equiv & \qquad \hat{T}^{\dagger}\hat{H}\hat{T} \\
=& \left(1 - i\epsilon\hat{S} - \frac{\epsilon}{2}\hat{S}^2 + \ldots\right)\left(\hat{H}^{(0)} + \epsilon\hat{H}^{(1)} + \epsilon^2\hat{H}^{(2)} \ldots\right)\left(1 + i\epsilon\hat{S} - \frac{\epsilon}{2}\hat{S}^2 + \ldots\right) \\
=& \hat{H}^{(0)} + \epsilon \underbrace{\left(\hat{H}^{(1)} + i\left(\hat{H}^{(0)}\hat{S} - \hat{S}\hat{H}^{(0)}\right)\right)}_{\hat{G}^{(1)}} + \qquad \qquad (\text{D.28}) \\
& + \epsilon^2 \underbrace{\left(\hat{H}^{(2)} + i\left(\hat{H}^{(1)}\hat{S} - \hat{S}\hat{H}^{(1)}\right) + \hat{S}\hat{H}^{(0)}\hat{S} - \frac{1}{2}\left(\hat{H}^{(0)}\hat{S}^2 + \hat{S}^2\hat{H}^{(0)}\right)\right)}_{\hat{G}^{(2)}} + \\
& + \epsilon^3\hat{G}^{(3)} + \ldots , \qquad \qquad (\text{D.29})
\end{aligned}$$

where

$$\begin{aligned}
\hat{G}^{(3)} =& \hat{H}^{(3)} + i\left(\hat{H}^{(2)}\hat{S} - \hat{S}\hat{H}^{(2)}\right) + \hat{S}\hat{H}^{(1)}\hat{S} - \frac{1}{2}\left(\hat{H}^{(1)}\hat{S}^2 + \hat{S}^2\hat{H}^{(1)}\right) \\
& + \frac{i}{2}\left(\hat{S}\hat{H}^{(0)}\hat{S}^2 + \hat{S}^2\hat{H}^{(0)}\hat{S}\right) - \frac{i}{6}\left(\hat{H}^{(1)}\hat{S}^3 + \hat{S}^3\hat{H}^{(1)}\right)
\end{aligned}$$

To remove a second-order degeneracy, we wish to find an $\hat{S}$ that removes those parts of $\hat{G}^{(1)}$ that couple degenerate and non-degenerate states. That is,

$$\left[\begin{array}{c|c} \left\langle k\middle|\hat{G}^{(1)}\middle|k'\right\rangle & \left\langle k\middle|\hat{G}^{(1)}\middle|s'\right\rangle \\ \hline \left\langle s\middle|\hat{G}^{(1)}\middle|k'\right\rangle & \left\langle s\middle|\hat{G}^{(1)}\middle|s'\right\rangle \end{array}\right] = \left[\begin{array}{c|c} \left\langle k\middle|\hat{H}^{(1)}\middle|k'\right\rangle & \mathcal{O}(\epsilon^2) \\ \hline \mathcal{O}(\epsilon^2) & \left\langle s\middle|\hat{H}^{(1)}\middle|s'\right\rangle \end{array}\right] , \tag{D.30}$$

where k denotes states outside the degenerate subspace, and s the degenerate states. The three kinds of blocks in Eqn. D.30 determine $\hat{S}$. The two blocks on the diagonal indicate that $\hat{S}$ must leave these blocks of $\hat{H}^{(1)}$ unchanged:

$$\begin{aligned} \left\langle k\middle|\hat{H}^{(1)}\middle|k'\right\rangle &= \left\langle k\middle|\hat{G}^{(1)}\middle|k'\right\rangle \Longrightarrow S_{kk'} = 0 \\ \left\langle s\middle|\hat{H}^{(1)}\middle|s'\right\rangle &= \left\langle s\middle|\hat{G}^{(1)}\middle|s'\right\rangle \Longrightarrow S_{ss'} = 0 \end{aligned}$$

The off-diagonal blocks give:

$$\begin{aligned} \mathcal{O}(\epsilon^2) &= \left\langle k\middle|\hat{G}^{(1)}\middle|s\right\rangle \\ &= \left\langle k\middle|\hat{H}^{(1)} + i\left(\hat{H}^{(0)}\hat{S} - \hat{S}\hat{H}^{(0)}\right)\middle|s\right\rangle \\ &\Longrightarrow S_{ks} = \frac{iH^{(1)}_{ks}}{\lambda^{(0)}_k - \lambda^{(0)}_s} = S^*_{sk} \ . \end{aligned} \tag{D.31}$$

Substituting $\hat{S}$ into Eqn. D.28, we obtain the transformed Hamiltonian. The $g_s \times g_s$ submatrix of $\hat{G}^{(2)}$ is

$$\begin{aligned} G^{(2)}_{ss'} &= i\left({\sum\!\!\!\!\!\!\int}'_k H^{(1)}_{sk}\frac{iH^{(1)}_{ks'}}{\lambda^{(0)}_k - \lambda^{(0)}_{s'}} - \frac{iH^{(1)}_{sk}}{\lambda^{(0)}_s - \lambda^{(0)}_k}H^{(1)}_{ks'}\right) + \\ &\quad \cancel{+ {\sum\!\!\!\!\!\!\int}'_k \left(\frac{iH^{(1)}_{sk}}{\lambda^{(0)}_s - \lambda^{(0)}_k}\lambda^{(0)}_k\frac{iH^{(1)}_{ks'}}{\lambda^{(0)}_k - \lambda^{(0)}_{s'}} - \frac{1}{2}\left(\lambda^{(0)}_s\frac{iH^{(1)}_{sk}}{\lambda^{(0)}_s - \lambda^{(0)}_k}\frac{iH^{(1)}_{ks'}}{\lambda^{(0)}_k - \lambda^{(0)}_{s'}} + \frac{iH^{(1)}_{sk}}{\lambda^{(0)}_s - \lambda^{(0)}_k}\frac{iH^{(1)}_{ks'}}{\lambda^{(0)}_k - \lambda^{(0)}_{s'}}\lambda^{(0)}_{s'}\right)\right)} \\ &= {\sum\!\!\!\!\!\!\int}'_k H^{(1)}_{sk}H^{(1)}_{ks'}\left(\frac{1}{\lambda^{(0)}_{s'} - \lambda^{(0)}_k} + \frac{1}{\lambda^{(0)}_s - \lambda^{(0)}_k}\right) \longrightarrow 2\,{\sum\!\!\!\!\!\!\int}'_k \frac{H^{(1)}_{sk}H^{(1)}_{ks'}}{\lambda^{(0)}_s - \lambda^{(0)}_k} \ , \end{aligned} \tag{D.32}$$

where the arrow in Eqn. D.32 results when the second-order degeneracy results from a eigenvalues that are equal at zeroth order – not just at first order.

The $g_s \times g_s$ submatrix of $\hat{G}^{(3)}$ is

$$
\begin{aligned}
G^{(3)}_{ss'} =& H^{(3)}_{ss'} + i\left(\sum\!\!\!\!\!\!\!\int_k{}' \, H^{(2)}_{sk} \frac{iH^{(1)}_{ks'}}{\lambda^{(0)}_k - \lambda^{(0)}_{s'}} - \frac{iH^{(1)}_{sk}}{\lambda^{(0)}_s - \lambda^{(0)}_k} H^{(2)}_{ks'} \right) + \\
&+ \sum\!\!\!\!\!\!\!\int_k{}' \left(\frac{iH^{(1)}_{sk}}{\lambda^{(0)}_s - \lambda^{(0)}_k} \sum\!\!\!\!\!\!\!\int_{k'}{}' \, H^{(1)}_{kk'} \frac{iH^{(1)}_{k's'}}{\lambda^{(0)}_{k'} - \lambda^{(0)}_{s'}} - \frac{1}{2} \sum\!\!\!\!\!\!\!\int_{s''} \left(H^{(1)}_{ss''} \frac{iH^{(1)}_{s''k}}{\lambda^{(0)}_{s''} - \lambda^{(0)}_k} \frac{iH^{(1)}_{ks'}}{\lambda^{(0)}_k - \lambda^{(0)}_{s'}} + \frac{iH^{(1)}_{sk}}{\lambda^{(0)}_s - \lambda^{(0)}_k} \frac{iH^{(1)}_{ks''}}{\lambda^{(0)}_k - \lambda^{(0)}_{s''}} H^{(}_{s'} \right.\right. \\
&+ \frac{i}{2} \left(\frac{iH^{(1)}_{sk'}}{\lambda^{(0)}_s - \lambda^{(0)}_{k'}} \lambda^{(0)}_{k'} \cancel{\delta_{k's''}} \frac{iH^{(1)}_{s''k}}{\lambda^{(0)}_{s''} - \lambda^{(0)}_k} \frac{iH^{(1)}_{ks'}}{\lambda^{(0)}_k - \lambda^{(0)}_{s'}} + \frac{iH^{(1)}_{sk}}{\lambda^{(0)}_{s'} - \lambda^{(0)}_k} \frac{iH^{(1)}_{ks''}}{\lambda^{(0)}_k - \lambda^{(0)}_{s''}} \lambda^{(0)}_{k'} \cancel{\delta_{k's''}} \frac{iH^{(1)}_{k's'}}{\lambda^{(0)}_{k'} - \lambda^{(0)}_{s'}} \right) + \\
&- \frac{i}{6} \left(H^{(1)}_{ss''} \frac{iH^{(1)}_{s''k}}{\lambda^{(0)}_{s''} - \lambda^{(0)}_k} \cancel{\frac{iH^{(1)}_{ks'''}}{\lambda^{(0)}_k - \lambda^{(0)}_{s'''}} \frac{iH^{(1)}_{k's'}}{\lambda^{(0)}_{k'} - \lambda^{(0)}_{s'}}} + \cancel{\frac{iH^{(1)}_{sk'}}{\lambda^{(0)}_s - \lambda^{(0)}_{k'}} \frac{iH^{(1)}_{s'''k}}{\lambda^{(0)}_{s'''} - \lambda^{(0)}_k}} \frac{iH^{(1)}_{ks''}}{\lambda^{(0)}_k - \lambda^{(0)}_{s''}} H^{(1)}_{s''s'} \right) \\
=& H^{(3)}_{ss'} + \sum\!\!\!\!\!\!\!\int_k{}' \left(\frac{H^{(2)}_{sk} H^{(1)}_{ks'}}{\lambda^{(0)}_{s'} - \lambda^{(0)}_k} + \frac{H^{(1)}_{sk} H^{(2)}_{ks'}}{\lambda^{(0)}_s - \lambda^{(0)}_k} \right) + \sum\!\!\!\!\!\!\!\int_k{}' \sum\!\!\!\!\!\!\!\int_{k'}{}' \frac{H^{(1)}_{sk} H^{(1)}_{kk'} H^{(1)}_{k's'}}{\left(\lambda^{(0)}_s - \lambda^{(0)}_k\right)\left(\lambda^{(0)}_{s'} - \lambda^{(0)}_{k'}\right)} \\
&- \frac{1}{2} \sum\!\!\!\!\!\!\!\int_k{}' \sum\!\!\!\!\!\!\!\int_{s''} \left(\frac{H^{(1)}_{ss''} H^{(1)}_{s''k} H^{(1)}_{ks'}}{\left(\lambda^{(0)}_{s''} - \lambda^{(0)}_k\right)\left(\lambda^{(0)}_{s'} - \lambda^{(0)}_k\right)} + \frac{H^{(1)}_{sk} H^{(1)}_{ks''} H^{(1)}_{s''s'}}{\left(\lambda^{(0)}_s - \lambda^{(0)}_k\right)\left(\lambda^{(0)}_{s''} - \lambda^{(0)}_k\right)} \right) .
\end{aligned}
\qquad \text{(D.33)}
$$

These formulas differ by a factor of one-half from Crawford & Kemble [82, 157], which may have a minor error (or perhaps I do).

D.3 Periodic Potentials

Periodic potentials arise frequently in modeling solids and other materials. For example, electrons moving through a crystal experience a periodic potential from the lattice of atoms. The free particle Hamiltonian has plane wave eigenfunctions, and by adding a periodic potential, one couples plane wave states that have the same energy. This leads to singularities in the formalism of non-degenerate perturbation theory, so one must replace the plane waves with a new function basis in the degenerate subspace – this is degenerate perturbation theory.

We illustrate this procedure in one dimension using periodic boundary conditions, which is the usual approach. Then, to clarify details, we impose alternative boundary conditions. Modifying the boundary conditions affects the Hilbert space of functions on which the Hamiltonian acts.

Denote the unperturbed Hamiltonian by $\hat{H}^{(0)} \equiv \nu\nabla^2$, where ν takes on different meanings for different models. For quantum mechanics, $\nu = -\hbar^2/(2m)$, so that $\hat{H}^{(0)} = -\hbar^2\nabla^2/(2m) = \hat{p}^2/(2m)$, where $\hat{p} = -i\hbar\nabla$ is the momentum. For a diffusing particle, $\nu = \mu k_b T$, where μ is the mobility, which describes the dissipative interactions of the particles with the medium. In low symmetry situations ν can be a tensor, e.g. for rod-like particles or crowded media with concentration gradients or other orienting influences.

The perturbing potential, $V(x;a)$, is a periodic function, $V(x+a) = V(x)$, which is controlled by a small parameter, ϵ, so the total Hamiltonian is:

$$\hat{H} = \nu\nabla^2 + \epsilon V(x;a) \ .$$

The resulting equations of motion for a state function $\phi(x,t)$ are:

$$\dot{\phi} = \nu\nabla^2\phi + \epsilon V(x;a)\phi \ .$$

For a time-independent potential, the time variable is easily integrated by substituting $\phi(x,t) = e^{\lambda t}\phi(x)$,

$$\lambda\phi(x) = \nu\nabla^2\phi(x) + \epsilon V(x;a)\phi(x) \ , \tag{D.34}$$

where λ is now the eigenvalue of our time-independent Hamiltonian. For quantum mechanics, $\lambda = E$, the energy. λ can be complex, and for a system in which ϕ represents a physical concentration, a positive real part of λ indicates the emergence of spatio-temporal patterns.

The periodic potential mixes eigenstates of the Laplacian, and some of these eigenstates will have the same eigenvalues. Nonetheless, these eigenfunctions are indeed different, and therefore have distinct sets of quantum numbers. In this case, these additional quantum numbers come from translational invariance of the total Hamiltonian. Translation by any integer multiple of a commutes with the full Hamiltonian, i.e. $\hat{T}_a\hat{H} = \hat{H}\hat{T}_a$. As discovered independently by Gaston Floquet[49], George W. Hill[52], Alexander M. Lyapunov[53], and Felix Bloch[66], the differential equations resulting from such a periodic potential have eigenfunctions that simultaneously diagonalizes the Laplacian and the translation operator. These eigenfunctions take the general form:

$$\psi_k = e^{ikx}u_k(x)\,,$$

where u_k has the same periodicity, a.

D.3.1 Periodic Boundary Conditions

The easiest boundary condition to consider is macroscopic periodicity – also known as Born–von Karman boundary conditions. For a one dimensional solid of N atoms on a lattice of spacing a, one implements periodic boundary conditions by requiring that functions defined on the lattice are smooth and continuous across the ends, i.e. $f(0) = f(Na)$ and also $f'(0) = f'(Na)$. The length of the lattice is $L = Na$.

With these boundary conditions, the eigenfunctions of ∇^2 are any linear combination of sines or cosines with wavelengths commensurate with L, which we write as

$$\phi_k^{(0)}(x) = \frac{e^{i\frac{2\pi k}{L}x}}{\sqrt{L}} = \frac{e^{i2\pi ku}}{\sqrt{L}}\,,$$

with $k \in \mathbb{Z}$ and $x = uL$ with $u \in [0,1]$. Note that $\sin(\pi ku)$ with an odd value of k would be continuous across the boundary, but its derivative would not be. This requires full periods of sine. Thus, requiring continuity of first derivatives ensures that all higher derivatives are also continuous. Since the $\phi_k^{(0)}$ form a complete basis, this further implies that all functions in this Hilbert space are infinitely smooth across the boundary.

These wave functions are normalized so that

$$\left\langle \phi_j^{(0)} \middle| \phi_k^{(0)} \right\rangle = \int_0^1 du \, \overbrace{\sqrt{g}}^{=L} \, \phi_j^{(0)*} \phi_k^{(0)} = \delta_{jk} \ .$$

The eigenvalues of $\hat{H}^{(0)} \phi_k^{(0)} = \lambda_k^{(0)} \phi_k^{(0)}$ are $\lambda_k^{(0)} = -\nu (2\pi k / L)^2$.

Since the domain of these functions is bounded, it provides compact support for the Hilbert space. This compactness causes the eigenvalues of the Laplacian to be discrete.

By construction, the perturbing potential of periodicity a also obeys these macroscopic periodic boundary conditions: $V(x) = V(x + nL) = V(x + nNa)$. The Fourier components of $V(u)$ are non-zero only for integer multiples of $K = 2\pi/a = 2\pi N/L$. Writing the potential as a function of dimensionless $u = x/L$:

$$V(u) = \sum_{p=-\infty}^{\infty} \tilde{V}_{pN} e^{i2\pi pNu} \ . \tag{D.35}$$

From this, one calculates the matrix elements of $V(u)$ in the unperturbed basis:

$$\begin{aligned} \mathcal{V}_{jk} &= \left\langle \phi_j^{(0)} \middle| V(u) \middle| \phi_k^{(0)} \right\rangle \\ &= \int_0^1 \frac{e^{-ijx}}{\sqrt{L}} V(u) \frac{e^{ikx}}{\sqrt{L}} L \, du \\ &= \sum_{p=-\infty}^{\infty} \tilde{V}_{pN} \int_0^1 e^{-i2\pi ju} e^{i2\pi pNu} e^{i2\pi ku} du \\ &= \sum_{p=-\infty}^{\infty} \tilde{V}_{pN} \delta_{j-k,pN} \ . \end{aligned} \tag{D.36}$$

By choosing the minimum potential energy to be zero energy, we ensure that the $p = 0$ Fourier component is zero, $\tilde{V}_0 = 0$, and therefore $\mathcal{V}_{kk} = 0$ for all k.

To write the matrix elements in a manifestly self-adjoint manner, we write the Fourier components of the potential in terms of an amplitude and a phase, $\tilde{V}_{pN} = |\tilde{V}_{pN}| \exp(i\theta_{pN})$. Since $V(u)$ is real, the Fourier coefficients $\tilde{V}_{pN} = \tilde{V}^*_{-pN}$, and therefore:

$$\begin{aligned}
|\tilde{V}_{pN}|\exp(i\theta_{pN}) &= |\tilde{V}_{-pN}|\exp(-i\theta_{-pN}) \\
\Longrightarrow \frac{|\tilde{V}_{pN}|}{|\tilde{V}_{-pN}|} &= \exp(i(\theta_{pN} + \theta_{-pN})) = 1 \\
\Longrightarrow \theta_{pN} &= -\theta_{-pN} \ .
\end{aligned}$$

Where the = 1 on the penultimate line follows from the constraints that the left side is real and positive, and the right side has a magnitude of one. Using this, we can reorganize the sum in the matrix element so that it is manifestly equal to its conjugate transpose:

$$\begin{aligned}
\mathcal{V}_{jk} &= \sum_{p=1}^{\infty}\left(\tilde{V}_{pN}\delta_{j-k,pN} + \tilde{V}_{-pN}\delta_{j-k,-pN}\right) \\
&= \sum_{p=1}^{\infty}\left(|\tilde{V}_{pN}|\exp(i\theta_{pN})\delta_{j-k,pN} + |\tilde{V}_{-pN}|\exp(i\theta_{-pN})\delta_{k-j,pN}\right) \\
&= \sum_{p=1}^{\infty}|\tilde{V}_{pN}|\left(e^{i\theta_{pN}}\delta_{j-k,pN} + e^{-i\theta_{pN}}\delta_{k-j,pN}\right) \ . \qquad \text{(D.37)}
\end{aligned}$$

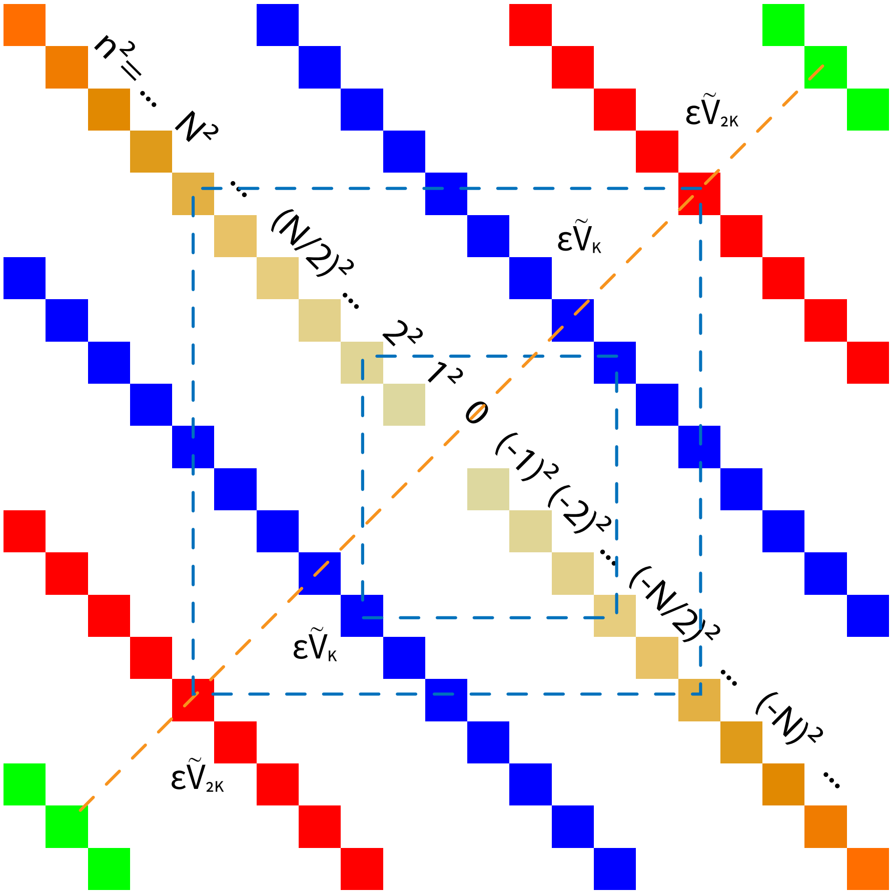

Figure D-1: The matrix is non-zero on diagonal stripes only. The blue, red, and green diagonal lines are fixed values of $\tilde{V}_{pN}$. The center diagonal is $\lambda_k^{(0)} = -\nu\left(2\pi k/L\right)^2$ is symmetric around its center point. Elements near the dashed orange line ($j = -k$) lead to near degeneracies. For example, the inner dashed blue box illustrates a two-by-two matrix with nearly equal diagonal elements.

Naively applying non-degenerate perturbation theory, one constructs the perturbative expansion for the eigenvalue:

$$\begin{aligned}
\lambda_k &= \lambda_k^{(0)} + \epsilon\cancel{\mathcal{V}_{kk}} + \epsilon^2 \sum_{j\neq k} \frac{\mathcal{V}_{kj}\mathcal{V}_{jk}}{\lambda_k^{(0)} - \lambda_j^{(0)}} + \mathcal{O}(\epsilon^3) \\
&= \lambda_k^{(0)} + \epsilon^2 \sum_{j\neq k} \frac{\left(\sum_{p_1=-\infty}^{\infty} \tilde{V}_{p_1 N}\delta_{k-j,p_1 N}\right)\left(\sum_{p_2=-\infty}^{\infty} \tilde{V}_{p_2 N}\delta_{j-k,p_2 N}\right)}{\lambda_k^{(0)} - \lambda_j^{(0)}} + \dots \\
&= \lambda_k^{(0)} + \epsilon^2 \sum_{p_1,p_2=-\infty}^{\infty} \frac{\tilde{V}_{p_1 N}\tilde{V}_{p_2 N}\delta_{p_1,-p_2}}{\lambda_k^{(0)} - \lambda_{k+p_2 N}^{(0)}} + \dots \\
&= \lambda_k^{(0)} + \epsilon^2 \sum_{p=-\infty}^{\infty} \frac{\left|\tilde{V}_{pN}\right|^2}{\lambda_k^{(0)} - \lambda_{k-pN}^{(0)}} + \dots \; . \qquad \text{(D.38)}
\end{aligned}$$

Here we encounter a problem: when $k \approx pN/2$, the denominator approaches zero, because $\lambda_k^{(0)} = \lambda_{-k}^{(0)}$. Introducing p_δ by

$$k = \frac{pN}{2} + p_\delta ,$$

Eqn. D.38 becomes:

$$\lambda_k = \lambda_k^{(0)} + \epsilon^2 \sum_{p=-\infty}^{\infty} \frac{\left|\tilde{V}_{pN}\right|^2}{-\nu \left(\frac{2\pi pN}{L}\right)^2 \frac{2p_\delta}{pN}} + \dots . \tag{D.39}$$

Clearly, when p_δ is zero or sufficiently small, we must use degenerate perturbation theory.

Figure D-1 illustrates the structure of the full Hamiltonian matrix. The system size $L = Na$ provides an IR cutoff, so the matrix elements are discrete rather than continuous. However, a has not been specified as a UV cutoff, so the matrix is infinite dimensional.

Fortunately, for large enough N there are so many zero elements in the Hamiltonian that applying degenerate perturbation theory is simple. While several states near $k = pN/2$ may have p_δ small enough to require degenerate treatment, each is connected to only one other state of similar energy. Other non-zero matrix elements are far enough away that they connect states of very different energy.

For each value of p in Eqn. D.37, we can solve the degeneracy by considering just a two-by-two matrix, like the one illustrated by the smaller blue dashed square in Fig. D-1 for the first Brillouin zone (BZ):

$$\begin{bmatrix} \lambda_{k-pN}^{(0)} & \epsilon\tilde{V}_{-pN} \\ \epsilon\tilde{V}_{pN} & \lambda_k^{(0)} \end{bmatrix} . \tag{D.40}$$

The eigenvalues of this matrix are the corrected eigenvalues up to first order:

$$\begin{aligned}\lambda_k^{(0+1)}(\pm) &= \overbrace{\frac{1}{2}\left(\lambda_k^{(0)} + \lambda_{k-pN}^{(0)} \pm 2\epsilon|\tilde{V}_{pN}|\sqrt{1+\left(\frac{\lambda_k^{(0)} - \lambda_{k-pN}^{(0)}}{2\epsilon|\tilde{V}_{pN}|}\right)^2}\right)}^{\text{eigenvalues of two-by-two matrix}} \\ &\xrightarrow{k=pN/2} \lambda_k^{(0)} \pm \epsilon|\tilde{V}_{pN}|\,. \end{aligned} \tag{D.41}$$

As shown on the last line, exactly at the BZ edge, $p_\delta = 0$, the perturbation splits the eigenvalues to produce a band gap. The exact same split appears at $-k$. Slightly away from the BZ edge, the diagonal elements of Eqn. D.40 are not equal. The larger unperturbed eigenvalue acquires a correction that smoothly connects it to the larger value at $p_\delta = 0$, and the smaller eigenvalue smoothly connects to the smaller value at the BZ edge. Thus, for p_δ positive, we can pull the larger of the unperturbed eigenvalues out of $\lambda^{(0+1)}(+)$, and the smaller out of $\lambda^{(0+1)}(-)$, to obtain:

$$0 < p_\delta \implies \begin{cases} \lambda_k^{(0+1)}(+) = \underbrace{\lambda_k^{(0)}}_{-\nu\left(\frac{2\pi k}{L}\right)^2} \quad \underbrace{+\epsilon|\tilde{V}_{pN}|\overbrace{\left(-\frac{\beta_k}{\alpha} + \sqrt{1+\left(\frac{\beta_k}{\alpha}\right)^2}\right)}^{F_+(k)}}_{\lambda_k^{(1)}} \\ \lambda_k^{(0+1)}(-) = \underbrace{\lambda_{k-pN}^{(0)}}_{-\nu\left(\frac{2\pi(k-pN)}{L}\right)^2} \quad \overbrace{-\epsilon|\tilde{V}_{pN}|\underbrace{\left(-\frac{\beta_k}{\alpha} + \sqrt{1+\left(\frac{\beta_k}{\alpha}\right)^2}\right)}_{F_+(k)}}^{\lambda_{k-pN}^{(1)}} \end{cases}, \tag{D.42}$$

where we have defined the ratio of energies,

$$\begin{aligned}\frac{\beta_k}{\alpha} &= \frac{\lambda^{(0)}_k - \lambda^{(0)}_{k-pN}}{2\epsilon|\tilde{V}_{pN}|} \\ &= -\frac{\nu \frac{2\pi\left(k-\frac{pN}{2}\right)}{L}\frac{2\pi pN}{L}}{\epsilon|\tilde{V}_{pN}|} \\ &= \underbrace{\frac{\lambda^{(0)}_{pN/2}}{\epsilon|\tilde{V}_{pN}|}}_{1/\alpha}\underbrace{\frac{4p_\delta}{pN}}_{\beta_k} .\end{aligned}$$

The ratio α is itself a ratio of energies: magnitude of the perturbation relative to exactly degenerate unperturbed eigenvalue. The ratio β_k is a ratio of integers: four times p_δ divided by the p-th harmonic of the perturbation's fundamental frequency:

$$\beta = \frac{4p_\delta}{pN} = \frac{4k}{pN} - 2 .$$

p_δ is the relative distance in Fourier space from exact degeneracy. Note that for $p_\delta < 0$, the relative magnitudes of $\lambda^{(0)}_k$ and $\lambda^{(0)}_{k-pN}$ are reversed, and thus they swap roles in Eqn. D.42. This role reversal will appear again when we construct a new eigenbasis below.

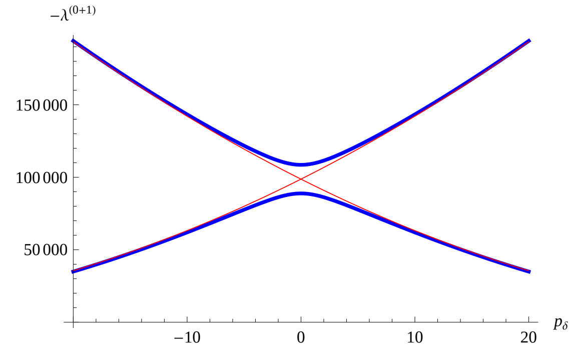

Figure D-2: Eigenvalues with first order corrections as a function of p_δ, see Eqn. D.42, in units of $\nu = 1$, $L = 1$, $\epsilon\left|\tilde{V}_{pN}\right| = \frac{1}{10}\lambda^{(0)}_{pN/2}$, and $pN = 100$.

An important feature of Eqn. D.42 is that both eigenvalues depend on $F_+(k)$, which tends to zero as $\beta >> \alpha$, i.e. far from BZ edge. We can also define an $F_-(k)$ with a minus sign in front of the square root, however it grows to $\approx -2\beta_k/\alpha$ far from the BZ edge. Fig. D-2 plots Eqn. D.42 for example values. Since both α and β may be small, one must take care in the order of applying limits or expanding in a series. All values of $\beta_k \leq \alpha$ are nearly degenerate in the sense that our perturbative expansion does not converge. To remedy this, we will construct a new eigenbasis from linear combinations of the unperturbed eigenfunctions that diagonalize the perturbation for nearly degenerate values of β_k, thus omitting these terms from our perturbative expansion.

To compute second order corrections, one would Taylor expand Eqn. D.42 to second order, choose a range of p_δ values to treat as degenerate, and exclude these values from the sum in Eqn. D.38, which provides additional second order corrections through intermediate states.

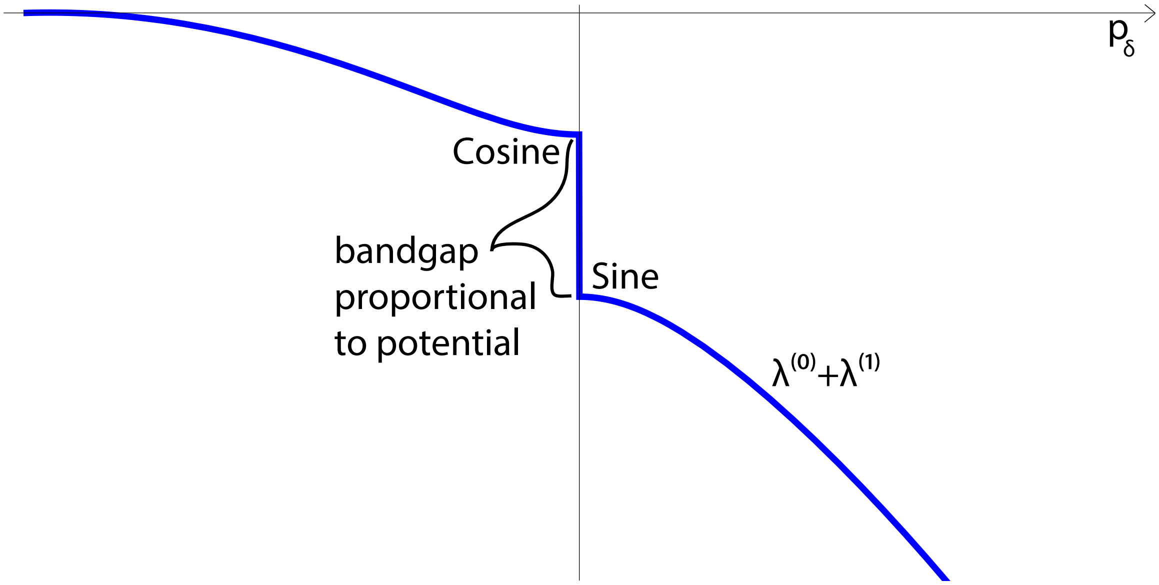

p_δ
Cosine
bandgap proportional to potential
Sine
$\lambda^{(0)}+\lambda^{(1)}$

Figure D-3: The periodic potential opens a gap in the spectrum at half the periodicity. Degenerate perturbation theory shows the perturbed eigenfunctions on either side of the gap connect with sine and cosine standing waves constructed from superpositions of the unperturbed basis functions.

Turning attention to the eigenfunctions. As the perturbation turns off, each perturbed eigenfunction connects with the unperturbed eigenfunction labeled by the corresponding unperturbed eigenvalue. When multiple eigenfunctions have the same eigenvalue, the perturbed eigenfunction connects with a particular linear combination of these *degenerate* eigenfunctions. Since e^{ikx} and e^{-ikx} have the same eigenvalue, $\lambda_{\pm k}^{(0)} = -k^2$, we must figure out the particular linear combination that connects with the perturbed eigenfunctions for each value of k. Away from exact degeneracy, the perturbation mixes states of similar but distinctly different eigenvalues, so one must apply quasi-degenerate perturbation theory. Exactly at the BZ edge, the perturbation mixes two eigenfunctions in the exact same degenerate subspace. Using the eigenvectors of the two-by-two matrix, we find that at the BZ edge, as $\epsilon \to 0$, the perturbed eigenfunctions connect with these two unperturbed eigenfunctions:

$$\begin{aligned}
\phi^{-}_{sk} &= \frac{e^{is\phi}e^{-i\frac{\phi_p}{2}}}{\sqrt{2\pi R_0}}\sqrt{\frac{2}{L}}\sin\left(\pi pNu + \frac{\phi_p}{2}\right) \\
\phi^{+}_{sk} &= \frac{e^{is\phi}e^{-i\frac{\phi_p}{2}}}{\sqrt{2\pi R_0}}\sqrt{\frac{2}{L}}\cos\left(\pi pNu + \frac{\phi_p}{2}\right) \ ,
\end{aligned}$$

where ϕ_p is the phase of $\tilde{r}_{pN}$. The sine mode has the more negative eigenvalue. This is essentially identical to the textbook analysis of a one-dimensional crystal that shows that electrons localize around the positively charged atomic sites.

Before computing eigenfunction corrections, we must construct a new eigenbasis of unperturbed eigenfunctions that prevent $\hat{V}$ from connect states of nearly equal energy. That is, we must diagonalize $\hat{V}$ in each two-dimensional k-subspace where $\beta_k \leq \alpha$.

To construct this new eigenbasis, we examine the eigenvectors of the two-by-two matrix, Eqn. D.40. Generally, the eigenvectors of a two-by-two matrix,

$$M = \begin{pmatrix} a & b \\ c & d \end{pmatrix} \ ,$$

are:

$$\vec{\boldsymbol{v}}_c^{\pm} = \begin{pmatrix} -d + \overbrace{\frac{\mathrm{Tr}(M)}{2} \pm \sqrt{\frac{\mathrm{Tr}(M)^2}{4} - \det(M)}}^{\text{eigenvalue}_\pm} \\ c \end{pmatrix} \propto \begin{pmatrix} b \\ -a + \underbrace{\frac{\mathrm{Tr}(M)}{2} \pm \sqrt{\frac{\mathrm{Tr}(M)^2}{4} - \det(M)}}_{\text{eigenvalue}_\pm} \end{pmatrix} = \vec{\boldsymbol{v}}_b^{\pm} \ ,$$

where $v_c^\pm$ represents the two vectors on the left, and $v_b^\pm$ the two on the right. $v_c^\pm$ points in the same directions as $v_b^\pm$ with a different magnitude – they are simply rescaled. Now, restrict attention to our self-adjoint matrices, $a = \lambda^{(0)}_{k-pN}$ and $d = \lambda^{(0)}_{k}$

and $b^* = c = \epsilon \tilde{V}_{pN}$. For $p_\delta \geq 0$, $a \geq d$ and the eigenvectors become:

$$\begin{aligned}
\vec{\boldsymbol{v}}_c^+ &= \begin{pmatrix} -\lambda_k^{(0)} + \lambda_k^{(0+1)}(+) \\ \epsilon|\tilde{V}_{pN}|e^{i\theta_{pN}} \end{pmatrix} \propto \begin{pmatrix} \epsilon|\tilde{V}_{pN}|e^{-i\theta_{pN}} \\ -\lambda_{k-pN}^{(0)} + \lambda_k^{(0+1)}(+) \end{pmatrix} = \vec{\boldsymbol{v}}_b^+ \\
\vec{\boldsymbol{v}}_c^- &= \begin{pmatrix} -\lambda_k^{(0)} + \lambda_k^{(0+1)}(-) \\ \epsilon|\tilde{V}_{pN}|e^{i\theta_{pN}} \end{pmatrix} \propto \begin{pmatrix} \epsilon|\tilde{V}_{pN}|e^{-i\theta_{pN}} \\ -\lambda_{k-pN}^{(0)} + \lambda_k^{(0+1)}(-) \end{pmatrix} = \vec{\boldsymbol{v}}_b^- \ .
\end{aligned}$$

Noting that these combinations of λ's simplify,

$$\begin{aligned}
-\lambda_k^{(0)} + \lambda_k^{(0+1)}(\pm) &= \epsilon|\tilde{V}_{pN}|F_\pm(k) \\
-\lambda_{k-pN}^{(0)} + \lambda_k^{(0+1)}(\pm) &= -\epsilon|\tilde{V}_{pN}|F_\mp(k),
\end{aligned}$$

and normalizing the vectors gives:

$$\hat{v}^\pm \equiv \hat{v}_c^\pm = \frac{1}{\sqrt{1+F_\pm(k)^2}} \begin{pmatrix} e^{-i\theta_{pN}/2}F_\pm(k) \\ e^{i\theta_{pN}/2} \end{pmatrix} = \begin{pmatrix} e^{-i\theta_{pN}/2} \\ -e^{i\theta_{pN}/2}F_\mp(k) \end{pmatrix} \frac{\pm 1}{\sqrt{1+F_\mp(k)^2}} = \hat{v}_b^\pm \ .$$

We show $\hat{v}_b^\pm$ as indication of the various identities the result from the special structure of $F_\pm$.

As above, we write the Fourier components of the potential in terms of an amplitude and a phase, $\tilde{V}_{pN} = |\tilde{V}_{pN}|\exp(i\theta_{pN})$, the new eigenfunctions of each degenerate subspaces described by an instance of the matrix in Eqn. D.40 are

$$\phi_k^\pm = \phi_k^{(0)} + \phi_{k-pN}^{(0)} e^{i\theta_{pN}} \underbrace{\left(-\frac{\beta}{\alpha} \pm \sqrt{1 + \left(\frac{\beta}{\alpha}\right)^2} \right)}_{F_\pm(k) = F_\pm(p(k), p_\delta(k))} \ . \tag{D.43}$$

For each non-zero Fourier mode, $\tilde{V}_{pN}$, with $p \in 1, 2, 3...$, we replace all the nearly degenerate basis functions $\phi_k^{(0)}$ around $k \approx \pm N(p - 1/2)$ with the new linear combination $\phi_k^\pm$. The matrix of the potential in this new basis is diagonal in this problematic region. How large a range of k is appropriate? The range of states to replace can be at most the N states between $(p-1)N$ and pN. Beyond this region, this particular combination of states becomes non-orthogonal. In principle, for small perturbations and large N, the range can be much smaller.

The integer p in Eqn. D.43 is the BZ number in a repeating zone scheme. For example, near the first BZ's edge, k in the range $0 < k \leq N$, $\phi_k^{(0)}$ gets paired with $\phi_{k'}^{(0)}$ in the range $-N < k \leq 0$. For the p-th BZ, $\phi^{(0)}_{(p-1)N<k\leq pN}$ gets paired with $\phi^{(0)}_{-pN<k'\leq-(p-1)N}$. If $\tilde{V}_{pN} = 0$ for a particular value of p, then there is no need to replace the original basis functions for that range of k.

The mixing coefficient $F_\pm(k)$ is more properly described as a function of

$$p(k) = (k + N/2) \text{ div } N$$

and

$$p_\delta(k) = (k \bmod (N/2)) - (N/2)\,,$$

because $\alpha = \alpha(p)$ and $\beta = \beta(p_\delta)$.

Exactly on the BZ boundary, $p_\delta = 0$ so $\beta = 0$, and the amplitude for left and right moving plane waves in $\phi_k^\pm$ are equal, which produces two standing waves. This is Bragg scattering. For an attractive potential, the lower energy standing wave, ϕ_k^- is a sine wave with peaks aligned with the potential.

An electron injected into such a material is described by a wave packet covering a range of wave numbers. The group velocity $v_g = \partial\lambda_k/\partial k$ is zero at the boundary of a BZ, so an electron described by a wave packet with momentum centered near the boundary of a BZ moves very slowly through the material.

Considering a purely sinusoidal potential, i.e. $p = 1$ only, this modified eigenbasis is orthogonal:

$$\begin{aligned}
\left\langle \phi_j^\pm \middle| \phi_k^\pm \right\rangle &= \left\langle \phi_{j-pN}^{(0)} \middle| \phi_{k-pN}^{(0)} \right\rangle + \left\langle \phi_j^{(0)} \middle| \phi_k^{(0)} \right\rangle e^{-i\theta_{pN}} F_\pm(j) e^{i\theta_{pN}} F_\pm(k) \\
&\quad + \left\langle \phi_j^{(0)} \middle| \phi_{k-pN}^{(0)} \right\rangle e^{-i\theta_{pN}} F_\pm(j) + \left\langle \phi_{j-pN}^{(0)} \middle| \phi_k^{(0)} \right\rangle e^{i\theta_{pN}} F_\pm(k) \\
&= \delta_{j,k}(1 + F_\pm(j)F_\pm(k)) + \delta_{j,k-pN} e^{-i\theta_{pN}} F_\pm(j) + \delta_{j-pN,k} e^{i\theta_{pN}} F_\pm(k)
\end{aligned}$$

The matrix elements in this new eigenbasis are related to the $\mathcal{V}_{jk}$ from Eqn. D.37.

We denote the new matrix elements with a superscript ±± to indicate the left and right eigenfunctions:

$$\begin{aligned}
\mathcal{V}^{\pm\pm}_{jk} &= \left\langle \phi^{\pm}_{j} \middle| V(u) \middle| \phi^{\pm}_{k} \right\rangle \\
&= \mathcal{V}_{j-N,k-N} + \mathcal{V}_{j,k} F_{\pm}(j) F_{\pm}(k) + \mathcal{V}_{j,k-N} e^{-i\theta_N} F_{\pm}(j) + \mathcal{V}_{j-N,k} e^{i\theta_N} F_{\pm}(k) \\
&= \left|\tilde{V}_N\right| \left(e^{i\theta_N} \delta_{j-k,N} + e^{-i\theta_N} \delta_{k-j,N} \right) \left(1 + F_{\pm}(j) F_{\pm}(k)\right) \\
&\quad + \left(e^{i\theta_N} \delta_{j-k+N,N} + e^{-i\theta_N} \delta_{k-N-j,N} \right) e^{-i\theta_N} F_{\pm}(j) + \left(e^{i\theta_N} \delta_{j-N-k,N} + e^{-i\theta_N} \delta_{k-j+N,N} \right) e^{i\theta_N} F_{\pm}(k) \\
&= \left|\tilde{V}_N\right| \left(e^{i\theta_N} \delta_{j-k,N} + e^{-i\theta_N} \delta_{k-j,N} \right) \left(1 + F_{\pm}(j) F_{\pm}(k)\right) \\
&\quad + \left(\delta_{j,k} + e^{-i2\theta_N} \delta_{k-j,2N} \right) F_{\pm}(j) + \left(e^{i2\theta_N} \delta_{j-k,2N} + \delta_{k,j} \right) F_{\pm}(k) \ ,
\end{aligned}$$

which equals zero for $j = -k$:

$$\begin{aligned}
\mathcal{V}^{\pm\pm}_{-k,k} &= \left|\tilde{V}_N\right| \left(e^{i\theta_N} \delta_{-2k,N} + e^{-i\theta_N} \delta_{2k,N} \right) \left(1 + F_{\pm}(-k) F_{\pm}(k)\right) \\
&\quad + \left(\delta_{-k,k} + e^{-i2\theta_N} \delta_{k,N} \right) F_{\pm}(-k) + \left(e^{i2\theta_N} \delta_{k,-N} + \delta_{k,-k} \right) F_{\pm}(k) \\
&= \left|\tilde{V}_N\right| \left(e^{i\theta_N} \delta_{-2k,N} + e^{-i\theta_N} \delta_{2k,N} \right) \left(1 + F_{\pm}(-k) F_{\pm}(k)\right) \\
&\quad + F_{\pm}(0) + F_{\pm}(0) + e^{-i2\theta_N} \delta_{k,N} F_{\pm}(-k) + e^{i2\theta_N} \delta_{k,-N} F_{\pm}(k) \\
&\quad ,
\end{aligned} \tag{D.44}$$

D.3.2 Limit of Infinity System Size

We now reduce wave number spacing to zero by taking the double limit $L, N \to \infty$ such that their ratio $L/N = a$ remains constant. Alternatively, we could have taken $a \to 0$ and $N \to \infty$ while keeping their product constant $L = Na$. To illustrate, we preserve a and take system size to infinity.

Taking both left and right boundaries to infinity and assuming periodic boundary conditions at infinity, the eigenfunctions of ∇^2 are any linear combination of sines or cosines with any wavelengths, which we write as $\phi^{(0)}_k(x) = e^{ikx}/\sqrt{2\pi}$ with $k \in \mathbb{R}$. This is normalized so that

$$\left\langle \phi^{(0)}_j \middle| \phi^{(0)}_k \right\rangle = \int_{-\infty}^{\infty} dx \, \phi^{(0)*}_j \phi^{(0)}_k = \delta(j - k) \ , \tag{D.45}$$

where this is a Dirac delta distribution, rather than the previous Kronecker delta. The eigenvalues of $\hat{H}^{(0)}\phi_k^{(0)} = \lambda_k^{(0)}\phi_k^{(0)}$ are now $\lambda_k^{(0)} = -\nu k^2$, and k has dimensions $[L]^{-1}$.

This unbounded domain is non-compact, and therefore the Hilbert space lacks compact support. This underlies the change of normalization for the eigenfunctions and switch to a continuous spectrum for the Laplacian.

The perturbing potential of periodicity a now offers the only length scale: $V(x) = V(x+na)$. As before, the Fourier components of $V(x)$ are non-zero only for integer multiples of $K = 2\pi/a$, so Eqn. D.35 applies again. Instead of using the integration variable $u = x/L$, one must integrate the dimensionful x from $[-\infty, \infty]$ and one obtains exactly the matrix elements of $V(x)$ as Eqn. D.37 with the Kronecker delta replaced by a Dirac delta function.

$$\mathcal{V}_{jk} = \sum_{n=-\infty}^{\infty} \tilde{V}_{nK}\delta(k - j + nK)\,, \tag{D.46}$$

As before, by choosing the minimum potential energy to be zero energy, we ensure that the $n = 0$ Fourier component is zero, $\tilde{V}_0 = 0$, and therefore $\mathcal{V}_{kk} = 0$ for all k.

To apply non-degenerate perturbation theory, one constructs the perturbative expansion for the eigenvalue:

$$\lambda_k \;=\; \lambda_k^{(0)} + \epsilon\cancel{\mathcal{V}_{kk}} + \epsilon^2 \int_{-\infty}^{\infty} dq \frac{\mathcal{V}_{kq}\mathcal{V}_{qk}}{\lambda_k^{(0)} - \lambda_q^{(0)} + i\epsilon'} + \mathcal{O}(\epsilon^3)\;, \tag{D.47}$$

where the $i\epsilon'$ prescription avoids the pole at $q = k$ on the real axis. This does not prevent the singularities that arise from Bragg scattering when attempting to apply non-degenerate perturbation theory. Carrying the integration leads to the same result as Eqn. D.38. Just as before, modes near the boundaries of Brillouin zones are nearly degenerate. Fig. D-1 carries over with the modification that the matrix indices are now continuous. The eigenvectors and eigenvalues of the matrix in Eqn. D.40 are essentially the same with N eliminated by taking its ratio with L and the identification that p_δ is now a real number instead of restricted to integers.

D.3.3 Non-Periodic Boundary Conditions

We now restrict the Hilbert space by replacing the periodic boundary conditions with non-periodic Dirichlet boundary conditions. This means that in setting up our original problem, Eqn. D.34, we specify the *value* of ϕ at the boundary. Alternatively, we could specify its derivative (Neumann B.C.) or a combination of the two. A constant offset satisfies a Dirichlet boundary condition, so our non-constant basis functions must equal zero at the boundaries. This forbids the cosine component of $\exp(ikx)$. The eigenfunctions of ∇^2 are sine waves with wavelengths commensurate with L, which we write as

$$\begin{aligned}\phi_k^{(0)}(x) &= \sqrt{\frac{2}{L}}\sin\left(\frac{2\pi k}{L}x\right)\\ &= \sqrt{\frac{2}{L}}\sin(2\pi k u)\ ,\end{aligned} \tag{D.48}$$

with $k \in \mathbb{Z}$. The eigenvalues of $\hat{H}^{(0)}\phi_k^{(0)} = \lambda_k^{(0)}\phi_k^{(0)}$ are $\lambda_k^{(0)} = -\nu(\pi k/L)^2$.

We now briefly consider a more general potential with periodicity a that is not necessarily commensurate with L, i.e. $N = L/a \in \mathbb{R}$ instead of being restricted to integers. In addition to non-commensurate periodicity, there may be a phase shift such that $V(x = 0) \neq 0$. As before, we require that $V(x) = V(x + na)$, so the Fourier components of $V(x)$ are non-zero only for integer multiples of $K = 2\pi/a = 2\pi N/L$, however these Fourier modes need not be the same as the eigenfunctions of the Laplacian:

$$\begin{aligned}V(x) &= \sum_{p=-\infty}^{\infty}\tilde{V}_{pN}\sin\left(\frac{2\pi pN}{L}(x - x_0)\right)\\ &= \sum_{p=-\infty}^{\infty}\tilde{V}_{pN}\sin\left(2\pi pN(u - u_0)\right)\ ,\end{aligned} \tag{D.49}$$

where x_0 is the smallest argument for which the potential is zero, i.e. $V(x_0) = 0$. Again, we switch to dimensionless coordinates $u = x/L$ and $u_0 = x_0/L$. From this, one calculates the matrix elements of $V(x)$ in the unperturbed basis:

$$\begin{aligned}\mathcal{V}_{jk} &= \left\langle \phi_j^{(0)} \middle| V(x) \middle| \phi_k^{(0)} \right\rangle \\ &= \sum_{p=-\infty}^{\infty} \tilde{V}_{pN} \int_0^1 \sin(\pi j u)\sin(\omega_p(u-u_0))\sin(\pi k u)2du\ , \end{aligned} \tag{D.50}$$

where $\omega_p \equiv 2\pi pL/a$ is the Fourier frequency of the potential. This expression causes immediate concern, because $\int \sin^3$ is zero – unless the integration does not cover a full period or phase shifts or wavelengths are non-commensurate. We investigate these exceptions below.

After making trigonometric substitutions, we have:

$$\begin{aligned}\mathcal{V}_{jk} &= \sum_{p=-\infty}^{\infty} \tilde{V}_{pN} \int_0^1 \left(e^{i\pi ju} - e^{-i\pi ju}\right)\left(e^{i\omega_p(u-u_0)} - e^{-i\omega_p(u-u_0)}\right)\left(e^{i\pi ku} - e^{-i\pi ku}\right)\frac{i}{4}du \\ &= \sum_{p=-\infty}^{\infty} \tilde{V}_{pN} \int_0^1 \left(e^{i\pi(j+k)u} + e^{-i\pi(j+k)u} - e^{i\pi(j-k)u} - e^{-i\pi(j-k)u}\right)\left(e^{i\omega_p(u-u_0)} - e^{-i\omega_p(u-u_0)}\right)\frac{i}{4}du \\ &= \sum_{p=-\infty}^{\infty} \tilde{V}_{pN} \int_0^1 \left(\cos(\pi(k-j)u) - \cos(\pi(k+j)u)\right)\left(\sin(\omega_p u)\cos(\omega_p u_0) - \cos(\omega_p u)\sin(\omega_p u_0)\right)du \\ &= \sum_{p=-\infty}^{\infty} \tilde{V}_{pN} \begin{pmatrix} \cos(\omega_p u_0) \\ -\sin(\omega_p u_0) \end{pmatrix} \cdot \int_0^1 \begin{pmatrix} \sin(\omega_p u) \\ \cos(\omega_p u) \end{pmatrix} \left(\cos(\pi(k-j)u) - \cos(\pi(k+j)u)\right)du \\ &= \sum_{p=-\infty}^{\infty} \tilde{V}_{pN} \begin{pmatrix} \cos(\omega_p u_0) \\ -\sin(\omega_p u_0) \end{pmatrix} \cdot \begin{pmatrix} (-1)^{j+k} - \cos(\omega_p) \\ \sin(\omega_p) \end{pmatrix} \frac{-2jk\omega_p(-1)^{j+k}}{((j-\omega_p/\pi)^2-k^2)((j+\omega_p/\pi)^2-k^2)\pi^2}\ . \end{aligned} \tag{D.51}$$

The three length scales, a, L, and x_0, make for a rich space of possible behaviors that [117, Aubry] has studied. Even when L/a is an integer, Fig. D-1 is not an accurate description for non-periodic boundary conditions. Examples in Fig. D-4 illustrate how the perturbation matrix now contains anti-diagonal stripes in addition to the diagonal stripes of the periodic case.

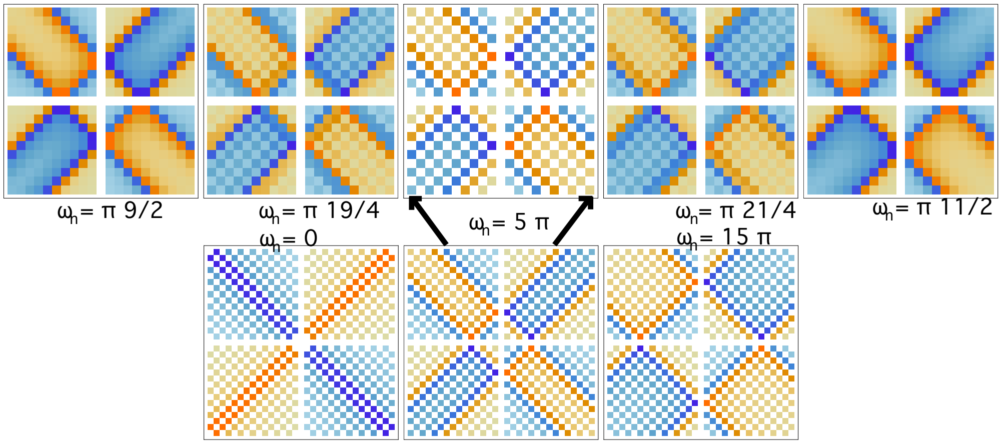

Figure D-4: Examples of $\mathcal{V}_{jk}$ in Fourier space for various values of ω_p. The lower row illustrates how wavelengths commensurate with L lead to alternating zero and non-zero values. The upper row illustrates how non-commensurate wavelengths blur the matrix into all non-zero values.

The system size L determines the spacing of the Laplacian's discretized eigenvalues. The wavelength of the potential, a, modifies the magnitude of the potential's Fourier coefficients in the basis of the Laplacian's eigenfunctions. One can segment the parameter space by considering three regimes for a: $a >> L$ to $a \approx L$ to $a << L$, and also whether L/a is irrational, rational, half-integer, or integer valued.

The matrix is symmetric in several ways: $\mathcal{V}_{jk} = \mathcal{V}_{kj}$, and $\mathcal{V}_{j,k} = -\mathcal{V}_{-j,k} = -\mathcal{V}_{j,-k}$, and also $\mathcal{V}_{-j,k} = \mathcal{V}_{-k,j}$. The diagonal and cross diagonal are equal with opposite sign. For $u_0 = 0$ and $L/a = N/2$ with integer N, the diagonals are:

$$-\mathcal{V}_{-kk} = \mathcal{V}_{kk} = \sum_{p=1}^{\infty} \frac{4\,\mathrm{Im}\left(\tilde{V}_{pN}\right) k^2 \left(1 - (-1)^{pN}\right)}{pN\pi(2k - pN)(2k + nN)} \,, \tag{D.52}$$

which illustrates why there are no poles in $\mathcal{V}_{jk}$: the denominator only equals zero when pN is even, which is exactly when the numerator is zero.

As expected, various restrictions on L/a, u_0, and the Laplacian's eigenfunctions can make all elements zero, $\mathcal{V}_{jk} = 0$. For example, taking $u_0 = m\pi/\omega_n$, with integer m, selects the upper element of the column vectors in the dot product in Eqn. D.51. Further requiring full-period eigenfunctions of the Laplacian restricts j and k to even values. In this case, if $L/a = N$ is integer, then $\omega_p = 2\pi pN$ and all elements zero.

Non-zero elements arise for odd values of j and k, or non-integer values of L/a.

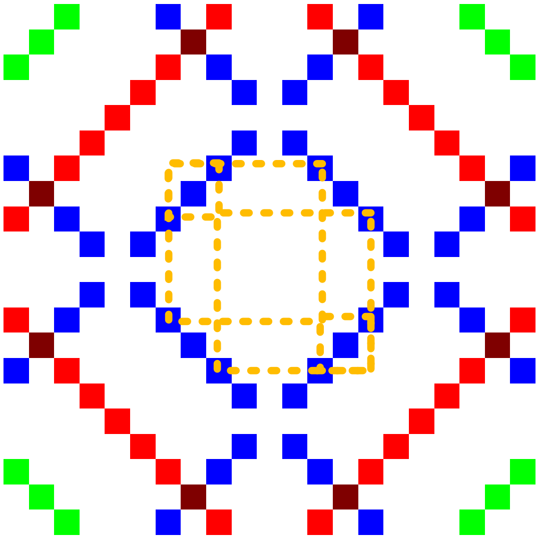

Figure D-5: Illustration of $\mathcal{V}_{jk}$ for a cosine potential in a space with sine eigenfunctions, such as a non-periodic compact space. The diagonal stripes are the same as Fig. D-1, and the anti-diagonal stripes are of equal and opposite magnitude. The two orange boxes indicate the near degeneracy that results from the anti-diagonal stripes crossing the center diagonal at $pN/2$, which is also where the off-diagonal stripes cause degeneracy. The four corners of the orange boxes that sit on the center diagonal represent states of nearly equal energies that get mixed by the perturbation.

An offset of $u_0 = (2m+1)\pi/2\omega_n$, with integer m, selects the lower element in the dot product in Eqn. D.51. In this case, if $L/a = N/2$ is integer or half integer, then $\omega_p = \pi p N$ and most elements are zero – but not all! This choice of u_0 corresponds to shifting the potential by a quarter period, so that Eqn. D.49 becomes:

$$V(x) = \sum_{p=-\infty}^{\infty} \tilde{V}_{pN} (-1)^m \cos\left(\pi p N u\right) \ . \tag{D.53}$$

This leads to $\mathcal{V}_{jk} \sim \int \sin^2 \cos$, which evaluates to a set of four Kronecker delta functions.Note that for real-valued $V(x)$, the Fourier coefficients are real, so $\tilde{V}_{-pN} = \tilde{V}_{pN}$.

For simplicity, take $m = 0$. In the following, we allow the more general eigenfunctions $\sin(\pi k u)$ with possibly odd values of k.

$$\mathcal{V}_{jk} = \sum_{p=-\infty}^{\infty} \tilde{V}_{pN} \frac{1}{2} \left(-\delta_{j,-k+pN} + \delta_{j,k+pN}\right) \ . \tag{D.54}$$

This matrix is illustrated in Fig. D-5. This has the same diagonal stripes as Fig. D-1 plus additional anti-diagonal stripes of equal and opposite magnitude.

Considering the non-degenerate perturbative expansion:

$$\lambda_k \quad = \quad \lambda_k^{(0)} + \epsilon \mathcal{V}_{kk} + \epsilon^2 \sum_{j \neq k} \frac{\mathcal{V}_{kj}\mathcal{V}_{jk}}{\lambda_k^{(0)} - \lambda_j^{(0)}} + \mathcal{O}(\epsilon^3) \ ,$$

The term linear in ϵ results from the anti-diagonal element crossing the main diagonal:

$$\mathcal{V}_{kk} = \begin{cases} -\frac{\tilde{V}_{nK}}{2} & \text{if } k = n\frac{K}{2} = (nN)\frac{\pi}{Na}, n \in \mathbb{Z} \\ 0 & \text{otherwise} \end{cases} \tag{D.55}$$

The term quadratic in ϵ has more structure than the periodic case:

$$\begin{aligned}
&\sum_{j \neq k} \frac{1}{4} \frac{1}{\lambda_k^{(0)} - \lambda_j^{(0)}} \sum_{n,m=-\infty}^{\infty} \tilde{V}_{nK}\tilde{V}_{mK}(-\delta_{n_k,-n_j+nN} + \delta_{n_k,n_j+nN})(-\delta_{n_j,-n_k+mN} + \delta_{n_j,n_k+mN}) \\
&\frac{1}{4} \sum_{n,m=-\infty}^{\infty} \tilde{V}_{nK}\tilde{V}_{mK} \sum_{j \neq k} \left(\frac{\delta_{n_k,-n_j+nN}\delta_{n_j,-n_k+mN}}{\lambda_k^{(0)} - \lambda_j^{(0)}} + \frac{\delta_{n_k,n_j+nN}\delta_{n_j,n_k+mN}}{\lambda_k^{(0)} - \lambda_j^{(0)}} - \frac{\delta_{n_k,-n_j+nN}\delta_{n_j,n_k+mN}}{\lambda_k^{(0)} - \lambda_j^{(0)}} - \frac{\delta_{n_k,n_j+nN}\delta_{n_j,-n_k}}{\lambda_k^{(0)} - \lambda_j^{(0)}} \right. \\
&\frac{1}{4} \sum_{n,m=-\infty}^{\infty} \tilde{V}_{nK}\tilde{V}_{mK} \left(\frac{\delta_{n_k,n_k-mN+nN}}{\lambda_k^{(0)} - \lambda_{-k+mK}^{(0)}} + \frac{\delta_{n_k,n_k+mN+nN}}{\lambda_k^{(0)} - \lambda_{k+mK}^{(0)}} - \frac{\delta_{n_k,-n_k-mN+nN}}{\lambda_k^{(0)} - \lambda_{k+mK}^{(0)}} - \frac{\delta_{n_k,-n_k+mN+nN}}{\lambda_k^{(0)} - \lambda_{-k+mK}^{(0)}} \right) \\
&\frac{1}{4} \sum_{n,m=-\infty}^{\infty} \tilde{V}_{nK}\tilde{V}_{mK} \left(\frac{\delta_{m,n}}{\lambda_k^{(0)} - \lambda_{-k+mK}^{(0)}} + \frac{\delta_{m,-n}}{\lambda_k^{(0)} - \lambda_{k+mK}^{(0)}} - \frac{\delta_{mN,nN-2n_k}}{\lambda_k^{(0)} - \lambda_{k+mK}^{(0)}} - \frac{\delta_{mN,-nN+2n_k}}{\lambda_k^{(0)} - \lambda_{-k+mK}^{(0)}} \right) \\
&\frac{1}{4} \sum_{n=-\infty}^{\infty} \left(\frac{\tilde{V}_{nK}\tilde{V}_{nK}}{\lambda_k^{(0)} - \lambda_{-k+nK}^{(0)}} + \frac{\tilde{V}_{nK}\tilde{V}_{-nK}}{\lambda_k^{(0)} - \lambda_{k+nK}^{(0)}} - \tilde{V}_{nK} \mathrm{IsInt}\left(\frac{2n_k}{N}\right) \left(\frac{\tilde{V}_{-2k+nK}}{\lambda_k^{(0)} - \lambda_{k-2k+nK}^{(0)}} + \frac{\tilde{V}_{2k-nK}}{\lambda_k^{(0)} - \lambda_{-k+2k-nK}^{(0)}} \right) \right) ,
\end{aligned} \tag{D.56}$$

where IsInt() is one if its argument is an integer and zero otherwise. Next, we exploit the fact that the sum ranges over positive and negative integers and also that $\lambda_k^{(0)} =$

$\lambda_{-k}^{(0)}$ and $\tilde{V}_{-nK} = \tilde{V}_{nK}$:

$$\begin{aligned}
&\frac{1}{4}\sum_{n=-\infty}^{\infty}\left(\frac{\tilde{V}_{-nK}\tilde{V}_{-nK}}{\lambda_k^{(0)} - \lambda_{k+nK}^{(0)}} + \frac{\tilde{V}_{nK}\tilde{V}_{-nK}}{\lambda_k^{(0)} - \lambda_{k+nK}^{(0)}} - \tilde{V}_{nK}\mathrm{IsInt}\left(\frac{2n_k}{N}\right)\left(\frac{\tilde{V}_{-2k+nK}}{\lambda_k^{(0)} - \lambda_{-k+nK}^{(0)}} + \frac{\tilde{V}_{2k-nK}}{\lambda_k^{(0)} - \lambda_{k-nK}^{(0)}}\right)\right)\\
&\frac{1}{4}\sum_{n=-\infty}^{\infty}\left(\frac{\tilde{V}_{nK}^2}{\lambda_k^{(0)} - \lambda_{k+nK}^{(0)}} - \mathrm{IsInt}\left(\frac{2n_k}{N}\right)\frac{\tilde{V}_{nK}\tilde{V}_{nK-2k}}{\lambda_k^{(0)} - \lambda_{k-nK}^{(0)}}\right)\\
&\frac{1}{4}\sum_{n=-\infty}^{\infty}\left(\frac{\tilde{V}_{nK}^2}{\lambda_k^{(0)} - \lambda_{k+nK}^{(0)}} - \mathrm{IsInt}\left(\frac{2n_k}{N}\right)\frac{\tilde{V}_{-nK}\tilde{V}_{-nK-2k}}{\lambda_k^{(0)} - \lambda_{k+nK}^{(0)}}\right)\\
&\frac{1}{2}\sum_{n=-\infty}^{\infty}\frac{\tilde{V}_{nK}\left(\tilde{V}_{nK} - \tilde{V}_{nK+2k}\mathrm{IsInt}\left(\frac{2n_k}{N}\right)\right)}{\lambda_k^{(0)} - \lambda_{k+nK}^{(0)}}\\
&\frac{1}{2}\sum_{n=-\infty}^{\infty}\frac{\tilde{V}_{nK}\left(\tilde{V}_{nK} - \tilde{V}_{nK-2k}\mathrm{IsInt}\left(\frac{2k}{K}\right)\right)}{\lambda_k^{(0)} - \lambda_{k-nK}^{(0)}}\ ,
\end{aligned} \tag{D.57}$$

which is degenerate when $k = nK/2$. While this satisfies the IsInt(), it generates $\tilde{V}_0$, which is zero, so the exactly degenerate case gets an additional term that is identical to the periodic boundary condition case:

$$\lambda_{nK/2} \quad = \quad \lambda_{nK}^{(0)} + \epsilon\left|\tilde{V}_{nK}\right|\left(-\frac{1}{2} \pm 1\right) + \mathcal{O}(\epsilon^2)\ ,$$

The case of near degeneracy is more complex, because the anti-diagonals mix states of similar energy where they cross the central diagonal. Instead of the two-by-two matrix encountered previously, we have the four-by-four matrix illustrated in Fig. D-5:

$$\begin{bmatrix}
\lambda_{n(K/2)+k_\delta}^{(0)} & -\epsilon\tilde{V}_{nK} & \epsilon\tilde{V}_{nK} & 0\\
-\epsilon\tilde{V}_{nK}^* & \lambda_{n(K/2)-k_\delta}^{(0)} & 0 & \epsilon\tilde{V}_{nK}\\
\epsilon\tilde{V}_{nK}^* & 0 & \lambda_{-n(K/2)+k_\delta}^{(0)} & -\epsilon\tilde{V}_{nK}\\
0 & \epsilon\tilde{V}_{nK}^* & -\epsilon\tilde{V}_{nK}^* & \lambda_{-n(K/2)-k_\delta}^{(0)}
\end{bmatrix}, \tag{D.58}$$

where $k_\delta = (n_\delta)\pi/L$ indicates the number of discrete wave number steps away from exact degeneracy. For each value of $|n| = 1, 2, 3, \ldots$, and each value of $|k_\delta L/\pi| = |p_\delta| = 1, 2, 3, \ldots$, there is a set of four nearly degenerate eigenvalues that are connected by

$V(x)$:

$$\left\{\lambda_s^{(0)}\middle| s = (-1)^a n\frac{K}{2} + (-1)^b k_\delta \text{ with } a, b \in \{0,1\}\right\} \ , \tag{D.59}$$

where we have introduced the binary parameters a and b. The eigenvalues of this matrix in Eqn. D.58 are:

$$\lambda_s = \left\{-\nu n^2 K^2 \left(1 \pm \left(\frac{k_\delta}{nK}\right)^2\right), -\nu n^2 K^2 \left(1 + \left(\frac{k_\delta}{nK}\right)^2\right) \pm 2\epsilon \left|\tilde{V}_{nK}\right| \sqrt{1 + \left(\frac{\nu n K k_\delta}{\epsilon \left|\tilde{V}_{nK}\right|}\right)^2}\right\} \ . \tag{D.60}$$

Bibliography

[1] Aristotle. *Historia animalium*. Trans. by D'Arcy Wentworth Thompson. The Clarendon Press, 1910 (circa 350 B.C.E.). URL: `https://archive.org/details/historiaanimaliu00aris_0/page/n263/mode/2up?q=embryo`.

[2] Euclid. *Euclid's Thirteen Elements*. Ed. by Thomas Little Heath. Trans. by Johan Ludvig Heiberg. 1908 (circa 300 B.C.E.). URL: `https://archive.org/details/thirteenbookseu03heibgoog`. Oldest extant copy of Euclid's elements from 850 C.E. found by Heiberg at the Vatican.

[3] Titus Carus Lucretius. *On the Nature of Things [*De rerum natura*]*. Trans. by William Ellery Leonard. 2008 (circa 60 B.C.E.). URL: `https://www.gutenberg.org/files/785/785-h/785-h.htm`.

[4] Leonardo da Vinci. *Paris Manuscript M*. Bibliothèque de l'Institut de France, 1500, 78v–79r. URL: `http://www.universalleonardo.org/work.php?id=323`. Late 1490s-1500. See all the pages scanned in Wikipedia. The tree rule is on page 78v The smallest of Leonardo's surviving manuscripts, Manuscript M focuses on the study of Euclid's geometry, ballistics and botany, with important theories regarding the growth of trees. This notebook also provides evidence of Leonardo's contacts with Donato Bramante, who became the most important high Renaissance architect, and designer of the new St. Peter's Basilica in Rome. The manuscript consists of 48 folios in their original binding.

[5] Leonardo da Vinci. *Paris Manuscript F*. Bibliothèque de l'Institut de France, 1508, p. 37v. URL: `http://www.universalleonardo.org/work.php?id=477`. 1508-1513. See all the pages scanned in Wikipedia. The spiralling water bubble is on page 37v. The main subjects of Manuscript F are water, the science of optics, geology and astronomy. Leonardo also poses interesting cosmological questions in this manuscript, as he speculates on the nature of light on the moon, the origins of its spots, and the appearance of the earth as it would be seen by someone standing on the moon. The compactness of the writing and homogeneity of writing style in this manuscript indicates that it was compiled during a relatively short time span. The manuscript comprises of 96 folios.

[6] Gerardus Mercator. *Nova et Aucta Orbis Terrae Descriptio ad Usum Navigantium Emendate Accommodata (Renaissance Latin for "New and more complete representation of the terrestrial globe properly adapted for use in navigation")*. 1569.

[7] Galileo Galilei. *Sidereus Nuncius*. Latin and English. Trans. by Albert Van Helden. 1610. URL: `https://archive.org/details/Sidereusnuncius00Gali`.

[8] Samuel de Champlain. *The Voyages and Explorations of Samuel de Champlain (1604-1616)*. Ed. by Edward Gaylord Bourne. Trans. by Annie Nettleton. 1616.

[9] Robert Hooke. *Micrographia, or, Some physiological descriptions of minute bodies made by magnifying glasses with observations and inquiries thereupon*. Royal Society, 1665. URL: `https://archive.org/details/mobot31753000817897`.

[10] Christiaan Huygens. *Horologium Oscillatorium*. Ed. by Ian Bruce. 1673. URL: `https://www.17centurymaths.com/contents/huygenscontents.html`.

[11] Isaac Newton. "Concerning the circular motion of fluids. (Philosophiae Naturalis Principia Mathematica. 3rd Ed. Book II Section 9)". In: (1687). Ed. by Ian Bruce. URL: `https://www.17centurymaths.com/contents/newtoncontents.html`.

[12] Isaac Newton. *Principia: the mathematical principles of natural philosophy [Philosophiae naturalis principia]*. Trans. by Andrew Motte. 1687 (July 5, 1687). URL: `https://archive.org/details/newtonspmathema00newtrich`.

[13] Leonard Euler. "Principia motus fluidorum (Principles of the motion of fluids)". Trans. by Walter Pauls. In: (). URL: `https://scholarlycommons.pacific.edu/euler-works/258/`. An English translation of Euler's article "Principia motus fluidorum" in which the Euler equation (in two- and three- dimensions) was established for the first time in 1752. The actual publication has been delayed by nine years. Finally, this article has been published in 1761 in Novi Commentarii Academiae Scientiarum Petropolitanae. https://www-n.oca.eu/etc7/EE250/texts/euler1761eng.pdf See also Truesdell, 1954 "Rational Fluid Mechanics" Volume II.

[14] Leonard Euler. "Principes généraux du mouvement des fluides (General principles concerning the motion of fluids)". In: *Mémoires de l'académie des sciences de Berlin* 11 (1755), pp. 274–315. URL: `https://scholarlycommons.pacific.edu/euler-works/226/`.

[15] Leonhard Euler. "Recherches sur la courbure des surfaces". In: *Mémoires de l'Académie des Sciences de Berlin* (1767), pp. 119–143. URL: `https://scholarlycommons.pacific.edu/cgi/viewcontent.cgi?article=1332&context=euler-works`. Translated http://eulerarchive.maa.org//docs/translations/E333.pdf.

[16] Joseph Louis Lagrange. "Mémoire sur la théorie du mouvement des fluides". In: (1781). URL: `https://gallica.bnf.fr/ark:/12148/bpt6k229223s/f697`.

[17] Gaspard Monge. "Mémoire sur la théorie des déblais et des remblais [Dissertation on the theory of cuttings and embankments]". In: *Memoires de la Académie Royale des Sciences* (1781), p. 666. URL: `https://gallica.bnf.fr/ark:/12148/bpt6k35800/f796`.

[18] Pierre Simon Laplace. “Mémoire sur la théorie de l’anneau de Saturne”. In: *Mémoires de l’Académie Royale des Sciences de Paris* (1787). URL: `http://archive.org/stream/oeuvrescomplte11lapluoft#page/274/mode/2up`.

[19] Luigi Galvani. “Commentary on the Effect of Electricity on Muscular Motion [*Aloysii Galvani De viribus electricitatis in motu musculari commentarius*]”. Trans. by Margaret Glover Foley. In: (1953). URL: `http://eccoprogram.it/wp-content/uploads/GALVANI-1953-Commentary-on-the-effects-of-electricity-on-muscular-motion-pp.-45-56-73-88.pdf`. The original text scanned at the Internet Archive is evidently a copy owned by Alessandro Volta (1745-1827).

[20] Alessandro Volta. “On the electricity excited by the mere contact of conducting substances of different species.” In: *Philosophical Transactions of the Royal Society* 90 (1800), pp. 403–431. ISSN: 0261-0523. DOI: `10.1098/rstl.1800.0018`.

[21] Thomas Young. “An essay on the cohesion of fluids”. In: *Philosophical Transactions of the Royal Society of London* 95 (Dec. 20, 1804), pp. 65–87. DOI: `10.1098/rstl.1805.0005`. URL: `https://royalsocietypublishing.org/doi/10.1098/rstl.1805.0005`.

[22] Pierre Simon marquis de Laplace. *Traité de Mécanique Céleste: "Supplément au dixième livre du traité de la mécanique céleste. Sur l’action capillaire" (65 p.) et "Supplément à la théorie de l’action capillaire" (12 p.)* Paris, France, 1805, pp. 1–79. URL: `http://sciences.amisbnf.org/fr/livre/traite-de-mecanique-celeste`. Laplace published his work on capillary action in two supplements to his book on celestial mechanics. The supplements were published in 1805. scans of the book are in archive.org.

[23] J.B.J. Fourier. “Théorie analytique de la chaleur”. In: (1822). URL: `https://books.google.com/books?id=TDQJAAAAIAAJ`.

[24] Claude-Louis Navier. “Memoire sur les lois mouvement des fluides”. In: *Mém. Acad. Sci. Inst. France* 6 (1822), pp. 389–440. URL: `https://perso.crans.org/epalle/M2/EC/Histoire/Navier1822MemoireSurLesLoisDuMouvementDesFluides.pdf`.

[25] Karl Friedrich Gauss. “General Investigations of Curved Surfaces”. Trans. by Translator: James Caddall Morehead and Adam Miller Hiltebeitel. In: (1827). URL: `https://www.gutenberg.org/ebooks/36856`.

[26] Georg Simon Ohm. *Die galvanische Kette, mathematisch bearbeitet*. German. 1827. URL: `https://archive.org/details/bub_gb_tTVQAAAAcAAJ/page/n3/mode/2up`.

[27] Robert Brown F.R.S. “XXVII. A brief account of microscopical observations made in the months of June, July and August 1827, on the particles contained in the pollen of plants; and on the general existence of active molecules in organic and inorganic bodies”. In: *Philosophical Magazine Series 2* 4.21 (1828), pp. 161–173. ISSN: 1941-5850. DOI: `10.1080/14786442808674769`.

[28] George Green. "An Essay on the Application of Mathematical Analysis to the Theories of Electricity and Magnetism". In: (1828). URL: `https://archive.org/details/mathematicalpape00greerich`. See the archive.org scan of "Mathematical papers of the late George Green".

[29] Robert Brown F.R.S. "XXIV. Additional remarks on active molecules". In: *Philosophical Magazine Series 2* 6.33 (1829), pp. 161–166. ISSN: 1941-5850. DOI: `10.1080/14786442908675115`.

[30] William Wordsworth. "The Prelude, Growth of a Poet's Mind". In: (1839). URL: `http://viscomi.sites.oasis.unc.edu/viscomi/coursepack/wordsworth/Wordsworth-Prelude.pdf`. Autobiographical blank verse epic poem about his development in the natural world. Started in 1798 and written intermittently until 1839. Published posthumously in 1850.

[31] George G. Stokes. "On the 'Theories of the Internal Friction of Fluids in Motion, and of the Equilibrium and Motion of Elastic Solids". In: (1845). URL: `https://pages.mtu.edu/~fmorriso/cm310/StokesLaw1845.pdf`.

[32] Claude Shannon. "A Mathematical Theory of Communication". In: *The Bell System Technical Journal* 27.3 (July), 4 (October) (1848). Vol. 27, pp. 379–423, 623–656, July, October, 1948., pp. 379–423, 623–656. URL: `https://people.math.harvard.edu/~ctm/home/text/others/shannon/entropy/entropy.pdf`.

[33] Herman von Helmholtz. "Vorläufiger Bericht über die Fortpflanzungsgeschwindigkeit der Nervenreizung. Archiv für Anatomie, Physiologie und Wissenschaftliche Medizin". In: (1850), pp. 71–73. URL: `https://archive.org/details/b28137346/page/n7/mode/2up`. By 'Hüftgeflecht' – Helmholtz very probably meant the offspring of the nervus ischiadicus.

[34] Bernhard Riemann. "The hypotheses on which geometry is based. [Koniglichen Gesellschaft der Wissenschaften zu Gottingen, vol. 13.]" Trans. by Roger Baker, Charles Christenson, and Henry Orde. In: (June 10, 1854). URL: `https://archive.org/details/bernardrgesamm00riemrich`. See paper "XIII" in translation:

[35] A Fick. "On liquid diffusion". In: *Philos. Mag. J. Sci* 10 (1855). DOI: `doi:10.1002/andp.18551700105`.

[36] Henry Darcy. "Les fontaines publiques de la ville de Dijon: exposition et application des principes à suivre et des formules à employer dans les questions de distribution d'eau..." In: (1856). URL: `https://gallica.bnf.fr/ark:/12148/bpt6k624312/f1n657.pdf`.

[37] Hermann von Helmholtz. "On integrals of the hydrodynamic equations that correspond to vortex motions [*Über Integrale der hydrodynamischen Gleichungen, welche den Wirbelbewegungen entsprechen.*]" In: *International Journal of Fusion Energy* 1.3-4 (1978), pp. 41–68. URL: `https://21sci-tech.com/Articles_2009/Helmholtz.pdf`. The original article is Ref. [38]. Another version of the pdf is linked here.

[38] "Über Integrale der hydrodynamischen Gleichungen, welche den Wirbelbewegungen entsprechen." ger. In: *Journal für die reine und angewandte Mathematik* 55 (1858), pp. 25–55. URL: `http://eudml.org/doc/147720`.

[39] Charles Darwin. *On the Origin of Species*. Nov. 24, 1859. URL: `https://archive.org/details/originofspecies00darwuoft/page/n5/mode/2up`.

[40] James Clerk Maxwell. "Illustrations of the dynamical theory of gases. Part I. On the motions and collisions of perfectly elastic spheres". In: *Philosophical Magazine* 19 (1860), pp. 19–32.

[41] James Clerk Maxwell. "Illustrations of the dynamical theory of gases. Part II. On the process of diffusion of two or more kinds of moving particles among one another". In: *Philosophical Magazine* 20 (1860), pp. 21–37.

[42] Josiah Willard Gibbs. "On the Form of the Teeth of Wheels in Spur Gearing". 1863. URL: `https://collections.library.yale.edu/catalog/16662400`.

[43] Wilhelm Friedrich Kühne. "Untersuchungen über das Protoplasma und die Contractilität". In: (1864). DOI: `10.5962/bhl.title.11169`.

[44] E. B. Christoffel. "Ueber die Transformation der homogenen Differentialausdrücke zweiten Grades." In: *Journal für die reine und angewandte Mathematik (Crelles Journal)* 1869.70 (1869), pp. 46–70. ISSN: 0075-4102. DOI: `10.1515/crll.1869.70.46`.

[45] Josiah Willard Gibbs. "A Method of Geometrical Representation of the Thermodynamic Properties of Substances by Means of Surfaces". In: *Transactions of the Connecticut Academy of Arts and Sciences* (1873), pp. 382–3. URL: `https://esm.rkriz.net/classes/ESM4714/methods/J.W.GibbsConnAcad_1873_Vol.II_Part-1-2_.pdf`.

[46] Josiah Willard Gibbs. "Graphical Methods in the Thermodynamics of Fluids". In: *Transactions of the Connecticut Academy of Arts and Sciences* (1873), pp. 309–381. URL: `https://esm.rkriz.net/classes/ESM4714/methods/J.W.GibbsConnAcad_1873_Vol.II_Part-1-2_.pdf`.

[47] James Clerk Maxwell. *Theory Of Heat*. 4th ed. 1875. URL: `https://archive.org/details/theory-of-heat`.

[48] Ludwig Boltzmann. "Über die Beziehung zwischen dem zweiten Hauptsatz der mechanischen Wärmetheorie und der Wahrscheinlichkeitsrechnung respektive den Sätzen über das Wärmegleichgewicht." In: *Sitzungsberichte der Kaiserlichen Akademie der Wissenschaften in Wien, Mathematisch-Naturwissenschaftliche Classe. Abt. II* 76 (1877), pp. 373–435. URL: `http://crystal.med.upenn.edu/sharp-lab-pdfs/2015SharpMatschinsky_Boltz1877_Entropy17.pdf`.

[49] Gaston Floquet. "Sur les équations différentielles linéaires à coefficients périodiques". In: *Annales scientifiques de l'É.N.S* 12 (1883), pp. 47–88. URL: `http://www.numdam.org/item?id=ASENS_1883_2_12__47_0`.

[50] Leonardo da Vinci. *The literary works of Leonardo da Vinci*. Italian and English. Trans. by Jean Paul Richter. 1883. URL: `https://archive.org/details/literaryworksofl01leonuoft/page/214/mode/2up`.

[51] Henri Poincaré. "Sur les courbes définies par les équations différentielles". In: *Journal de Mathématiques Pures et Appliquées* 4 (1885), pp. 167–244.

[52] George William Hill. "On the part of the motion of the lunar perigee which is a function of the mean motions of the sun and moon". In: *Acta Mathematica* 8.1 (1886), pp. 1–36. ISSN: 0001-5962. DOI: `10.1007/bf02417081`. URL: `https://projecteuclid.org/journals/acta-mathematica/volume-8/issue-none/On-the-part-of-the-motion-of-the-lunar-perigee/10.1007/BF02417081.full`.

[53] Alexander Mihailovich Lyapunov. "The general problem of the stability of motion". Trans. by Edouard Davaux and A. T. Fuller. In: *International Journal of Control* 55.3 (1992), pp. 531–534. ISSN: 0020-7179. DOI: `10.1080/00207179208934253`.

[54] Karl Pearson. *The grammar of science*. 1892. URL: `https://archive.org/details/grammarofscience00pearuoft`.

[55] John William Strutt. *The Theory of Sound*. Vol. 2. Macmillan, 1896. URL: `https://archive.org/details/theoryofsound02raylrich/page/n7/mode/2up`. The perturbation theory was a new addition in the second volume. The first volume was published in 1877.

[56] Josiah Willard Gibbs. *Elementary Principles in Statistical Mechanics – Developed with Especial Reference to the Rational Foundation of Thermodynamics*. Charles Scribner's Sons, 1902. URL: `https://www.gutenberg.org/files/50992/50992-pdf.pdf`.

[57] A Einstein. "On the movement of small particles suspended in stationary liquids required by the molecular-kinetic theory of heat". In: *Annalen der Physik* 17 (1905), pp. 549–560. URL: `https://en.wikipedia.org/wiki/%C3%9Cber_die_von_der_molekularkinetischen_Theorie_der_W%C3%A4rme_geforderte_Bewegung_von_in_ruhenden_Fl%C3%BCssigkeiten_suspendierten_Teilchen`.

[58] William Sutherland. "LXXV. A dynamical theory of diffusion for non-electrolytes and the molecular mass of albumin". In: *Philosophical Magazine Series 6* 9.54 (1905), pp. 781–785. ISSN: 1941-5982. DOI: `10.1080/14786440509463331`.

[59] Marion Smoluchowski. "Zur kinetischen Theorie der Brownschen Molekularbewegung und der Suspensionen". In: *Annalen der Physik* 21 (14) (1906), pp. 756–780. DOI: `10.1002/andp.19063261405`. URL: `http://myweb.rz.uni-augsburg.de/~eckern/adp/history/historic-papers/1906_326_756-780.pdf`.

[60] M. Jean Perrin. *Brownian Movement and Molecular Reality*. Trans. by F. Soddy. London: Taylor and Francis, 1910. URL: `http://web.mit.edu/swangroup/footer/perrin_bm.pdf`.

[61] Edwin B Wilson and C L E Moore. "Differential Geometry of Two Dimensional Surfaces in Hyperspace". In: *Proceedings of the American Academy of Arts and Sciences* 52.6 (1916), p. 269. ISSN: 0199-9818. DOI: `10.2307/20025687`.

[62] D'Arcy Wentworth Thompson. *On Growth and Form*. Cambridge University Press, 1917. URL: `https://archive.org/details/ongrowthform00thom`.

[63] Albert Einstein. "Relativity; the special and general theory". Trans. by Robert W. Lawson. In: (1920). URL: `https://archive.org/details/cu31924011804774`.

[64] Albert Einstein. *The Meaning of Relativity: Four Lectures Delivered at Princeton University, May, 1921*. Methuen & Company Limited, 1922. URL: `https://archive.org/details/meaningofrelativ00eins`.

[65] Erwin Schrödinger. "Quantisierung als Eigenwertproblem". Trans. by Oliver F. Piattella. In: *Annalen der Physik* 385 (13 1926), pp. 437–490. DOI: `10.1002/andp.19263851302`. URL: `http://ofp.cosmo-ufes.org/uploads/1/3/7/0/13701821/quantisation_as_an_eigenvalue_problem.pdf`. See the original German text.

[66] Felix Bloch. "Über die Quantenmechanik der Elektronen in Kristallgittern". In: *Zeitschrift für Physik* 52.7–8 (1929), pp. 555–600. ISSN: 0044-3328. DOI: `10.1007/bf01339455`.

[67] JH Van Vleck. "On σ-type doubling and electron spin in the spectra of diatomic molecules". In: *Physical Review* 33.4 (1929), pp. 467–506.

[68] Kurt Gödel. "On formally undecidable propositions of Principia Mathematica and related systems". Trans. by Martin Hirzel. In: (1931). URL: `https://hirzels.com/martin/papers/canon00-goedel.pdf`.

[69] E. D. Adrian and B. H. C. Matthews. "The interpretation of potential waves in the cortex". In: *The Journal of Physiology* 81.4 (1934), pp. 440–471. ISSN: 0022-3751. DOI: `10.1113/jphysiol.1934.sp003147`.

[70] Richard Courant. *Differential and Integral Calculus, Volumes 1 & 2*. 1934.

[71] O Jordahl. "The Effect of Crystalline Electric Fields on the Paramagnetic Susceptibility of Cupric Salts". In: *Physical Review* (Jan. 1934). URL: `http://link.aps.org/doi/10.1103/PhysRev.45.87`.

[72] A. M. Turing. "On Computable Numbers, with an Application to the Entscheidungsproblem". In: *Proceedings of the London Mathematical Society* s2-42.1 (1937), pp. 230–265. ISSN: 0024-6115. DOI: `10.1112/plms/s2-42.1.230`.

[73] Claude Elwood Shannon. "A symbolic analysis of relay and switching circuits". In: *Trans. of the American Institute of Electrical Engineers* 57.12 (1938), pp. 713–723. ISSN: 0095-9197. DOI: `10.1109/ee.1938.6431064`. URL: `http://hdl.handle.net/1721.1/11173`.

[74] Joseph Needham, Arnošt Kleinzeller, Margaret Miall, Mary Dainty, Dorothy M. Needham, and A.S.C. Lawrence. "IS MUSCLE CONTRACTION ESSENTIALLY AN ENZYME-SUBSTRATE COMBINATION?" In: *Nature* 150.3793 (1942), pp. 46–49. ISSN: 0028-0836. DOI: `10.1038/150046a0`.

[75] Szent-Gyorgyi. *Muscular Contraction.* 1943. URL: `http://actin.aok.pte.hu/archives/pdf/StudiesIII_all.pdf#page=22`.

[76] "On the Theory of Superconductivity". In: *The Journal of Experimental and Theoretical Physics (JETP)* 20 (1950). DOI: `10.1007/978-3-540-68008-6_4`.

[77] A. L. Hodgkin and A. F. Huxley. "A quantitative description of membrane current and its application to conduction and excitation in nerve". In: *The Journal of Physiology* 117.4 (1952), pp. 500–544. ISSN: 0022-3751. DOI: `10.1113/jphysiol.1952.sp004764`.

[78] A. M. Turing. "The Chemical Basis of Morphogenesis". In: *Philosophical Transactions of the Royal Society of London. Series B, Biological Sciences* 237.641 (1952), pp. 37–72. ISSN: 00804622. URL: `https://royalsocietypublishing.org/doi/10.1098/rstb.1952.0012`.

[79] J.D. Watson and F.H.C. Crick. "Molecular Structure of Nucleic Acids: A Structure for Deoxyribose Nucleic Acid". In: *Nature* 171.4356 (1953), pp. 737–738. ISSN: 0028-0836. DOI: `10.1038/171737a0`.

[80] A.A. Abrikosov. "The magnetic properties of superconducting alloys". In: *Journal of Physics and Chemistry of Solids* 2.3 (1957), pp. 199–208. ISSN: 0022-3697. DOI: `10.1016/0022-3697(57)90083-5`.

[81] F. Charles Frank. "On the theory of liquid crystals". In: *Discussions of the Faraday Society* 25 (1958), pp. 19–28. ISSN: 0366-9033. DOI: `10.1039/df9582500019`.

[82] Edwin Crawford Kemble. "The fundamental principles of quantum mechanics: with elementary applications". In: (Jan. 1958), p. 611. URL: `http://books.google.com/books?id=SifVAAAAMAAJ&printsec=frontcover`.

[83] P.B. Green. "Wall structure and lateral formation in the alga Bryopsis". In: *American Journal of Botany* 47 (1960), pp. 476–481.

[84] E.H. Lockwood. *A Book of Curves.* Cambridge University Press, 1961.

[85] Thomas F. Roth and Keith R Porter. "Yolk protein uptake in the oocyte of the mosquito". In: *The Journal of Cellular Biology* 20 (1964). URL: `https://rupress.org/jcb/article-pdf/42/1/202/1263237/202.pdf`.

[86] Mark Kac. "Can One Hear the Shape of a Drum?" In: *The American Mathematical Monthly* 73.4 (1966), pp. 1–23. ISSN: 00029890, 19300972. URL: `http://www.jstor.org/stable/2313748`.

[87] Charles B. Balogh. "Asymptotic expansions of the modififed Bessel function of the third kind of imaginary order". In: *SIAM J. App. Math.* 15.5 (1967), pp. 1315–1323.

[88] Benoit B. Mandelbrot. "How Long Is the Coast of Britain? Statistical Self-Similarity and Fractional Dimension". In: *Science* 156.3775 (1967), pp. 636–638. ISSN: 0036-8075. DOI: `10.1126/science.156.3775.636`.

[89] Aristid Lindenmayer. "Mathematical models for cellular interactions in development I. Filaments with One-sided Input". In: *Journal of Theoretical Biology* 18.3 (1968), pp. 280–299. ISSN: 0022-5193.

[90] Aristid Lindenmayer. "Mathematical models for cellular interactions in development II. Simple and branching filaments with two-sided inputs". In: *Journal of Theoretical Biology* 18.3 (1968), pp. 300–315. ISSN: 0022-5193. DOI: `10.1016/0022-5193(68)90080-5`. URL: `http://www0.cs.ucl.ac.uk/staff/p.bentley/teaching/L6_reading/lsystems.pdf`.

[91] Toku Kanaseki and Ken Kadota. "The "Vesicle in a Basket": A Morphological Study of the Coated Vesicle Isolated from the Nerve Endings of the Guinea Pig Brain, with Special Reference to the Mechanism of Membrane Movements". In: *The Journal of Cell Biology* 42.1 (1969), pp. 202–220. ISSN: 0021-9525. DOI: `10.1083/jcb.42.1.202`.

[92] P.B. Canham. "The minimum energy of bending as a possible explanation of the shape of the human red blood cell". In: *J. Theoretical Biology* 26 (1970), pp. 61–81.

[93] David G. Ebin and Jerrold Marsden. "Groups of Diffeomorphisms and the Motion of an Incompressible Fluid". In: *Annals of Mathematics* (1970). URL: `https://www.jstor.org/stable/1970699`.

[94] Orsay Group. "Simplified elastic theory for Smectics C". In: *Solid State Comm.* 9 (1971), pp. 653–655.

[95] Milton Abramowitz and Irene A. Stegun. *Handbook of Mathematical Functions.* Dover Publications, Inc., 1972. ISBN: 0-486-61272-4.

[96] S.I. Anisimov and I.E. Dzyaloshinskii. "A new type of disclination in liquid crystals and the stability of disclinations of various types". In: *Soviet Physics JETP* 36 (Oct. 1, 1972), pp. 774–779.

[97] VL Berezinskii. "Destruction of long-range order in one-dimensional and two-dimensional systems possessing a continuous symmetry group". In: *Sov. Phys. JETP* 34.3 (1972), pp. 610–616.

[98] P.E. Cladis and M. Kleman. "Non-singular disclinations of strength S=+1 in nematics". In: *Journal de Physique* 33 (Jan. 14, 1972), pp. 591–598.

[99] A. Gierer and H. Meinhardt. "A theory of biological pattern formation". In: *Kybernetik* 12.1 (1972), pp. 30–39. ISSN: 0023-5946. DOI: `10.1007/bf00289234`.

[100] John M Kosterlitz and DJ Thouless. "Long range order and metastability in two dimensional solids and superfluids. (Application of dislocation theory)". In: *Journal of Physics C: Solid State Physics* 5.11 (1972), p. L124.

[101] Robert B. Meyer. "On the existence of even indexed disclinations in nematic liquid crystals". In: *Philosophical Magazine* 27 (Mar. 23, 1972), pp. 405–424.

[102] Wolfgang Helfrich. "Elastic properties of lipid bilayers: theory and possible experiments". In: *Zeitschrift fur Naturforschung C* 28c (1973), pp. 693–703.

[103] Kenneth G. Wilson and J. Kogut. "The renormalization group and the ε expansion". In: *Physics Reports* 12.2 (1974), pp. 75–199. ISSN: 0370-1573. DOI: `10.1016/0370-1573(74)90023-4`.

[104] Barbara M.F. Pearse. “Coated vesicles from pig brain: Purification and biochemical characterization”. In: *Journal of Molecular Biology* 97.1 (1975), pp. 93–98. ISSN: 0022-2836. DOI: `10.1016/s0022-2836(75)80024-6`.

[105] F. Brochard, P.G. de Gennes, and P. Pfeuty. “Surface tension and deformation of membrane structures: relation to two-dimensional phase transitions”. In: *J. Phys (Paris)* 37 (1976), pp. 1099–1104.

[106] Manfred do Carmo. *Differential geometry of curves and surfaces*. 1976. ISBN: 0132125897. URL: `http://www2.ing.unipi.it/griff/files/dC.pdf`.

[107] Hans Meinhardt. “Morphogenesis of Lines and Nets”. In: *Differentiation* 6 (1976), pp. 117–123. DOI: `10.1111/j.1432-0436.1976.tb01478.x`.

[108] Charles Eames and Ray Eames. *Powers of Ten*. 1977. URL: `https://www.youtube.com/watch?v=55Gpm1Q0abk`.

[109] Dieter Forster, David R. Nelson, and Michael J. Stephen. “Large-distance and long-time properties of a randomly stirred fluid”. In: *Physical Review A* 16.2 (1977), pp. 732–749. ISSN: 1050-2947. DOI: `10.1103/physreva.16.732`.

[110] G. J. Mitchison. “Phyllotaxis and the Fibonacci Series: An explanation is offered for the characteristic spiral leaf arrangement found in many plants.” In: *Science* (Apr. 1977). DOI: `10.1126/science.196.4287.270`.

[111] Ingrid Carlbom and Joseph Paciorek. “Planar Geometric Projections and Viewing Transformations”. In: *ACM Comput. Surv.* 10.4 (Dec. 1978), pp. 465–502. ISSN: 0360-0300. DOI: `10.1145/356744.356750`. URL: `https://doi.org/10.1145/356744.356750`.

[112] Charles Y. Young, Ronald Pindak, Noel A. Clark, and Robert B. Meyer. “Light-scattering study of two-dimensional molecular-orientation fluctuations in freely suspended ferroelectric liquid-crystal films”. In: *Phys. Rev. Lett.* 40 (1978), pp. 773–776.

[113] N. D. Mermin. “The topological theory of defects in ordered media”. In: *Reviews of Modern Physics* 51.3 (1979), pp. 591–648. ISSN: 0034-6861. DOI: `10.1103/revmodphys.51.591`.

[114] G. J. Mitchison. “A model for vein formation in higher plants”. In: *Proceedings of the Royal Society of London. Series B. Biological Sciences* 207.1166 (1980), pp. 79–109. ISSN: 0080-4649. DOI: `10.1098/rspb.1980.0015`.

[115] R. C. T. da Costa. “Quantum mechanics of a constrained particle”. In: *Phys. Rev. A* 23 (4 Apr. 1981), pp. 1982–1987. DOI: `10.1103/PhysRevA.23.1982`. URL: `https://link.aps.org/doi/10.1103/PhysRevA.23.1982`.

[116] JD Murray. “A pre-pattern formation mechanism for animal coat markings”. In: *Journal of Theoretical Biology* 88.1 (1981), pp. 161–199. ISSN: 0022-5193. DOI: `https://doi.org/10.1016/0022-5193(81)90334-9`. URL: `http://www.sciencedirect.com/science/article/pii/0022519381903349`.

[117] S Aubry. “The devil’s stair case transformation in incommensurate lattices”. In: *The Riemann Problem, Complete Integrability and Arithmetic Applications* (1982), pp. 221–245.

[118] P.G. de Gennes and C. Taupin. “Microemulsions and the flexibility of oil/water interfaces”. In: *Journal of Physical Chemistry* 86 (1982), pp. 2294–2304.

[119] Benoit B. Mandelbrot. *The fractal geometry of nature*. Times Books, 1982. ISBN: 0716711869.

[120] Hans Meinhardt. *Models of Biological Pattern Formation*. Academic Press, 1982. URL: `https://www.researchgate.net/publication/281202174_Models_of_Biological_Pattern_Formation_Academic_Press_London_1982`.

[121] Leslie Valiant. “A Theory of the Learnable”. In: *Communications of the ACM* 27.11 (1984). DOI: `10.1145/1968.1972`.

[122] “On Growth and Form, Fractal and Non-Fractal Patterns in Physics”. In: (1985). DOI: `10.1007/978-94-009-5165-5`.

[123] Mehran Kardar, Giorgio Parisi, and Yi-Cheng Zhang. “Dynamic Scaling of Growing Interfaces”. In: *Physical Review Letters* 56 (9 1986).

[124] H. Kleinert. “Thermal softening of curvature elasticity in membranes”. In: *Physical Letters* 114A (5 Feb. 24, 1986), pp. 263–268.

[125] D.R. Nelson and L. Peliti. “Fluctuations in membranes with crystalline and hexatic order”. In: *Journal de Physique* 48 (1987), pp. 1085–1092.

[126] F David. “Geometry and field theory of random surfaces and membranes”. In: *Statistical Mechanics of Membranes and Surfaces, Jerusalem, Israel*. Jerusalem Winter School for Theoretical Physics SACLAY-SPHT-T-88-193 (May 1988), p. 68.

[127] L.I. Schiff. *Quantum mechanics*. McGraw-Hill, 1988. URL: `http://books.google.com/books?id=KioDTwEACAAJ`.

[128] H.S. Seung and D.R. Nelson. “Defects in flexible membranes with crystalline order”. In: *Phys. Rev. A* 38 (2 1988), p. 1005.

[129] J E Heuser and R G Anderson. “Hypertonic media inhibit receptor-mediated endocytosis by blocking clathrin-coated pit formation.” In: *The Journal of cell biology* 108.2 (1989), pp. 389–400. ISSN: 0021-9525. DOI: `10.1083/jcb.108.2.389`.

[130] A. Yu. Kitaev and L. S. Levitov. “Superconductivity of quasiperiodic layer structures”. In: *Zh. Eksp. Teor. Fiz.* 95 (1989), pp. 311–321. URL: `http://jetp.ras.ru/cgi-bin/dn/e_068_01_0176.pdf`.

[131] Michael P Philpott, Martin R Green, and Terence Kealey. “Human hair growth in vitro”. In: *Journal of cell science* 97.3 (1990), pp. 463–471. URL: `http://jcs.biologists.org/content/joces/97/3/463.full.pdf`.

[132] Przemyslaw Prusinkiewicz and Aristid Lindenmayer. *The Algorithmic Beauty of Plants*. The Virtual Laboratory. 1990. ISBN: 9780387946764. DOI: `10.1007/978-1-4613-8476-2`. URL: `http://algorithmicbotany.org/papers/abop/abop.pdf`. See also the many papers at the Algorithmic Botany website.

[133] Nathan Seiberg. "Notes on Quantum Liouville Theory and Quantum Gravity". In: *Progress in Theoretical Physics* Supplement 102 (1990), pp. 319–349.

[134] F. David and S. Leibler. "Vanishing tension of fluctuating membranes". In: *J. Phys. II France* 1 (1991), pp. 959–976.

[135] Yoshi Fukui and Shinya Inoue. "Cell division in dictyostelium with special emphasis on actomyosin organization in cytokinesis". In: *Cell Motility and the Cytoskeleton* 18 (1991), pp. 41–54.

[136] Erwin Kreyszig. *Differential Geometry.* Dover Publications, 1991.

[137] L. S. Levitov. "Phyllotaxis of flux lattices in layered superconductors". In: *Physical Review Letters* 66.2 (1991), pp. 224–227. ISSN: 0031-9007. DOI: `10.1103/physrevlett.66.224`.

[138] L.S. Levitov. "Fibonacci numbers in botany and physics: Phyllotaxis". In: *Pis'maZh. Eksp.Teor.Fiz* 54 (Nov. 1991), pp. 542–545.

[139] F.C. MacKintosh and T.C. Lubensky. "Orientational order, topology, and vesicle shapes". In: *Phys. Rev. Lett.* 67 (9 1991), p. 1169.

[140] Udo Seifert, Karin Berndl, and Reinhard Lipowsky. "Shape transformations of vesicles: phase diagrams for spontaneous-curvature and bilayer coupling models". In: *Physical Review A* 44 (2 1991), pp. 1182–1202.

[141] Philip Nelson and Thomas Powers. "Rigid Chiral Membranes". In: *Phys. Rev. Lett.* 69.23 (1992), pp. 3409–3412.

[142] M. C. Cross and P. C. Hohenberg. "Pattern formation outside of equilibrium". In: *Reviews of Modern Physics* 65.3 (1993), pp. 851–1112. ISSN: 0034-6861. DOI: `10.1103/revmodphys.65.851`.

[143] P. G. de Gennes. *The Physics of Liquid Crystals.* Oxford Unversity Press, 1993. ISBN: 0 19 851785 8.

[144] M. Goulian, R. Bruinsma, and P. Pincus. "Long-Range Forces in Heterogeneous Fluid Membranes". In: *EPL (Europhysics Letters)* 22.2 (1993), pp. 145–150. ISSN: 0295-5075. DOI: `10.1209/0295-5075/22/2/012`.

[145] Philip Nelson and Thomas Powers. "Renormalization of chiral couplings in tilted bilayer membranes". In: *J. Phys. II France* 3 (1993), pp. 1535–1569.

[146] M.S. Spector, S. Sprunt, and J.D. Litster. "Novel dynamical mode in a tilted smectic liquid-crystal film". In: *Phys. Rev. E* 47 (2 1993), pp. 1101–1107.

[147] David R. Nelson. *Ch. 5 of Fluctuating geometries in statistical mechanics and field theory. Defects in superfluids, superconductors and membranes.* Les Houches LXII, Elsevier Science, 1994. Chap. 5, pp. 423–477.

[148] Richard M. Schoen and Shing-Tung Yau. *Lectures on differential geometry*. Conference Proceedings and Lecture Note. International Press, 1994, p. 414. ISBN: 1571460128. URL: `https://books.google.com/books?id=d4VtQgAACAAJ`.

[149] Ramamurti Shankar. "Principles of quantum mechanics". In: (Jan. 1994), p. 676. URL: `http://www.springer.com/physics/quantum+physics/book/978-0-306-44790-7`.

[150] Albert-László Barabási and H. Eugene Stanley. *Fractal Concepts in Surface Growth*. Cambridge University Press, 1995.

[151] Timothy Halpin-Healy and Yi-Cheng Zhang. "Kinetic roughening phenomena, stochastic growth, directed polymers and all that. Aspects of multidisciplinary statistical mechanics". In: *Physics Reports* 254.4–6 (1995), pp. 215–414. ISSN: 0370-1573. DOI: `10.1016/0370-1573(94)00087-j`.

[152] Thomas Powers and Philip Nelson. "Fluctuating Membranes with Tilt Order". In: *J. Phys. II France* 5 (1995), pp. 1671–1678.

[153] John Toner and Yuhai Tu. "Long-Range Order in a Two-Dimensional Dynamical XY Model: How Birds Fly Together". In: *Physical Review Letters* 75.23 (1995), pp. 4326–4329. ISSN: 0031-9007. DOI: `10.1103/physrevlett.75.4326`.

[154] Tamás Vicsek, András Czirók, Eshel Ben-Jacob, Inon Cohen, and Ofer Shochet. "Novel Type of Phase Transition in a System of Self-Driven Particles". In: *Physical Review Letters* 75.6 (1995), pp. 1226–1229. ISSN: 0031-9007. DOI: `10.1103/physrevlett.75.1226`.

[155] John Cardy and Uwe C. Täuber. "Theory of Branching and Annihilating Random Walks". In: *Physical Review Letters* 77.23 (1996), pp. 4780–4783. ISSN: 0031-9007. DOI: `10.1103/physrevlett.77.4780`.

[156] R.M.L. Evans. "Theoretical study of fluid membranes of spherical topology with internal degrees of freedom". In: *Phys. Rev. E* 53 (1 1996), pp. 935–949.

[157] Robert W. Field. "5.76 Molecular Spectra and Molecular Structure, Spring 1996". In: (1996). URL: `http://hdl.handle.net/1721.1/49430`.

[158] Matteo Marsili, Amos Maritan, Flavio Toigo, and Jayanth R. Banavar. "Stochastic growth equations and reparametrization invariance". In: *Reviews of Modern Physics* 68.4 (1996), pp. 963–983. ISSN: 0034-6861. DOI: `10.1103/revmodphys.68.963`.

[159] J.M. Park. "Kosterlitz-Thouless transitions on a fluctuating surface of genus zero". In: *Phys. Rev. E* 54 (1996), pp. 5414–5419.

[160] A. N. Shalaginov. "Flucturations and light scattering in free-standing smectic-C films". In: *Phys. Rev. E* 53.4 (1996), pp. 3623–3628.

[161] Joachim Krug. "Origins of scale invariance in growth processes". In: *Advances in Physics* 46.2 (1997), pp. 139–282.

[162] Francois Nedelec, T. Surrey, A.C. Maggs, and Stanislas Leibler. "Self-organization of microtubules and motors". In: *Nature* 389 (Sept. 18, 1997), pp. 305–308.

[163] Steven Rosenberg. *The Laplacian on a Riemannian Manifold: An Introduction to Analysis on Manifolds*. London Mathematical Society Student Texts. Cambridge University Press, Jan. 1997, p. 172. DOI: `10.1017/CBO9780511623783`.

[164] Udo Seifert. "Configurations of fluid membranes and vesicles". In: *Advances in physics* 46.1 (1997), pp. 13–137.

[165] Thomas Surrey, Francois Nedelec, Stanislas Leibler, and Eric Karsenti. "Physical properties determining self-organization of microtubules and motors". In: *Science* 292 (May 11, 1997), pp. 1167–1171.

[166] Geoffrey B. West, James H. Brown, and Brian J. Enquist. "A General Model for the Origin of Allometric Scaling Laws in Biology". In: *Science* 276.5309 (1997), pp. 122–126. ISSN: 0036-8075. DOI: `10.1126/science.276.5309.122`.

[167] J. B. Fournier and L. Peliti. "Paired defects in nematic surfactant bilayers". In: *Phys. Rev. E* 58.6 (1998), R6919–R6922.

[168] Hyun-Woo Lee and Leonid Levitov. "Universality in Phyllotaxis: a Mechanical Theory". In: *Symmetry in Plants*. Published in March 1998 in Symmetry in Plants (a book) and then posted on the arxiv years later: 1998. DOI: `10.1142/9789814261074_0024`. URL: `https://arxiv.org/pdf/2101.02652.pdf`.

[169] John Toner and Yuhai Tu. "Flocks, herds, and schools: A quantitative theory of flocking". In: *Physical Review E* 58.4 (1998), pp. 4828–4858. ISSN: 1539-3755. DOI: `10.1103/physreve.58.4828`.

[170] R. A. Barrio, C. Varea, J. L. Aragón, and P. K. Maini. "A two-dimensional numerical study of spatial pattern formation in interacting Turing systems". In: *Bulletin of Mathematical Biology* 61.3 (May 1999), pp. 483–505. ISSN: 1522-9602. DOI: `10.1006/bulm.1998.0093`. URL: `https://doi.org/10.1006/bulm.1998.0093`.

[171] Geoffrey B. West, James H. Brown, and Brian J. Enquist. "A general model for the structure and allometry of plant vascular systems". In: *Nature* 400.6745 (1999), pp. 664–667. ISSN: 0028-0836. DOI: `10.1038/23251`.

[172] Geoffrey B. West, James H. Brown, and Brian J. Enquist. "The Fourth Dimension of Life: Fractal Geometry and Allometric Scaling of Organisms". In: *Science* 284.5420 (1999), pp. 1677–1679. ISSN: 0036-8075. DOI: `10.1126/science.284.5420.1677`.

[173] Mehran Kardar. "Roughness and ordering of growing films". In: *Physica A: Statistical Mechanics and its Applications* 281.1–4 (2000), pp. 295–310. ISSN: 0378-4371. DOI: `10.1016/s0378-4371(00)00028-5`.

[174] Charles W. Misner, Kip S. Thorne, and John A. Wheeler. *Gravitation*. Freeman San Francisco, CA, 2000.

[175] Leonard M. Sander. "Diffusion-limited aggregation: A kinetic critical phenomenon?" In: *Contemporary Physics* 41.4 (2000), pp. 203–218. ISSN: 0010-7514. DOI: `10.1080/001075100409698`.

[176] *Branching in Nature, Dynamics and Morphogenesis of Branching Structures, from Cell to River Networks.* Centre de Physique des Houches. 2001. ISBN: 9783540418887. DOI: `10.1007/978-3-662-06162-6`.

[177] Ha Youn Lee and Mehran Kardar. "Macroscopic equations for pattern formation in mixtures of microtubules and motors". In: *Phys. Rev. E* 64 (2001), p. 056113.

[178] Y. Couder, L. Pauchard, C. Allain, M. Adda-Bedia, and S. Douady. "The leaf venation as formed in a tensorial field". In: *The European Physical Journal B - Condensed Matter and Complex Systems* 28.2 (2002), pp. 135–138. ISSN: 1434-6028. DOI: `10.1140/epjb/e2002-00211-1`.

[179] Jordi Faraudo. "Diffusion equation on curved surfaces. I. Theory and application to biological membranes". In: *The Journal of Chemical Physics* 116.13 (2002), pp. 5831–5841. DOI: `10.1063/1.1456024`. URL: `https://doi.org/10.1063/1.1456024`.

[180] Randall D. Kamien. "The geometry of soft materials: a primer". In: *Rev. Mod. Phys.* 74 (2002), pp. 953–971.

[181] Randall D. Kamien. "The geometry of soft materials: a primer". In: *Reviews of Modern Physics* 74.4 (2002), pp. 953–971. ISSN: 0034-6861. DOI: `10.1103/revmodphys.74.953`.

[182] Yonathan Kozlovsky and Michael M. Kozlov. "Stalk Model of Membrane Fusion: Solution of Energy Crisis". In: *Biophysical Journal* 82.2 (2002), pp. 882–895. ISSN: 0006-3495. DOI: `10.1016/s0006-3495(02)75450-7`.

[183] Maher Moakher. "Means and Averaging in the Group of Rotations". In: *SIAM Journal on Matrix Analysis and Applications* 24.1 (2002), pp. 1–16. ISSN: 0895-4798. DOI: `10.1137/s0895479801383877`.

[184] David R. Nelson. *Defects and Geometry in Condensed Matter Physics*. Cambridge University Press, 2002.

[185] R. Osserman. *A Survey of Minimal Surfaces.* Dover Phoenix editions. Dover Publications, 2002. ISBN: 9780486495149. URL: `https://books.google.com/books?id=WHN444vBvioC`.

[186] Henning Schmidgen. "Of frogs and men: the origins of psychophysiological time experiments, 1850–1865". In: *Endeavour* 26.4 (2002), pp. 142–148. ISSN: 0160-9327. DOI: `10.1016/s0160-9327(02)01466-7`.

[187] Eric W. Weisstein. *Tractrix.* from MathWorld, A Wolfram Web Resource, 2002. URL: `http://mathworld.wolfram.com/Tractrix.html`.

[188] Francois David. *Chap. 7 of Statistical Mechanics of Membranes 2nd Ed. Geometry and Field Theory of Random Surfaces and Membranes.* World Scientific Publ., 2003. Chap. 7, pp. 149–210.

[189] Kenneth Falconer. *Fractal Geometry: Mathematical Foundations and Applications.* John Wiley & Sons, Ltd, Sept. 19, 2003. ISBN: 9780470848616. DOI: `10.1002/0470013850`.

[190] Thomas D Pollard and Gary G Borisy. "Cellular Motility Driven by Assembly and Disassembly of Actin Filaments". In: *Cell* 112.4 (2003), pp. 453–465. ISSN: 0092-8674. DOI: `10.1016/s0092-8674(03)00120-x`.

[191] Gerald A. Edgar. *Classics On Fractals.* 2004. ISBN: 9780367157265. URL: `https://www.routledge.com/Classics-On-Fractals/Edgar/p/book/9780367157265`.

[192] Alexander Fotin, Yifan Cheng, Piotr Sliz, Nikolaus Grigorieff, Stephen C. Harrison, Tomas Kirchhausen, and Thomas Walz. "Molecular model for a complete clathrin lattice from electron cryomicroscopy". In: *Nature* 432.7017 (2004), pp. 573–579. ISSN: 0028-0836. DOI: `10.1038/nature03079`.

[193] Jemal Guven. "Membrane geometry with auxiliary variables and quadratic constraints". In: *Journal of Physics A: Mathematical and General* 37.28 (2004), p. L313. ISSN: 0305-4470. DOI: `10.1088/0305-4470/37/28/l02`. eprint: `math-ph/0404064`.

[194] M. F. Islam, A. M. Alsayed, Z. Dogic, J. Zhang, T. C. Lubensky, and A. G. Yodh. "Nematic Nanotube Gels". In: *Phys. Rev. Lett.* 92 (2004), p. 088303.

[195] Charles Kittel. *Introduction to Solid State Physics.* John Wiley & Sons, 2004.

[196] George W. Koch, Stephen C. Sillett, Gregory M. Jennings, and Stephen D. Davis. "The limits to tree height". In: *Nature* 428.6985 (2004), pp. 851–854. ISSN: 0028-0836. DOI: `10.1038/nature02417`.

[197] Eric M. Kramer and Michael H. Borkowski. "Wood grain patterns at branch junctions: modeling and implications". In: *Trees* 18.5 (2004), pp. 493–500. ISSN: 0931-1890. DOI: `10.1007/s00468-004-0322-2`.

[198] Marco Cosentino Lagomarsino. *Biologically Inspired Problems Concerning Semiflexible Filaments. Organization in Plant Cell Geometries, and Hydrodynamics of Propulsion.* 2004. Chap. Chapter 3: Microtubules Confined in a Quasi-Two-Dimensional Planar Geometry. ISBN: 90-77209-08-5.

[199] A. Pattanaporkratana, C. S. Park, J. E. Maclennan, and N. A. Clark. "Manipulation of Islands on Freely Suspended Smectic Films and Bubbles Using Optical Tweezers". In: *Ferroelectrics* 310 (2004), pp. 131–135. DOI: `DOI:10.1080/00150190490510537`. URL: `http://www.informaworld.com/index/713617930.pdf`.

[200] Brian J. Peter, Helen M. Kent, Ian G. Mills, Yvonne Vallis, P. Jonathan G. Butler, Philip R. Evans, and Harvey T. McMahon. "BAR Domains as Sensors of Membrane Curvature: The Amphiphysin BAR Structure". In: *Science* 303.5657 (2004), pp. 495–499. ISSN: 0036-8075. DOI: `10.1126/science.1092586`.

[201] Andrea Prosperetti. "Bubbles". In: *Physics of Fluids* 16.6 (2004), pp. 1852–1865. ISSN: 1070-6631. DOI: `10.1063/1.1695308`.

[202] Przemyslaw Prusinkiewicz. "Modeling plant growth and development". In: *Current Opinion in Plant Biology* 7.1 (2004), pp. 79–83. ISSN: 1369-5266. DOI: `10.1016/j.pbi.2003.11.007`.

[203] Erik M Rauch and Mark M Millonas. “The role of trans-membrane signal transduction in turing-type cellular pattern formation”. In: *Journal of Theoretical Biology* 226.4 (2004), pp. 401–407. ISSN: 0022-5193. DOI: `10.1016/j.jtbi.2003.09.018`. URL: `http://www.sciencedirect.com/science/article/pii/S0022519303003588`.

[204] V. Vitelli and D.R. Nelson. “Defect generation and confinement in corrugated topographies”. In: *Phys. Rev. E* 70 (2004), p. 051105.

[205] V. Vitelli and A. Turner. “Anomalous coupling between between topological defects and curvature”. In: *Phys. Rev. Lett.* 93 (2004), p. 215301.

[206] Joshua Zimmerberg and Stuart McLaughlin. “Membrane Curvature: How BAR Domains Bend Bilayers”. In: *Current Biology* 14.6 (2004), R250–R252. ISSN: 0960-9822. DOI: `10.1016/j.cub.2004.02.060`.

[207] Attila G. Császár, Gábor Czakó, Tibor Furtenbacher, Jonathan Tennyson, Viktor Szalay, Sergei V. Shirin, Nikolai F. Zobov, and Oleg L. Polyansky. “On equilibrium structures of the water molecule”. In: *The Journal of Chemical Physics* 122.21 (2005), p. 214305. ISSN: 0021-9606. DOI: `10.1063/1.1924506`.

[208] Boris Khesin and VI Arnold. “Topological fluid dynamics”. In: *Notices AMS* 52.1 (2005), pp. 9–19. URL: `https://www.ams.org/journals/notices/200501/fea-khesin.pdf`.

[209] Martin Michael Müller, Markus Deserno, and Jemal Guven. “Interface-mediated interactions between particles: A geometrical approach”. In: *Physical Review E* 72.6 (2005), p. 061407. ISSN: 1539-3755. DOI: `10.1103/physreve.72.061407`.

[210] Adam Runions, Martin Fuhrer, Brendan Lane, Pavol Federl, Anne-Gaëlle Rolland-Lagan, and Przemyslaw Prusinkiewicz. “Modeling and visualization of leaf venation patterns”. In: *ACM Transactions on Graphics (TOG)* 24.3 (2005), pp. 702–711. ISSN: 0730-0301. DOI: `10.1145/1073204.1073251`.

[211] Alexander Zumdieck, Marco Cosentino Lagomarsino, Catalin Tanase, Karsten Kruse, Bela Mulder, Marileen Dogterom, and Frank Julicher. “Continuum description of the cytoskeleton: ring formation in the cell cortex”. In: *Phys. Rev. Lett.* 95 (2005), p. 258103.

[212] R Capovilla and J Guven. “Helfrich-Canham bending energy as a constrained nonlinear sigma model”. In: *Journal of Physics: Mathematical and General* 38 (2006), pp. 2593–2597.

[213] E Crivellato and D Ribatti. “Aristotle: the first student of angiogenesis”. In: *Leukemia* 20.7 (2006), pp. 1209–1210. ISSN: 0887-6924. DOI: `10.1038/sj.leu.2404256`.

[214] P. Gutjahr, R. Lipowsky, and J. Kierfeld. “Persistence length of semiflexible polymers and bending rigidity renormalization”. In: *Europhysics Letters* 76.6 (2006), pp. 994–1000.

[215] Jemal Guven. “Laplace pressure as a surface stress in fluid vesicles”. In: *Journal of Physics A: Mathematical and General* 39.14 (2006), p. 3771. ISSN: 0305-4470. DOI: `10.1088/0305-4470/39/14/019`.

[216] Eric M. Kramer. “Wood Grain Pattern Formation: A Brief Review”. In: *Journal of Plant Growth Regulation* 25.4 (2006), pp. 290–301. ISSN: 0721-7595. DOI: `10.1007/s00344-006-0065-y`.

[217] Allen R. Sanderson, Robert M. Kirby, Chris R. Johnson, and Lingfa Yang. “Advanced Reaction-Diffusion Models for Texture Synthesis”. In: *Journal of Graphics, GPU, and Game Tools* 11.3 (2006), pp. 47–71. ISSN: 2151-237X. DOI: `10.1080/2151237x.2006.10129222`.

[218] Stefanie Sick, Stefan Reinker, Jens Timmer, and Thomas Schlake. “WNT and DKK determine hair follicle spacing through a reaction-diffusion mechanism”. In: *Science* 314.5804 (2006), pp. 1447–1450. URL: `http://science.sciencemag.org/content/314/5804/1447`.

[219] Shigeo Takamori, Matthew Holt, Katinka Stenius, Edward A. Lemke, Mads Grønborg, Dietmar Riedel, Henning Urlaub, Stephan Schenck, Britta Brügger, Philippe Ringler, Shirley A. Müller, Burkhard Rammner, Frauke Gräter, Jochen S. Hub, Bert L. De Groot, Gottfried Mieskes, Yoshinori Moriyama, Jürgen Klingauf, Helmut Grubmüller, John Heuser, Felix Wieland, and Reinhard Jahn. “Molecular Anatomy of a Trafficking Organelle”. In: *Cell* 127.4 (2006), pp. 831–846. ISSN: 0092-8674. DOI: `10.1016/j.cell.2006.10.030`.

[220] V. Vitelli, J. B. Lucks, and D. R. Nelson. “Crystallography on curved surfaces”. In: *Proc. Natl. Acad. Sci. U.S.A.* 103 (2006), p. 12323.

[221] V. Vitelli and D.R. Nelson. “Nematic textures on spherical shells”. In: *Phys. Rev. E* 74 (2006), p. 021711.

[222] Eric W. Weisstein. *Complete Elliptic Integral of the Second Kind.* from MathWorld, A Wolfram Web Resource, 2006. URL: `http://mathworld.wolfram.com/CompleteEllipticIntegraloftheSecondKind.html`.

[223] Alexander Zaitsev. “Messaging to extra-terrestrial intelligence”. In: *arXiv preprint physics/0610031* (2006).

[224] Leonid Levitov. *How much number theory do you have to know to be a sunflower?* June 2007. URL: `http://www.mit.edu/~levitov/FibonacciPhyllotaxis.pdf`.

[225] Martin Michael Müller. “Theoretical Studies of Fluid Membrane Mechanics”. Johannes Gutenberg-Universität Mainz, Nov. 2007, p. 244. DOI: `10.25358/openscience-1697`. URL: `https://openscience.ub.uni-mainz.de/handle/20.500.12030/1699`.

[226] A Pereira, PMJ Trevelyan, U Thiele, and S Kalliadasis. “Dynamics of a horizontal thin liquid film in the presence of reactive surfactants”. In: *Physics of Fluids* 19 (2007), p. 112102.

[227] Benedict J. Reynwar, Gregoria Illya, Vagelis A. Harmandaris, Martin M. Müller, Kurt Kremer, and Markus Deserno. “Aggregation and vesiculation of membrane proteins by curvature-mediated interactions”. In: *Nature* 447.7143 (2007), pp. 461–464. ISSN: 0028-0836. DOI: `10.1038/nature05840`.

[228] Adam Runions, Brendan Lane, and Przemyslaw Prusinkiewicz. “Modeling Trees with a Space Colonization Algorithm”. In: *Eurographics Workshop on Natural Phenomena*. Eurographics Workshop on Natural Phenomena. 2007.

[229] Eric W. Weisstein. *Hypergeometric Differential Equation*. from MathWorld, A Wolfram Web Resource, 2007. URL: `http://mathworld.wolfram.com/HypergeometricDifferentialEquation.html`.

[230] Eric W. Weisstein. *Pseudosphere*. from MathWorld, A Wolfram Web Resource, 2007. URL: `http://mathworld.wolfram.com/Pseudosphere.html`.

[231] Guihua Yu, Anyuan Cao, and Charles M. Lieber. “Nanotechnology meets bubbleology”. In: *Nature Nanotechnology* 2 (2007), pp. 339–340.

[232] V Braun, T Brelidze, MR Douglas, and BA Ovrut. “Eigenvalues and eigenfunctions of the scalar Laplace operator on Calabi-Yau manifolds”. In: *Journal of High Energy Physics* 2008 (2008), p. 120.

[233] Wei Chen, Margit Foss, Kuo-Fu Tseng, and Dahong Zhang. “Redundant Mechanisms Recruit Actin into the Contractile Ring in Silkworm Spermatocytes”. In: *PLoS Biology* 6.9 (2008), e209. ISSN: 1544-9173. DOI: `10.1371/journal.pbio.0060209`.

[234] Carlos Escudero. “Geometric Principles of Surface Growth”. In: *Physical Review Letters* 101.19 (2008), p. 196102. ISSN: 0031-9007. DOI: `10.1103/physrevlett.101.196102`.

[235] John R. Frank and Mehran Kardar. “Defects in nematic membranes can buckle into pseudospheres”. In: *Physical Review E* 77.4 (Apr. 2008). Preprint: `https://doi.org/10.48550/arXiv.0710.5870`. URL: `https://doi.org/10.1103/PhysRevE.77.041705`.

[236] Eric M. Kramer, Michael Lewandowski, Satvik Beri, Jessica Bernard, Matthew Borkowski, Michael H. Borkowski, Laura Ann Burchfield, Brenda Mathisen, and Jennifer Normanly. “Auxin Gradients Are Associated with Polarity Changes in Trees”. In: *Science* (June 2008). DOI: `10.1126/science.1156130`. URL: `https://www-science-org.libproxy.mit.edu/doi/epdf/10.1126/science.1156130`.

[237] Martin Loose, Elisabeth Fischer-Friedrich, Jonas Ries, Karsten Kruse, and Petra Schwille. “Spatial Regulators for Bacterial Cell Division Self-Organize into Surface Waves in Vitro”. In: *Science* 320.5877 (2008), pp. 789–792. ISSN: 0036-8075. DOI: `10.1126/science.1154413`.

[238] Carlos A. Lugo and Alan J. McKane. “Quasicycles in a spatial predator-prey model”. In: *Phys. Rev. E* 78 (5 Nov. 2008), p. 051911. DOI: `10.1103/PhysRevE.78.051911`. URL: `https://link.aps.org/doi/10.1103/PhysRevE.78.051911`.

[239] *Protein Structure and Function*. Oxford University Press, 2008.

[240] Hans Meinhardt. “The Algorithmic Beauty of Sea Shells”. In: *The Virtual Laboratory* (2009). ISSN: 1431-939X. DOI: `10.1007/978-3-540-92142-4`.

[241] Akiko Nakamasu, Go Takahashi, Akio Kanbe, and Shigeru Kondo. “Interactions between zebrafish pigment cells responsible for the generation of Turing patterns”. In: *Proceedings of the National Academy of Sciences* 106.21 (2009), pp. 8429–8434. URL: `http://www.pnas.org/content/106/21/8429`.

[242] Rob Phillips, Tristan Ursell, Paul Wiggins, and Pierre Sens. “Emerging roles for lipids in shaping membrane-protein function”. In: *Nature* 459.7245 (2009), pp. 379–385. ISSN: 0028-0836. DOI: `10.1038/nature08147`.

[243] Christophe Almarcha, Philip MJ Trevelyan, Patrick Grosfils, and Anne De Wit. “Chemically driven hydrodynamic instabilities”. In: *Phys. Rev. Lett.* 104.4 (2010), p. 044501. URL: `https://doi.org/10.1103/PhysRevLett.104.044501`.

[244] P Castro-Villarreal. “Brownian motion meets Riemann curvature”. In: *Journal of Statistical Mechanics* P08006 (Jan. 2010). DOI: `10.1088/1742-5468/2010/08/P08006`. see arxiv preprint.

[245] Elisabeth Fischer-Friedrich, Giovanni Meacci, Joe Lutkenhaus, Hugues Chaté, and Karsten Kruse. “Intra- and intercellular fluctuations in Min-protein dynamics decrease with cell length”. In: *Proceedings of the National Academy of Sciences* 107.14 (2010), pp. 6134–6139. ISSN: 0027-8424. DOI: `10.1073/pnas.0911708107`.

[246] Inbal Hecht, David A Kessler, and Herbert Levine. “Transient localized patterns in noise-driven reaction-diffusion systems”. In: *Phys. Rev. Lett.* 104.15 (2010), p. 158301. URL: `https://doi.org/10.1103/PhysRevLett.104.158301`.

[247] Shigeru Kondo and Takashi Miura. “Reaction-Diffusion Model as a Framework for Understanding Biological Pattern Formation”. In: *Science* 329.5999 (2010), pp. 1616–1620. ISSN: 0036-8075. DOI: `10.1126/science.1179047`.

[248] Shigeru Kondo and Takashi Miura. “Reaction-diffusion model as a framework for understanding biological pattern formation”. In: *science* 329.5999 (2010), pp. 1616–1620. URL: `http://science.sciencemag.org/content/329/5999/1616`.

[249] V. M. Savage, L. P. Bentley, B. J. Enquist, J. S. Sperry, D. D. Smith, P. B. Reich, and E. I. von Allmen. “Hydraulic trade-offs and space filling enable better predictions of vascular structure and function in plants”. In: *Proceedings of the National Academy of Sciences* 107.52 (2010), pp. 22722–22727. ISSN: 0027-8424. DOI: 10.1073/pnas.1012194108.

[250] Ari M Turner, Vincenzo Vitelli, and David R Nelson. “Vortices on curved surfaces”. In: *Reviews of Modern Physics* 82.2 (2010), p. 1301. URL: https://doi.org/10.1103/RevModPhys.82.1301.

[251] Justin S Bois, Frank Jülicher, and Stephan W Grill. “Pattern formation in active fluids”. In: *Phys. Rev. Lett.* 106.2 (2011), p. 028103. URL: https://doi.org/10.1103/PhysRevLett.106.028103.

[252] Thomas Butler and Nigel Goldenfeld. “Fluctuation-driven Turing patterns”. In: *Phys. Rev. E* 84 (1 July 2011), p. 011112. DOI: 10.1103/PhysRevE.84.011112. URL: https://link.aps.org/doi/10.1103/PhysRevE.84.011112.

[253] C Haselwandter, M Calamai, M Kardar, A Triller, and R Azeredo da Silveira. “Formation and Stability of Synaptic Receptor Domains”. In: *PRL* 106.23 (June 2011).

[254] Pilnam Kim, Manouk Abkarian, and Howard A. Stone. “Hierarchical folding of elastic membranes under biaxial compressive stress”. In: *Nature Materials* 10.12 (2011), pp. 952–957. ISSN: 1476-1122. DOI: 10.1038/nmat3144.

[255] Max C. Watson, Evgeni S. Penev, Paul M. Welch, and Frank L. H. Brown. “Thermal fluctuations in shape, thickness, and molecular orientation in lipid bilayers”. In: *The Journal of Chemical Physics* 135.24 (2011), p. 244701. ISSN: 0021-9606. DOI: 10.1063/1.3660673.

[256] David P. Feldman. *Chaos and Fractals: An Elementary Introduction.* Oxford University Press, Oct. 12, 2012. ISBN: 9780199566440. URL: https://global.oup.com/academic/product/chaos-and-fractals-9780199566440.

[257] Luca Giomi and M Cristina Marchetti. “Polar patterns in active fluids”. In: *Soft Matter* 8.1 (2012), pp. 129–139. DOI: 10.1039/c1sm06077e.

[258] Jacob Halatek and Erwin Frey. “Highly canalized MinD transfer and MinE sequestration explain the origin of robust MinCDE-protein dynamics.” In: *Cell reports* 1.6 (June 2012), pp. 741–52. ISSN: 2211-1247. DOI: 10.1016/j.celrep.2012.04.005. URL: http://www.ncbi.nlm.nih.gov/pubmed/22813748.

[259] Bo Li, Yan-Ping Cao, Xi-Qiao Feng, and Huajian Gao. “Mechanics of morphological instabilities and surface wrinkling in soft materials: a review”. In: *Soft Matter* 8.21 (2012), pp. 5728–5745. ISSN: 1744-683X. DOI: 10.1039/c2sm00011c.

[260] F. Landis Markley, Yang Cheng, John Lucas Crassidis, and Yaakov Oshman. “Averaging Quaternions”. In: *Journal of Guidance, Control, and Dynamics* 30.4 (2012), pp. 1193–1197. ISSN: 0731-5090. DOI: 10.2514/1.28949. See this earlier version of the paper on NASA’s websitehttps://ntrs.nasa.gov/archive/nasa/casi.ntrs.nasa.gov/20

[261] Guillaume Salbreux, Linda K. Barthel, Pamela A. Raymond, and David K. Lubensky. “Coupling Mechanical Deformations and Planar Cell Polarity to Create Regular Patterns in the Zebrafish Retina”. In: *PLoS Computational Biology* 8.8 (2012), e1002618. ISSN: 1553-734X. DOI: `10.1371/journal.pcbi.1002618`.

[262] Pavel Grinfeld. “Introduction to Tensor Analysis and the Calculus of Moving Surfaces”. In: (2013). DOI: `10.1007/978-1-4614-7867-6`.

[263] Eyal Ben Isaac, Uri Manor, Bechara Kachar, Arik Yochelis, and Nir S Gov. “Linking actin networks and cell membrane via a reaction-diffusion-elastic description of nonlinear filopodia initiation”. In: *Phys. Rev. E* 88.2 (2013), p. 022718. URL: `https://doi.org/10.1103/PhysRevE.88.022718`.

[264] M Cristina Marchetti, Jean-François Joanny, Sriram Ramaswamy, Tanniemola B Liverpool, Jacques Prost, Madan Rao, and R Aditi Simha. “Hydrodynamics of soft active matter”. In: *Reviews of Modern Physics* 85.3 (2013), p. 1143. DOI: `10.1103/RevModPhys.85.1143`.

[265] Yoshiki Sasai. “Cytosystems dynamics in self-organization of tissue architecture”. In: *Nature* 493.7432 (2013), p. 318. URL: `https://www.nature.com/articles/nature11859`.

[266] Linus J. Schumacher, Thomas E. Woolley, and Ruth E. Baker. “Noise-induced temporal dynamics in Turing systems”. In: *Phys. Rev. E* 87 (4 Apr. 2013), p. 042719. DOI: `10.1103/PhysRevE.87.042719`. URL: `https://link.aps.org/doi/10.1103/PhysRevE.87.042719`.

[267] Abraham D. Stroock, Vinay V. Pagay, Maciej A. Zwieniecki, and N. Michele Holbrook. “The Physicochemical Hydrodynamics of Vascular Plants”. In: *Annual Review of Fluid Mechanics* 46.1 (2013), pp. 615–642. ISSN: 0066-4189. DOI: `10.1146/annurev-fluid-010313-141411`.

[268] Christian Westendorf, Jose Negrete, Albert J Bae, Rabea Sandmann, Eberhard Bodenschatz, and Carsten Beta. “Actin cytoskeleton of chemotactic amoebae operates close to the onset of oscillations”. In: *Proceedings of the National Academy of Sciences* (2013), p. 201216629. URL: `http://www.pnas.org/content/pnas/early/2013/02/15/1216629110.full.pdf`.

[269] Danelle Devenport. “The cell biology of planar cell polarity”. In: *Journal of Cell Biology* 207.2 (2014), pp. 171–179. ISSN: 0021-9525. DOI: `10.1083/jcb.201408039`.

[270] Nikta Fakhri, Alok D Wessel, Charlotte Willms, Matteo Pasquali, Dieter R Klopfenstein, Frederick C MacKintosh, and Christoph F Schmidt. “High-resolution mapping of intracellular fluctuations using carbon nanotubes”. In: *Science* 344.6187 (2014), pp. 1031–1035.

[271] Edouard Hannezo, Jacques Prost, and Jean-Francois Joanny. “Theory of epithelial sheet morphology in three dimensions”. In: *Proceedings of the National Academy of Sciences* 111.1 (2014), pp. 27–32. ISSN: 0027-8424. DOI: `10.1073/pnas.1312076111`.

[272] M. S. Jablin, K. Akabori, and J. F. Nagle. “Experimental Support for Tilt-Dependent Theory of Biomembrane Mechanics”. In: *Physical Review Letters* 113.24 (2014), p. 248102. ISSN: 0031-9007. DOI: `10.1103/physrevlett.113.248102`.

[273] K Vijay Kumar, Justin S Bois, Frank Jülicher, and Stephan W Grill. “Pulsatory patterns in active fluids”. In: *Physical Review Letters* 112.20 (2014), p. 208101. URL: `https://doi.org/10.1103/PhysRevLett.112.208101`.

[274] Ryoko Minamino and Masaki Tateno. “Tree Branching: Leonardo da Vinci’s Rule versus Biomechanical Models”. In: *PLoS ONE* 9.4 (2014), e93535. DOI: `10.1371/journal.pone.0093535`.

[275] Karin Nienhaus and G Ulrich Nienhaus. “Fluorescent proteins for live-cell imaging with super-resolution”. In: *Chemical Society Reviews* 43.4 (2014), pp. 1088–1106.

[276] Piotr Szwedziak, Qing Wang, Tanmay A M Bharat, Matthew Tsim, and Jan Löwe. “Architecture of the ring formed by the tubulin homologue FtsZ in bacterial cell division”. In: *eLife* 3 (2014), e04601. ISSN: 2050-084X. DOI: `10.7554/elife.04601`.

[277] Kip S. Thorne. *The science of Interstellar*. W.W. Norton & Company, 2014.

[278] Hiroaki Yamanaka and Shigeru Kondo. “In vitro analysis suggests that difference in cell movement during direct interaction can generate various pigment patterns in vivo”. In: *Proceedings of the National Academy of Sciences* 111.5 (2014), pp. 1867–1872. DOI: `10.1073/pnas.1315416111`.

[279] Junko Yoshida, Ayumi Oshikata-Miyazaki, Seiichi Yokoo, Satoru Yamagami, Toshiaki Takezawa, and Shiro Amano. “Development and evaluation of porcine atelocollagen vitrigel membrane with a spherical curve and transplantable artificial corneal endothelial grafts”. In: *Investigative ophthalmology & visual science* 55.8 (2014), pp. 4975–4981. DOI: `10.1167/iovs.14-14211`.

[280] T. W. Crowther, H. B. Glick, K. R. Covey, C. Bettigole, D. S. Maynard, S. M. Thomas, J. R. Smith, G. Hintler, M. C. Duguid, G. Amatulli, M.-N. Tuanmu, W. Jetz, C. Salas, C. Stam, D. Piotto, R. Tavani, S. Green, G. Bruce, S. J. Williams, S. K. Wiser, M. O. Huber, G. M. Hengeveld, G.-J. Nabuurs, E. Tikhonova, P. Borchardt, C.-F. Li, L. W. Powrie, M. Fischer, A. Hemp, J. Homeier, P. Cho, A. C. Vibrans, P. M. Umunay, S. L. Piao, C. W. Rowe, M. S. Ashton, P. R. Crane, and M. A. Bradford. “Mapping tree density at a global scale”. In: *Nature* 525.7568 (2015), pp. 201–205. ISSN: 0028-0836. DOI: `10.1038/nature14967`.

[281] Yoshimi Nakano, Masatoshi Yamaguchi, Hitoshi Endo, Nur Ardiyana Rejab, and Misato Ohtani. “NAC-MYB-based transcriptional regulation of secondary cell wall biosynthesis in land plants”. In: *Frontiers in Plant Science* 6 (2015), p. 288. ISSN: 1664-462X. DOI: `10.3389/fpls.2015.00288`.

[282] Daniela Rus and Michael T. Tolley. “Design, fabrication and control of soft robots”. In: *Nature* 521.7553 (2015), pp. 467–475. ISSN: 0028-0836. DOI: `10.1038/nature14543`.

[283] Martin Bouda, Joshua S. Caplan, and James E. Saiers. “Box-Counting Dimension Revisited: Presenting an Efficient Method of Minimizing Quantization Error and an Assessment of the Self-Similarity of Structural Root Systems”. In: *Frontiers in Plant Science* 7 (2016), p. 149. ISSN: 1664-462X. DOI: `10.3389/fpls.2016.00149`.

[284] Chi Hin Chan, Magdalena Czubak, and Marcelo M Disconzi. “The formulation of the Navier-Stokes equations on Riemannian manifolds”. In: *arXiv* (2016). DOI: `10.48550/arxiv.1608.05114`.

[285] COMSOL. *Multiphysics*. Version 5.2a. 2016. URL: `https://www.comsol.com`.

[286] Mevlana C Gemici, Danilo Rezende, and Shakir Mohamed. “Normalizing flows on riemannian manifolds”. In: *arXiv preprint arXiv:1611.02304* (2016).

[287] Sankaran Nampoothiri. “Stability of patterns on thin curved surfaces”. In: *Phys. Rev. E* 94 (2 Aug. 2016), p. 022403. DOI: `10.1103/PhysRevE.94.022403`. URL: `https://link.aps.org/doi/10.1103/PhysRevE.94.022403`.

[288] Taha Sochi. “Introduction to Tensor Calculus”. In: *arXiv* (2016). DOI: `10.48550/arxiv.1603.01660`.

[289] Taha Sochi. “Principles of Differential Geometry”. In: *arXiv* (2016). DOI: `10.48550/arxiv.1609.02868`.

[290] Dominik Thalmeier, Jacob Halatek, and Erwin Frey. “Geometry-induced protein pattern formation”. In: *Proceedings of the National Academy of Sciences* 113.3 (2016), pp. 548–553. ISSN: 0027-8424. DOI: `10.1073/pnas.1515191113`. URL: `http://www.pnas.org/content/113/3/548`.

[291] Giulio Vandin, Davide Marenduzzo, Andrew B. Goryachev, and Enzo Orlandini. “Curvature-driven positioning of Turing patterns in phase-separating curved membranes”. In: *Soft Matter* 12 (17 2016), pp. 3888–3896. DOI: `10.1039/C6SM00340K`. URL: `http://dx.doi.org/10.1039/C6SM00340K`.

[292] Silvanus Alt, Poulami Ganguly, and Guillaume Salbreux. “Vertex models: from cell mechanics to tissue morphogenesis”. In: *Philosophical Transactions of the Royal Society B: Biological Sciences* 372.1720 (2017), p. 20150520. ISSN: 0962-8436. DOI: `10.1098/rstb.2015.0520`.

[293] Tommaso Biancalani, Farshid Jafarpour, and Nigel Goldenfeld. “Giant Amplification of Noise in Fluctuation-Induced Pattern Formation”. In: *Phys. Rev. Lett.* 118 (1 Jan. 2017), p. 018101. DOI: `10.1103/PhysRevLett.118.018101`. URL: `https://link.aps.org/doi/10.1103/PhysRevLett.118.018101`.

[294] Francis Corson, Lydie Couturier, Hervé Rouault, Khalil Mazouni, and François Schweisguth. “Self-organized Notch dynamics generate stereotyped sensory organ patterns in Drosophila”. In: *Science* 356.6337 (2017). ISSN: 0036-8075. URL: `https://science.sciencemag.org/content/356/6337/eaai7407`.

[295] Ana R. Fialho, Nelson R. Bernardino, Nuno M. Silvestre, and Margarida M. Telo da Gama. “Effect of curvature on cholesteric liquid crystals in toroidal geometries”. In: *Phys. Rev. E* 95 (1 Jan. 2017), p. 012702. DOI: `10.1103/PhysRevE.95.012702`. URL: `https://link.aps.org/doi/10.1103/PhysRevE.95.012702`.

[296] Edouard Hannezo, Colinda L.G.J. Scheele, Mohammad Moad, Nicholas Drogo, Rakesh Heer, Rosemary V. Sampogna, Jacco van Rheenen, and Benjamin D. Simons. “A Unifying Theory of Branching Morphogenesis”. In: *Cell* 171.1 (2017), 242–255.e27. ISSN: 0092-8674. DOI: `10.1016/j.cell.2017.08.026`.

[297] Hisao Honda. “The world of epithelial sheets”. In: *Development, Growth & Differentiation* 59.5 (2017), pp. 306–316. ISSN: 0012-1592. DOI: `10.1111/dgd.12350`.

[298] John F. Nagle. “Experimentally determined tilt and bending moduli of single-component lipid bilayers”. In: *Chemistry and Physics of Lipids* 205 (2017), pp. 18–24. ISSN: 0009-3084. DOI: `10.1016/j.chemphyslip.2017.04.006`.

[299] S. Nampoothiri and A. Medhi. “Role of curvature and domain shape on Turing patterns”. In: *ArXiv e-prints* (May 2017). arXiv: `1705.02119 [cond-mat.soft]`.

[300] Adam Runions, Miltos Tsiantis, and Przemyslaw Prusinkiewicz. “A common developmental program can produce diverse leaf shapes”. In: *New Phytologist* 216.2 (2017), pp. 401–418. ISSN: 0028-646X. DOI: `10.1111/nph.14449`. URL: `http://algorithmicbotany.org/papers/leaves.nph.2017.pdf`.

[301] Suraj Shankar, Mark J. Bowick, and M. Cristina Marchetti. “Topological Sound and Flocking on Curved Surfaces”. In: *Phys. Rev. X* 7 (3 Sept. 2017), p. 031039. DOI: `10.1103/PhysRevX.7.031039`. URL: `https://link.aps.org/doi/10.1103/PhysRevX.7.031039`.

[302] Sai Yu, Hailong Wang, Yong Ni, Linghui He, Mingyuan Huang, Yuan Lin, Jin Qian, and Hongyuan Jiang. “Tuning interfacial patterns of molecular bonds via surface morphology”. In: *Soft Matter* 13 (35 2017), pp. 5970–5976. DOI: `10.1039/C7SM01278K`. URL: `http://dx.doi.org/10.1039/C7SM01278K`.

[303] Katharina Dürre, Felix C Keber, Philip Bleicher, Fridtjof Brauns, Christian J Cyron, Jan Faix, and Andreas R Bausch. “Capping protein-controlled actin polymerization shapes lipid membranes”. In: *Nature communications* 9 (2018). DOI: `10.1038/s41467-018-03918-1`.

[304] Marko Kaksonen and Aurélien Roux. “Mechanisms of clathrin-mediated endocytosis”. In: *Nature Reviews Molecular Cell Biology* 19.5 (2018), pp. 313–326. ISSN: 1471-0072. DOI: `10.1038/nrm.2017.132`.

[305] Pearson W. Miller, Norbert Stoop, and Jörn Dunkel. “Geometry of Wave Propagation on Active Deformable Surfaces”. In: *Phys. Rev. Lett.* 120 (26 June 2018), p. 268001. DOI: `10.1103/PhysRevLett.120.268001`. URL: `https://link.aps.org/doi/10.1103/PhysRevLett.120.268001`.

[306] DJG Pearce, Perry W Ellis, Alberto Fernandez-Nieves, and L Giomi. "Geometrical control of active turbulence in curved topographies". In: *arXiv preprint arXiv:1805.01455* (2018). URL: `https://arxiv.org/abs/1805.01455`.

[307] Faustino Sánchez-Garduño, Andrew L Krause, Jorge A Castillo, and Pablo Padilla. "Turing-Hopf Patterns on Growing Domains: the Torus and the Sphere". In: *Journal of Theoretical Biology* (2018). URL: `https://doi.org/10.1016/j.jtbi.2018.09.028`.

[308] John R. Frank, Jemal Guven, Mehran Kardar, and Henry Shackleton. "Pinning of Diffusional Patterns by Non-Uniform Curvature". In: *European Physical Letters* (2019).

[309] Marios Hadjieleftheriou. 2019. URL: `https://libspatialindex.org/en/latest/`. See also the python package for this: rtree.

[310] L. Mesarec, W. Góźdź, A. Iglič, V. Kralj-Iglič, E. G. Virga, and S. Kralj. "Normal red blood cells' shape stabilized by membrane's in-plane ordering". In: *Scientific Reports* 9.1 (2019), p. 19742. DOI: `10.1038/s41598-019-56128-0`.

[311] Martin Chaplin. *Water Molecule.* 2020. URL: `http://www1.lsbu.ac.uk/water/water_molecule.html`. If the website is down, see the Archive's copy.

[312] Jean Gallier and Jocelyn Quaintance. "Differential Geometry and Lie Groups, A Computational Perspective". In: *Geometry and Computing* (2020). ISSN: 1866-6795. DOI: `10.1007/978-3-030-46040-2`.

[313] Ivan Marusic and Susan Broomhall. "Leonardo da Vinci and Fluid Mechanics". In: *Annual Review of Fluid Mechanics* 53.1 (2020), pp. 1–25. ISSN: 0066-4189. DOI: `10.1146/annurev-fluid-022620-122816`.

[314] Tzer Han Tan, Jinghui Liu, Pearson W Miller, Melis Tekant, Jörn Dunkel, and Nikta Fakhri. "Topological turbulence in the membrane of a living cell". In: *Nature Physics* 16.6 (2020), pp. 657–662.

[315] Tzer Han Tan, Jinghui Liu, Pearson W. Miller, Melis Tekant, Jörn Dunkel, and Nikta Fakhri. "Topological turbulence in the membrane of a living cell". In: *Nature Physics* 16.6 (2020), pp. 657–662. ISSN: 1745-2473. DOI: `10.1038/s41567-020-0841-9`.

[316] Frank Tavares. "Could Future Homes on the Moon and Mars Be Made of Fungi?" In: (2020). URL: `https://www.nasa.gov/feature/ames/myco-architecture`.

[317] Joshua Batson, C. Grace Haaf, Yonatan Kahn, and Daniel A. Roberts. "Topological obstructions to autoencoding". In: *Journal of High Energy Physics* 2021.4 (2021), p. 280. DOI: `10.1007/jhep04(2021)280`.

[318] Ashley L Beckwith, Jeffrey T Borenstein, and Luis F Velásquez-García. "Tunable plant-based materials via in vitro cell culture using a Zinnia elegans model". In: *Journal of Cleaner Production* 288 (2021), p. 125571.

[319] Jinghui Liu, Jan F. Totz, Pearson W. Miller, Alasdair D. Hastewell, Yu-Chen Chao, Jörn Dunkel, and Nikta Fakhri. "Topological braiding and virtual particles on the cell membrane". In: *Proceedings of the National Academy of Sciences* 118.34 (2021), e2104191118. ISSN: 0027-8424. DOI: `10.1073/pnas.2104191118`.

[320] Peter Petersen. "Classical Differential Geometry". In: (2021). URL: `https://www.math.ucla.edu/~petersen/DiffGeo.pdf`.

[321] Alfredo Sciortino and Andreas R. Bausch. "Pattern formation and polarity sorting of driven actin filaments on lipid membranes". In: *Proceedings of the National Academy of Sciences* 118.6 (2021), e2017047118. ISSN: 0027-8424. DOI: `10.1073/pnas.2017047118`.

[322] Farzan Vafa, Mark J. Bowick, Boris I. Shraiman, and M. Cristina Marchetti. "Fluctuations can induce local nematic order and extensile stress in monolayers of motile cells". In: *Soft Matter* 17.11 (2021), pp. 3068–3073. ISSN: 1744-683X. DOI: `10.1039/d0sm02027c`.

[323] Manon C. Wigbers, Tzer Han Tan, Fridtjof Brauns, Jinghui Liu, S. Zachary Swartz, Erwin Frey, and Nikta Fakhri. "A hierarchy of protein patterns robustly decodes cell shape information". In: *Nature Physics* 17.5 (2021), pp. 578–584. ISSN: 1745-2473. DOI: `10.1038/s41567-021-01164-9`.

[324] Ashley L Beckwith, Jeffrey T Borenstein, and Luis F Velásquez-García. "Physical, mechanical, and microstructural characterization of novel, 3D-printed, tunable, lab-grown plant materials generated from Zinnia elegans cell cultures". In: *Materials Today* 54 (2022), pp. 27–41.

[325] Alison K Cheeseman and Edward R Vrscay. "Estimating the Fractal Dimensions of Vascular Networks and Other Branching Structures: Some Words of Caution". In: *Mathematics* 10.5 (2022), p. 839. DOI: `10.3390/math10050839`.

[326] *Historical Estimates of World Population, before 1950.* 2022. URL: `https://www.census.gov/data/tables/time-series/demo/international-programs/historical-est-worldpop.html`.

[327] Ludwig A. Hoffmann, Livio Nicola Carenza, Julia Eckert, and Luca Giomi. "Theory of defect-mediated morphogenesis". In: *Science Advances* 8.15 (2022), eabk2712. DOI: `10.1126/sciadv.abk2712`.

[328] Ryosuke Nishide and Shuji Ishihara. "Pattern Propagation Driven by Surface Curvature". In: *Physical Review Letters* 128.22 (2022), p. 224101. ISSN: 0031-9007. DOI: `10.1103/physrevlett.128.224101`.

[329] Amit R. Singh, Travis Leadbetter, and Brian A. Camley. "Sensing the shape of a cell with reaction diffusion and energy minimization". In: *Proceedings of the National Academy of Sciences* 119.31 (2022), e2121302119. ISSN: 0027-8424. DOI: `10.1073/pnas.2121302119`.

[330] Farzan Vafa. "Defect dynamics in active polar fluids vs. active nematics". In: *Soft Matter* 18.42 (2022), pp. 8087–8097. ISSN: 1744-683X. DOI: `10.1039/d2sm00830k`.

[331] Farzan Vafa and L. Mahadevan. "Active Nematic Defects and Epithelial Morphogenesis". In: *Physical Review Letters* 129.9 (2022), p. 098102. ISSN: 0031-9007. DOI: `10.1103/physrevlett.129.098102`.

[332] Giorgio Volpe, Clemens Bechinger, Frank Cichos, Ramin Golestanian, Hartmut Löwen, Matthias Sperl, and Giovanni Volpe. "Active matter in space". In: *npj Microgravity* 8.1 (2022), p. 54. ISSN: 2373-8065. DOI: `10.1038/s41526-022-00230-7`.

[333] Huizhen Xu, Alessandro Giannetti, Yuki Sugiyama, Wenna Zheng, René Schneider, Yoichiro Watanabe, Yoshihisa Oda, and Staffan Persson. "Secondary cell wall patterning—connecting the dots, pits and helices". In: *Open Biology* 12.5 (2022), p. 210208. DOI: `10.1098/rsob.210208`.

[334] European Space Agency. *Telling time on the Moon.* Feb. 2023. URL: `https://www.esa.int/Applications/Navigation/Telling_time_on_the_Moon`.

[335] Elizabeth Gibney. "What time is it on the Moon?" In: *Nature* 614.7946 (2023), pp. 13–14. ISSN: 0028-0836. DOI: `10.1038/d41586-023-00185-z`.

[336] Miguel A. Herrada and Jens G. Eggers. "Path instability of an air bubble rising in water". In: *Proceedings of the National Academy of Sciences* 120.4 (2023), e2216830120. ISSN: 0027-8424. DOI: `10.1073/pnas.2216830120`.

[337] Hiroshi Noguchi. "Disappearance, division, and route change of excitable reaction-diffusion waves in deformable membranes". In: *Scientific Reports* 13.1 (2023), p. 6207. DOI: `10.1038/s41598-023-33376-9`.

[338] Jacopo Romano, Benoît Mahault, and Ramin Golestanian. "Dynamical theory of topological defects I: the multivalued solution of the diffusion equation". In: *arXiv* (2023).

[339] Vidar Skogvoll, Jonas Rønning, Marco Salvalaglio, and Luiza Angheluta. "A unified field theory of topological defects and non-linear local excitations". In: *arXiv* (2023).

[340] Masato Tanaka, S. Macrae Montgomery, Liang Yue, Yaochi Wei, Yuyang Song, Tsuyoshi Nomura, and H. Jerry Qi. "Turing pattern–based design and fabrication of inflatable shape-morphing structures". In: *Science Advances* 9.6 (2023), eade4381. DOI: `10.1126/sciadv.ade4381`.

[341] Farzan Vafa, David R Nelson, and Amin Doostmohammadi. "Active topological defect absorption by a curvature singularity". In: *arXiv* (2023).